Three-dimensional numerical modelling of subduction/collision and lithospheric deformation

Dissertation
zur Erlangung des akademischen Grades

"Doktor der Naturwissenschaften"
im Promotionsfach Geologie/Paläontologie

am Fachbereich Chemie, Pharmazie und Geowissenschaften
der Johannes Gutenberg Universität Mainz

von
Adina E. PÜSÖK

geb. in Zalău (Rumänien)

JOHANNES GUTENBERG UNIVERSITÄT MAINZ

JG|U

Mainz, June 2016

D77

Dekan:

1. Berichterstatter:
2. Berichterstatter:
3. Berichterstatter:

Datum der mündlichen Prüfung: 03.06.2016

I would like to dedicate this thesis to my parents, Mariana and András.

Declaration

I hereby declare that except where specific reference is made to the work of others, the contents of this dissertation are original and have not been submitted in whole or in part for consideration for any other degree or qualification in this, or any other University. This dissertation is the result of my own work and includes nothing which is the outcome of work done in collaboration, except where specifically indicated in the text.

Erklärung

Ich versichere hiermit gemäß §10 Abs. 3d der Promotionsordnung des Fachbereichs 09 (Chemie, Pharmazie und Geowissenschaften) der Johannes Gutenberg-Universität Mainz vom 24.07.2007, die als Dissertation vorgelegte Arbeit selbständig und nur unter Verwendung der in der Arbeit angegebenen Hilfsmittel verfasst zu haben. Ich habe oder hatte die hier als Dissertation vorgelegte Arbeit nicht als Prüfungsarbeit für eine staatliche oder andere wissenschaftliche Prüfung eingereicht. Ich hatte weder die jetzt als Dissertation vorgelegte Arbeit noch Teile davon bei einer anderen Fakultät bzw. einem anderen Fachbereich als Dissertation eingereicht.

Adina E. PÜSÖK
Mainz, June 2016

Abstract

One of the most striking features of plate tectonics and lithospheric deformation is the India-Asia collision zone. It is no surprise then that understanding the formation and evolution of the abnormally thick and high Himalaya-Tibet region has been the focus of many tectonic and numerical models. While some of these models have successfully illustrated some of the basic physics of continental collision, none can simultaneously represent active processes such as subduction, underthrusting, delamination, channel flow or extrusion, which are thought to be important during continental convergence, since these mechanisms require the lithosphere to interact with the underlying mantle. Integrated 3-D models of lithosphere and mantle dynamics are needed to overcome these limitations.

In this thesis, I perform systematic 3-D numerical simulations using the code LaMEM, and combine the numerical results with insights from semi-analytical models and scaling analysis to explore some fundamental aspects of continental collision and mountain-building dynamics in an India-Asia collision framework. I applied the models to investigate (i) how subduction and collision affect mountain-building processes and how large topographic plateaus can form in an integrated lithospheric and upper-mantle scale model, (ii) appropriate numerical and theoretical techniques for studying lithospheric deformation at convergent margins, and (iii) how the shape and convergence of Greater India affected the subsequent tectonic evolution of central and SE Asia.

Obtaining anomalously high topographic amplitudes has been a challenge in previous 3-D collision models because contrasting processes simultaneously affect the development of topography. On one hand, continental collision promotes topography build-up through indentation. On the other hand, it also leads to slab break-off and lateral extrusion of material, which act to lower the topography. In a first part of the thesis (Chapter 3), 3-D results suggest that slab pull alone is insufficient to generate high topography, and that external forcing and the presence of heterogeneous strong blocks, such as the Tarim Basin, are necessary to create and shape anomalously high topographic fronts and plateaus. Moreover, different modes of surface expression are predicted in continental collision models, thus improving our understanding of how mountain-belts are formed and sustained.

In the second part, I discuss a common numerical problem of the marker-in-cell method for staggered grids, that of conservative advection of markers (Chapter 2), and I test the effect of rheological approximations on mantle and lithosphere dynamics in a geometrically simplified model setup of subduction/collision (Chapter 4). The model results exhibit a wide range of behaviors depending on the rheological law employed: from linear viscous to temperature-dependent visco-elasto-plastic rheology that takes into account both diffusion and dislocation creep. These two studies demonstrate that the choice of rheology or numerical techniques can radically alter slab dynamics and topography evolution. A combined effort of improving numerical methods and understanding dynamics of complex systems will be needed for future studies.

Finally, in Chapter 5, I present a new type of 3-D forward models to investigate how the India-Eurasia convergence in the last 120 Ma has been accommodated by subduction in the Neo-Tethys, and how the shape of Greater India affects collision dynamics. The results show the spontaneous formation and merging of a double subduction system, which resulted in a stable intra-oceanic subduction with a trench-trench-trench triple junction. The collision dynamics is controlled by upper plate parameters and the size and shape of the Greater India extension, which in turn controls the timing of collision and deformation pattern.

Overall, this work demonstrates the importance of coupling lithosphere and mantle dynamics for the study of convergent margins, and represents fundamental progress on understanding the formation of mountain belts.

Kurzfassung

Die Kollisionszone Indien-Asien stellt eines der beeindruckendsten Phänomene in der Plattentektonik und Lithosphärendeformation dar. So überrascht es kaum, dass die ungewöhnlich mächtige und hoch liegende Region Himalaya-Tibet im Zentrum vieler tektonischer und numerischer Modelle stand. Einige dieser Modelle erklären grundlegende physikalische Prozesse kontinentaler Kollisionen. Jedoch kann bisher keines gleichzeitige aktive Prozesse wie Subduktion, Unterschiebung, Delaminierung, Channel Flow oder Extrusion einbeziehen. Da diese Mechanismen die Interaktion der Lithosphäre mit dem darunter liegenden Mantel beschreiben, wird angenommen, dass ihnen während kontinentaler Konvergenz Bedeutung zukommt. Um die Prozesse in ihrer Komplexität vollständig zu erfassen, sind somit 3D-Modelle integrierter Lithosphären- und Manteldynamik erforderlich.

In dieser Arbeit führe ich systematische numerische Simulationen mit Hilfe der Software LaMEM in 3D durch und kombiniere die numerischen Ergebnisse mit Erkenntnissen aus semi-analytischen Modellen und Skalenanalysen, um einige fundamentale Aspekte zur Kontinent-Kollision und Gebirgsbildungsdynamik im Kontext der Indien-Asien-Kollision herauszuarbeiten. Mittels der numerischen Modelle untersuche ich (i) den Einfluss von Subduktion und Kollision auf gebirgsbildende Prozesse und die mögliche Mächtigkeit topographischer Plateaus in Modellen, die die räumliche Skala der Lithosphäre und des oberen Mantels umfassen, (ii) verschiedene numerischer und theoretische Techniken zum Studium von Lithosphärendeformation an konvergenten Plattengrenzen, sowie (iii) die Auswirkungen der Form und Driftbewegung des indischen Subkontinents auf die folgende tektonische Entwicklung von Zentral- und Südostasien.

Weil gegensätzlich wirkende Prozesse die Entwicklung der Topographie beeinflussen, war es in früheren 3D-Kollisionsmodellen eine besondere Herausforderung, Topographie mit so überaus hoher Ausprägung zu erreichen. Einerseits begünstigt die kontinentale Kollision die sich aufbauende Topographie durch Materialstauchung, andererseits führt sie zum "slab break off" und lateraler Materialextrusion, die eine Topographieabsenkung zur Folge hat. In einem ersten Abschnitt dieser Arbeit (Kapitel 3) weisen Ergebnisse von 3D-Modellen darauf hin, dass "slab pull" allein keine ausreichend hohe Topographie herbeiführt. Somit sind zusätzliche Kräfte und feste, heterogene Blöcke, wie das Tarim Becken, notwendig

zur Ausbildung anormal hoher topographischer Fronten und Plateaus. Des Weiteren sind verschiedene Arten von Oberflächenerscheinungen beschrieben, die zu unserem Verständnis der Entstehung von Erhaltung von Gebirgsgürteln beitragen.

In einem zweiten Teil (Kapitel 2) diskutiere ich ein typisches numerisches Problem der "marker-in-cell" Methode für "staggered grids", die erhaltende Advektion von Markern, und teste den Einfluss rheologischer Näherungen auf Mantel- und Lithosphärendynamik in einem geometrisch vereinfachten Modellaufbau zur Subduktion/Kollision (Kapitel 4). Die Ergebnisse veranschaulichen eine große Bandbreite verschiedenen Verhaltens in Abhängigkeit von angewandten rheologischen Gesetzmäßigkeiten, von linear-viskos bis hin zu temperaturabhängiger visko-elasto-plastischer Rheologie, die sowohl Diffusions- als auch Versetzungskriechen einschließt. Diese beiden Studien zeigen, dass die Wahl von Rheologie und numerischem Verfahren die Plattendynamik und Topographieentwicklung in Modellen drastisch verändern kann.

Zuletzt präsentiere ich in Kapitel 5 einen neuen Typ von 3D-Vorwärtsmodellen zur Untersuchung, in welchem Maße die Indien-Eurasien-Konvergenz der letzten 120 Ma mit Subduktion in der Neo-Tethys wechselwirkte, und wie die Form von Indien die Kollisionsdynamik beeinflusst. Die Ergebnisse zeigen die spontane Bildung und Verschmelzung von doppelten Subduktionssystemen, welche eine stabile Intra-Ozean-Subduktion mit einer Graben-Graben-Graben Dreifach-Schnittstelle zur Folge hat. Die Kollisionsdynamik wird durch die Parameter der oberen Lithosphärenplatte sowie die Größe und Form Indiens kontrolliert, was wiederum den Zeitpunkt der Kollision und das Deformationsmuster steuert.

Zusammenfassend demonstriert diese Arbeit die Notwendigkeit der Kombination von Lithosphären- und Manteldynamik zur Untersuchung konvergenter Plattengrenzen und treibt unser Verständnis der Bildung von Gebirgsgürteln grundlegend voran.

Table of contents

List of figures

List of tables

Chapter 1

Introduction

"Mountains are Earth's undecaying monuments."
Nathaniel Hawthorne

Without doubt, one of the most striking features of plate tectonics and lithospheric deformation is the India-Asia collision zone, which formed when the Indian continent collided with Eurasia, around 50 million years ago (e.g., *Patriat and Achache* [1984]; *Royden et al.* [2008]). The rise of the abnormally thick Tibetan plateau, the deformation at its Eastern and Western syntaxes, the transition from subduction to collision and uplift, and the interaction of tectonics and climate are processes not fully understood. The goal of this thesis is to develop theoretical and computational tools and insights that contribute to the developing understanding of subduction and collision dynamics, of how mountain belts form and evolve, with a special focus on the India-Asia collision zone.

1.1 Subduction, continental collision and plate tectonics

Most of the major mountain belts and orogenic plateaus on Earth, including the Himalayas and the Tibetan Plateau, are found within the overlying plate of subduction and/or collision zones. Understanding mountain-building processes and the driving forces of plate tectonics has been one of the long-term goals of solid earth sciences community.

The Earth is a highly dynamic planet, far more so than the other terrestrial planets of the Solar System, and one that has continuously altered its surface over geological time. This dynamism is manifested in the opening and closure of ocean basins and the associated movements of continents, known as continental drift. The theory of plate tectonics, which combines these last concepts - continental drift and sea-floor spreading, was put forward in the 1960s by Hess, Dietz, Vine, Matthews and co-workers to explain many of the major

structural features of the Earth's surface. More importantly, it has provided the framework to explain the distribution of earthquakes and volcanoes, and it explains why the oceanic lithosphere is never older than about 180 Ma and why only the continents have preserved the Earth's geological record for the past 4 Ga.

According to the theory of plate tectonics, the Earth's outer layer is divided into rigid plates of continental and oceanic lithosphere that, through time, move relative to each other and slide over a weak asthenosphere. The asthenosphere can deform like a viscous fluid under stress. However, the theory of plate tectonics is based on several assumptions, the most important of which are (e.g., [*Forsyth and Uyeda*, 1975]):

1. New plate material is generated at mid-ocean ridges, or constructive plate boundaries, by sea-floor spreading (e.g., the Mid-Atlantic Ridge).

2. The Earth's surface area is constant, therefore the generation of new plate material must be balanced by the destruction of plate material elsewhere at destructive plate boundaries. Such boundaries are called either subduction zones, marked by the presence of deep ocean trenches and volcanic island arcs, or collision zones marked usually by large mountain belts (e.g., India-Asia collision).

3. Plates are rigid and deformation mainly takes place at plate boundaries.

As a consequence of these three assumptions, and particularly the third assumption, much of the Earth's geological activity is concentrated at plate boundaries (Figure 1.1). However, it is also clear that the assumption of perfectly rigid plates is not entirely accurate, as there are several diffuse plate boundaries, where deformation is not localized, but occurs over a broader range, the India-Asia collision zone being the perfect example (Figure 1.1).

Before moving into the more specific India-Asia collision zone, some major questions concerning dynamics of subduction and continental collision remain outstanding for the scientific community. These are related to:

- **Plate-driving forces.** One of the most important questions associated with plate tectonics is why plates move and what drives them. It is accepted nowadays that plate tectonics is an expression of the convective regime in the underlying mantle, but the link between individual mantle convection cells and plate movement is not clear because plate boundaries are not fixed, and move relative to one another and relative to places of mantle upwelling (i.e., hot-spots) [*Steinberger*, 2000; *Torsvik et al.*, 2010].

  Figure 1.2 provides a simplified overview of the forces that are thought to affect the movement of lithospheric plates at convergent margins. Subduction is primarily driven

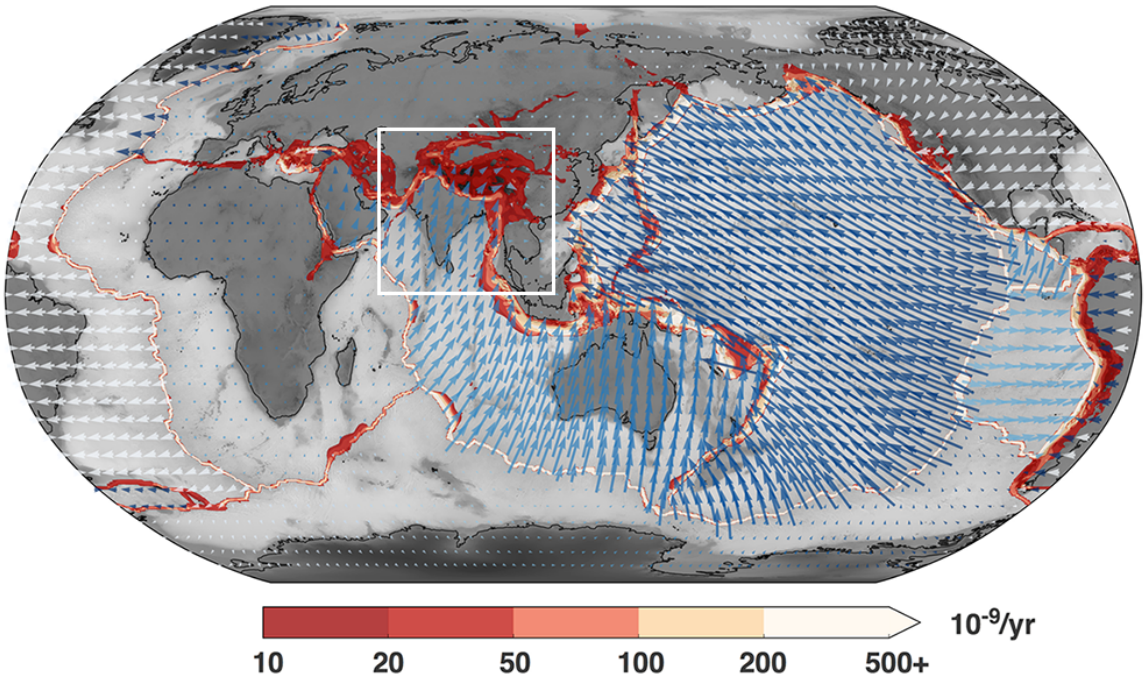

Fig. 1.1 Global map of surface velocities and the second invariant of strain rate (from *Moresi* [2015]). The surface velocities show the location and extent of plates, while the strain rate map highlights the fact that most of the deformation is concentrated at plate boundaries (high strain rates), while the continent interiors have little or no deformation (low strain rates). In some places, deformation occurs over broader regions, especially following mountain belts. These are called diffuse plate boundaries. The white rectangle indicates the study area in this thesis, the India-Asia collision zone.

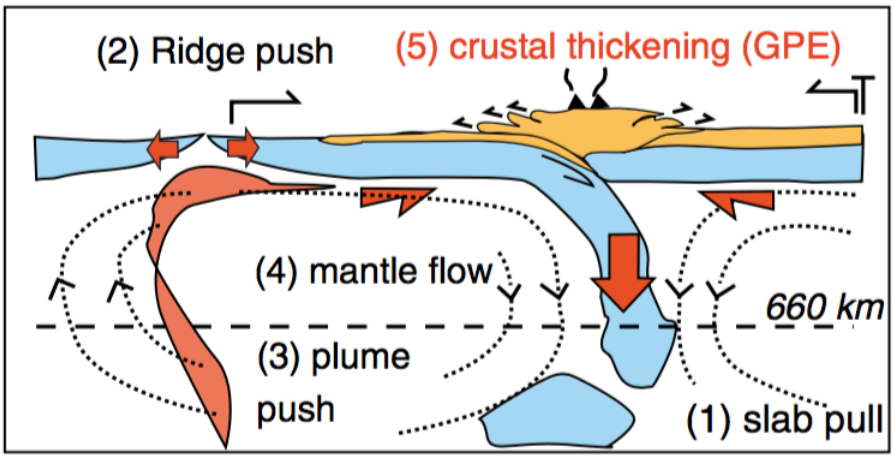

Fig. 1.2 Cartoon illustrating major plate-driving forces during mountain building at convergent margins (from *Faccenna et al.* [2013]).

by slab-pull or the gravitational descent of old, cold lithosphere into the mantle, and once a plate starts subducting it pulls younger lithosphere behind it. Other major forces include ridge push, plume push, mantle flow drag, and more recently proposed, slab suction in regions where the slab has descended into the lower mantle (e.g., Andes, India-Asia collision).

It is agreed that slab-pull is the most effective of the plate driving forces, and a consequence of this is that all plates converge at subduction zones at relatively high speeds that vary between 6.5 and 10.6 cm/yr (i.e., *Schellart et al.* [2007]). Moreover, the velocities of present-day plate motions appear to be constant, indicating a state of dynamic equilibrium where a balance exists between the driving and resistive forces. However, each plate moves at its own rate, which suggests that the relative importance of the driving and resistive forces must vary from plate to plate. It seems unlikely that any single force is the sole driving mechanism of plate motions.

When continental collision occurs, forces related to crustal thickening are also important (Figure 1.2). Chapter 3 includes a more in depth discussion regarding plate driving forces during continental collision, within the India-Asia collision framework.

- **Subduction dynamics.** What are the factors controlling subduction style? How does the plate deform during subduction? How is subduction initiated? How is magmatism generated at subduction zones?

Subduction zones are sites where oceanic lithosphere is being destroyed (or subducted) and are key locations for the short-term and the long-term recycling of chemical elements within the mantle, and volcanism on Earth. Numerous analog and numerical models have yielded systematic understanding of many features of subduction such as: the relation between trench and plate velocities [*Funiciello et al.*, 2008; *Stegman et al.*, 2006], the shapes of trenches and island arcs [*Morra et al.*, 2006; *Schellart et al.*, 2007], the mode or style of subduction [*Bellahsen et al.*, 2005; *Ribe*, 2010; *Schellart*, 2008; *Stegman et al.*, 2010a] and the sinking speed of the slab [*Ribe*, 2010]. In detail, however, subduction zones are complicated by a wide variety of factors that can influence the style of plate boundary, some of which are explored in more detail in Chapter 4.

- **Transition from oceanic subduction to continental collision.** How does subduction evolve during continental collision? The reorganization of force balance during the onstart of collision is a highly dynamic process that represents a recurrent topic in this thesis. Chapters 3-5 highlight some important observations in this respect.

- **Collision dynamics.** How is the deformation accommodated during continental collision? How do mountain belts form and why not all mountain belts look the same?

  When an ocean closes and two continental plates meet at a destructive boundary, the continents themselves collide. Such collisions result in intense deformation at the edges of the colliding plates. Neither continent can be subducted into the mantle due to the buoyancy of continental crust, so the forces that drive the plate movement prior to collision are brought to act directly on the continental lithosphere itself (i.e., the energy is transformed into gravitational potential energy). At this stage, further convergence of the plates must be taken up by deforming one or both of the plates of continental lithosphere. Under such strong compressive forces, the lithosphere contracts through folding and faulting of rocks (e.g., *Beaumont et al.* [2004]; *Burg and Chen* [1984]; *Burg et al.* [1994]). Deformation becomes distributed and can extend hundreds of kilometres into the continental interior because continental plates are weak (e.g., *Molnar* [1988]; *Molnar and Tapponnier* [1975]). However, systematic differences occur between major mountain belts, such as the Tibet-Himalaya, the Alps or the Andes, suggesting that regional differences are important.

Although much of the research presented here addresses general questions about subduction and collision, I have chosen to focus attention on the applications of this work to the India-Asia collision since it is the best example in which subduction, continental collision, and mountain building can be studied in a global plate tectonics perspective.

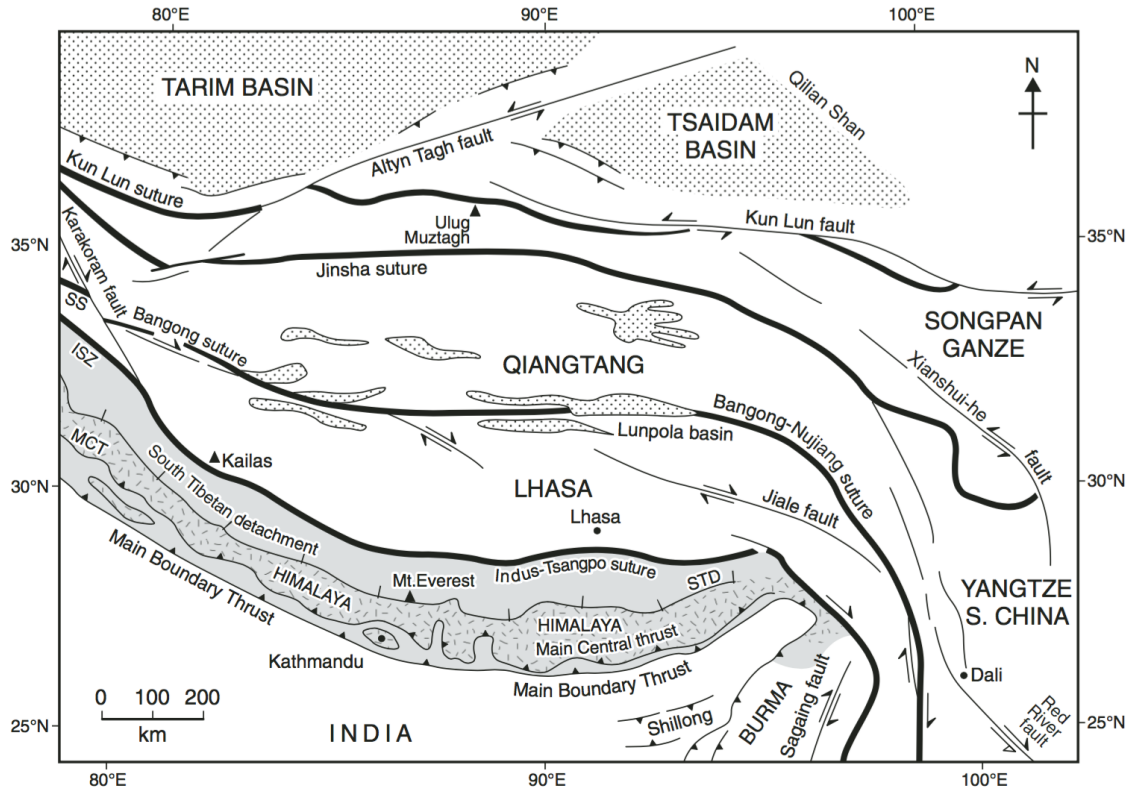

Fig. 1.3 Map of the Tibetan Plateau showing approximate boundaries of the major terranes, suture zones, and strike-slip faults (from *Searle* [2007]). Abbreviations: ISZ-Indus suture zone, MCT-Main Central Thrust, SS-Shyok suture and STD-South Tibetan Detachment.

1.2 India-Asia collision zone

The Himalayan-Tibetan orogen was created by the Indo-Asian collision over the past 50 Ma. This orogen is the youngest and most spectacular active continent collision belt on Earth, and it is the most studied research area on Earth.

Prior to plate tectonics theory, *Argand* [1924] and *Holmes* [1965] thought that the Himalayan Mountains and Tibetan Plateau had been raised due to the northern edge of the Indian craton under-thrusting the entire region, causing shortening and thickening of the crust to ∼80 km. This perspective remains widely accepted, but recent ideas suggest that the development of the plateau should be evaluated within the context of the large dynamic system related to subduction of oceanic lithosphere beneath central and SE Asia.

This tectonic boundary is complex and changes character along its length. Tibet is the largest, highest and flattest plateau on Earth with an average elevation exceeding 5 km, and includes over 80% of the world's land surface higher than 4 km. The bordering Himalayas

and the Karakoram Mountains, include the only peaks on Earth reaching more than 8 km above sea level. The Tibetan Plateau is bound by the Tarim and Qaidam Basins to the north, the Himalayan, Karakoram, and Pamir mountain chains to its south and west but its eastern margin is more diffuse, with something reminiscent of a large-scale flow (Figure 1.3).

The Tibetan plateau is a collage of continental blocks (terranes) (e.g., *Yin and Harrison* [2000]) that were added successively to the Eurasian plate during the Paleozoic and Mesozoic (Figure 1.3). The sutures between these terranes are marked by scattered occurrences of ophiolitic material (rocks characteristic of oceanic crust). From north to south and from older to younger, the main Tibetan crustal blocks are: the Kunlun-Qaidam, Songpan-Ganze, Qiangtang, and Lhasa terranes [*Allegre et al.*, 1984; *Patriat and Achache*, 1984; *Searle*, 2007; *Tapponnier et al.*, 2001; *Yin and Harrison*, 2000].

The Indian sub-continent consists of a Precambrian shield, which itself is composed of different terranes. The northern margin, the Himalayan fold-and-thrust belt, bounds the Tibetan Plateau. The boundary between them, the Indus-Tsangpo Suture, which can be traced by a line of ophiolite outcrops, marks the boundary between the Indian and Asian plates (e.g., *Burg and Chen* [1984]). The Himalayas represent the traditional accretionary wedge formed by folding and thrusting of sediments scrapped off the subducting slab. It consists of three main units: (i) The Lesser Himalaya between the Main Boundary Thrust and the Main Frontal Thrust, (ii) the High Himalaya between the Main Central Thrust and the South Tibetan Detachment, and (iii) the Tethys Himalaya between the South Tibetan Detachment and the Indus-Tsangpo Suture (Figure 1.3).

1.2.1 Modern challenges in understanding the dynamics of India-Asia collision zone

Today, the challenge lies in refining our understanding of the dynamics of India-Asia collision by elucidating the connections between the wealth of observations available and the underlying processes occurring at depth. Decades of study have produced data sets across various disciplines, including: active tectonics, Cenozoic geology, seismicity, global positioning system (GPS) measurements, seismic profiles, tomography, gravity anomalies, mantle-crustal anisotropy, paleomagnetism, geochemistry or magnetotelluric (MT) studies. Some notable data sets include:

- **GPS velocity field.** GPS measurements show distributed deformation across the entire collision zone. They also indicate that the current convergence of India relative to Asia is at approximately 4 - 5 cm/yr [*Gan et al.*, 2007; *Liang et al.*, 2013]. However, only a small fraction of this amount is accommodated within the Himalayan range. The rest of

the convergence is, thus, absorbed within the Tibetan Plateau and its adjacent regions. The present-day deformation of the Tibetan Plateau is dominated by N-S shortening, E-W extension and eastward motion in the southern and central plateau (e.g., *Royden et al.* [2008]). How this surface motion is accommodated at depth remains unclear.

- **Earthquake distribution.** The distribution of earthquakes across the Tibetan Plateau is further evidence for diffuse internal deformation resulting from continental collision. However, seismicity of the Tibetan Plateau is mainly restricted to the upper 15 - 30 km of the crust (e.g., [*Wei et al.*, 2010]). Some scientists attribute this lack of substantial seismicity underneath the Moho as evidence that the Asian mantle lithosphere is weak [*Jackson*, 2002; *Maggi et al.*, 2000], while others point out that some processes can be well explained if the crust resides above a strong mantle lithosphere [*Burov and Watts*, 2006].

- **Seismic surveys.** Low S-wave velocity zones detected within the lower crust have been interpreted as areas with partial melt [*Jiang et al.*, 2011; *Nabelek et al.*, 2009]. It is debated whether these zones are discrete patches [*Nabelek et al.*, 2009] or whether they form a widespread weak layer [*Jiang et al.*, 2011]. Flow in these widespread weak zones is assumed to contribute to the lateral growth of the Tibetan Plateau [*Clark et al.*, 2005; *Clark and Royden*, 2000].

  In the southern part of the plateau, seismic reflectivity surveys show that the Indian lithosphere is underplating the Asian lithosphere for about 500 km (e.g., *Nabelek et al.* [2009]; *Owens and Zandt* [1997]; *Schulte-Pelkum et al.* [2005]).

  Finally, tomography studies reveal a high-velocity anomaly beneath central and SE Asia that extends below the 660 km transition to the lower mantle. They are inferred to be subducted slab with a complex structure. Moreover, a down-welling high-velocity anomaly down to $\sim$400 km depth is interpreted as the subducting continental Indian mantle lithosphere (e.g., [*Replumaz et al.*, 2004; *Royden et al.*, 2008; *Van der Voo et al.*, 1999]).

- **Geology.** Different styles of deformation have been observed at the surface: fold and thrust belts consistent with N-S shortening, normal faults consistent with E-W extension, and large strike-slip faults that cut through the whole lithosphere [*Burg and Chen*, 1984; *Searle*, 2007; *Tapponnier et al.*, 2001]. It is clear that the Tibetan lithosphere is complex, composed of fragments of different ages, compositions, temperatures, and rheology, which affect the deformation style within.

Each of these data sets stands as a different piece in the puzzle of the India-Asia collision. However, same data sets can support a number of competing and sometimes mutually exclusive mechanisms for the uplift of the Tibetan Plateau (e.g., *Klemperer* [2006]; *Royden et al.* [2008]). For example, the mantle lithosphere beneath Tibet has been proposed to be cold, hot, thickened by shortening, or thinned by viscous instability. Other controversies include the degree of mechanical coupling between the crust and deeper lithosphere and the nature of large-scale deformation. It is no surprise then, that several hypotheses emerged over time trying to explain the amount of continental shortening and the anomalous rise of the Tibetan Plateau (Figure 1.4):

1. Wholescale underthrusting of the Indian plate below the Asian continent [*Argand*, 1924; *Owens and Zandt*, 1997].

2. The thin-sheet model or distributed homogeneous shortening [*England and Houseman*, 1986; *England and McKenzie*, 1982; *Houseman and England*, 1986].

3. Homogeneous thickening of a weak, hot Asian crust, involving a large amount of magmatism [*Dewey and Burke*, 1973; *Tilmann et al.*, 2003].

4. Slip-line field model to account for the brittle deformation in and around the Tibetan Plateau and to explain extrusion of SE Tibet away from Indian indentor [*Molnar and Tapponnier*, 1975; *Tapponnier and Molnar*, 1976; *Tapponnier et al.*, 2001]. The same group also propose a time-dependent model for the growth of Tibetan plateau [*Tapponnier et al.*, 2001], in which successive intracontinental subduction zones maintain the stepwise growth and rise of the plateau.

5. Lower crustal flow models for the exhumation of the Himalayan units and lateral spreading of the Tibetan plateau [*Beaumont et al.*, 2001, 2004; *Clark et al.*, 2005; *Clark and Royden*, 2000; *Royden et al.*, 1997, 2008].

6. Delamination or convective removal of the lithospheric mantle induced isostatic movement, lifting the Tibetan Plateau [*Molnar*, 1988; *Molnar et al.*, 1993].

These models were applied either to the Tibetan Plateau or the Himalayan syntaxes and were able to explain the formation of specific tectonic and geological features. The thin-sheet model has emerged as a more successful (or at least more widely used) model and can explain the overall thickening and the horizontal velocity field of the Tibetan Plateau. However, one of its major shortcomings is that it cannot simultaneously represent channel flow and gravitational collapse of the mantle lithosphere [*Lechmann et al.*, 2011], since

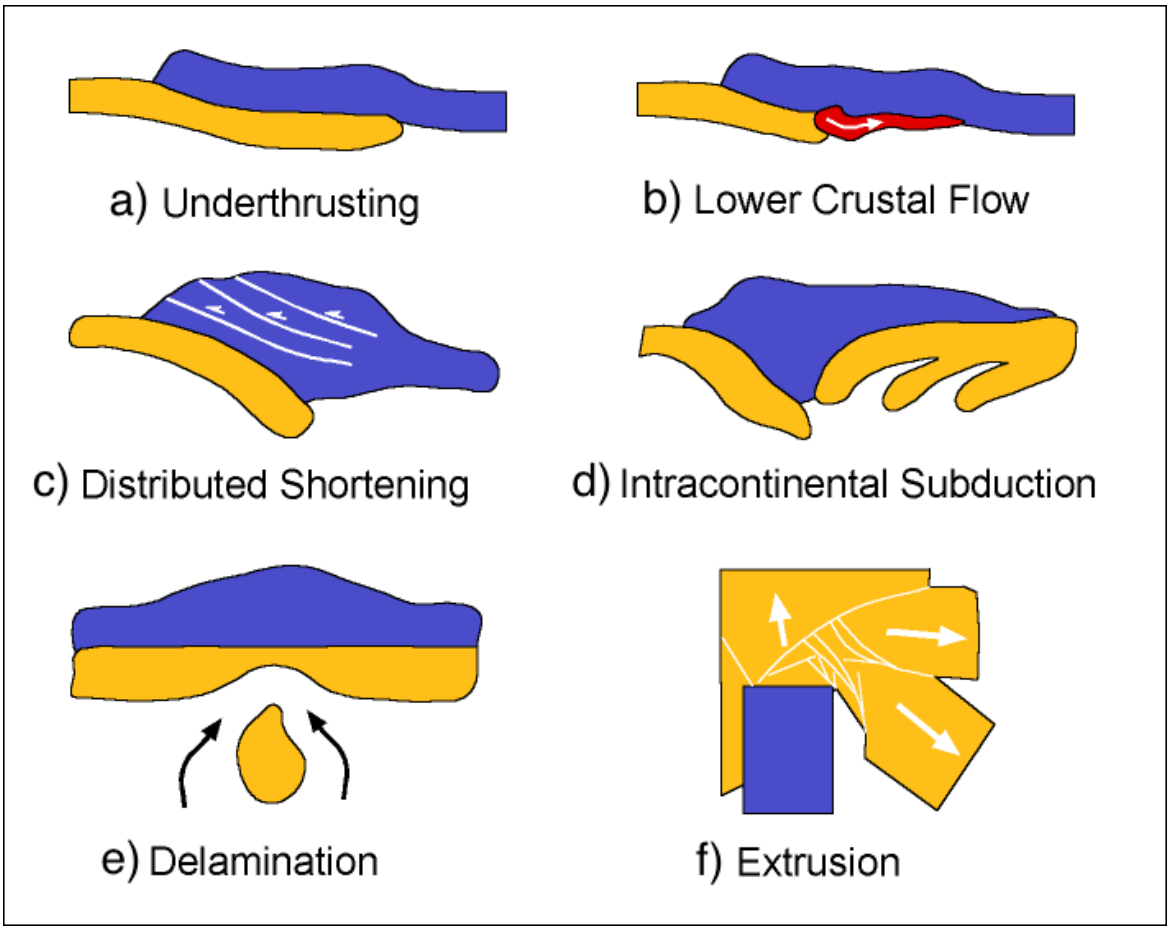

Fig. 1.4 Schematic cartoons of tectonic models proposed to explain the thickening and uplift of the Tibetan Plateau. (Source: http://www.geo.arizona.edu/∼ozacar/models∼1.htm)

these mechanisms require the lithosphere to interact with the underlying mantle, or to have a vertically non-homogeneous rheology.

Moreover, the majority of these models are based on simplifying assumptions to reduce the geometrical, rheological and mechanical complexity, the computational costs, or imposing a certain deformation style (i.e., channel flow). Such simplifications make it difficult to determine the relative importance of different deformation processes during continental collision.

Thus, specific questions concerning the dynamics of India-Asia collision still remain:

- **Uplift of the Himalayas and Tibetan Plateau.** How did the crust beneath Himalaya and Tibet reach double-crustal thickness (normal continental crust is 35-40 km thick, whereas the crust beneath the Himalaya and Tibet is 70-100 km thick)? Which mechanisms help sustain the high topographic amplitudes? Moreover, it is not immediately clear why an area as broad as the Tibetan Plateau should be uplifted so high compared to other mountain belts following collision. Another major question is whether the Tibetan Plateau has risen continuously or diachronously. Different views include a rise in several pulses (e.g., *Fielding* [1996]; *Molnar et al.* [1993]) or an early rise of the southern and central plateau and a later rise of the northern and eastern parts (e.g., *Cook and Royden* [2008]; *Rowley* [2007]; *Royden et al.* [2008]).

- **Present-day deformation.** Which and where the proposed models (i.e., Figure 1.4) can be applied? How do lithosphere heterogeneities and rheology affect the deformation pattern? What is the degree of mechanical coupling between the crust and deeper lithosphere? The nature of the mechanical layering of the lithosphere, especially, is one of the most discussed topics in lithosphere dynamics. Models of continental rheology are split in two: (i) the “jelly sandwich" model (e.g., *Burov and Watts* [2006]), in which the strength resides in a strong crustal and in a strong mantle layer, and (ii) the “creme-brulee" model (e.g., *Jackson* [2002]) in which the lithospheric strength is concentrated in the upper crust and the mantle is assumed to be weak.

- **Convergence history.** What is the deformation history and evolution of this plate boundary? What are the driving forces that sustain the high convergence rate of India? How was the subduction accommodated in the Neo-Tethys? What is the fate of the subducting slab once collision starts? Chapter 5 will focus on the convergence of India in the last 120 Ma, which is famous for its speed attained in the Late Cretaceous when it moved at more than 16 cm/yr (e.g., *Besse and Courtillot* [1988]; *Patriat and Achache* [1984]).

- **Curvature and syntaxes.** Why do the Himalayas have a convex curvature? What about the deformation of the prominent Himalayan syntaxes: Nanga Parbat in the west and Namche Barwa in the east? Geological studies show that the deformation around these syntaxes is dramatic and they deform the Indus-Tsangpo Suture (e.g., *Treloar and Coward* [1991]; *Zeitler et al.* [2001]). Their location at the corners of the Indian Plate and their distinct 3-D geometry are topics of ongoing research.

- **Interaction between tectonics and climate.** Is it the Himalayas that affects the Indian monsoon or the other way around? The interaction between tectonics and climate has been previously studied in order to understand long-term evolution of continental topography [*Molnar et al.*, 1993]. One of the most important results show that mountain belts modify rainfall through the effects of orography, or the development of a rain shadow on one side of mountain belts. However, orographic precipitation may also enhance topographic uplift [*Beaumont et al.*, 2001, 2004].

1.3 Goals of this thesis

It is evident that finding answers to these questions will require a series of models derived from geophysical, geochemical and geological observations to be tested with physically consistent numerical models. 3-D models are emerging as powerful tools to understand the dynamics of coupled systems. Recent computational advances not only allow us to use complex rheology with higher resolution as compared to previous 3-D models of convergent margins (i.e., *Capitanio et al.* [2010]; *Li et al.* [2013]; *Magni et al.* [2014]; *Moresi et al.* [2014]; *Sternai et al.* [2014]), but also run simulations in real time. Moreover, the ability to run fast 3-D simulations also allows us to analyze large data sets and develop scaling laws that are applicable to complex 3-D problems (see Chapter 3). However, fully 3-D models of the dynamics of continent collision zones have only been developed very recently, and presently most research groups have relied on certain explicit assumptions for their codes.

In this thesis, I use 3-D numerical models to simulate lithospheric deformation while simultaneously taking mantle flow and a free surface into account. I then combine the numerical results with insights from semi-analytical models and scaling analysis to explore some fundamental aspects of continental collision and mountain-building dynamics in an India-Asia collision framework. I applied the models to investigate (i) how subduction and collision affect mountain-building processes and how large topographic plateaus can form in an integrated lithospheric and upper-mantle scale model, (ii) appropriate numerical and theoretical techniques for studying lithospheric deformation at convergent margins, and (iii)

how the shape and convergence of Greater India affected the subsequent tectonic evolution of central and SE Asia.

Most of the results contained here, as well as the lessons learned, are applicable much more broadly than the limited context of India-Asia subduction and collision zone. For example, insights gained through this work may prove useful in developing theories about other tectonic settings such as the Alps or the Andes. Finally, methods and codes developed in this thesis for the study of continental collisions will provide a basis for more sophisticated models of subduction/collision evolution dynamics. The following section describes the method used to study these questions together with its challenges.

1.4 Methodology

1.4.1 Theoretical framework

In the rest of this chapter I provide a brief outline of the theoretical and computational framework in which my research was conducted. Both the theory and the computational tools that I use to obtain solutions to the governing equations have been developed and described in many papers available in the scientific literature. The summary provided here is intended only to inform the reader unfamiliar with these fields. Following this background material is a section outlining the chapters of the thesis and their main conclusions.

Governing equations

Convection in the mantle and lithosphere deformation is generally considered to be well described by the Stokes equation for a highly viscous creeping fluid with a low Reynolds number. More specifically, the Stokes equations represent a continuum mechanics approximation where the equations used to describe geological and geophysical processes consist of a set of balance equations for mass and momentum together with their constitutive relationships (e.g., *Turcotte and Schubert* [2002]). These equations of conservation of mass and momentum, assuming incompressibility, and together with energy conservation, are given by:

$$\frac{\partial \tau_{ij}}{\partial x_j} - \frac{\partial p}{\partial x_i} + \rho g_i = 0 \tag{1.1}$$

$$\frac{1}{K}\frac{Dp}{Dt} - \alpha \frac{DT}{Dt} + \frac{\partial v_i}{\partial x_i} = 0 \tag{1.2}$$

$$\rho C_p \frac{DT}{Dt} = \frac{\partial}{\partial x_i}\left(\lambda \frac{\partial T}{\partial x_i}\right) + H. \tag{1.3}$$

Velocity (v_i), pressure (p) and temperature (T) represent the primary unknowns. Other variables, $x_i (i = 1,2,3)$ denotes Cartesian coordinates following the Einstein summation convention, $\tau_{ij} = \sigma_{ij} + p\delta_{ij}$ is the Cauchy stress deviator, ρ density, g_i the gravity acceleration vector, K the bulk modulus, α the thermal expansion coefficient, C_p the specific heat, λ thermal conductivity, H volumetric heat source, and D/Dt stands for the material time derivative, respectively.

The volumetric heat source includes shear heating, controlled by efficiency parameter $0 \leq \chi \leq 1$, and the radiogenic heat (A):

$$H = \chi \tau_{ij} \left(\dot{\varepsilon}_{ij} - \dot{\varepsilon}_{ij}^{el} \right) + \rho A. \tag{1.4}$$

Equation (1.1) states that pressure gradients are balanced by gradients in viscous strain and by buoyancy, while equation (1.2), the continuity equation, states that the divergence of the velocity field is the result of elastic compressibility and thermo-elasticity. Finally, equation (1.3) states that changes in temperature are the result of heat advection, conduction and production (including internal radiogenic heat, shear heating etc.).

Constitutive equations

The study of rock deformation subjected to stress is commonly called rock *rheology*, from Greek meaning "everything flows" and was coined by E.C. Bingham [*Turcotte and Schubert*, 2002]. The rheology of rocks depends on a large number of parameters, including temperature, pressure, stress, grain size, melt or water content.

The Earth is composed of solid rocks that behave in a rigid way on short length and time scales. However, this behaviour breaks down over longer length and time scales and in the mantle where temperatures are significantly higher. At depth, over long timescales rocks begin to behave more as fluids than as rigid solids. For this reason, shear waves can pass through the Earth, but on longer timescales of millions of years the mantle convects, slowly driving plate tectonics. The property that describes how they flow is viscosity, which also gives an indication of the strength of the material. The viscosity of the lithosphere is determined by the geothermal gradient and by the nature of the rocks that are present at different depths within it.

The mathematical description of the rheology of a rock is given by a set of constitutive equations that relate stress to strain rates. In geodynamics, the rock rheology is commonly described as a combination of three rheologies: elastic, viscous, and plastic. Before we describe each rheology separately, the visco-elasto-plastic constitutive equation for the deviatoric stress is given by:

$$\dot{\varepsilon}_{ij} = \dot{\varepsilon}_{ij}^{el} + \dot{\varepsilon}_{ij}^{vs} + \dot{\varepsilon}_{ij}^{pl} \tag{1.5}$$

$$= \frac{\overset{\diamond}{\tau}_{ij}}{2G} + \dot{\varepsilon}_{II}^{vs}\frac{\tau_{ij}}{\tau_{II}} + \dot{\varepsilon}_{II}^{pl}\frac{\tau_{ij}}{\tau_{II}}, \tag{1.6}$$

where $\dot{\varepsilon}_{ij} = \frac{1}{2}(\frac{\partial v_i}{\partial x_j} + \frac{\partial v_j}{\partial x_i}) - \frac{1}{3}\frac{\partial v_k}{\partial x_k}\delta_{ij}$ is the deviatoric strain rate tensor, $\dot{\varepsilon}_{ij}^{el}$, $\dot{\varepsilon}_{ij}^{vs}$, $\dot{\varepsilon}_{ij}^{pl}$ are the elastic, viscous and plastic components, respectively, $\overset{\diamond}{\tau}_{ij} = \frac{\partial \tau_{ij}}{\partial t} + \tau_{ik}\omega_{kj} - \omega_{ik}\tau_{kj}$ is the Jaumann objective stress rate, $\omega_{ij} = \frac{1}{2}(\frac{\partial v_i}{\partial x_j} - \frac{\partial v_j}{\partial x_i})$ is the spin tensor, G is the elastic shear modulus, and the subscript $_{II}$ denotes the square root of the second invariant of a corresponding tensor, e.g., for the deviatoric stress $\tau_{II} = \left(\frac{1}{2}\tau_{ij}\tau_{ij}\right)^{1/2}$. Equation (1.5) enters equation (1.1) to solve for velocity, pressure and temperature.

Viscous creep. Deformation in the Earth's mantle is mainly governed by solid-state viscous creep and is irreversible. Viscous creep relates to different mechanisms of deformation inside the crystal lattice [*Turcotte and Schubert*, 2002] and can include: diffusion creep, dislocation creep, grain boundary sliding and Peierls creep. Then, the magnitude of the viscous creep strain rate is subdivided into each component [*Popov and Sobolev*, 2008]:

$$\dot{\varepsilon}_{II}^{vs} = \dot{\varepsilon}_{diff} + \dot{\varepsilon}_{disl} + \dot{\varepsilon}_{GBS} + \dot{\varepsilon}_{Peir}. \tag{1.7}$$

- *Diffusion creep* describes the deformation due to the microscopic motion of defects in the crystal lattice under applied stress, which results in the bulk deformation of the crystalline solid. The macroscopic deformation resulting from diffusion creep can be described by a relationship between deviatoric stress τ and strain rate $\dot{\varepsilon}$:

$$\dot{\varepsilon}_{diff} = B_{diff} r^{-m_{diff}} exp(\frac{H_{diff}}{RT})\tau \tag{1.8}$$

  where B_{diff} is a prefactor, r the grain size, m_{diff} the grain size exponent, R the universal gas constant and $H_{diff} = E_{diff} + pV_{diff}$ the activation enthalpy, E_{diff} and V_{diff} are the activation energy and volume, and p, T and τ are pressure, temperature and stress. B_{diff} can also include factors that depend on water fugacity and melt content (e.g., *Hirth and Kohlstedt* [2003]). In the equation above, strain rate is linearly dependent on stress, thus resulting in a Newtonian rheology for otherwise constant parameters.

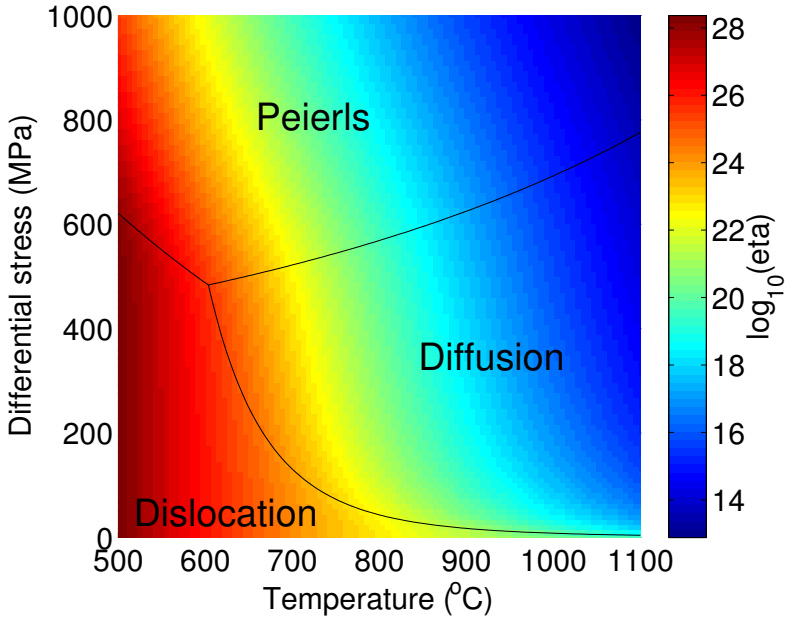

Fig. 1.5 Logarithm of effective viscosity for dry olivine calculated using parameters from *Kameyama et al.* [1999]. Black solid lines separate the domains in which a particular creep mechanism dominates.

- *Grain boundary sliding* describes the deformation due to sliding of grains along boundaries and is similar to diffusion creep:

$$\dot{\varepsilon}_{GBS} = B_{GBS} r^{-m_{GBS}} exp(\frac{H_{GBS}}{RT}) \tau^{n_{GBS}} \tag{1.9}$$

  where B_{GBS} is a constant prefactor, m_{GBS} the grain size exponent, $H_{GBS} = E_{GBS} + pV_{GBS}$ the activation enthalpy, E_{GBS} and V_{GBS} are the activation energy and volume, and n_{GBS} is the stress exponent.

- *Dislocation creep* relates to the deformation resulting from the movement of line defects in a crystal, known as dislocations. Once the stress acting on a crystal overcomes the resisting forces, dislocations become mobile. The motion of each dislocation results in deformation of the crystal, as the different atomic planes are displaced. The macroscopic expression of this kind of dislocation motion is commonly written as:

$$\dot{\varepsilon}_{disl} = B_{disl} exp(-\frac{H_{disl}}{RT}) \tau^{n_{disl}} \tag{1.10}$$

where B_{disl}, $H_{disl} = E_{disl} + pV_{disl}$ and n_{disl} are prefactor, activation enthalpy and stress exponent of dislocation creep. Dislocation creep is non-Newtonian, as n takes values larger than 1, and is independent of grain size.

- Finally, when the motion of dislocations in a crystal is hindered by resistance forces, such as the Peierls stress, the resulting mechanism is called *Peierls creep*. The Peierls stress describes the energy that is needed to move a dislocation inside a crystal without thermal activation above the Peierls potential hill to the next stable position. The macroscopic deformation associated with Peierls creep is described as (e.g., *Kameyama et al.* [1999]):

$$\dot{\varepsilon}_{Peir} = B_{Peir} exp\left[-\frac{H_{Peir}}{RT}(1-\beta)^2\right]\left(\frac{\tau_{II}}{\beta\,\tau_{Peir}}\right)^s, \tag{1.11}$$

where B_{Peir} is a prefactor, $H_{Peir} = E_{Peir} + pV_{Peir}$ the activation enthalpy, τ_{Peir} the Peierls stress and β and s are exponents that are used in fitting this law to experimental data. The Peierls creep is much more dependent on stress as compared to temperature. For this reason, it is often called low-temperature plasticity.

Figure 1.5 shows the effective creep viscosity (i.e., from equation 1.7) for dry olivine using parameters from *Kameyama et al.* [1999] in a stress-temperature field. The domains in which a particular creep mechanism dominates are marked by black solid lines. The GBS mechanism was not included in this plot.

Elastic deformation. At low temperatures, pressures and stresses, and on short timescales, rocks deform elastically. A purely elastic material that is deformed under a given force returns to its original state once the force is removed. For small deformations, the behaviour of such a material can be described by Hooke's law, which states that stress, σ, varies linearly with the strain, ε. In the incompressible isotropic case, which is considered throughout the whole thesis, we can then relate the deviatoric stress to the deviatoric strain:

$$\tau_{ij} = 2G\varepsilon_{ij}, \tag{1.12}$$

where G is the shear modulus.

Plastic failure. Experiments on rocks showed that there is a maximum shear stress that rocks can withstand before failing, which is known as Byerlee's law. In our method, plastic

failure occurs by enforcing the Drucker-Prager yield criterion. The magnitude of the plastic strain rate ($\dot{\varepsilon}_{II}^{pl}$) is then determined from:

$$\tau_{II} \leq \tau_Y = \sin(\phi)\, p + \cos(\phi)\, c, \tag{1.13}$$

where ϕ is the friction angle, and c is the cohesion.

The Drucker-Prager criterion is a simplification to the classical Mohr-Coulomb plasticity model (in 2-D they are identical) [*Vermeer and de Borst*, 1984] described as:

$$\tau_{II} \leq \tau_Y = -0.5(\tau_{xx} + \tau_{zz}) \sin(\phi) + \cos(\phi)\, c, \tag{1.14}$$

where $\tau_{II} = (0.5(\tau_{xx}^2 + \tau_{xz}^2) + \tau_{zz}^2)^{0.5}$ is the second invariant of the total stress tensor. Usually $\phi = 30^\circ$ and $c \approx 20 - 40$ MPa.

1.4.2 Computational framework

The governing and constitutive equations described above result in an elliptic system of equations with strongly varying coefficients (a couple of orders magnitude), which are then discretized in the 3-D parallel code LaMEM (Lithosphere and Mantle Evolution Model) [*Kaus et al.*, 2016]. Staggered grid finite differences method (FD) is used to discretize the equations in space, which is a low-order but stable discretization for incompressible fluid flow. The advantage of FD over FE (finite element) methods is its lower computational cost, which allows high resolution modelling of 3-D lithospheric problems.

An internal free surface is implemented using a so-called sticky air approach [*Crameri et al.*, 2012; *Schmeling et al.*, 2008], which assigns a relatively low but nonzero viscosity to the air phase, together with an appropriate stabilization method [*Kaus et al.*, 2010] to allow for sufficiently large time steps. Thus, the geological topography of the free surface is explicitly tracked by an internal 2-D grid that covers the entire domain.

The marker-in-cell (MIC) method [*Gerya and Yuen*, 2003; *Harlow and Welch*, 1965] is used to track material properties and implement material advection in an Eulerian kinematical framework. To prevent spurious clustering of the material particles (markers), we use a combination of a 4^{th}-order Runge-Kutta method with a conservative velocity interpolation scheme (*Jenny et al.* [2001], Chapter 2).

However, in a large physical domain with high resolution, the solutions to the governing equations become computationally extensive, even for FD, and multiprocessor (parallel) computing systems are needed to handle such large simulations. LaMEM is written in C and uses the Portable, Extensible Toolkit for Scientific Computation library (PETSc) [*Balay et al.*, 2014]. PETSc is an advanced numerical software library that contains a range of inher-

ently parallel data structures, pre-conditioners and solvers, developed mainly for scientific computing and with the aim to remove the need of multi-processor communication (MPI or Message Passing Interface), leaving the programmer to focus on the overall computation and detailed physics of the simulation. Thus, LaMEM uses a range of solvers within the PETSc framework, including Galerkin multigrid pre-conditioners combined with Newton iterations for nonlinearities to solve the non-linear system of equations. More solver details used in LaMEM can be found in *Kaus et al.* [2016].

The geological problems become numerically challenging as the rheology of rocks varies non-linearly with depth and temperature (from elasto-plastic at surface and low temperatures to viscous at higher temperatures and depth). Therefore, much of this work has concentrated on linear viscous problems where the potential form of equations were more convenient for numerical convergence and analysis. However, Chapter 4 focuses on the effect of non-linear rheology, which takes into account the full capabilities of LaMEM.

The 3-D simulations presented here were run on Mogon (HPC Mainz) and Juqueen (Jülich Supercomputer Centre). Vizualization of 3-D models has been a challenging part of this work, but the great parallel and scripting capabilities of the *ParaView* software (www.paraview.org) have made this task more feasible. Hence, new visualisation tools (i.e., python scripting in *ParaView*) had to be developed to efficiently handle large datasets, by automatically plotting and analysing 3-D results. The 2-D results shown in various chapters and appendices were obtained and visualized using *MatLab* (www.mathworks.com/products/matlab/).

1.5 Thesis structure

The main content of this thesis is organized into four different research chapters and two appendices. All four research chapters are conceived as independent chapters and therefore have their own abstract, introduction, method, results, discussion and conclusion. Chapter 2 discussed a common problem in geodynamic modeling, that of non-conservative marker advection. This is complemented by Appendix A with additional tests and a discussion on an efficient method for marker control. Chapter 3 discusses development of topography in 3-D continental collision models by providing a large number of numerical simulations and scaling methods. Supporting information to Chapter 3 is given in Appendix B. Chapter 4 discusses the effect of rheological approximations common in geodynamic modeling on results of subduction/collision model. Finally, Chapter 5 proposes a new type of lithospheric-scale numerical simulations with application on the convergence of India in the last 120 Ma. While every chapter investigates a problem of its own, each topic relates back to the question: What are the best practices in modelling subduction and collision and what impor-

tant messages can we take from it? Thus, a final Chapter 6 contains some concluding remarks.

Chapter 2. On the quality of velocity interpolation schemes for marker-in-cell method and staggered grids. Usually in geodynamic codes, velocity interpolation from grid points to marker locations is performed without preserving the zero divergence of the velocity field at the interpolated locations (i.e., non-conservative). Such interpolation schemes can induce non-physical clustering of markers when strong velocity gradients are present [*Jenny et al.*, 2001; *Meyer and Jenny*, 2004; *Wang et al.*, 2015] and this may, eventually, result in empty grid cells, a serious numerical violation of the marker-in-cell method. In this paper, I rigorously compare different interpolation schemes in combination with multiple advection schemes on Stokes problems with strong velocity gradients, which are discretized using a finite difference method. I report on the quality of these methods for 2- D and 3-D staggered grids and find optimal ones that reduce the dispersion or clustering of markers, reducing the need of unphysical marker control. *This work is submitted as Pusok, A.E., Kaus, B.J.P., Popov, A.A. (2016), "On the quality of velocity interpolation schemes for marker-in-cell method and staggered grids" to Pure and Applied Geophysics.*

Chapter 3. Development of topography in 3-D continental collision models. In this chapter, I investigate the dynamics of continental collisions and analyzed the conditions under which large topographic plateaus can form in an integrated lithospheric and upper-mantle scale model, with a particular focus on the India-Asia collision zone. The study is novel in that it found ways of how simple geodynamic formulations are still viable and useful to the scientific community. I developed tools to generalize the question of mountain belt formation and evolution using numerical results and scaling laws. *This work is in press as Pusok, A. E., and B. J. P. Kaus (2015), "Development of topography in 3-D continental-collision models", Geochem. Geophys. Geosyst., 16, doi:10.1002/ 2015GC005732.*

Chapter 4. The effect of rheological approximations in 3-D numerical simulations of subduction/collision. In this chapter, I test the effect of rheological approximations on mantle and lithosphere dynamics in a geometrically simplified 3-D model setup in which the dynamics of subduction and collision is entirely driven by slab-pull (i.e., “free subduction"). The models exhibit a wide range of behaviours depending on the rheological law employed: from linear to temperature-dependent visco-elasto-plastic rheology that takes into account both diffusion and dislocation creep. Results suggest that rheology exerts a strong effect on slab morphology (i.e., style of break-off), trench migration rates and topography in the upper plate (i.e., presence of a back-arc basin).

Chapter 5. 3-D Numerical simulations of Greater India reconstructions and its convergence with Eurasia for the last 120 Ma. A new type of 3-D lithospheric and mantle-scale numerical models are developed to investigate how the India-Eurasia convergence has been accommodated by subduction in the Neo-Tethys, and how the shape of Greater India affects collision dynamics. The numerical models show the spontaneous formation and merging of a double subduction system, which resulted in a stable intra-oceanic subduction with a trench-trench-trench triple junction. The collision dynamics is controlled by the upper plate rheology and the size and shape of the Greater India extension, which controls the timing of collision and deformation pattern.

Chapter 6. Conclusions. This chapter briefly summarizes the findings of previous chapters.

The chapters of this thesis represent progress in the development of numerical simulations of subduction and continental collision and show the importance of coupling lithosphere and mantle dynamics for the study of convergent margins. As a final remark, this thesis grew along with the the development of LaMEM, thus considerable effort was also put in optimising and running large-scale long-term models.

Chapter 2

On the quality of velocity interpolation schemes for marker-in-cell method and staggered grids*

2.1 Summary

The marker-in-cell method is generally considered a flexible and robust method to model the advection of heterogenous non-diffusive properties (i.e., rock type or composition) in geodynamic problems. In this method, Lagrangian points carrying compositional information are advected with the ambient velocity field on an immobile, Eulerian grid. However, velocity interpolation from grid points to marker locations is often performed without preserving the zero divergence of the velocity field at the interpolated locations (i.e., non-conservative). Such interpolation schemes can induce non-physical clustering of markers when strong velocity gradients are present [*Jenny et al.*, 2001] and this may, eventually, result in empty grid cells, a serious numerical violation of the marker-in-cell method. To remedy this at low computational costs, *Jenny et al.* [2001] and *Meyer and Jenny* [2004] proposed a simple, conservative velocity interpolation scheme for 2-D staggered grid, while *Wang et al.* [2015] extended the formulation to 3-D finite element methods. Here, we adapt this formulation for 3-D staggered grids (correction interpolation) and we report on the quality of multiple velocity interpolation methods for 2-D and 3-D staggered grids. We test the interpolation

*Submitted to *Pure and Applied Geophysics* as Pusok, A.E., Kaus, B.J.P., Popov, A.A. (2016), On the quality of velocity interpolation schemes for marker-in-cell method and staggered grids.

schemes in combination with different advection schemes on Stokes problems with strong velocity gradients, which are discretized using a finite difference method. Our results suggest that a conservative formulation reduces the dispersion or clustering of markers and that the density of markers remains steady over time considerably reducing the need of unphysical marker control.

2.2 Introduction

Chemical variations are present at all scales in the Earth's mantle and lithosphere. Thus, using an accurate treatment for advecting material properties, such as chemical heterogeneities, is often required and of great importance in geodynamic modeling [*Gerya*, 2010]. One of the most popular methods is to combine the use of Lagrangian points (markers, tracers or particles) with an immobile, Eulerian grid (i.e., *Gerya* [2010]; *Harlow and Welch* [1965]; *Woidt* [1978]). This method, also known as the marker-in-cell (MIC) method, is generally considered a flexible and robust method [*Gerya and Yuen*, 2003; *van Keken et al.*, 1997] and has been used to advect most or all fields, including composition or temperature (i.e., *Gerya* [2010]).

The general algorithm of the MIC method involves (1) velocity interpolation from the Eulerian grid to Lagrangian markers carrying compositional information, (2) time-integrated advection of markers, and (3) interpolation of material properties from the displaced markers back to the Eulerian grid by using a weighted-distance averaging. The MIC method has great potential, with zero diffusion (neglecting errors in position due to advection error), and the possibility of resolving features narrower than the grid spacing, as compared to grid-based advection methods (i.e., Ch. 8, *Gerya* [2010]).

However, velocity interpolation from grid points to marker locations is often performed without preserving the zero divergence of the velocity field at the interpolated locations (i.e., non-conservative). Such interpolation schemes can induce non-physical clustering of markers when strong velocity gradients are present [*Jenny et al.*, 2001; *Meyer and Jenny*, 2004] and this may, eventually, result in empty grid cells, a serious numerical violation of the MIC method. Proposed solutions to this problem include using higher mesh resolutions and/or marker densities, or repeatedly controlling the marker distribution (i.e., inject/delete), but which does not have an established physical background.

To remedy this at low computational costs, *Jenny et al.* [2001] and *Meyer and Jenny* [2004] proposed a simple, conservative velocity interpolation (CVI) scheme for 2-D staggered grids. Their results show considerable advantage over the more common interpolation schemes such as first-order formulations. *Wang et al.* [2015] extended the formulation to 3-D

finite elements, again yielding promising results relative to common interpolation schemes. However, their results cannot be directly applied to staggered grids, commonly used in finite difference and finite volume methods (i.e., *Gerya and Yuen* [2003]), because they have different node locations for each velocity component (Figure 2.1). Therefore, an adapted implementation of this scheme is required for 3-D staggered grids, and will be one of the topics of the current investigation.

Furthermore, the choice of velocity interpolation method varies throughout the geodynamic modeling community. The preferred ones, linear and quadratic schemes, are sufficiently accurate for many flow problems [*Gerya and Yuen*, 2003; *Tackley and King*, 2003; *van Keken et al.*, 1997], but known to be prone to the marker clustering problem described above. Therefore, our main motivation for this study stems from the fact that, the quality of various velocity interpolation schemes has not been rigorously documented for 2-D and 3-D staggered grids. In this paper, we test multiple interpolation schemes in combination with different advection schemes on Stokes problems with strong velocity gradients, which are discretized using a finite difference method. Our aim is to report on the quality of these methods for 2-D and 3-D staggered grids and find optimal ones that reduce the dispersion or clustering of markers, reducing the need of unphysical marker control.

The manuscript is organized as follows. First, we adapt the formulations from both *Jenny et al.* [2001] and *Wang et al.* [2015] for 3-D staggered grids (i.e., correction interpolation) and we describe other methods (i.e., direct interpolation) used in this study. We then perform numerical tests with these velocity interpolations by using established benchmarks, and finally, we discuss the implications of our results for the geodynamic modeling community.

2.3 Method

2.3.1 Governing equations

We illustrate the effect of conservative velocity interpolation and particle divergence by either imposing a zero-divergence flow field or by solving the Stokes equations, which also satisfies a zero-divergence condition. The Stokes equations represent a continuum mechanics approximation where the equations used to describe geological and geophysical processes consist of a set of balance equations for mass and momentum together with their constitutive relationships (i.e., *Turcotte and Schubert* [2002]). Therefore, the equations for conservation of mass and momentum, assuming incompressibility and neglecting thermal diffusion, are

given by:

$$\frac{\partial \sigma_{ij}}{\partial x_j} = -\rho g_i, \tag{2.1}$$

$$\frac{\partial v_i}{\partial x_i} = 0. \tag{2.2}$$

where i, j represent spatial directions following the Einstein summation convention, $\sigma_{ij} = -P + \tau_{ij}$ is the total stress tensor with $P = -\sigma_{ij}/3$ the pressure and τ_{ij} the deviatoric stress tensor, ρ the fluid density, g_i the gravitational acceleration, v_i the velocity and x_i the spatial coordinate.

These equations are discretised on a 2-D staggered grid in a MATLAB code and on a 3-D staggered grid in LaMEM [*Kaus et al.*, 2016]. In 2-D, we use a variable viscosity constitutive relationship: $\tau_{ij} = 2\eta\dot{\varepsilon}_{ij}$, where η is the Newtonian viscosity and $\dot{\varepsilon}_{ij}$ is the deviatoric strain rate tensor, defined as: $\dot{\varepsilon}_{ij} = \frac{1}{2}\left(\frac{\partial v_i}{\partial x_j} + \frac{\partial v_j}{\partial x_i}\right)$. The 3-D code LaMEM uses non-linear constitutive relationships that describe a visco-elasto-plastic rheology (details in *Kaus et al.* [2016]). We test the velocity interpolation schemes on established benchmarks and geodynamically relevant tests.

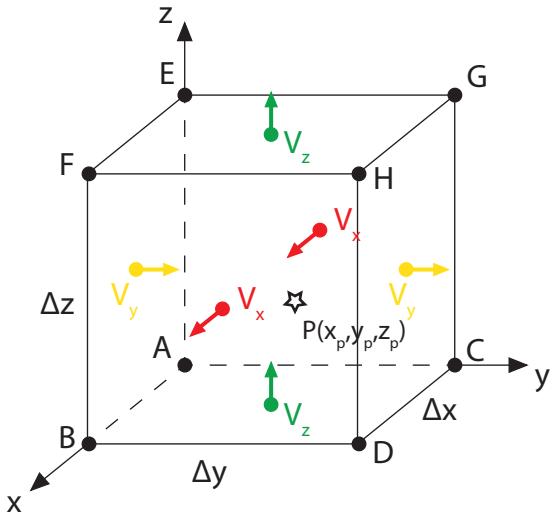

Fig. 2.1 Schematic diagram showing 3-D staggered grid, node locations and name convention used in this study. Compared to finite element schemes, where the velocity components are collocated in the grid nodes, the staggered grid velocities are located on face centres in 3-D and on grid edges in 2-D. To illustrate the interpolation examples, $P(x_p, y_p, z_p)$, represents a marker inside the grid cell.

2.3.2 Velocity interpolation methods for staggered grid

In this section, we describe the velocity interpolations used in this study, with detailed equations in the Appendix A.1. We distinguish between two velocity interpolation approaches: (1) direct interpolation, from the velocity points to markers, and (2) correction interpolation, by applying the method of *Jenny et al.* [2001] and *Wang et al.* [2015], which require interpolation from staggered points to grid nodes. The interpolation stencils for one staggered grid velocity component are shown in Figure 2.2 and they reflect the influence area or volume on the grid in which the marker velocity is affected.

1. Direct interpolation. On staggered grids, as compared to finite element methods, the velocity points are located in the middle of the grid edges (2-D) or on the centre of the grid faces (3-D) (Figure 2.1). Therefore, the usual approach is to interpolate each velocity component separately, in a control volume defined by the staggered points, to the marker (i.e., Figure 2.2, **Lin**). Close to boundaries, we use the boundary conditions to extend the stencil accordingly. We call this, a direct interpolation between staggered grid nodes and marker locations.

The choice for the type of direct interpolation can be broad, but it is worth mentioning that the use of a higher-order interpolation scheme produces undesirable numerical fluctuations in scalar, vector and tensor properties interpolated close to sharp transitions (i.e., *Fornberg* [1995]; *Gerya* [2010]). This scenario frequently occurs in geodynamic models, hence first or second-order velocity interpolations have been preferred and may be sufficiently accurate for many flow problems [*Gerya and Yuen*, 2003; *Tackley and King*, 2003; *van Keken et al.*, 1997]. For this reason, we test first order (linear - **Lin**), second order (quadratic - **Q2**, spline quadratic - **SQ2**) or a combination of first and second order (**L1Q2**, **L1SQ2**) direct interpolations. As the order increases, the interpolation stencil also increases, allowing a wider area of influence for the interpolated value (Figure 2.2). In 2-D, the bi-linear interpolation stencil involves 4 points, while in 3-D, it has 8 points with a tri-linear interpolation scheme. The second-order schemes have 9-points stencils in 2-D and 27-points stencils in 3-D. Details on the interpolation equations used are found in Appendix A.1.

Part of the direct interpolation schemes, we also test an empirical relationship (**LinP**, communication with T. Gerya), in which the marker velocity is interpolated from both velocity points and pressure points:

$$V_i^P = AV_i^{Lin} + (1-A)V_i^{pressure}, \tag{2.3}$$

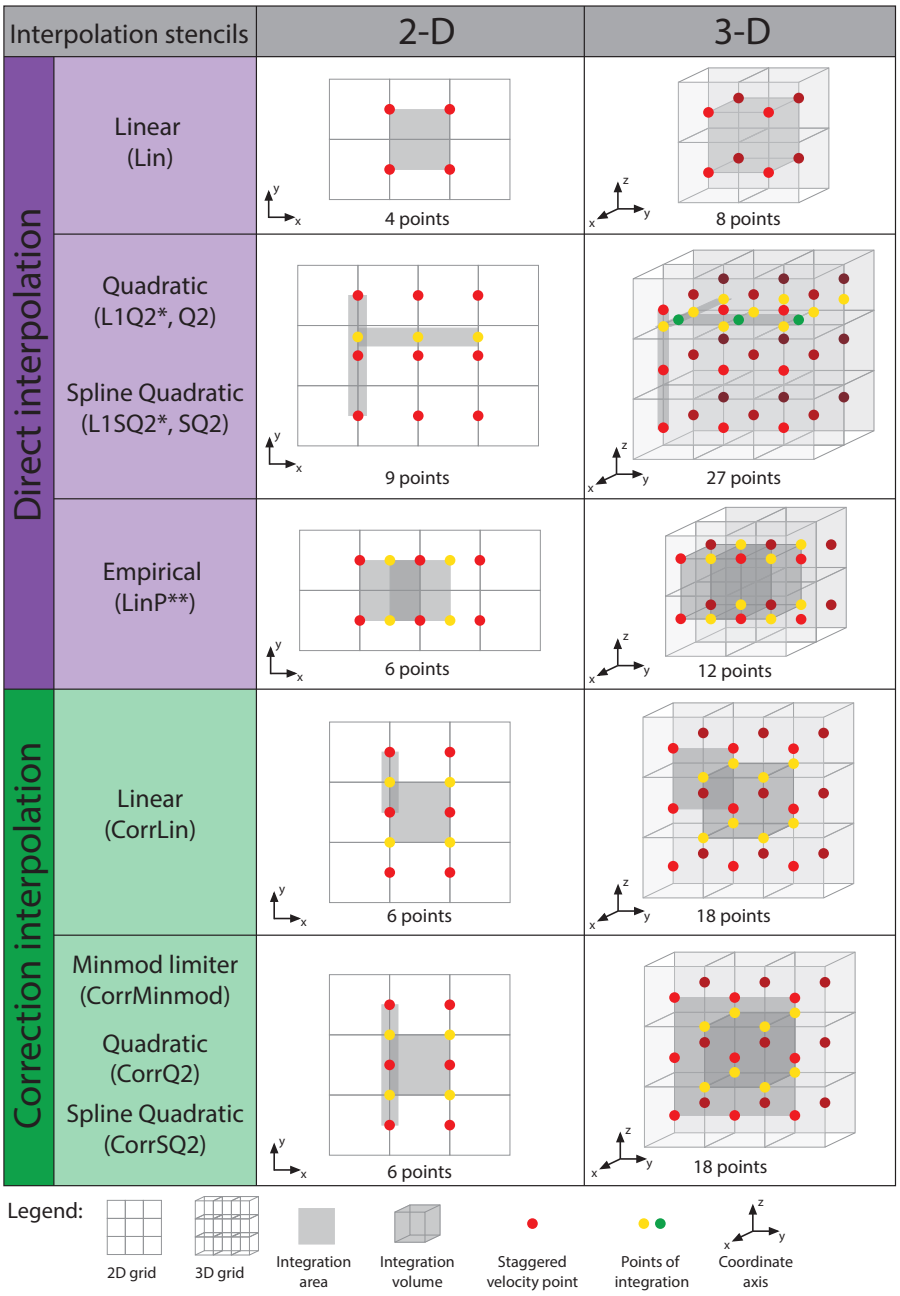

Fig. 2.2 Interpolation stencils for one staggered grid velocity component (i.e., V_x), with equivalent stencils applied for the other velocity components. Direct interpolation schemes involve interpolation from staggered points to markers. The correction interpolation follows the method from *Jenny et al.* [2001] (see text for details). For this interpolation, we vary the method of interpolation from staggered points to grid nodes, necessary for staggered grids to apply Eq. 2.4. (*) **L1Q2** and **L1SQ2** represent a combination of linear interpolation in the perpendicular direction and a quadratic interpolation in the parallel direction. (**) From communication with T. Gerya. **LinP** involves a combination of linear interpolation from velocity points and pressure points. See main text and Appendix A.1 for more details on the equations of interpolation schemes.

where V_i^P is the marker velocity component i at point P, V_i^{Lin} is the velocity component calculated using a bi-linear (2-D) or tri-linear (3-D) from the staggered points to the marker (same as **Lin** scheme), $V_i^{pressure}$ is the velocity component interpolated linearly from the pressure points, and A is an empirical coefficient, which is taken to be equal to $2/3$. The velocity in the pressure points, $V_i^{pressure}$, is calculated using a linear interpolation from the neighboring staggered points, as seen in Figure 2.2. This method is relatively easy to implement, as it is an extension from the **Lin** method, but care should be taken for calculating $V_i^{pressure}$ in the boundary cells, where boundary conditions must also be applied to ensure a divergence-free flow everywhere in the domain.

2. Correction interpolation. The second approach, the correction interpolation, follows the method proposed by *Jenny et al.* [2001] and *Meyer and Jenny* [2004] and extended to 3-D finite element method by *Wang et al.* [2015]. Their scheme suggests that for a volume in which the velocity is defined in the corner points (Figure 2.1), the value at any point $P(x_p, y_p, z_p)$ can be calculated as:

$$V_i^P = V_i^L + \Delta V_i, \tag{2.4}$$

where V_i^P is the conservative velocity interpolated at the marker, V_i^L is the velocity interpolated through a bi-linear (2-D) or tri-linear (3-D) from the nodes to point P, and ΔV_i is a correction term, first proposed by *Jenny et al.* [2001] and extended to 3-D by *Wang et al.* [2015]. In the local 3-D control volume as shown in Figure 2.1b, the V_i^L velocity is defined using a tri-linear interpolation scheme with second order accuracy:

$$\begin{aligned} V_i^L(x_p,y_p,z_p) = (1-x_p) &\times (1-y_p) \times [(1-z_p) \times V_i^A + z_p \times V_i^E] + \\ x_p \ &\times (1-y_p) \times [(1-z_p) \times V_i^B + z_p \times V_i^F] + \\ (1-x_p) \times \ \ &y_p \ \times [(1-z_p) \times V_i^C + z_p \times V_i^G] + \\ x_p \ \times \ \ &y_p \ \times [(1-z_p) \times V_i^D + z_p \times V_i^H], \end{aligned} \tag{2.5}$$

where V_i denotes velocity components (V_x, V_y, V_z) and (x_p, y_p, z_p) are the local coordinates of point P in the control volume. The local coordinates are calculated by transforming the interpolation volume into a unit cube. The correction terms are defined as:

$$\Delta V_x = x_p(1-x_p)(C_{10}+z_pC_{12}) \tag{2.6}$$

$$\Delta V_y = y_p(1-y_p)(C_{30}+x_pC_{31}) \tag{2.7}$$

$$\Delta V_z = z_p(1-z_p)(C_{20}+y_pC_{23}) \tag{2.8}$$

$$C_{12} = \frac{\Delta x}{2\Delta y}[-V_y^A+V_y^B+V_y^C-V_y^D+V_y^E-V_y^F-V_y^G+V_y^H] \tag{2.9}$$

$$C_{23} = \frac{\Delta z}{2\Delta x}[-V_x^A+V_x^B+V_x^C-V_x^D+V_x^E-V_x^F-V_x^G+V_x^H] \tag{2.10}$$

$$C_{31} = \frac{\Delta y}{2\Delta z}[-V_z^A+V_z^B+V_z^C-V_z^D+V_z^E-V_z^F-V_z^G+V_z^H] \tag{2.11}$$

$$C_{10} = \frac{\Delta x}{2\Delta z}[V_z^A-V_z^B-V_z^E+V_z^F]+\frac{\Delta x}{2\Delta y}[V_y^A-V_y^B-V_y^C+V_y^D+C_{31}] \tag{2.12}$$

$$C_{20} = \frac{\Delta z}{2\Delta x}[V_x^A-V_x^B-V_x^E+V_x^F+C_{12}]+\frac{\Delta z}{2\Delta y}[V_y^A-V_y^C-V_y^E+V_y^G] \tag{2.13}$$

$$C_{30} = \frac{\Delta y}{2\Delta x}[V_x^A-V_x^B-V_x^C+V_x^D]+\frac{\Delta y}{2\Delta z}[V_z^A-V_z^C-V_z^E+V_z^G+C_{23}] \tag{2.14}$$

The 2-D expressions of the equations above can be obtained by eliminating one velocity component (i.e., V_z). The corrections in Eq. (6-14) come from a representation of each velocity component that is quadratic in the parallel direction and linear in the perpendicular direction. This makes the correction method second-order accurate.

Equation (2.4) requires that the velocity is known in the corner nodes, which is true for finite element discretizations [*Wang et al.*, 2015]. For staggered grid discretizations, an extra step is needed to apply the correction interpolation, which is to interpolate velocity from the staggered points to the corner nodes. *Jenny et al.* [2001] proposed a linear interpolation coupled with a *minmod* slope limiter for 2-D staggered grid (see Appendix A.1). However, this method has not been tested on 3-D staggered grids. Therefore, one of the aims of this paper is to adapt this method for 3-D staggered grid by looking at the robustness of different interpolation schemes to calculate the nodal velocities (i.e., V_i^{A-H}) for the correction interpolation.

The final scheme of the correction interpolation for staggered grids involves: (1) interpolation of velocity from staggered points to grid nodes, (2) linear interpolation in the control area/volume defined by grid nodes, and (3) applying velocity corrections to the marker velocity. We keep steps (2) and (3) the same, and for step (1) we test a linear interpolation (**CorrLin**), a linear interpolation coupled with a *minmod* limiter (**CorrMinmod**), a quadratic interpolation (**CorrQ2**) and a spline quadratic interpolation (**CorrSQ2**). All the stencils for these tests are the same for 2-D, with 6 points, and 3-D, with 18 points (Figure 2.2). We

note that the stencils for correction interpolation are intermediary in size to the direct linear interpolation schemes and second order direct interpolation schemes.

Having described the interpolation methods used in this study, we also test the combination of interpolation-advection scheme on marker behaviour since geodynamic codes employ different advection schemes. The simplest and easiest to implement is the first-order Euler advection scheme (first-order accuracy in both space and time). However, for most problems, a second or fourth-order Runge-Kutta scheme proves to be sufficiently accurate to advect the markers [*Gerya and Yuen*, 2003; *McNamara and Zhong*, 2004; *Moresi et al.*, 2003]. The forth-order Runge-Kutta advection scheme is very accurate in space (fourth-order accuracy) but less accurate in time (first-order accuracy). Therefore in this study, the markers are advected at every time step by a either a first order (Euler), second order (Runge-Kutta 2) or forth order (Runge-Kutta 4) accurate in space schemes.

The interpolation and advection schemes described above were implemented for testing in two staggered grid codes, 2-D MATLAB code and 3-D LaMEM.

2.4 Results

In this section, we investigate the quality of velocity interpolation schemes in both 2-D and 3-D staggered grids. We have chosen different numerical experiments in which markers behave differently, such that we can capture all possible artifacts due to velocity interpolation. The flow in all these problems is incompressible, so ideally, no particle convergence (clusters) or divergence (empty cells) should occur. Markers were initialized on a regular grid with each marker perturbed from its grid position by a random amount of up to half a grid spacing, in order to eliminate artifacts due to marker alignment. For one set of experiments, the initial marker distribution remains constant.

Moreover, for steady state flow problems, the markers are passively advected through the interpolated velocity field and do not affect the flow. In the case of active advection, or time-dependent advection problems, the composition field carried by the particles can have a feedback on the solution of Stokes equations (Eq. 3.2-3.3). Time-stepping is done using a Courant-Friedrichs-Lewy condition which limits the size of the time step based on the grid size, maximum velocity and a stability constant (CFL).

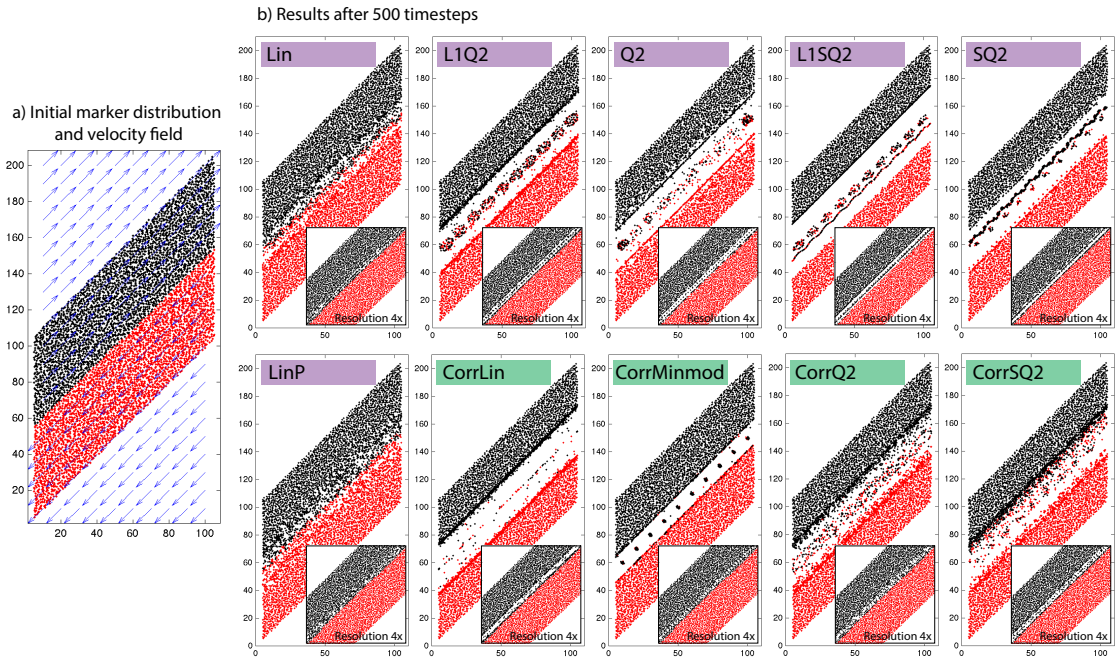

Fig. 2.3 Results using a zero-divergence flow with a sharp interface. a) Initial marker distribution and velocity field. The model setup is dimensionless with size $L = 110$ in the x-direction and $H = 210$ in the y-direction. The flow is set as: $V_x = 1, V_y = 1$, if $(y - L/2) > x$, and $V_x = -1, V_y = -1$ otherwise. We use a time step $\Delta t = CFL \times \Delta x$, where Δx is the grid size and $CFL = 0.5$, and periodic boundary conditions which recycle markers that go outside the domain. The boundary between the black and the red markers reflects the change in polarity in the velocity field. b) Results after 500 time steps with different interpolation routines for Runge-Kutta 4th order advection scheme and for two resolutions: 11 x 21 cells and 44 x 84 cells in the lower right corners.

2.4.1 Steady-state flow problems

Opposing flow on an interface (2-D)

The first experiment is a simple test, in which we impose a zero-divergence opposing flow on an interface as shown in Figure 2.3a. This setup can be imagined as a subduction interface or as shearing of two materials. The interface is at 45° angle to the boundaries of the domain to observe interpolation effects for both velocity components (V_x and V_y), and reflects a change in polarity in the velocity field. The figure caption contains details for reproducing the setup.

Figure 2.3b shows results for every interpolation scheme for Runge-Kutta 4th order advection scheme, and for two grid resolutions: a coarser resolution of 11 x 21 cells, and a finer resolution of 44 x 84 cells. The coarser resolution helps to visualize the behavior of each interpolation scheme in the proximity of a sharp velocity change. At the interface, the flow suggests a rotational component, such that if interpolation is conservative, there will be no rotational dispersion of markers. This case is observed only for **LinP**, and partially for **Lin**, while in the other cases rotational dispersion (i.e., **Q2**, **CorrQ2**, **CorrLin**) or rotational collapse (i.e., **CorrMinmod**, **L1Q2**) is observed. The width of the band in which artifacts can occur is determined by interpolation stencil (i.e., second order stencils have wider bands) and grid size (higher resolution produces smaller bands). Using a higher resolution helps to diminish the extent of these artifacts, improving the behavior of the interpolation scheme, noticed especially for **CorrMinmod**.

SolCx benchmark (2-D)

We benchmark our Matlab 2-D code with the SolCx test [*Duretz et al.*, 2011b; *Zhong*, 1996], which provides an analytical solution for 2-D incompressible Stokes flow with a sharp lateral viscosity jump (Figure 2.4a). The non-dimensional domain has a unit aspect ratio and is discretised by 32 x 32 cells. The viscosity jump of 10^4 is located in the middle of the domain. The flow is driven by an internal sinusoidal force (due to a sinusoidal density distribution) and has free slip mechanical boundary conditions. We set an initial markers distribution of 25 markers/cell, which is passively advected after every time step using the velocity solution from the staggered points. This 2-D test has been used for benchmarking high viscosity contrast experiments [*Duretz et al.*, 2011b; *Moresi et al.*, 1996; *Thielmann et al.*, 2014], and was shown as a good example for the problem of marker clustering and empty cells in a finite element formulation [*Wang et al.*, 2015].

Figure 2.4b shows the summary of results obtained with different interpolation and advection schemes for the SolCx benchmark. The plots display the marker density for every cell, with marker artifacts shown in extreme colors: dark blue colors represent cells devoid

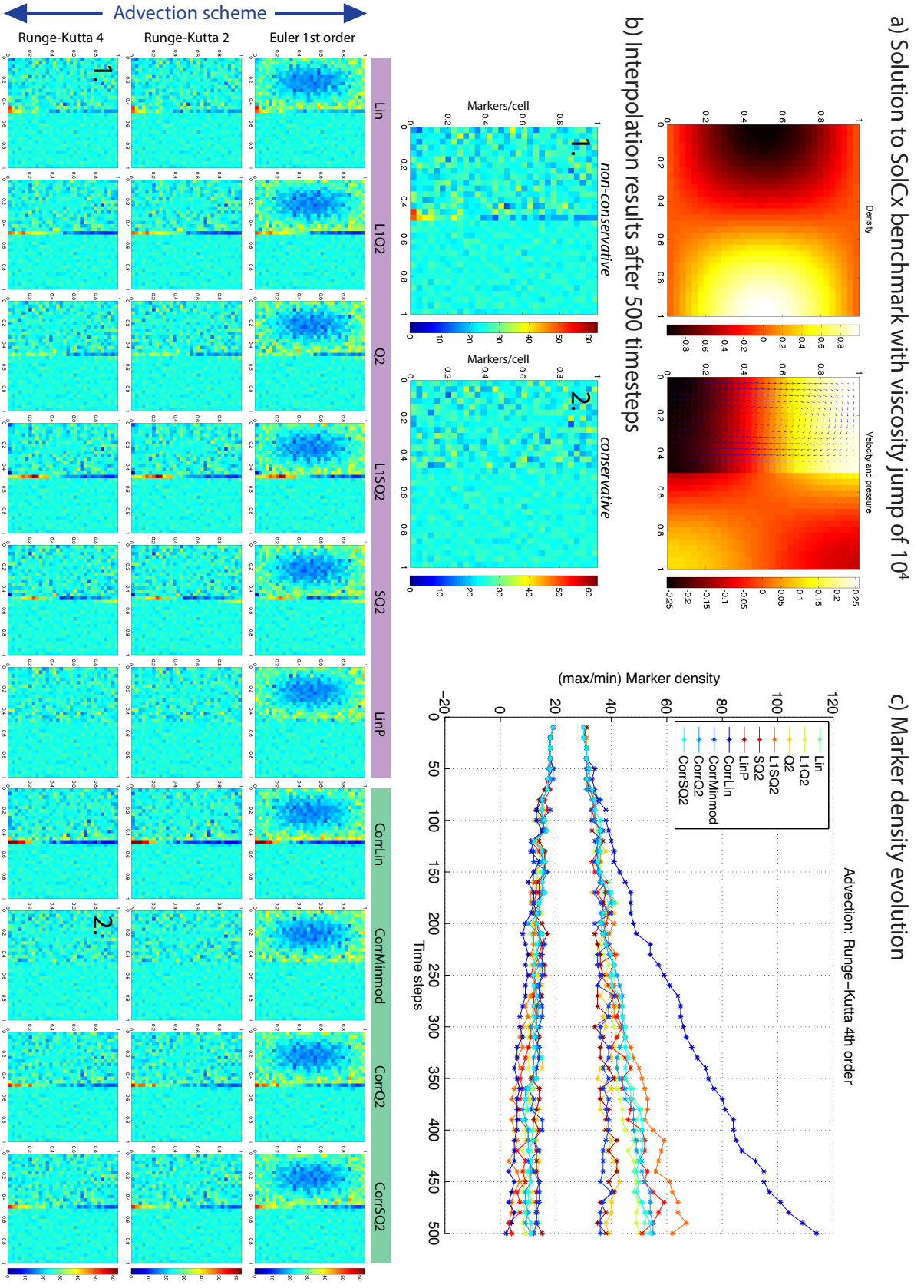
a) Solution to SolCx benchmark with viscosity jump of 10^4
Density
Velocity and pressure
b) Interpolation results after 500 timesteps
Markers/cell
non-conservative
conservative
c) Marker density evolution
Advection: Runge−Kutta 4th order
(max/min) Marker density
Time steps
Lin
L1Q2
Q2
L1SQ2
SQ2
LinP
CorrLin
CorrMinmod
CorrQ2
CorrSQ2
Advection scheme
Runge-Kutta 4
Runge-Kutta 2
Euler 1st order

Fig. 2.4 Results using the benchmark SolCx [*Duretz et al.*, 2011b] with a viscosity jump of 10^4, resolution 32 x 32 cells. a) Density and solution variables: pressure and velocity field. The viscosity jump in the middle of the domain produces a sharp boundary in the field velocity. b) Particle density after 500 time steps. The initial particle distribution is the same for all cases with random particle distribution of approximately 25particles/cell. c) Marker density evolution. Conservative methods have stable curves with constant distribution of markers. Empty cells are colored in blue, while clusters are shown in red.

of markers, while red colors represent marker accumulations. All the major artifacts occur at the viscosity jump, while a general large-scale divergence of the flow is also noticed for the first order, Euler advection scheme. This suggests that using a higher order advection scheme is considerably better than using a first order scheme. Moreover, the artifacts due to advection occur independently of the interpolation scheme, enforcing the statement that the MIC method has zero diffusion due to advection errors.

On the other hand, artifacts produced by a certain velocity interpolation method are present for all advection schemes, suggesting that using a higher order advection method will not improve the overall quality of the interpolation. The majority of the interpolation methods tested produce clustering and empty cells at the viscosity jump. The methods that performed the best results, with no clustering or empty cells regardless of the advection scheme, are **LinP** and **CorrMinmod**. Extensive experiments (Appendix A.2) further suggest these two methods are also independent of the magnitude of viscosity jumps, initial marker distribution and resolution for this particular setup. Artifacts due to direct linear and quadratic interpolation methods (**Q2**, **Lin**) also have a lower amplitude, though further tests (Appendix A.2) show that these methods are sensitive to the magnitude of the viscosity jump, with artifacts visible at a viscosity jump greater than 10^3.

An observation of the correction interpolation methods suggests that the choice of the interpolation needed for the extra step in interpolating from staggered points to the corner nodes (i.e., difference between **CorrLin** and **CorrMinmod**) is critical. **CorrLin** method produced the most pronounced artifacts, while as discussed above, results with **CorrMinmod** produced no artifacts. The reason why the other two interpolations tested, **CorrQ2** and **CorrSQ2**, are intermediate in quality despite a second order interpolation scheme to the nodes, is unclear.

Figure 2.4c shows the evolution of marker density (maximum and minimum number of markers/cell) for all interpolation methods for Runge-Kutta 4th order advection scheme. This plot helps to further discriminate between the interpolation schemes, as a conservative scheme would keep the marker density constant throughout the simulation. The observations in

Figure 2.4b are also reflected here, with the **CorrMinmod**, **LinP** and **Q2** methods producing a constant density distribution throughout the simulation.

2.4.2 Time-dependent advection problems

Rayleigh-Taylor instability (2-D)

The second test is the Rayleigh-Taylor instability (similar setup as *van Keken et al.* [1997]) to illustrate the behavior of interpolation schemes in a geodynamically relevant problem with an active advection (Figure 2.5a). In this setup, the flow is driven by compositional density differences as a higher density material (ρ_r) sits on top of a lower density material (ρ_0). The interface between the two fluids has a small perturbation to initiate flow. In this set of experiments we set a viscosity contrast η_r/η_0 of 10^3, but other viscosity contrasts were also tested (not shown). The model domain has a unit aspect ratio, with a resolution of 64 x 64 cells, and an initial marker distribution of 25 markers/cell. The markers are advected after every time step with the ambient velocity field and allowed to actively affect the flow field by interpolating back to the grid the material properties carried by the particles.

Figure 2.5c displays the evolution of marker density over time for all interpolation methods. Compared to the SolCx benchmark, the marker densities are relatively stable, suggesting that the velocity field for this Rayleigh-Taylor setup does not constitute a difficult problem for interpolation and artifacts occur only in combination with the least conservative methods. Results in Figure 2.5b with **Lin** and **CorrMinmod** interpolation schemes, and extended results in Appendix A.2 confirm this observation. The interpolation schemes that performed poorly in previous section (i.e., **CorrLin**), also produce larger artifacts and unstable density evolutions in this setup. A higher viscosity contrast is expected to produce different results, and more interpolation schemes prone to artifacts.

Subduction with/without sticky air (pseudo 3-D)

The following section presents results using the 3-D code LAMEM (Lithosphere and Mantle Evolution Model) [*Kaus et al.*, 2016]. The model setup represents a pseudo-3-D subduction model after [*Agrusta et al.*, 2014] (Figure 2.6a) and includes a downgoing plate with a weak layer, subducting beneath an upper plate. The domain extends 2000 km in x direction, 20 km in y direction and 700 in z direction, with a computational resolution of 256 x 4 x 128 cells. We impose a half-space cooling model for the thermal structure of the lithosphere (80 Ma age) and an adiabatic gradient of 0.5°C/km in the mantle. The plates have a composite visco-elasto-plastic rheology, while the mantle is kept Newtonian (see Figure 2.6 for details on the material parameters), as we are interested only in producing variable viscosity contrasts and

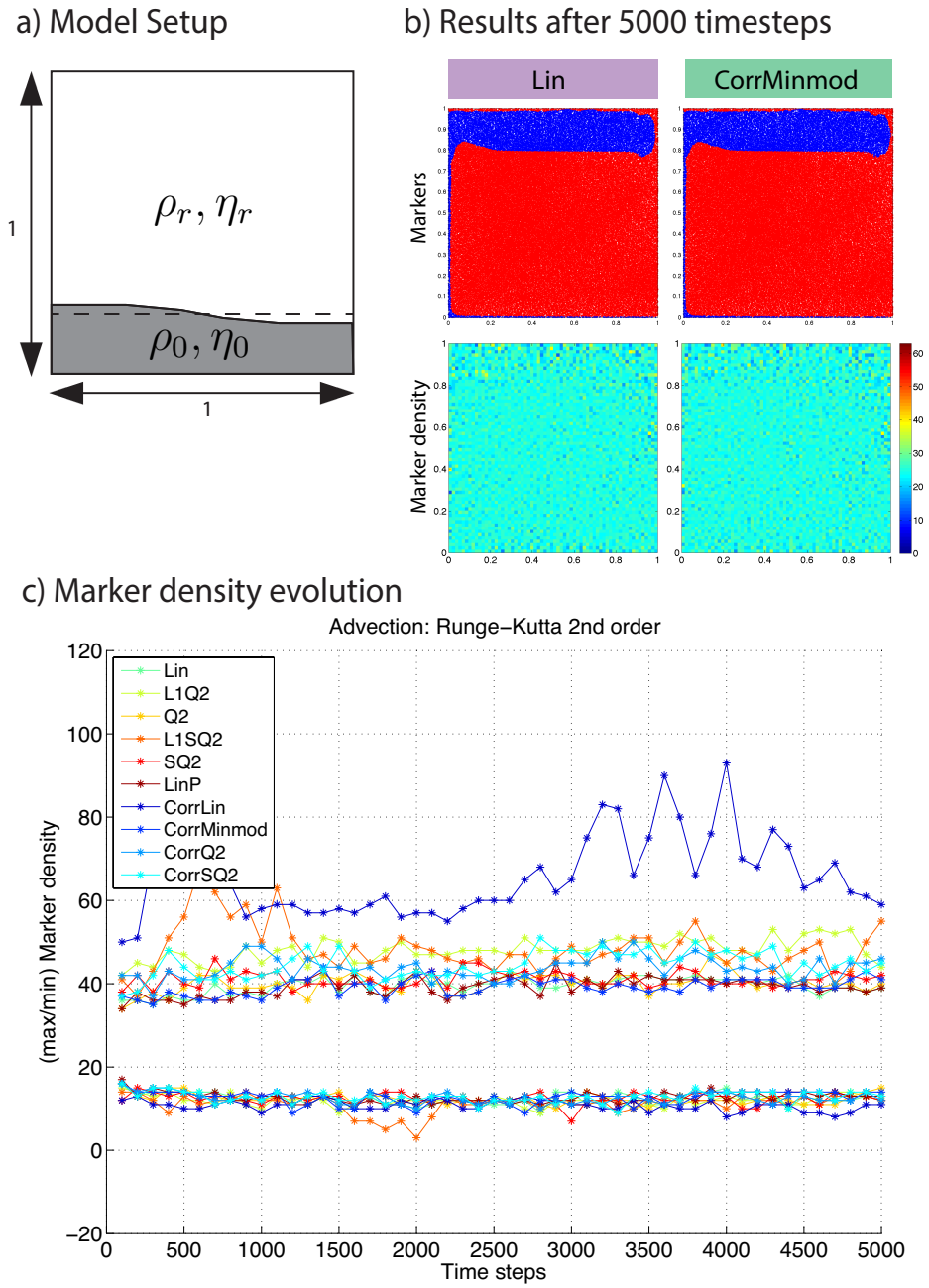

Fig. 2.5 Results for the Rayleigh-Taylor instability with a viscosity contrast of 10^3 and resolution 64 x 64 cells. a) Model Setup. b) Marker distribution and density for **Lin** and **CorrMinmod** schemes after 5000 time steps. c) Evolution of marker density for all interpolation schemes. The majority of interpolation schemes produce a stable marker density over time.

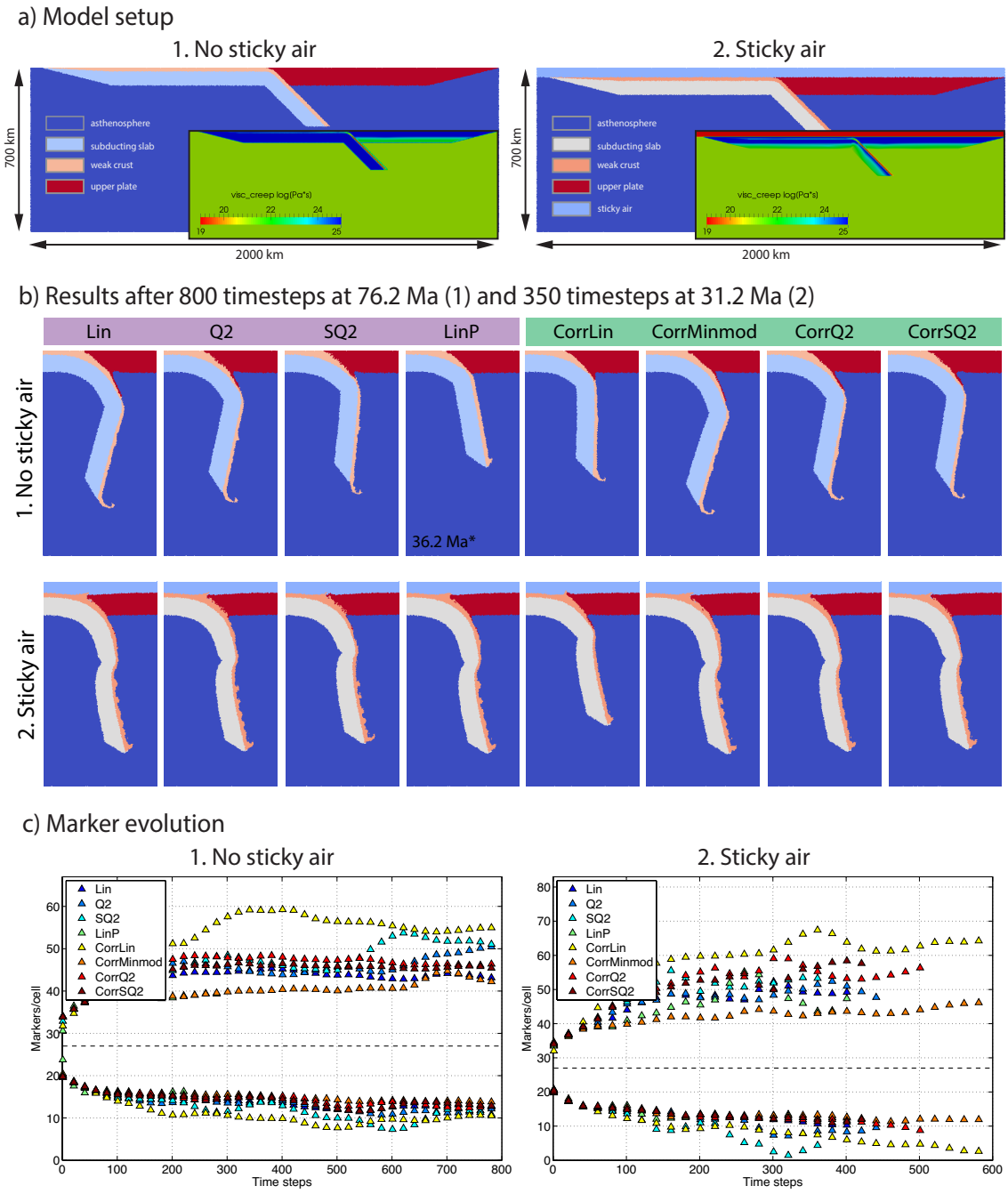

Fig. 2.6 Results for the subduction setup with/out sticky air (pseudo 3-D). a) Model Setup and viscosity structure. Thermal structure: half-space cooling model for an 80 Ma old lithosphere, and an adiabatic gradient of 0.5°C/km in the mantle. The rheology of phases is the following: the mantle has a constant viscosity of 1e21 Pa.s, for the subducting slab and upper plate, a dislocation creep profile for dry olivine from *Hirth and Kohlstedt* [2003] is used, and for the weak crust, a wet quartzite profile from *Ranalli* [1995] is used. We use a Drucker-Prager criterion for plasticity and we use a shear modulus G = 50 GPa. b) Marker distribution at 76.2 Ma (800 time steps) for simulations without sticky-air, and at 36.2 Ma (400 time steps) for simulations with sticky air. Results are shown for different interpolation schemes using a 4th order Runge-Kutta advection scheme. c) Marker density evolution for different interpolation schemes and advection schemes. The simulation without sticky air and using **LinP** stopped before reaching an evolved stage for reasons described in Discussion.

a complex velocity field. The initial marker distribution of 27 markers/cell is random, but it is kept the same for all simulations. The boundary conditions are free-slip on all sides.

Previous authors [*Kaus et al.*, 2010; *Schmeling et al.*, 2008] have shown that the type of upper boundary condition ("free slip" or "free surface") is important for subduction modeling. While finite element models can easily incorporate free surface boundary conditions, the implementation for staggered grids is more difficult. Instead, a common technique used by finite difference codes is to employ an internal free surface together with a stabilization algorithm [*Kaus et al.*, 2010], by using a "sticky air" with a very high viscosity due to computational restrictions (we use 10^{18} Pa.s). Topography can develop in these circumstances [*Crameri et al.*, 2012].

Hence, we perform tests on two setups: (1) subduction without sticky air, and (2) subduction with sticky air, allowing for a geological topography in the model (Figure 2.6a). A number of viscosity jumps, where numerical artifacts due to marker interpolation may occur, can be identified: the slab-asthenosphere boundary ($> 10^3$ viscosity jump), the weak layer-upper plate boundary ($> 10^4$ viscosity jump) and the sticky air-plate boundary ($\sim 10^5$ viscosity jump). The latter and the largest in magnitude is present only in simulations with sticky-air.

Figure 2.6b shows the distribution of markers after (1) 800 time steps for simulations without sticky air and (2) 350 time steps for simulations with sticky air. The results are for different interpolation schemes, using a 4th order Runge Kutta scheme for advection. As expected, the quality of the interpolation scheme is noticeable at the viscosity boundaries, for example, the weak crust-upper plate boundary, where some methods produce smooth interfaces. In simulations without sticky air, the **CorrMinmod** and **Lin** maintain a relatively sharp boundary, while the **SQ2** method produces a diffuse boundary, suggesting that in the later case, markers on one sides of the viscosity jump are advected with velocities belonging to the other side of the jump.

The marker interfaces are even more dramatic for simulations with sticky-air. Subduction is more vigorous than for simulations without sticky air, and hence, the relative motion between the slab and upper plate is higher. At the slab-mantle interface, markers are strongly affected by this rapid motion, with ripples forming along the subducting slab. The markers at the crust-upper plate interface show more irregularity, with air markers (light blue) often trapped in the subduction channel. The only exception is recorded for **LinP** interpolation.

The stability of interpolation methods is clearly visible in the marker evolution plots (Figure 2.6c), where marker density remains stable for conservative methods, and unstable and divergent for non-conservative methods. The **CorrMinmod** interpolation gives the least divergence of the markers (orange trend) for both setups. The empirical approach **LinP** and

the direct linear interpolation (**Lin**) produce remarkable good results, though they become highly unstable in simulations with sticky air.

2.5 Discussion

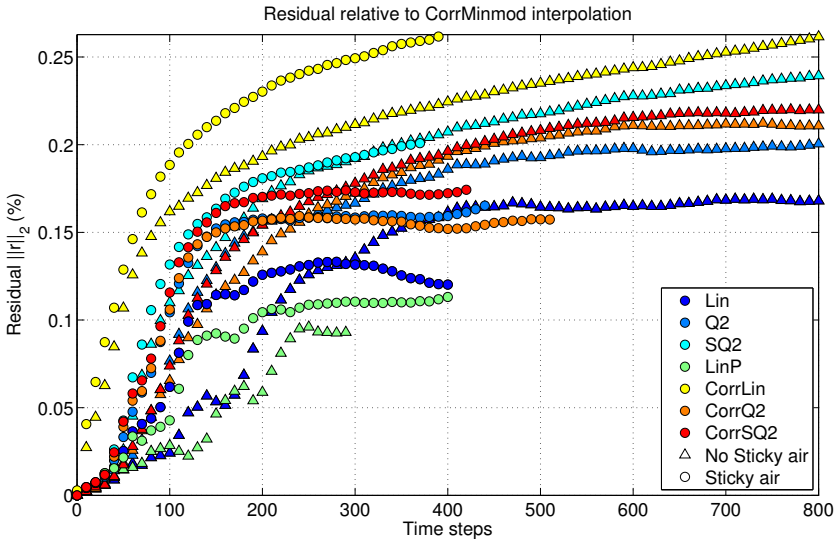

Fig. 2.7 Residuals or degree of difference between the results for different interpolation schemes relative to results obtained with the direct linear interpolation method **Lin**.

In this study, we report on the quality of velocity interpolation for marker-in-cell method for 2-D and 3-D staggered grids. Marker artifacts (clustering and dispersion of particles) are insensitive to numerical discretization (they occur both in finite element and finite difference discretizations), resolution or advection methods. Instead, they are caused by interpolation methods in the proximity of large viscosity and/or velocity jumps. Our results from multiple experiments suggest that the **CorrMinmod** method, first proposed by *Jenny et al.* [2001] and *Meyer and Jenny* [2004], is a conservative velocity interpolation independent of viscosity contrasts, resolution, or initial marker distribution. The empirical **LinP** method comes in closely, performing considerably better than the other direct interpolation schemes (i.e., **Lin**, **Q2**). A small advantage of **CorrMinmod** over **LinP** is related to implementation, as the latter one requires an extra layer of ghost cells that must take into account the boundary conditions to keep the divergence free condition. Moreover, our results suggest that numerical artifacts due to interpolation become visible when the viscosity jump is larger than 10^3.

The MIC method is widely used in problems with a large number of material components (heterogeneities). Therefore, an accurate advection of the markers is required. An important

observation in Figure 2.6b is that some interpolation methods (i.e., **SQ2**, **CorrLin**) produce very different results compared to others (i.e., **Lin**, **LinP**, **CorrMinmod**), despite the fact that time increments (Δt) have been kept identical throughout the simulations. This suggests that different interpolation schemes produce small variations in marker positions, which accumulate on a longer time scale. We quantify the difference between the simulation results by computing a residual, r, relative to the correction interpolation scheme (**CorrMinmod**), defined as:

$$||r||_2 = ||x_{i,p} - x_{i,p}^{CorrMinmod}||_2, \tag{2.15}$$

where $x_{i,p}$ is the marker fraction of phase p in cell i, and $||r||_2$ is the 2-norm of the residual r. This residual quantifies the difference in the distribution of markers between two simulations. We choose the **CorrMinmod** method as the reference because it gave the best overall results in all our tests. The residuals are plotted in Figure 2.7, in which we observe similar trends for both setups with/out sticky air. The **LinP** produces the smallest residual relative to **CorrMinmod** method, suggesting that these two methods are the closest in behavior. The **Lin** method follows closely the trend of **LinP**, which is expected, since the empirical approach is an extension of the linear method. We propose that the quality of the interpolation method is reflected in the magnitude of the residuals, as the methods that produce the largest residuals (i.e., **CorrLin**, **SQ2**) are also shown in Figure 2.6b to be unstable and to diverge, producing clustering and empty cells.

The large differences in the residual between different methods is a serious problem, and has large implications for tracer and chemical transport problems in fluid dynamics (i.e., advection of fine features, such as low-viscosity fluids or trace elements). The magnitude of the residuals shown in Figure 2.7 is small (plotted in percentage), but using an incorrect interpolation method the residuals can increase considerably in time and would lead to erroneous simulation results. One such method is the **CorrLin**, which would be interpreted as applying the results from *Wang et al.* [2015] directly to staggered grid without prior consideration. Therefore, the choice of the interpolation method needed for the extra step in the correction method is critical.

While an effective MIC method should have an even distribution of markers, in fact the method requires only non-empty cells. Clustering of markers then becomes mainly a problem of increasing computational memory required by the simulation. Figure 2.3 shows that with increasing resolution, more interpolation schemes will satisfy this MIC condition (i.e., **Q2**, **CorrMinmod**, **CorrQ2**). However, LaMEM is more sensitive to the non-uniform distribution of markers because interpolation of material properties from markers to the grid

is performed in four control volumes (centre cells, and three cells related to each velocity component). This implies that the simulation will stop if one of the edge volumes is empty even if the center volume has markers. This can be seen in Figure 2.6c for sticky air, in which we plot centre volume marker densities, and where simulations were stopped before they reached empty centre cells. The simulation without sticky air and **LinP** was stopped for this reason before it evolved to 76.2 Ma like the other simulations. We argue that this aspect, further discriminates between the quality of the velocity interpolations, since it is very sensitive to a non-uniform marker distribution. For this reason, the correction interpolation approach (i.e., **CorrMinmod**) performed better or maintained a more uniform marker distribution than direct linear interpolation methods (Figure 2.6c).

Our results suggest that conservative schemes (**CorrMinmod**, **LinP**) reduce considerably the occurrence of empty cells, but might not eliminate it completely. Increasing the resolution and/or marker densities potentially solves this. However, the MIC is a computationally expensive method, especially in 3-D, such that limiting the number of markers is preferable. As such, controlling the marker distribution (i.e., inject/delete) can be useful in cases when it happens. We propose that a marker control routine based on an approximate Voronoi diagram algorithm [*Mishin*, 2011; *Velić et al.*, 2008], combined with a conservative velocity interpolation and a 4th order Runge-Kutta advection scheme can provide a powerful advection tool in geodynamic models.

While we provide a range of experiments to test the interpolation schemes, other extreme setups might pose different problems, and the methods we propose the best (**CorrMinmod** and **LinP**) might be prone to these problems, as we expect similar behaviors whenever large viscosity contrasts are encountered. Moreover, these methods could be similarly applied for the treatment of other fields, such as temperature.

2.6 Conclusion

We test two interpolation approaches, direct and correction interpolation, in combination with different advection schemes on Stokes problems with strong velocity gradients, which are discretized on 2-D and 3-D staggared grids using finite differences. We show that a conservative formulation reduces the dispersion or clustering of markers and that the density of markers remains steady over time, reducing the need of unphysical marker control. An empirical adaptation of the linear direct interpolation and the correction method, provided that the choice of interpolation method from the staggered points to grid nodes is appropriate (i.e., using a *minmod* limiter), give the best results.

Chapter 3

Development of topography in 3-D continental collision models*

3.1 Summary

Understanding the formation and evolution of high mountain belts, such as the Himalayas and the adjacent Tibetan Plateau, has been the focus of many tectonic and numerical models. Here, we employ 3-D numerical simulations to investigate the role that subduction, collision and indentation play on lithosphere dynamics at convergent margins, and to analyze the conditions under which large topographic plateaus can form in an integrated lithospheric and upper-mantle scale model. Distinct dynamics are obtained for the oceanic subduction side (trench retreat, slab roll-back) and the continental-collision side (trench advance, slab detachment, topographic uplift, lateral extrusion). We show that slab-pull alone is insufficient to generate high topography in the upper-plate, and that external forcing and the presence of strong blocks such as the Tarim Basin are necessary to create and shape anomalously high topographic fronts and plateaus. Moreover, scaling is used to predict four different modes of surface expression in continental-collision models: (I) low-amplitude homogenous shortening, (II) high-amplitude homogenous shortening, (III) Alpine-type topography with topographic front and low plateau, and (IV) Tibet-Himalaya-type topography with topographic front and high plateau. Results of semi-analytical models suggest that the Argand number governs the formation of high topographic fronts, while the amplitude of plateaus is controlled by the initial buoyancy ratio of the upper plate. Applying these results to natural examples, we

*In press as Pusok, A. E., and B. J. P. Kaus (2015), Development of topography in 3-D continental-collision models, *Geochem. Geophys. Geosyst.*, 16, doi:10.1002/ 2015GC005732.

show that the Alps belong to regime (III), the Himalaya-Tibet to regime (IV), whereas the Andes-Altiplano fall at the boundary between regimes (III)-(IV).

3.2 Introduction

Mountain belts and orogenic plateaus are mostly found within the upper plate of active or fossil subduction zones (continental subduction/collision that gave rise to the Tibetan or Iranian plateaus), oceanic subduction (Altiplano), or during intracontinental geodynamic settings (Colorado Plateau). While mountain belts are relatively narrow and long features of the Earth's surface, orogenic plateaus are broad and topographically high regions with an effect on global atmospheric circulation and climate [*Molnar et al.*, 1993].

All mountain belts and orogenic plateaus evolve differently from one another as the result of specific combinations of surface and mantle processes [*Dewey and Bird*, 1970; *Molnar and Lyon-Caen*, 1988; *Royden*, 1993]. Proposed mechanisms of crustal thickening, accompanying mountain formation, involve some combination of lower crustal flow [*Beaumont et al.*, 2001, 2004; *Lamb and Hoke*, 2007; *McQuarrie and Chase*, 2000; *Royden et al.*, 1997, 2008], homogeneous crustal thickening ([*England and McKenzie*, 1982] and references herein), delamination or thermo-mechanical erosion of the mantle lithosphere [*Bao et al.*, 2015; *François et al.*, 2014; *Le Pourhiet et al.*, 2006].

The collision between India and Asia is the largest present-day example of continental deformation and has consequently received the most attention. The collision, which started roughly 50 Myr ago [*Lippert et al.*, 2014; *Patriat and Achache*, 1984; *Replumaz et al.*, 2010], resulted in the uplift of the Himalayas and the Tibetan Plateau. Understanding the formation and evolution of the Himalayan-Tibetan region has drawn considerable interest in the scientific community, and open questions address the transition from subduction to collision and uplift, the driving forces of the India-Asia orogeny (i.e., ridge push, slab pull, or slab suction), the style of deformation inside the orogeny and at its Eastern and Western syntaxes, and the rise of the abnormally thick Tibetan plateau.

The crust beneath the Himalayas and Tibet reaches double the normal crustal thickness and, although some of the seismicity and deformation appears to occur in narrow linear zones, much of it is diffuse within the orogeny. As such, mechanisms for double crustal thickness are highly disputed and include wholescale underthrusting of Indian lithospheric mantle under Tibet (Argand model, 1924), distributed homogeneous shortening or the thin-sheet model [*England and McKenzie*, 1982; *Houseman and England*, 1986], slip-line field model to explain extrusion of Eastern side of Tibet away from Indian indentor [*Tapponnier et al.*, 1986] or lower crustal flow models for the exhumation of Himalayan units and lateral

spreading of the Tibetan plateau [*Beaumont et al.*, 2001, 2004; *Clark and Royden*, 2000; *Royden et al.*, 1997]. Of these, the thin-sheet model has successfully illustrated some of the basic physics of continental collision and has the advantage of a 3-D model being reduced to 2-D, but one of its major shortcomings is that it cannot simultaneously represent channel flow and gravitational collapse of the mantle lithosphere [*Lechmann et al.*, 2011; *Medvedev and Podladchikov*, 1999a,b], since these mechanisms require the lithosphere to interact with the underlying mantle or to have a vertically non-homogeneous rheology. None of the previous models can simultaneously represent active processes such as subduction, underthrusting, delamination, channel flow or extrusion, which are thought to be important during continental convergence.

More recently, 3-D models are emerging as important tools to understand the dynamics of coupled systems. However, the models simulating the dynamics of continent collision zones have relied on certain explicit assumptions, such as replacing part of the asthenosphere with various types of boundary conditions that mimic the effect of mantle flow in order to focus on the lithospheric/crustal deformation [*Yang and Liu*, 2009, 2013], or reduced the scale of the simulations and imposed symmetry aspects of the collision [*Li et al.*, 2013]. Previous 3-D models of continental subduction/collision have focused on collisions with a continental corner [*Li et al.*, 2013], collisions with small continents [*Magni et al.*, 2014; *Moresi et al.*, 2014] or large scale continental-collisions of India-Asia [*Capitanio and Replumaz*, 2013; *Replumaz et al.*, 2014]. However, exploring the development of topography in these models has received much less attention, despite the fact that topography is the best-known constraint in natural collision settings.

Here, we employ the parallel 3-D code LaMEM [*Fernandez and Kaus*, 2014; *Lechmann et al.*, 2011], capable of simulating lithospheric deformation while simultaneously taking mantle flow and an internal free surface into account. We present topographic results of a set of lithospheric and mantle scale simulations in which the Indian lithosphere is subducted and/or indented into Asia. In this study, we address the question of how large topographic plateaus, such as the Tibetan Plateau, form in an integrated lithospheric and upper-mantle scale model and why this particular orogeny is so different from other mountain belts. The purpose of the present work is not to model in detail the Himalayan-Tibet orogeny but rather, by carrying out numerical experiments on the subduction/collision dynamics in geometrically simple configurations, to gain more understanding of the formation and evolution of high mountain belts and orogenic plateaus.

We begin with a discussion of our choice of numerical model, which is followed by scaling of important mountain building processes. We then present long-term, large-scale 3-D numerical models performed to simulate the mantle-lithosphere system of a subduc-

tion/collision zone, and relate these results with our scaling analysis. Finally, we discuss the implications of our results with regard to the India-Asia collision zone and other natural orogenic systems.

3.3 Method

We use a continuum mechanics approximation where the equations used to describe geological and geophysical processes consist of a set of balance equations for mass and momentum together with their constitutive relationships.

The Stokes equations for conservation of mass and momentum, assuming incompressibility and neglecting thermal diffusion, are given by:

$$\frac{\partial \sigma_{ij}}{\partial x_j} = -\rho g_i, \tag{3.1}$$

$$\frac{\partial v_i}{\partial x_i} = 0. \tag{3.2}$$

where i, j represent spatial directions following the Einstein summation convention, $\sigma_{ij} = -P + \tau_{ij}$ is the total stress tensor with $P = -\sigma_{ij}/3$ the pressure and τ_{ij} the deviatoric stress tensor, ρ the fluid density, g_i the gravitational acceleration, v_i the velocity and x_i the spatial coordinate. The continental lithosphere is assumed to behave as a continuous medium deforming by steady state creep over long time intervals [*Turcotte and Schubert*, 2002], given by a variable viscosity constitutive relationship:

$$\tau_{ij} = 2\eta \dot{\varepsilon}_{ij} \tag{3.3}$$

where η is the Newtonian viscosity, constant for each material phase, and $\dot{\varepsilon}_{ij}$ is the deviatoric strain rate tensor, defined as:

$$\dot{\varepsilon}_{ij} = \frac{1}{2}\left(\frac{\partial v_i}{\partial x_j} + \frac{\partial v_j}{\partial x_i}\right) \tag{3.4}$$

These equations are solved numerically in LaMEM (Lithosphere and Mantle Evolution Model) [*Fernandez and Kaus*, 2014; *Lechmann et al.*, 2011], a 3-D parallel, finite difference staggered grid code. The domain is a 3-D Cartesian box in which a Lagrangian particle-in-cell method is used for accurately tracking distinct material domains as they undergo extensive deformation due to creeping flow. We also employ an internal free surface with a free surface

stabilization algorithm [*Kaus et al.*, 2010] that allows for the development of topography. The code is written in C and uses the PETSc library [*Balay et al.*, 2014].

In section 3.6.1, we also use the 2-D finite element code MILAMIN_VEP [*Crameri and Kaus*, 2010; *Kaus*, 2010] to solve for the deformation of a viscous wedge, reproducing the model setup and boundary conditions from *Medvedev* [2002]. More details can be found in section 3.6.1.

3.3.1 3-D Model Setup

The initial model setup was built using a simplified tectonic map of the India-Asia collision zone, such as the one from *Li et al.* [2013] (Fig. 3.1a). The Himalayan belt formed on the site of subduction of the Tethyan Ocean, active at least from the Jurassic [*Patriat and Achache*, 1984], which accreted the Indian continental block against the Asian continent. The overall geometry of the collision zone involves the indentation of India into Asia, marked by the red line in Fig. 3.1a, with curved syntaxes at the eastern and western margins. On a regional scale, the collision zone is bounded laterally by oceanic subduction, beneath Makran and beneath SE Asia (Sumatra), marked by green lines in Fig. 3.1a. Since the collision belt formed as a result of closing the Tethys ocean, we transition from oceanic subduction to continental collision in our model setup (Fig. 3.1b-c).

The numerical model domain extends 5100 km laterally in both x and y directions and 1000 km in the z direction (Fig. 3.1c). In the interest of simplicity in the models and because the shape of Greater India is still highly debated (see review [*Ali and Aitchison*, 2005]), the Indian continent is approximated as a square shape extending 2100 km x 2100 km laterally (map view Fig. 3.1b). We note that a similar geometry of the model setup was also explored in analogue models [*Bajolet et al.*, 2013].

The subducting oceanic plate has a uniform thickness of 60 km while the continental indentor and the upper plate have a uniform thickness of 100 km. The subduction is already initiated and the down-going plate extends to 250 km depth because subduction in the Tethys Ocean was already ongoing for a considerable time before the onstart of continental collision [*Patriat and Achache*, 1984]. The amount of oceanic material consumed up to the point of proximity of India and Eurasian plate is estimated to be at least 7000 km [*Van der Voo et al.*, 1999]. This means that some parameters, such as the initial strength of slab-pull and convergence velocity, are underestimated in our model.

The plate structure includes the crust and mantle lithosphere, each defined by two properties: viscosity and density as described in the governing equations (Eq. 3.2-3.4). Fig. 3.1c shows a total of 8 individual phases with 16 free parameters. To systematically explore

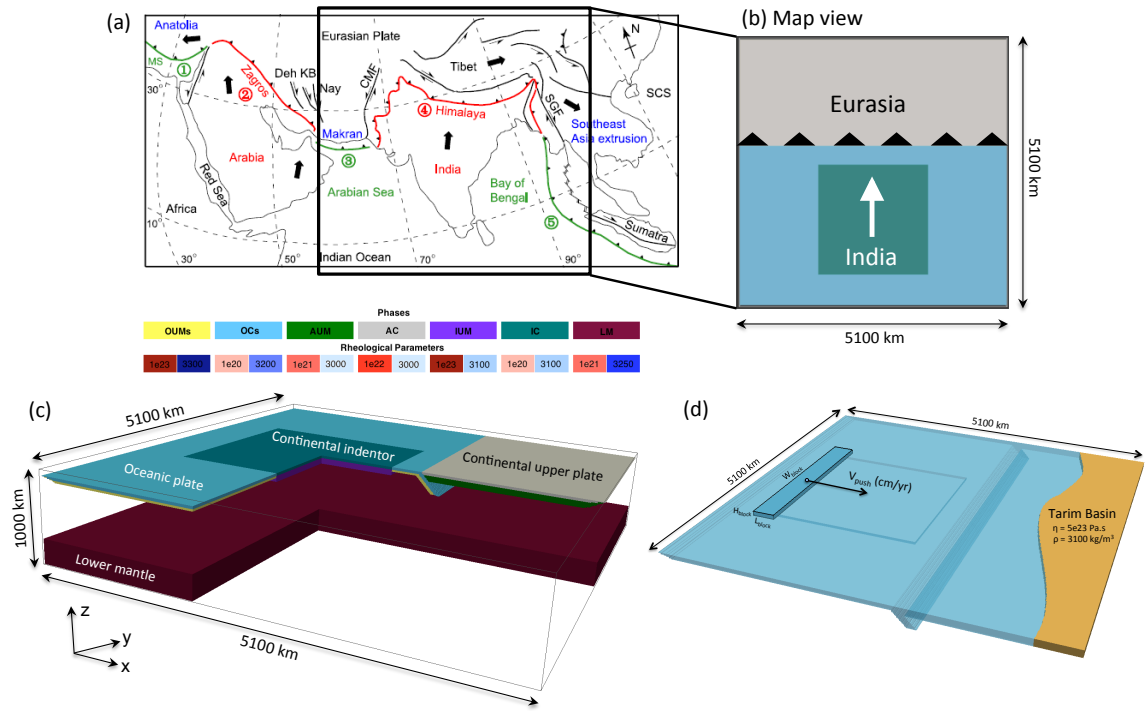

Fig. 3.1 a) Simplified tectonic map of the India-Asia zone from [*Li et al.*, 2013]. The major plate boundaries are marked by: green line - oceanic subduction, red line - continental collision. b) Map view of the numerical setup used in this study. The Indian continent is approximated as a rigid, square shaped body and has the dimensions of 2100 km x 2100 km in x and y directions. c) 3-D perspective of the model setup, that was sliced twice along the x and y planes for a clearer image. The model contains an oceanic plate with a continental indentor that subducts beneath a continental upper plate. Phases: OUM - Oceanic Upper Mantle Lithosphere, OC - Oceanic Crust, AUM - Asian Upper Mantle Lithosphere, AC - Asian Crust, IUM - Indentor Upper Mantle Lithosphere, IC - Indentor Crust, LM - Lower Mantle. Rheological properties are marked in the additional colorbar with: red - viscosity and blue - density. Phases are visualized using a finer pseudo-mesh of the particles that is 4 times higher resolution than the numerical grid. d) Implementation of external forcing in the model. The continental indentor is pushed with a given velocity V_{push}. We also test the presence of irregularly-shaped heterogeneous crustal blocks such as the Tarim Basin in the N of the Tibetan Plateau, for which we prescribe standard material properties.

all the free parameters would require a minimum of $2^{(2*8)} = 65536$ runs, far exceeding computational resources.

In order to reduce the number of simulations needed, we make further simplifications and assumptions in our model. Firstly, we assume that the focus in this study is on the lithosphere deformation and choose reference values for the upper mantle asthenosphere ($\eta = 10^{20}$ Pa.s, $\rho = 3200$ kg/m^3). At 660 km depth, the transition to the lower mantle is marked by a viscosity jump of one order magnitude and a density difference of 50 kg/m^3 [*Quinteros et al.*, 2010] which gives the best results of slab behavior in numerical models compared to tomographic observations. We also impose a result obtained in different numerical tests of simple subduction not shown here which found that a viscosity contrast between slab and asthenosphere less than 10^3 Pa.s results in an unstable, fragmented slab, contrary to tomographic observations of slab dynamics [*Replumaz et al.*, 2004; *Ribe et al.*, 2007].

While the topography of India-Asia collision is well known, the rheological structure of the lithosphere is often the subject of debate. To the present day, parameters for India-Asia collision zone are unknown or only theoretically approximated, such as viscosity of the upper or lower crust under the Tibetan Plateau [*Clark and Royden*, 2000; *Copley and McKenzie*, 2007]. Rather than focus on the true value of the parameters, our approach is therefore to use weak/strong or low/high values for the parameters, with the aim of understanding the importance of the varied parameters to the system (see parameter values in Table 3.1).

Simulation sets

Set	Factor	No. of simulations
1	FS	46
2	FS + SB	18
3	EF	18
4	EF + SB	12

Range and parameters varied

Name	Value
ρ_{AUM}, ρ_{AC}	3000-3100 kg/m^3
ρ_{IUM}	3100-3200 kg/m^3
ρ_{IC}	3000-3100 kg/m^3
ρ_{OC}	3100-3200 kg/m^3
η_{AUM}, η_{AC}	1e21-1e23 Pa.s
η_{IUM}	1e22-1e23 Pa.s
η_{IC}	1e20-1e21 Pa.s

Table 3.1 Summary of the cases and parameters varied in this study. Symbols stand for: FS - Free subduction, SB - strong blocks and EF - external forcing.

The far end of the oceanic plate is triangular in cross-section to mimic a mid-ocean ridge, a method generally used in numerical models to ensure that the lithosphere does not sink in the mantle [*Capitanio et al.*, 2011; *Duretz et al.*, 2011a; *Magni et al.*, 2012; *Moresi et al.*, 2014; *van Hunen and Allen*, 2011]. Using this 'mid-ocean ridge' method, the dynamics is controlled entirely by the balance between internal forces and plate convergence is entirely driven by slab-pull (i.e., without push force). However, another common approach is to impose a given velocity at which the plates are pushed from the sides [*François et al.*, 2014; *Li et al.*, 2013]. Instead of following one method or another, we test both cases in the interest of addressing yet another problem: the driving force in the India-Asia collision.

Commonly, slab pull is proposed as the main plate-driving force [*Turcotte and Schubert*, 2002]. However, in the case of India-Asia, the Indian continental lithosphere is considered too buoyant to actively drive subduction and slab pull is believed to be reduced to its minimum, given the inferred repeated episodes of slab break-off [*Chemenda et al.*, 2000; *Replumaz et al.*, 2010]. Thus, external forcing or the effect of far-field forces, has to be invoked [*Chemenda et al.*, 2000; *Li et al.*, 2008] in order to sustain the on-going convergence of India towards Eurasia at about 5 cm/yr, an almost constant rate since the beginning of the collision 50 Myr ago [*Patriat and Achache*, 1984].

Proposed forces include: ridge push, plume push, mantle-flow drag and slab suction [*Faccenna et al.*, 2013]. Of these, *Ghosh et al.* [2006] suggested that the Indian ridge push, which is due to the thermal thickening of the oceanic lithosphere, is still insufficient to sustain the India-Asia orogeny. Plume push was proposed to explain the high convergence velocities (of more than 16 cm/yr) [*Cande and Stegman*, 2011; *van Hinsbergen et al.*, 2011] during the emplacement of the Deccan traps. However, the effect of plume activity was identified important for India-Asia only between 70 and 45 Myr ago [*Cande and Stegman*, 2011], such that at the present day it is negligible in the force balance. Mantle-flow drag and slab suction were also proposed as an efficient mechanism for rapid continental plate motions [*Becker and Faccenna*, 2011]. Slab suction suggests that when large accumulations of slab, such as the one beneath India, sink into the lower mantle, a strong suction force is created that in turn induces a large overturning mantle flow, strong enough to drive the plates together [*Conrad and Lithgow-Bertelloni*, 2004; *Faccenna et al.*, 2013].

Whatever the nature of forces needed to sustain the convergence of India, we acknowledge the need for having external forcing in our model. Therefore, we perform a set of simulations with free subduction (FS), in which the dynamics is controlled entirely by the balance between internal forces (slab pull), and another set of simulations with external forcing (EF), where we imposed internal boundary conditions (pushing), seen in Fig. 3.1d and Table 3.1. External forcing is referred here as an integrated force needed to sustain the present-day

convergence of India towards Eurasia (∼5cm/yr) and is implemented numerically as internal Dirichlet boundary conditions.

We also test the effect of heterogeneous crustal blocks (SB or strong blocks) in the upper plate, such as the Tarim Basin in the N of the Tibetan Plateau. Several studies [*England and Houseman*, 1985; *Molnar and Tapponnier*, 1981; *Neil and Houseman*, 1997; *Vilotte et al.*, 1984] suggested that regions such as the Tarim Basin are stronger and more resistant to deformation than the surrounding continental lithosphere, and this can lead to enhancement of deformation around their edges.

Thus, four sets of simulations have been performed: 1) simulations with free subduction and no strong blocks (FS), 2) simulations with free subduction and strong blocks (FS+SB), 3) simulations with pushing and no strong blocks (EF), and 4) simulations with pushing and strong blocks (EF+SB). Details of the simulations are listed in Table 3.1 and Table B.1 in Appendix B.

The mechanical boundary conditions in our numerical domain are free slip on all boundaries and sticky air on top [*Schmeling et al.*, 2008]. The thickness of the air layer is 60 km and its viscosity is 10^{18} Pa.s, consistent with benchmark studies [*Crameri et al.*, 2012]. Finally, we assume an isothermal system and neglect erosion. In this study, we tested the importance of a large number of parameters and the approach was to run a consistent set of 3-D simulations with a numerical resolution of $170 \times 170 \times 33$ cells (grid resolution of 30 km in each direction). The discretized system of equations was solved computationally using a fully coupled method with an algebraic multigrid solver for the velocity block, provided by PETSc. Simulations were performed on MOGON (JGU Mainz) and JUQUEEN (Jüelich) high-performance clusters.

3.4 Scaling analysis

3.4.1 Mountain building and gravitational potential energy

Palaeomagnetic data from India and Tibet, and the observed distribution of topography suggest that much of the post-Eocene convergence of India with Asia has been taken up by deformation within Asia that involved crustal thickening [*Liu-Zeng et al.*, 2008; *Tapponnier et al.*, 2001; *Wang et al.*, 2013]. Generally, to form mountain ranges, horizontal forces must be applied to lithospheric plates, to drive them together and to cause crustal shortening and thickening. Isostatic compensation of the thickened crust then buoys up the mountain range to form high topographic amplitudes relative to the lowlands. When crustal shortening occurs, the forces driving the material together do work against resistive stresses, mainly

against gravity. Thus, the formation of both mountains and crustal roots is associated with an increase in gravitational potential energy (GPE), and part of the work done by forces that drive the plates together creates that potential energy.

The GPE per unit area of a column of material above a given depth can be calculated as the integral of the lithostatic pressure from the Earth's surface to that depth (Fig. 3.2a) [*England and McKenzie*, 1982; *Molnar and Lyon-Caen*, 1988; *Schmalholz et al.*, 2014; *Turcotte and Schubert*, 2002]. If we consider the depth of compensation at the bottom of the crustal root, the change in GPE between an elevated area (mountains) and the lowlands can be written as (see Appendix B for details):

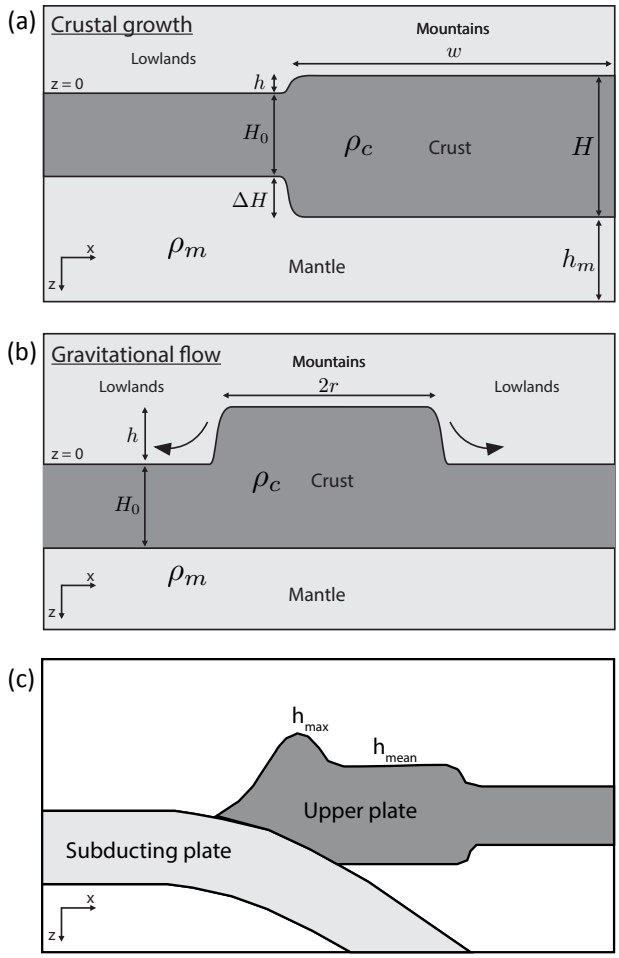

Fig. 3.2 a) Sketch of building gravitational potential energy in mountain building. b) Sketch of forces during gravitational flow. c) Definition of h_{mean} and h_{max}. If the difference between h_{max} and h_{mean} is at least 1 km high, we define as having a topographic front.

$$\Delta GPE = \rho_c g h(\frac{h}{2} + H_0 + \Delta H) - \Delta\rho g \frac{\Delta H^2}{2} \tag{3.5}$$

$$= \rho_c g h(\frac{h}{2} + H_0 + \frac{\Delta H}{2}). \tag{3.6}$$

Molnar and Lyon-Caen [1988] explored further the considerations for GPE in the formation of mountain ranges. They showed that when the forces driving the plates together can no longer supply the energy needed to elevate a high range or a plateau higher, the mountain range is likely to grow laterally in width instead of increasing in height because more work must be done to increase the range in height than laterally.

Moreover, it can be shown with a simple mathematical argument that shortening a half-width area, $w/2$, to elevate it to a height h, requires half the energy required to elevate an area of width w. This suggests that extra energy is available to further elevate the mountain range of width $w/2$. We explore the importance of this statement due to its connection to shortening a homogeneous layer versus shortening a heterogeneous layer (i.e., with strong crustal blocks). In the presence of heterogenous crustal blocks, where less material is available for deformation (i.e., shorter width), the energy has a finite space for propagation and we can expect further uplift, compared to a homogenous layer case. This will be seen later in simulation results with or without the presence of strong blocks.

3.4.2 Argand number

Based on considerations of GPE, *England and McKenzie* [1982] defined the Argand number, which is the ratio between an estimate of the excess pressure, $P(L)$, arising from a crustal thickness contrast of order L, and the stress required to deform the medium at a strain rate characteristic of the system, $\tau(\dot{\varepsilon}_0)$:

$$Ar = \frac{P(L)}{\tau(\dot{\varepsilon}_0)}. \tag{3.7}$$

The Argand number predicts that at high values, the excess pressure will dominate and the material will flow due to pressure gradients, while for a low Argand number, the viscous stresses are high and can sustain higher pressures and higher elevations. As such, the Argand number can be interpreted as a measure of the competition between two processes: relaxation in the vertical plane due to buoyancy forces which tends to produce a plane strain situation, and a horizontal flow controlled by the geometry and the boundary conditions in the horizontal plane.

Different formulations of the Argand number can be found in the literature, but we note that formulations that contain only initial values [*England and McKenzie*, 1982] have a greater advantage over those that need information about the final stages of evolution (i.e., *Bajolet et al.* [2013]). This suggests that initial conditions prior to collision already allow prediction of the outcome of the simulation. Therefore, we keep with the original formulation from *England and McKenzie* [1982], where the Argand number for a viscous material is given by:

$$Ar = \frac{\rho_c g H_0 \left(1 - \frac{\rho_c}{\rho_m}\right)}{\eta (u_0/H_0)} \tag{3.8}$$

where $\dot{\varepsilon}_0 = u_0/H_0$ is the characteristic strain rate, η is the effective viscosity, ρ_c and ρ_m are the densities of the crust and mantle, u_0 convergence velocity, H_0 thickness of lithosphere, and g is the gravitational acceleration.

3.4.3 Gravitational flow

When the forces driving convergence and sustaining mountain growth are removed or diminished (as a result of slab break-off), the system will try to minimize the excess of GPE. Let us consider an elevated area of radius r as in Fig. 3.2b, surrounded by lowlands, with a difference in height of h. If no forces are applied, the material will flow laterally by gravitational flow, and the topographic amplitude decreases exponentially with time following the equation:

$$h = h_0 \mathrm{e}^{-\frac{t}{t_r}} \tag{3.9}$$

where h_0 is the maximum amplitude before gravitational flow and t_r the characteristic time for exponential relaxation of the flanks, given by:

$$t_r = \frac{4\eta H_0}{\rho_c g r^2} \tag{3.10}$$

All scaling parameters are listed in Table 3.2 and detailed analysis is provided in the Appendix B.

Parameter	Definition and Comments	Dimensional Units	Expression or Range
ρ_c	density of crust/lithosphere	kg/m^3	3000-3100 kg/m^3
ρ_m	density of mantle	kg/m^3	3200 kg/m^3
L	length scale, $L = H_0$	m	70-120km
g	acceleration due to gravity	m/s^2	10 m/s^2
u_0	convergence velocity	m/s	0.1-6 m/s
η	viscosity	Pa.s	$10^{20} - 10^{23}$ Pa.s
H_0	thickness of the lithosphere	m	70-120km
W_0	width of the lithosphere	m	-
h	elevation	m	0-10km
ΔH	thickness of the lithospheric root	m	-
w	width of the mountain range, $w = 2r$	m	-
ΔGPE	difference in gravitational potential energy	Pa	$\rho_c g h(\frac{h}{2} + H_0 + \frac{\Delta H}{2})$
P_L	lith. pressure beneath the lowlands	Pa	-
P_M	lith. pressure beneath the mountains	Pa	-
σ	shear stress	Pa	$\eta u_0 / H_0$
Ar	Argand number	-	$[\rho_c g H_0^2 (1 - \frac{\rho_c}{\rho_m})]/(\eta u_0)$
Rm	Ramberg number	-	$[\rho_c g H_0^2]/(\eta u_0)$
t_r	relaxation time	s	$(4\eta H_0)/(\rho_c g r^2)$
t_c	characteristic time	s	H_0/u_0
t^*	convergence or dimensionless time corresponding to the total convergence in units of the initial thickness, H_0	-	t/t_c
β	shortening factor, W_0/W	-	$W_0/(W_0 - t^* H_0)$
h_{max}	maximum reachable height	m	$\Delta\rho H_0/\rho_m$

Table 3.2 Parameters used in the scaling analysis of mountain building processes.

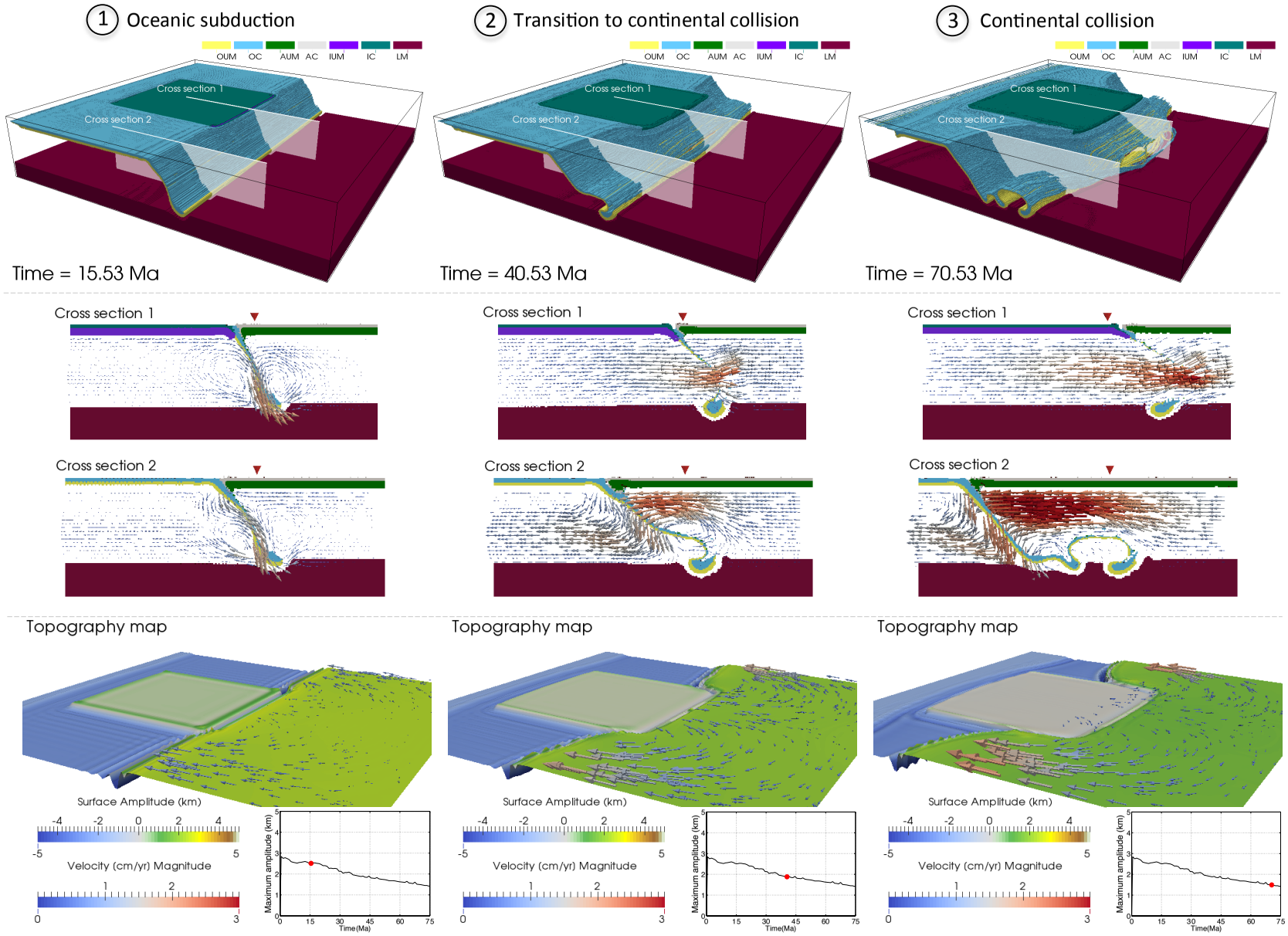
1 Oceanic subduction
2 Transition to continental collision
3 Continental collision
OUM OC AUM AC IUM IC LM
Cross section 1
Cross section 2
Time = 15.53 Ma
Time = 40.53 Ma
Time = 70.53 Ma
Cross section 1
Cross section 2
Topography map
Surface Amplitude (km)
-4 -2 0 2 4
-5 5
Velocity (cm/yr) Magnitude
1 2
0 3
Maximum amplitude (km)
Time(Ma)
0 15 30 45 60 75

Fig. 3.3 Evolution of the reference model. The top row shows evolution of slab shape, where the time axis is to the left. In the middle row, two cross sections are shown, one in the center of the continental collision, one in the oceanic subduction side. Mantle velocity vectors are shown as glyphs and the red triangles represent the initial position of the trench. On the bottom row, we show the topography maps of the model and the surface velocity arrows. In each of the lower-right corners, the evolution of the maximum amplitude in the upper plate is displayed. We distinguish between 3 stages of evolution: 1) Oceanic subduction, 2) Transition to continental collision and 3) Continental collision. The first stage is characterized by uniform oceanic subduction, with trench retreat. In the second stage, when the continent reaches the subduction zone, the onstart of collision is marked by trench advance in the continental side and a slight increase in topographic amplitude in the upper plate. The final stage is marked by very different regimes between the oceanic and continental sides. Beneath the continental collision we have trench advance and slab break-off, while on the oceanic side we have continuous subduction, trench retreat and slab roll-back. This complex dynamics strongly influence the surface features, through the strong lateral flow of material in the upper plate.

3.5 Numerical results

3.5.1 Reference Model

In this section, we summarize the results of a large number of numerical simulations of continental subduction, collision and indentation. We start by describing the evolution and general aspects of a reference model that satisfy a number of geophysical and geological evidence. For a better readability, we will use the acronyms: FS - free subduction, SB - strong blocks and EF - external forcing for the rest of the paper.

The evolution of the reference model (FS, without SB) is presented through material phase fields, velocity vectors and topography maps for different stages of subduction/collision (Fig. 3.3). As the model progresses in time, we distinguish 3 stages of evolution given by the dominant active process in front of the continental indentor: 1) oceanic subduction, 2) transition from oceanic subduction to continental collision, and 3) continental collision.

1. Oceanic subduction. This stage of evolution is characterized by oceanic subduction along the entire subduction front. This is an inherently 2-D process, since there are no lateral variations along the subduction trench. The system is driven by slab-pull, which depends on the slab buoyancy given by the density contrast between lithosphere and asthenosphere, and the extent of the slab. The oceanic slab is denser than the asthenosphere, and as subduction progresses, slab pull increases with increasing negative buoyancy. Under these conditions, when an oceanic plate subducts beneath a continental upper plate, we observe trench retreat

and slab roll-back (Fig. 3.3 stage 1), consistent with observations from other 2-D or 3-D numerical models [*Schellart et al.*, 2007; *Stegman et al.*, 2006]. When the slab reaches the transition zone to the lower mantle there is a slowdown in the subduction velocities. However, the largest impact on the slab velocities is the onstart of continental collision at approximately 15.5 Myr (Fig. 3.3 stage 2). During this initial stage, topography is marked by a deep subduction trench and by high elevation in the upper plate at the plate boundary, consistent with topographic profiles of the present-day Makran trench [*Ellouz-Zimmermann et al.*, 2007; *Kukowski et al.*, 2001].

2. Transition from oceanic subduction to continental collision. The second stage marks the arrival of the continental indentor at the subduction trench (Fig. 3.3 stage 2). Continental material is considerably lighter than the oceanic material, providing a very strong positive buoyancy force to resist slab pull. The force balance is disturbed and this stage mainly marks the time interval needed for the system to equilibrate under the new conditions. At the continent-continent boundary, the trench switches to either stationary or advancing regime [*Magni et al.*, 2012]. The forward motion of the continental indentor is accompanied by a build-up in topography in the upper plate. The lateral extent of this topographic front is controlled by the width of the indentor. At the ocean-continent boundary, trench retreat starts to be overridden by forced lateral extrusion of material in the upper plate, favoured by the advancing continent. Another consequence of the change in the force balance is that by resisting subduction beneath the continent, the slab starts thinning from the center towards the edges of the continent, incipient of slab detachment.

3. Continental collision. The last stage is dominated by continental collision in the center of the domain with oceanic subduction at the sides. Fig. 3.3 stage 3, shows results at 70.53 Myr, which we consider an evolved state due to the position of the indenting continent relative to the upper plate. The continent is hard to subduct and strongly resists subduction. At this stage, the slab is completely detached beneath the continent, but remains continuous and coherent beneath the oceanic side, taking a complex structure along the subduction/collision front (Fig. 3.3 stage 3). The surface velocity field shows extensive lateral extrusion and gravitational collapse, favoured by both continental indentation and trench roll back at the sides of the continent [*Li et al.*, 2013]. This strongly lowers the topographic amplitudes in the upper plate, an important process lacking in previous 2-D models.

The evolution of the maximum topographic amplitude in the upper plate (shown in the lower-right corners in Fig. 3.3) shows an increase immediately after collision. However, extensive lateral extrusion of material in the upper plate is induced by the difference in GPE between the collision area dominated by compression and the oceanic subduction dominated by extension, resulting in a decrease of the overall maximum topography.

The main features described in this section for each of these evolution stages occur in the rest of the simulations (the range of parameter values explored can be seen in Table 3.1). As such, we will not discuss further aspects of slab dynamics or mantle flow. Instead, we focus on the build-up of topography and its evolution. Simulations were generally stopped when the indenter had moved about 2/5 of the way into the upper plate, since this point corresponds roughly to the configuration of present-day collision of India with Asia.

3.5.2 Effect of external forcing

We summarize all simulation results in Fig. 3.4, where the topographic amplitude is plotted against the convergence velocity, u_0. Each point represents the mean topographic amplitude over time for one simulation, while the upper limit of the error bars represents the maximum amplitude in the upper plate ever reached in the model. Applying the same reasoning, we also plot with red markers examples from natural mountain ranges: Alps, Andes and Himalaya-Tibet.

Simulations with FS (with/without SB) do not reach convergence velocities higher than 2 cm/yr and average elevations higher than 3 km, marked by the horizontal red line. On the other hand, simulations with EF reach convergence velocities up to 6.5 cm/yr and average elevations up to 7 km. Velocities in simulations with EF reach more than the pushing velocity, $V_{push} = 5$ cm/yr, due to the superposition of slab pull: if subduction is facilitated by other factors, such as low friction between slab and upper plate, then higher velocities are obtained. The SB seem to also have an influence on the velocities in simulations with EF, as higher velocities are observed in the case without SB. This could be due to the fact that SB provide extra resistance against convergence as deformation is accommodated in a smaller area. We also observe that simulations with EF and SB resulted in significantly higher topographies compared to same simulations without SB (shown in green circles). On the other hand, the effect of SB in simulations with FS was not very pronounced, as shown in light blue circles.

Fig. 3.4 shows that in order to obtain higher topographic amplitudes, comparable to the ones in Himalaya-Tibet and the Andes, higher convergence rates are required, which can be reproduced by employing EF in the model.

The individual effects of EF and the presence of SB on topography can be seen in Fig. 3.5. Topographic maps for four different simulations are shown, in which the parameters values are kept the same and the only difference between them are the boundary conditions: FS or EF and with/without SB. Fig. 3.5(a-b) show that FS, driven by slab pull alone cannot create large elevations over long periods of time, since the energy provided by slab pull is small and gravitational flow of the material and the lateral extrusion of material at the sides become the dominant processes. On the contrary, if more energy is provided to the system, with

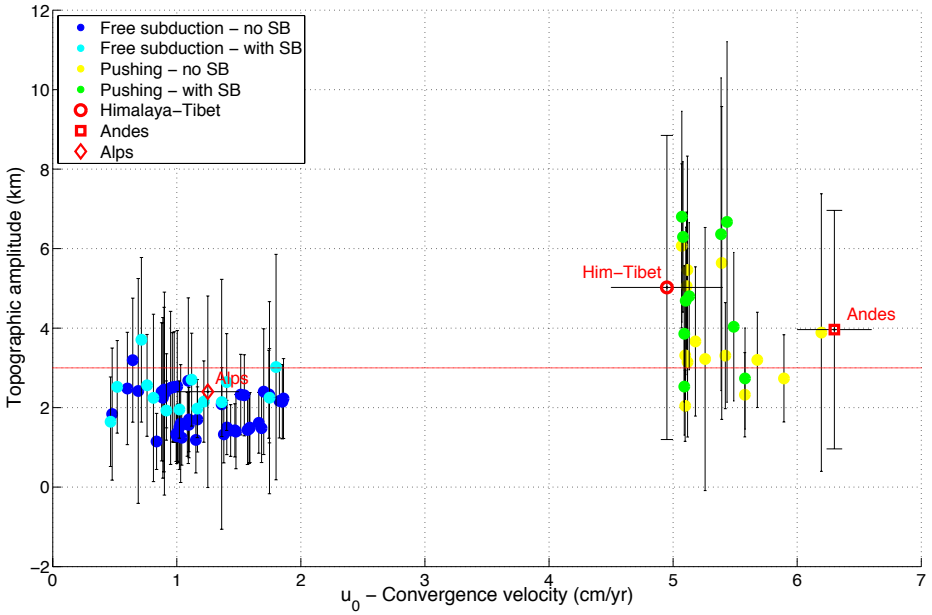

Fig. 3.4 Model elevation plotted against the convergence velocity. Each point represents a model simulation, where the point shows the mean elevation, the upper value of the error bars represents the maximum amplitude reached in the simulation and the lower value is symmetrical to the maximum amplitude with respect to the mean. Colours are distinguished for different sets of simulations: dark blue - free subduction with no strong blocks (FS), light blue - free subduction with strong blocks (FS+SB), yellow - pushing without strong blocks (EF), and green - pushing with strong blocks (EF+SB). The red markers represent values from natural mountain ranges: Alps (max. elevation 4.810 km), Andes (max. elevation 6.962 km) and Himalaya-Tibet (max. elevation 8.848 km). Results show that higher topographic amplitudes require higher convergence rates, obtained by employing external forcing and strong blocks in the model.

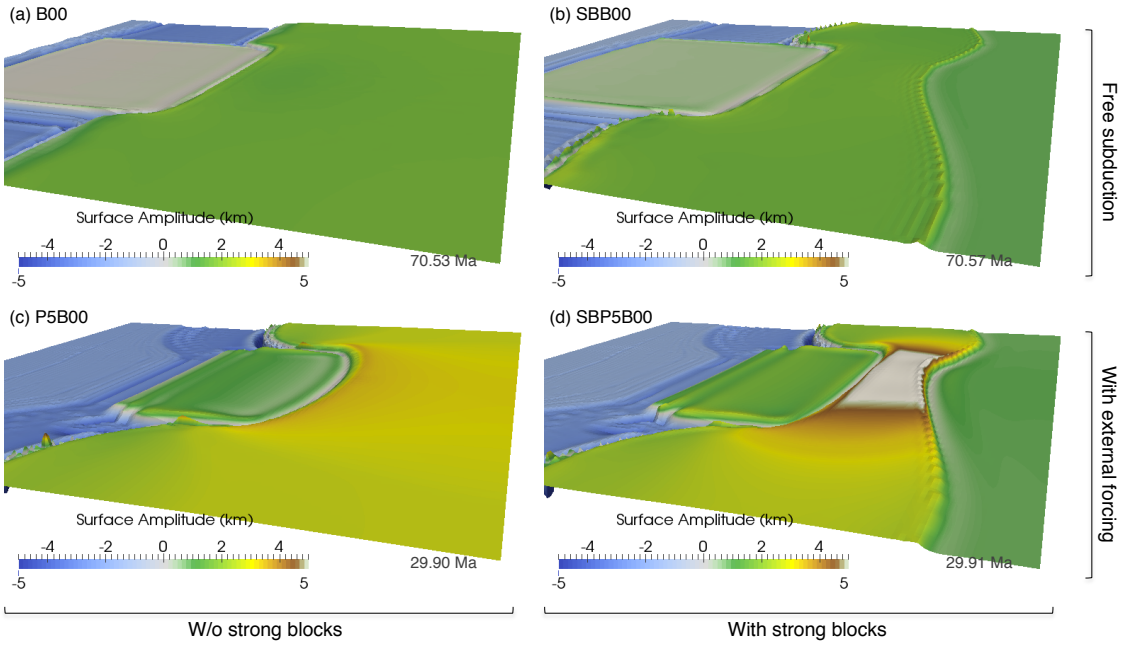

Fig. 3.5 Effect of external forcing on the topography of the upper plate. Each picture represents a topography map for an advanced simulation result (the time chosen for comparison is chosen depending on the position of the indenting continent relative to the oceanic trenches at the sides. a-b) Simulation results with free subduction after 70 Myr. c-d) Simulation results with external forcing (V_{push} = 5 cm/yr) after 30 Myr. The results show that with external forcing, more energy is spent to build higher topography. The strong blocks localize the deformation and stops lateral-outwards propagation of topographic growth, and promotes further vertical topographic growth. For visualization, the amplitudes have a vertical exaggeration of a factor $\times 20$.

convergence velocities approximately 5 times higher (EF), topographic growth is steady over time and represents the dominant process. Moreover, the SB (Fig. 3.5b and 3.5d) are resistant to deformation compared to the surrounding continental lithosphere, preserving a relatively low-elevation region. Crustal thickening is inhibited within the strong region, whereas it is enhanced at the boundary of the block where there is a steep topographic gradient. This is in agreement with previous numerical results [*England and Houseman*, 1985; *Molnar and Tapponnier*, 1981; *Neil and Houseman*, 1997].

Comparing Fig. 3.5c with 3.5d, we notice that after reaching a certain altitude at the collision boundary, topographic growth spreads favorably in a lateral fashion. However, when propagation cannot be spread laterally anymore, due to the presence of limiting blocks, further vertical topographic growth is promoted (Fig. 3.5d). Thus, SB localize deformation and affect the lateral propagation of topographic growth.

The evolution of topography for simulations with FS can be characterized by 2 stages: 1) growth and 2) collapse. In Fig. 3.6, we show detailed results for simulation B00 that was shown previously in Fig. 3.5a. There is an initial stage of topographic growth driven by slab pull, but once slab break-off sets in, gravitational flow and lateral extrusion of the material become dominant. In Fig. 3.6a, E-W topographic cross-sections are plotted for different time steps to show the evolution in time. The topographic amplitude grows until 22 Ma since the start of the model run, when it reaches the maximum value. This stage coincides with the time when slab detachment is finalized (Fig. 3.5c), and slab pull loses its driving power. Without a driving mechanism, topographic growth ceases and gravitational flow coupled with lateral extrusion of material, which is favored by the oceanic subduction, become dominant and lower the topographic amplitudes (Fig. 3.6b). The lateral extrusion of material can be inferred from the steady decrease in amplitude of the lowlands (arrows marked as *LE*).

The way the material of an elevated area spreads laterally due to gravitational flow is shown in Fig. 3.6d, where we fit Equation (B.24) to the decreasing model topographic amplitudes. The curve fits the data for a narrow width, consistent with numerical observations in Fig. 3.6c of a narrow topographic front. The deviations from the fit are attributed to the effect of lateral extrusion of the material, which enhances the topographic gradient between mountains and lowlands, accelerating the flow of material.

The example in Fig. 3.6 shows that processes at depth in FS simulations, such as slab detachment (i.e., by decreasing u_0) strongly influence surface processes. Two stages of topographic evolution are distinguished in this case: 1) dominantly growth and 2) dominantly gravitational flow, where the onset of gravitational flow is marked by slab detachment. In contrast, in simulations with EF only one stage of dominant topographic growth is observed, suggesting that the energy input through the pushing boundary conditions is sufficient to

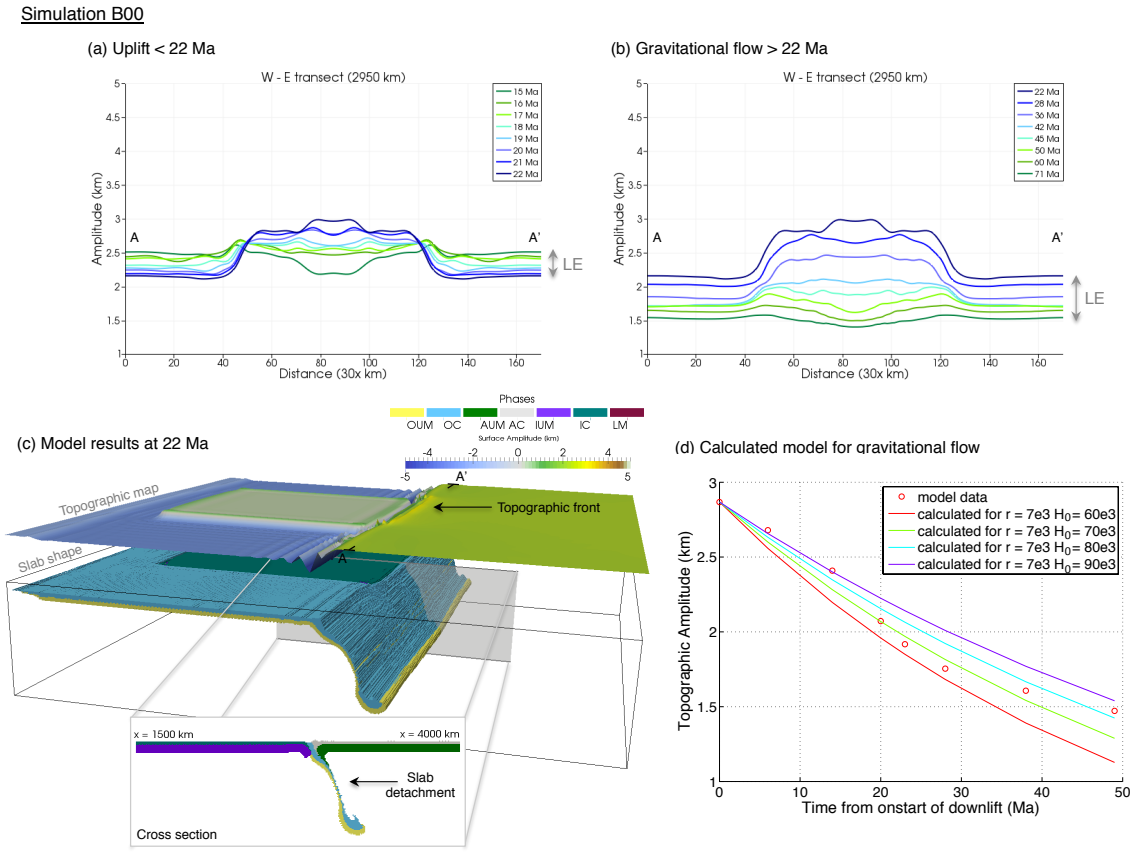

Fig. 3.6 Temporal evolution of topography in simulation B00 with free subduction and no strong blocks. a) Until 22 Myr we have a topographic growth stage, that results in a narrow topographic front at the collision boundary. b) When slab detachment occurs at about 22 Myr, the driving force is diminished and slab pull is at the minimum, gravitational flow and lateral extrusion of the material become dominant and lower the topographic amplitudes. c) Simulation results at 22 Myr. The maximum amplitude in the upper plate occurs in a narrow front at the collision zone. d) Calculated (Eq. B.24) vs model amplitude during gravitational flow.

sustain growth over a long period of time. In this case, processes at depth have a smaller influence on the topography evolution. This can also be seen in Fig. 3.10 and will be explained later.

The results in this section and the summary in Fig. 3.4 clearly show that the convergence velocity plays an important role in building higher topography in the upper plate, mainly by supplying the system with more energy needed to sustain topographic growth over time. However, we note that for one particular value of convergence velocity, there is a large range of topographic amplitudes or different responses from the system (i.e., for $u_0 \sim 5$ cm/yr, mean amplitude values plot between 2-7 km). Therefore, other factors must play an important role, which we explore next.

3.5.3 Topography analysis

Using the Argand number and the relaxation time defined in section 3.4, we plot the maximum topographic amplitude versus the mean topographic amplitude in Fig. 3.7, where each point represents one simulation result at an advanced stage. The time needed to reach this stage differs for every simulation and depends on the convergence velocity, such that it takes longer for FS simulations compared to EF simulations. Because of this, a dimensionless characteristic time is introduced ($t^*=t/t_c$, see Table 3.2), and referred to it as convergence time. The majority of the simulation results in Fig. 3.7 have a convergence time of 8-10, meaning that the total shortening has taken 8-10 lengthscales (H_0). The colorbars in Fig. 3.7 represent: a) $\log_{10}$(Ar), b) the relaxation time, t_r, and c) a buoyancy ratio equal to the ratio between the initial mean topographic amplitude and the initial thickness, h_0/H_0, measured just before the collision. The definition of h_{max} and h_{mean} is shown in Fig. 3.2c, and state that, if there is a difference of at least 1 km between them, we expect to have a topographic front. This is marked by the topographic front line (TFL). When h_{max} is equal to h_{mean}, the deformation reflects homogeneous shortening, which is shown in Fig. 3.7 by the HSL line (homogeneous shortening line). Therefore, the region between the two lines will be referred as the homogenous shortening band (HSB) and all simulations that plot outside this band show a topographic front of at least 1 km higher relative to the plateau.

In Fig. 3.7a, simulations with a very low Argand number (Ar $<<$ 1) generally plot outside the TFL line, while simulations with a high Argand number (Ar $>>$ 1), plot inside the HSB. This suggests that homogenous shortening dominates the system for a low Argand number, while a high Argand number promotes boundary thickening and formation of topographic fronts. Indeed, all simulations with a low Argand number show a topographic front while simulations with a high Ar number do not show a topographic front. This is in agreement with previous studies that, if Ar is small (i.e., the effective viscosity of the medium is large)

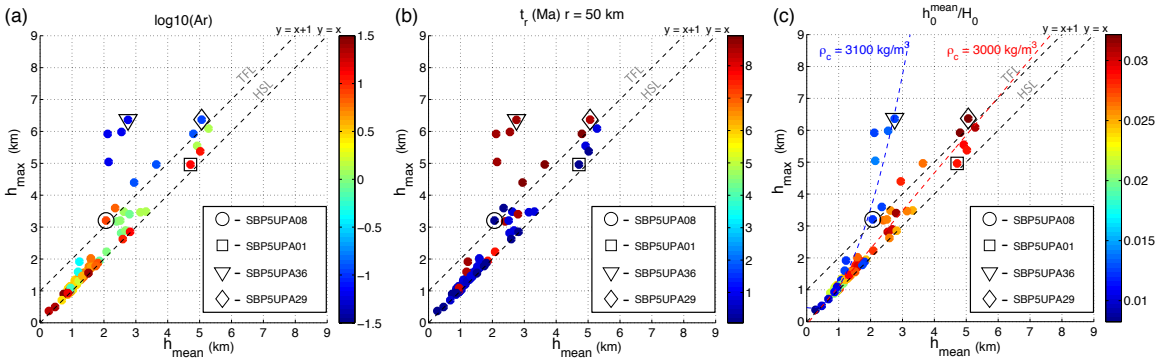

Fig. 3.7 Maximum amplitude plotted against the mean amplitude in the upper plate. Colorbars represent: a) $\log_{10}$(Ar), b) the relaxation time, c) the ratio h_0/H_0, which is the ratio between the initial mean amplitude and the initial thickness prior to collision. The grey dotted lines represent: HSL (homogeneous shortening line) for $y = x$ and TFL (topographic front line) for $y = x+1$, meaning that if we have a 1 km difference between h_{max} and h_{mean}, a topographic front is present. The region between the TFL and HSL is referred as the homogenous shortening band (HSB) In figure b) the relaxation times were calculated for a general case with a radius of 50 km. In figure c) the coloured dotted lines represent polynomial fits for different densities of the crust, with red for $\rho_c = 3000$ kg/m^3 and blue for $\rho_c = 3100$ kg/m^3. The simulations with black markers will be shown later into more detail in Fig. 3.8 as: (I) - SBP5UPA08, (II) - SBP5UPA01, (III) - SBP5UPA36, (IV) - SBP5UPA29.

the flow will be governed by boundary conditions and crustal thickness variations will not influence the flow. On the other hand, if Ar is large, the forces arising from crustal thickness variations will be dominant and the effective viscosity of the medium will not be high enough to support appreciable elevation contrasts [*England and Houseman*, 1986; *England and McKenzie*, 1982; *Houseman and England*, 1986].

The dependence of topographic fronts on the medium parameters can be also seen in Fig. 3.7b, where h_{max} and h_{mean} are now plotted against the relaxation time. We see a similar trend that simulations with high relaxation times ($t_r > 8$ Myr) plot outside the TFL line, while simulations with lower relaxation times ($t_r < 8$ Myr) plot inside the HSB. The significance of the relaxation time is the ability of the system to sustain topographic fronts for a longer period of time before they flow due to pressure gradients.

Fig. 3.7c shows that the initial buoyancy also plays an important role, especially in determining the final mean amplitude in the upper plate (h_{mean}). The figure shows that there are two clear trends, a blue trend with low values of h_0/H_0, corresponding to simulations that have a higher density of the crust, and a red trend with high values of h_0/H_0 that corresponds to simulations with a lower density of the crust. We note that the maximum amplitude does not seem to be affected as much as the mean amplitude or the amplitude of the plateau. This

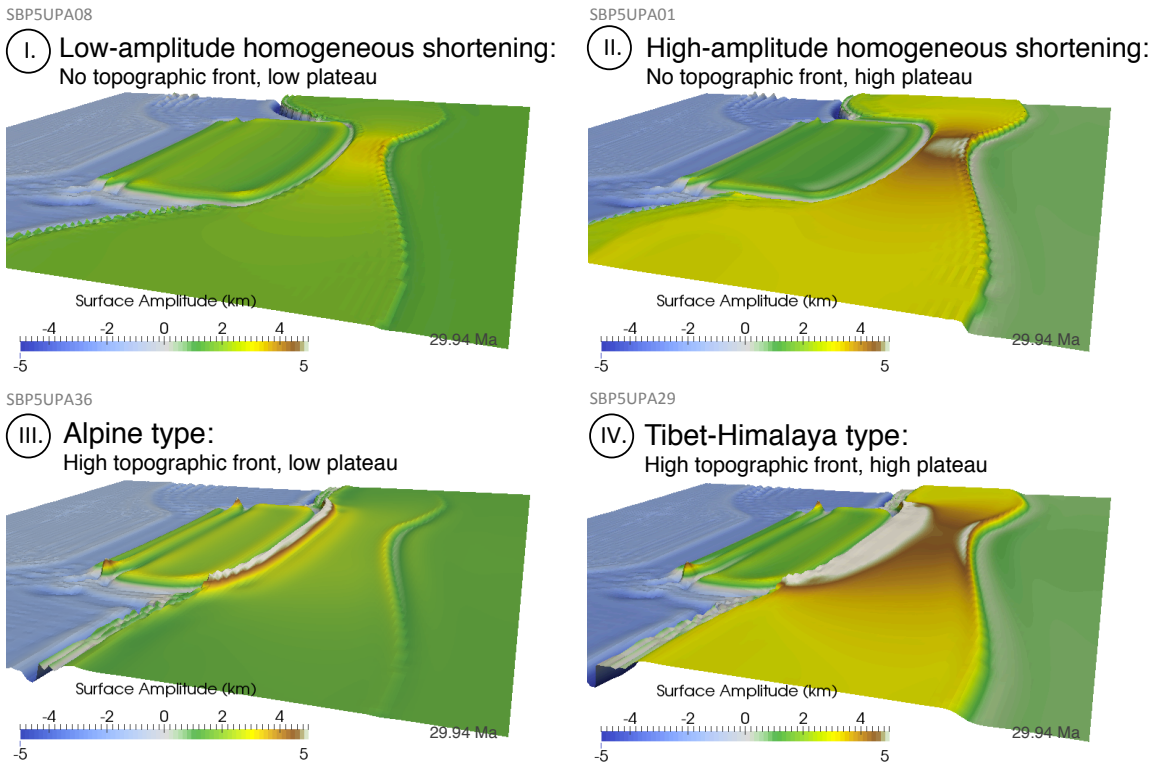

Fig. 3.8 Simulation results and different modes of surface expressions. (I) Low-amplitude homogeneous shortening, (II) High-amplitude homogeneous shortening, (III) Alpine type topography with a high topographic front and low plateau and (IV) Tibet-Himalaya type topography with both a high topographic front and high plateau. Each picture represents the topography map for simulations with external forcing and strong blocks.

suggests that the initial buoyancy is important for the topography of the plateau. A simple explanation is that the evolution of topographic amplitude during homogenous shortening depends on the crustal density and a compression factor β [*Turcotte and Schubert*, 2002] (see Table 3.2 and Appendix B for more details). As such, during compression, the topographic amplitude of a lighter crust increases faster than for a denser crust. This phenomenon is also observed in our numerical results, that simulations with a lighter crust develop higher topographic amplitudes compared to simulations with a less dense crust.

Looking at the simulation results plotted with black markers in Fig. 3.7, four different surface expressions are observed (shown in Fig. 3.8). Simulations type (I) and (II), plotting close to the HSB in Fig. 3.7, are consistent with our reasoning of homogenous shortening model, one with low amplitudes and the other with high amplitudes. On the other hand, type (III) and (IV), both with low Argand numbers, show a high topographic front at the collision zone. Type (III) represents a very narrow mountain range, reminiscent of the Alps,

while type (IV), with both a high topographic front and a high plateau (>5 km high) is more reminiscent of the Himalaya-Tibet range.

Based on these observations and interpretation of Fig. 3.7, results can be collapsed into a regime diagram shown in Fig. 3.9. The TFL divides the diagram into two regions: one with topographic fronts and very low Argand number and one without topographic fronts, high Argand number and dominated by homogenous shortening. Moreover, the initial buoyancy, marked by the blue dotted line, controls the mean topographic amplitude and divides the diagram into 2 other regions, of low and high plateau. The histogram in the lower-right corner shows that the sampling of simulation results was relatively uniform, with a convergence time t* = 8-10. Thus, four modes of surface deformation can be distinguished in Fig. 3.9: (I) - no topographic front and low plateau, (II) - no topographic front and high plateau, (III) - with topographic front and low plateau, and (IV) - with topographic front and high plateau. To summarize this part of results, we show that different combinations of input energy and material properties within the overriding plate, can lead to different topographic expressions of continental collisions.

3.6 Discussion

3.6.1 Interpretation of our results and time evolution of the regime diagram

The dynamics of subduction/collision models presented here are consistent with those obtained in previous 3-D numerical studies [*Capitanio and Replumaz*, 2013; *Li et al.*, 2013; *Magni et al.*, 2014; *Moresi et al.*, 2014]. During oceanic subduction, characteristic processes include trench retreat and slab roll-back, while trench advance and slab detachment are characteristic for continental collision. In models that include a plastic rheology of the crust [*Li et al.*, 2013; *Moresi et al.*, 2014], back-arc spreading and marginal sea opening have also been observed. Such mechanism is not reproducible in our model, which we attribute to the viscous rheology used. On the other hand, all previous 3-D models that incorporate lithosphere and mantle dynamics are either completely dynamic (free subduction) or have kinematic boundary conditions. Here, we study the effect of both cases (FS and EF).

While our model is simplified in terms of both rheology and geometry, we believe it displays some important observations that were lacking in previous 2-D models with more complex rheologies. These are: coupling of surface topography with deep processes, development of complex slab shape and mantle flow and its effect on topography, the influence of a laterally finite continent, and the effect of irregular strong blocks. We show results from a large set of numerical simulations (at least 5 times more simulations than

previous 3-D studies) and we perform an analysis of topography that was obtained in a dynamic and integrated model.

We show that continental collisions can result in different surface expressions that are controlled by the Argand number and a buoyancy ratio characteristic for the upper plate.

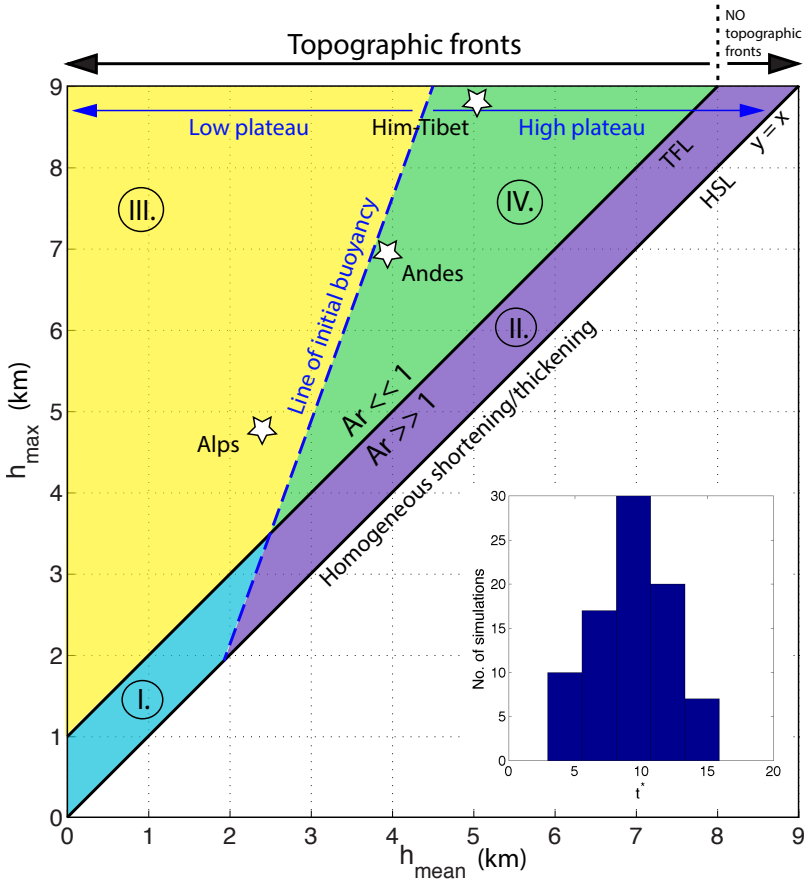

Fig. 3.9 Regime diagram for h_{max} vs. h_{mean} with both axes in km. The combination h_{max} and h_{mean} can be predicted using only two dimensionless numbers: the Argand number (the *England and McKenzie* [1982] formulation) and the buoyancy ratio equal to the ratio h_0/H_0. Four modes of surface expressions in continental collision and mountain building can be distinguished: (I) - with no topographic front and low plateau, (II) - with no topographic front and high plateau, (III) - with topographic front and low plateau and (IV) - with topographic front and high plateau. The stars represent the average and maximum values for the Alps, Andes and Himalaya-Tibet. Annotated lines: HSL - homogeneous shortening line, and TFL - topographic front line. The regime diagram was built based on the results of the scaling analysis shown in Fig. 3.7. The histogram in the lower-right corner shows the distribution of the characteristic time, t*, which is the amount of shortening occurred in the model or non-dimensionless convergence. The majority of the simulations results were taken at a characteristic time t* = 8-10.

Low Argand number promotes high topographic fronts while a high buoyancy ratio promotes higher mean elevations. *Bajolet et al.* [2013] obtained similar conclusions in analogue models: if the upper plate has a low viscosity and high buoyancy number (their buoyancy number is similar to the Argand number) it is impossible to build topography (i.e., experiment with white silicone in [*Bajolet et al.*, 2013]). The dynamics of topography build-up observed here in numerical models is also consistent with their analogue experiments: topography growth at the continent-continent boundary coupled with lateral flow at the sides.

However, the evolution of topography also varies with time, depending on changes/stability in the force balance. Therefore, the position of one simulation in the regime diagram in Fig. 3.9 (or configuration h_{max} and h_{mean}) will be time dependent. The results presented in Fig. 3.7 and Fig. 3.9 were taken at a fixed point in time. Here, we investigate how simulation results evolve in time relative to the regime diagram.

Fig. 3.10 shows the time evolution of N-S topographic profiles, taken in the center of the domain, perpendicular to the collision front, for the simulations presented in Fig. 3.8 and representative for the 4 modes of topography. For high Argand number, the increase in topographic amplitude is uniform over time and formation of topographic fronts is suppressed, suggesting that topographic growth is governed by homogeneous shortening. On the other hand, for low Argand number, a high topographic front is formed at very early stages (after only 3 Myr after start of collision). Once it has reached a maximum amplitude (7 km high for c) and 6.5 km for d)), the topographic growth spreads laterally, and the wavelength of the topographic front increases at the same time as the plateau increases steadily in time. The rate of plateau growth in c) is about 50 m/Myr, a case with $\rho_c = 3100$ kg/m^3, while the rate of plateau growth in d) is 90 m/Myr with $\rho_c = 3000$ kg/m^3.

Since these simulations have both EF and SB, all four cases register only one stage of topographic evolution: continuous growth. In contrast, we have shown that FS simulations, where deep processes dictate the dynamics of the system, record 2 stages of topographic evolution: growth and gravitational collapse. For all our further considerations in this section, we assume that the driving force is kept constant and is strong enough to promote topographic growth over time (i.e., consider EF).

It has been shown that details of the evolution of topographic fronts or orogenic wedges cannot be obtained analytically [*Medvedev*, 2002], for which numerical models are needed. However, a good understanding of how orogenic wedges form in viscous materials came from analogue, analytical, semi-analytical (thin sheet approximations) and in numerical models by various authors [*Buck and Sokoutis*, 1994; *Medvedev*, 2002; *Royden*, 1996]. Viscous wedges are believed to form due to the basal traction of the subducting slab beneath the upper plate, which represents the motion of a basal boundary of linear viscosity at constant velocity.

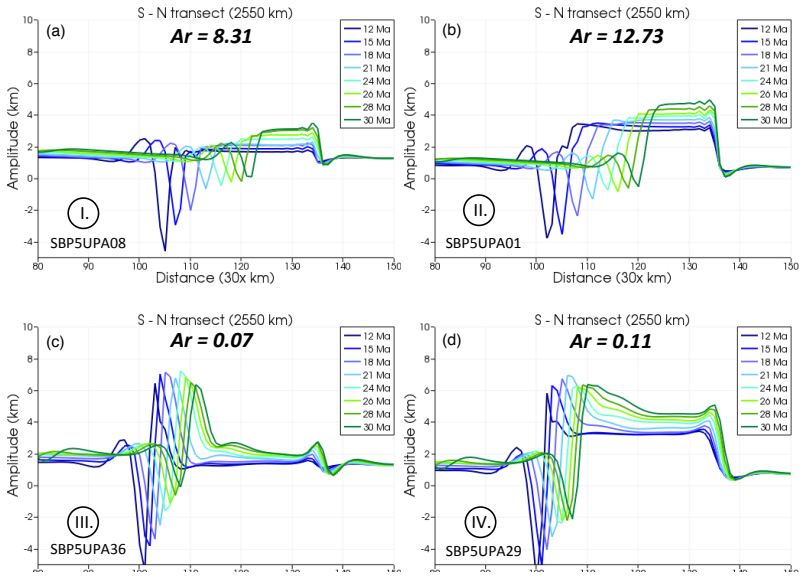

Fig. 3.10 Evolution of topographic amplitude in time for simulations displayed in Fig. 3.8: a) SBP5UPA08, b) SBP5UPA01, c) SBP5UPA36, d) SBP5UPA29. Cross-sections are taken in the center of the domain perpendicular to the collision front (parallel to the x-axis and perpendicular to y-axis). These simulations are representative for the four modes of surface expressions described in Fig. 3.9.

Medvedev [2002] showed that the amplitude and wavelength of viscous orogenic wedges varies in time and with the Ramberg number (*Rm*), a number similar to Argand number (see Table 3.2) [*Weijermars and Schmeling*, 1986]. Equivalently, the dependence of topographic fronts on the Argand number and time was also shown in our models in Fig. 3.7a and Fig. 3.10.

To explain the relevance of viscous wedges for our 3-D results, we have reproduced the numerical results from *Medvedev* [2002] using the same initial setup and boundary conditions (neglecting isostasy and erosion) with the 2-D finite element code MILAMIN_VEP [*Crameri and Kaus*, 2010; *Kaus*, 2010]. The details of the initial setup and boundary conditions can be found in *Medvedev* [2002].

In Fig. 3.11a, we show how the maximum amplitude of the wedge evolves in time and depends on the *Rm* or *Ar*. For a high Argand number, the maximum amplitude increases initially and flattens out very rapidly. A high Argand number favors gravitational collapse and the material becomes very unstable, unable to sustain higher elevations. Instead, for a low Argand number, the wedge registers continuous growth.

On the other hand, the deformation of the topographic plateau appears to be governed mainly by homogenous shortening, as can be seen in Fig. 3.11b. The black dotted line

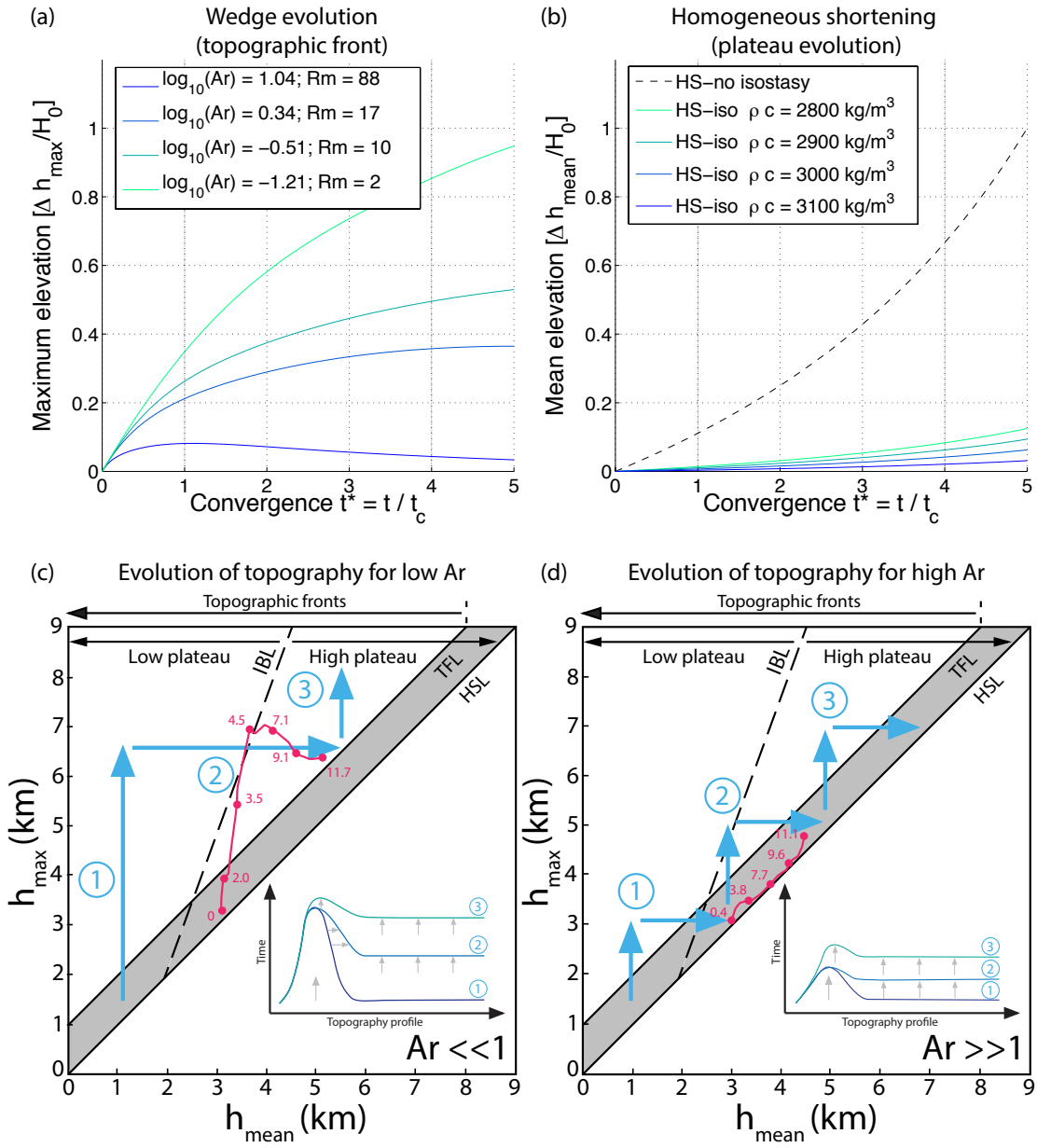

Fig. 3.11 Evolution of topography in time in relation to the regime diagram. a) Evolution of the maximum amplitude of a wedge in a viscous model using the 2-D numerical code MILAMIN_VEP [*Crameri and Kaus*, 2010; *Kaus*, 2010] and the initial model setup from *Medvedev* [2002]. Isostasy is neglected in the model setup. b) Evolution of the mean amplitude of a material with/out isostasy [*Turcotte and Schubert*, 2002] (see Appendix B for equations). c) Temporal evolution of a model with a low Argand number in relation to the regime diagram. d) Time evolution of a model with a high Argand number in relation to the regime diagram. Evolution of topography in numerical simulations are plotted with red traces: c) for SBP5UPA29 with $Ar = 0.11$, d) for SBP5UPA01 with $Ar = 12.73$. The numbers show the characteristic times (t*). In both c) and d) the blue arrows and the time profiles in the lower-right corners represent generalized cases for low/high Argand number.

shows the evolution of topography in the absence of isostatic considerations, while the coloured lines show evolutions calculated with Airy isostasy for different crustal densities [*Turcotte and Schubert*, 2002]. The results from both Fig. 3.11a-b will be discussed together in relation to the regime diagram, since formation of topographic fronts and plateaus is pseudo-synchronous in our 3-D models.

For a low Argand number, it is expected that at initial stages, the amplitude of the topographic front increases fast relative to the amplitude of the plateau (see results at t*=1 in Fig. 3.11a-b). However, homogenous shortening of the plateau catches up over time (t*=4) when the amplitude difference between the topographic front and plateau is drastically reduced. This suggests that when maximum elevations in wedges are reached, convergence will continue as homogenous shortening and the range builds outward, growing into a high plateau. The interpretation of evolution of topography for a low Argand number is seen in Fig. 3.11c in relation to the regime diagram and 3-D model results.

At high Argand number, the topographic growth can be characterized as incremental, while the overall deformation is due to homogenous shortening. At early stages (t*=1), small topographic fronts can form, but they soon become undistinguishable from the thickening of the rest of the plateau. Again, in relation to the regime diagram and the 3-D results, the evolution of topography for a high Argand number will always follow the HSL with short episodes of small topographic fronts (Fig. 3.11d).

The initial buoyancy ratio (h_0/H_0) will control the magnitude of the horizontal jumps in the regime diagram evolution (arrows in Fig. 3.11c-d). A lower crustal density will promote higher jumps, while a higher crustal density will promote smaller jumps.

3.6.2 Implications for the India-Asia collision zone

In order to draw geodynamical conclusions from the numerical experiments, we discuss the results mainly with reference to the India-Asia collision. However, we remind that these numerical experiments did not intend to model this tectonic area in detail, but to point out some important physical processes and the influence of the different parameters.

In collisional systems, the growth and shape of a mountain belt is controlled by the equilibrium between body and boundary forces [*England and McKenzie*, 1982]. Boundary forces are the driving forces favoring collision, whereas buoyancy forces resist it. Our results show that the shape and elevation of mountain ranges can vary depending on the boundary conditions (convergence velocities) or internal factors (material properties, factors that control buoyancy), but also in the evolution stage they are in. We present four end-member models that characterize an advanced evolution stage: (I) - low-amplitude homogenous shortening, (II) - high-amplitude homogenous shortening, (III) - high topographic front,

low plateau (Alpine type) and (IV) - high topographic front, high plateau (Himalayan-Tibet type). However, a variety of transitional forms of topography will exist between these 4 end-members that will also have a time component of evolution.

The Himalaya-Tibet range is one of the most striking features of the Earth's surfaces and it shows a very high topographic front and a high plateau. If we plot the present day values of h_{max} and h_{mean} in Fig. 3.9 (the star points represent the average and maximum values for the Alps, Andes and Himalaya-Tibet), we can see that the Himalaya-Tibet fall in type (IV), where we also obtain numerical results with high topographic fronts and plateaus. The Alps fall in type (III) with a topographic front and low plateau. Modes (I) and (II) of topography are harder to distinguish in nature, as the surface expression of homogenous shortening alone is unclear to identify.

The Andes seem to have a type (III) topography expression with an incipient transition to type (IV), which could explain the presence and development of the Altiplano. However, the tectonic regime for the Andes (oceanic subduction) differs from the one considered here (continental collision). *Capitanio et al.* [2011] showed that variations in slab thickness, arising from the age of the Nazca plate, can explain the morphology of the Andean orogeny. Their model setup has a very similar geometry to the one used here, with main difference being the nature of the indentor. In *Capitanio et al.* [2011], the 'indentor' represents old and thick oceanic material, while here we use a continental indentor, for which we tested a range of properties (see Table 3.1). This suggests that while our aim is to model continental collisions, we obtained a general set where models of oceanic subduction can also be included. Therefore, if the present-day configuration of the Nazca-South American plates subduction zone stays the same, the extent of the Altiplano may increase in height with time.

Plotting the topography for the Tibet-Himalaya, Alps and the Andes (Fig. 3.12), we notice that our model lacks another feature of natural systems. Both the Himalaya and the Central and Western Alps (i.e., the high topographic fronts) are accretionary wedges made from sediments scraped off the subducting plate and not part of the upper plate as in our models. As such, the Himalaya is made of Indian plate material, while the Central and Western Alps are made of European plate material. We attribute the lack of accretionary wedges in our models to the strong coupling between the crust and upper mantle lithosphere and the resolution employed. A multi-layered lithosphere structure would allow for the decoupling of the upper crust from the lower crust and accretion of material into a wedge. This could potentially add more elevation to the topographic front, as the highest amplitudes in mountain belts are registered in accretionary wedges.

However, a secondary topographic front can be noticed immediately after the suture lines for the Alps and Himalaya-Tibet in Fig. 3.12a-b (profiles), suggesting that the upper plate

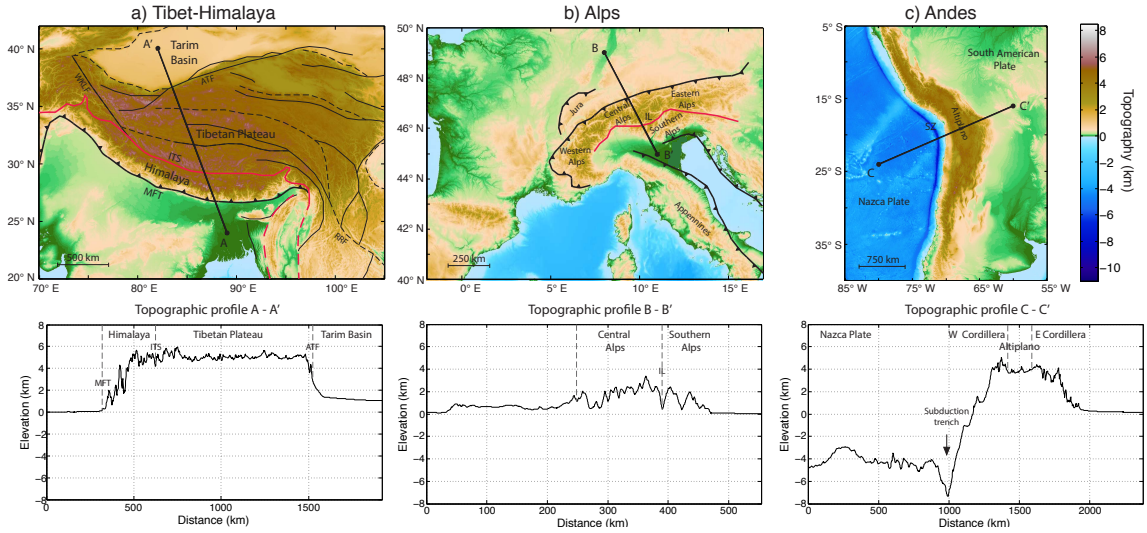

Fig. 3.12 Topographic maps and profiles in natural orogens from the ETOPO1 model [*Amante and Eakins*, 2009]. a) Tibet-Himalaya - the geological setting was modified from *Tapponnier et al.* [2001]. b) Alps - the geological setting was modified from *Schmid et al.* [2004]. c) Andes - the tectonic boundary between the Nazca and the South American plates is marked by the deep subduction trench. The bold lines represent major faults and the red lines represent sutures. Abbreviations: a) ITS - Indus-Tsangpo Suture, MFT - Main Frontal Thrust, ATF - Altyn Tagh Fault, RRF - Red River Fault, b) IL - Insubric Line, c) SZ - subduction zone. Cross sections have a direction from the subducting/collision plate to the upper plate, same as we plotted for the numerical simulations.

still deforms in the way we describe in this study. A simpler profile is also shown for the Andes (Fig. 3.12c), where the entire deformation is taken by the upper plate and allows for the formation of a topographic front (Western Cordillera) and a plateau (Altiplano).

The topographic cross-sections in Fig. 3.12 also show that the difference in topographic fronts and plateaus are not very pronounced in nature as compared to our models. The difference between the Himalaya and Tibet comes mainly from the different relief: high relief in the Himalaya and low relief in the Tibet, which is attributed to the very high erosion rates in the Himalaya and low in Tibet. The effect of erosion in models may decrease considerably the amplitudes in the topographic fronts [*Beaumont et al.*, 2001].

Based on the time evolutions in Fig. 3.10c-d, and the experiments in Fig. 3.11, we propose that topographic fronts are likely to grow earlier and faster than their corresponding plateaus. It is known from climate, sedimentary and paleontology studies [*Garzione et al.*, 2000; *Hoke et al.*, 2014] that the Himalayas rose first in the Eocene, while the Tibetan Plateau was uplifted later in the Oligocene-Miocene, consistent with our scenario in case (IV) (Fig. 3.8, Fig. 3.10). Therefore, it is likely that the topography of Tibet-Himalaya at the early stages of collision might have looked more Andean-like, as suggested by some studies [*Ding et al.*, 2005, 2014]. However, others argue that the uplift of Tibetan Plateau happened early, that by 40 Myr ago the plateau already had modern elevations [*Wang et al.*, 2008]. In all our models with topographic fronts, plateaus occur as a secondary feature after development of topographic fronts, suggesting a post-Himalaya uplift of the Tibetan Plateau.

We have also shown the importance of the buoyancy in development of high plateaus. The source of buoyancy considered here and displayed by the line of buoyancy in diagram Fig. 3.9, is purely isostatic, with the density of the upper plate as the main controller. We recognize that buoyancy can also arise from different sources, especially from large temperature gradients. The evolution and chemical signature of volcanism in Tibet, which migrated northwards over time [*Bouilhol et al.*, 2013], led to the proposal of a very hot asthenosphere beneath the Tibetan Plateau [*England and Houseman*, 1989; *England et al.*, 1988; *Houseman et al.*, 1981; *Molnar et al.*, 1993], which could provide additional buoyancy to uplift the plateau. This mechanism in which hot, upwelling asthenosphere mantle replaces some of the lower lithosphere, was also applied to other continental plateaus, such as the Altiplano or the Canadian Cordilleras [*Bao et al.*, 2015; *Barnes and Ehlers*, 2009; *Hatzfeld and Molnar*, 2010].

While our motivation for investigating the effect of free subduction and external forcing lies in understanding the forces necessary to explain the present day convergence rate between India and Eurasia of approximately 5 cm/yr inferred from the GPS velocity field [*Bilham et al.*, 1997; *Liang et al.*, 2013], simulating slab suction or plume push would require the use

of a much larger model domain, if not a global domain, which is not currently possible. In all our simulations, we obtain very complex slab and mantle flow dynamics. We have shown that beneath continental collision we obtain slab detachment, while beneath the oceanic side, slab subducts continuously and coherently. Due to the change in material properties at the transition to the lower mantle, slab is likely to buckle and accumulate. This is consistent with observations from tomographic studies beneath the India-Asia collision [*Replumaz et al.*, 2004; *Van der Voo et al.*, 1999]. Therefore, in relation to the studies that promote slab suction as the main driving force [*Faccenna et al.*, 2013], we agree that in order to build anomalously high elevations, you need considerable convergence velocities. Lower-amplitude orogenies can be explained with lower convergence velocities, for which slab pull alone might be enough. One such orogeny might be the Alpine orogeny.

Finally, the model results presented here might be altered if more complex rheologies are considered. It is known, for example, that the deformation of a Newtonian fluid is far more diffuse than that of a power-law material under same conditions. Indeed, early thin-sheet calculations with power-law rheologies [*England and McKenzie*, 1982; *Houseman and England*, 1986] show that high amplitudes are reached faster and for a larger range of Argand numbers than for viscous rheologies. Similar observations can be expected for future 3-D models with more complex rheologies.

3.7 Conclusion

A large number of subduction-collision simulations with free subduction and external forcing have been performed in this study. We obtain complex 3-D dynamics with distinct behaviors beneath the continental collision and oceanic subduction at the sides. We show that building topography is an interplay between providing the energy to the system and the ability of that system to store it over longer periods of time. External pushing and the presence of strong blocks such as the Tarim Basin are necessary to create both high topographic fronts (Himalayas) and plateaus (Tibetan Plateau). Upper plate material properties also give a signature to the topographic amplitude. Using the Argand number, which is a function of the convergence velocity and upper plate parameters, and the initial buoyancy of the upper plate, we can predict different modes of topographic expressions in continental collision models. Our results show that the shape and elevation of mountain ranges can vary depending on the boundary conditions or internal factors, but also on the evolution stage they are in.

Chapter 4

The effect of rheological approximations in 3-D numerical simulations of subduction/collision

4.1 Summary

Subduction and collision zones evolve differently from one another as the result of specific combinations of surface and mantle processes. These differences arise for several reasons, such as different rheological properties, different amounts of regional isostatic compensation, and different mechanisms by which forces are applied to the convergent plates. Previous 3-D geodynamic models of subduction/collision processes have used various rheological approximations, making numerical results difficult to compare, since there is no clear image on the extent of these approximations on the dynamics. Here, we employ the code LaMEM to perform high-resolution long-term 3-D simulations of subduction/continental collision in an integrated lithospheric and upper-mantle scale model. We test the effect of rheological approximations on mantle and lithosphere dynamics in a geometrically simplified model setup in which the dynamics of subduction and collision is entirely driven by slab-pull (i.e., "free subduction"). The models exhibit a wide range of behaviours depending on the rheological law employed: from linear to temperature-dependent visco-elasto-plastic rheology that takes into account both diffusion and dislocation creep. Rheology exerts a strong effect on slab morphology, trench migration rates and topography in the upper plate. For example, we find that slab dynamics varies drastically between end member models: in viscous approximations, there is no slab break-off, while for a non-linear visco-elasto-plastic rheology, slab break-off occurs at the corners of the indenting continent. In an intermediate

case, for weaker non-linear rheologies and linear viscous approximations coupled with plasticity and elasticity, break-off initiates beneath continental collision. Moreover, opening of a back-arc basin is observed only in simulations with non-linear viscous rheology.

4.2 Introduction

Subduction of oceanic lithosphere is a fundamental part of plate tectonics. Subduction is driven by the gravitational descent of old, cold lithosphere into the mantle, and once a plate starts subducting it pulls younger lithosphere behind it. Thus, recycling cold lithosphere into the interior provides an important source of buoyancy for mantle convection (e.g., *Richter* [1973]).

Numerous analog (e.g., *Bellahsen et al.* [2005]; *Faccenna et al.* [2007]; *Funiciello et al.* [2008, 2006, 2003]; *Jacoby* [1973, 1976]; *Kincaid and Olson* [1987]; *Schellart* [2004, 2008, 2010]) and numerical models (e.g., *Capitanio and Morra* [2012]; *Capitanio et al.* [2009]; *Di Giuseppe et al.* [2008]; *Enns et al.* [2005]; *Li and Ribe* [2012]; *Manea and Gurnis* [2007]; *Manea et al.* [2011]; *Morra et al.* [2009, 2006]; *Ribe* [2010]; *Schellart et al.* [2007]; *Schmeling et al.* [2008]; *Stegman et al.* [2010a, 2006, 2010b]) have yielded systematic understanding of many features of subduction such as: the relation between trench and plate velocities [*Funiciello et al.*, 2008; *Stegman et al.*, 2006], the shapes of trenches and island arcs [*Morra et al.*, 2006; *Schellart et al.*, 2007], the mode or style of subduction [*Bellahsen et al.*, 2005; *Ribe*, 2010; *Schellart*, 2008; *Stegman et al.*, 2010a] and the sinking speed of the slab [*Ribe*, 2010].

These studies have shown that, in detail, subduction zones are complicated by a wide variety of factors that can influence the style of plate boundary. But the greatest factor remains the rheology of the lithosphere. In particular, the negative buoyancy of the slab is resisted by the bending at the subduction hinge, the viscous drag from the ambient upper mantle [*Bellahsen et al.*, 2005; *Conrad and Hager*, 1999; *Forsyth and Uyeda*, 1975] or the resistive force of the upper plate [*Sharples et al.*, 2014]. In other words, different strengths of the lithosphere and mantle may impede subduction by resisting deformation at the trench [*Becker et al.*, 1999; *Conrad and Hager*, 1999; *Sharples et al.*, 2014].

Moreover, subduction zones are also strongly linked to orogenic belts. Most of the major mountain belts and orogenic plateaus are found within the overlying plate of active or fossil subduction and/or collision zones [*Dewey and Bird*, 1970; *Molnar and Lyon-Caen*, 1988]. Moreover, they evolve differently from one another as the result of specific combinations of surface and mantle processes. These differences arise for several reasons, such as different rheological properties, different amounts of regional isostatic compensation,

and different mechanisms by which forces are applied to the convergent plates (e.g., [*Molnar and Lyon-Caen*, 1988]). Therefore, to understand formation of mountain belts means firstly to understand evolution of convergent margins, subduction and collision.

The motivation for this study stems from the fact that, despite the obvious control of rheology on the dynamics of subduction/collision, previous 3-D geodynamic models (e.g., *Capitanio et al.* [2009]; *Li and Ribe* [2012]; *Li et al.* [2013]; *Magni et al.* [2014]; *Pusok and Kaus* [2015]; *Stegman et al.* [2010a]; *Sternai et al.* [2014]) have used various rheological approximations, making numerical results difficult to compare, since the extent of how rheology affects subduction/collision dynamics in 3-D numerical models remains unclear. Thus, we are interested to understand the type of differences due to rheological approximations can occur in 3-D models of subduction/collision. For this, we employ the code LaMEM [*Kaus et al.*, 2016] to test the effect of rheological approximations on subduction and collision dynamics in a geometrically simplified 3-D model setup of an integrated lithospheric and upper-mantle scale model. We use the "sticky-air" approach to allow for the development of topography. The dynamics of subduction and collision is entirely driven by slab-pull (i.e., "free subduction").

4.3 Method

We model 3-D subduction and collision processes by employing the 3-D finite difference staggered grid code LaMEM (Lithosphere and Mantle Evolution Model) [*Kaus et al.*, 2016] that solves a set of conservation equations together with their constitutive relationships. The coupled system of momentum, mass, and energy conservation equations, with velocity (v_i), pressure (p) and temperature (T) as primary unknowns, are given by:

$$\frac{\partial \tau_{ij}}{\partial x_j} - \frac{\partial p}{\partial x_i} + \rho g_i = 0, \tag{4.1}$$

$$\frac{1}{K}\frac{Dp}{Dt} - \alpha\frac{DT}{Dt} + \frac{\partial v_i}{\partial x_i} = 0, \tag{4.2}$$

$$\rho C_p \frac{DT}{Dt} = \frac{\partial}{\partial x_i}\left(\lambda \frac{\partial T}{\partial x_i}\right) + H, \tag{4.3}$$

where $x_i (i = 1,2,3)$ denotes Cartesian coordinates, $\tau_{ij} = \sigma_{ij} + p\delta_{ij}$ is the Cauchy stress deviator, ρ density, g_i the gravitational acceleration, K the bulk modulus, α the thermal expansion coefficient, C_p the specific heat, λ thermal conductivity, H volumetric heat source,

and D/Dt stands for the material time derivative, respectively. The visco-elasto-plastic constitutive equation for the deviatoric strain rate tensor is given by:

$$\dot{\varepsilon}_{ij} = \dot{\varepsilon}_{ij}^{el} + \dot{\varepsilon}_{ij}^{vs} + \dot{\varepsilon}_{ij}^{pl} \tag{4.4}$$

$$= \frac{\overset{\diamond}{\tau}_{ij}}{2G} + \dot{\varepsilon}_{II}^{vs}\frac{\tau_{ij}}{\tau_{II}} + \dot{\varepsilon}_{II}^{pl}\frac{\tau_{ij}}{\tau_{II}}, \tag{4.5}$$

where $\dot{\varepsilon}_{ij} = \frac{1}{2}(\frac{\partial v_i}{\partial x_j} + \frac{\partial v_j}{\partial x_i}) - \frac{1}{3}\frac{\partial v_k}{\partial x_k}\delta_{ij}$ is the deviatoric strain rate tensor, $\dot{\varepsilon}_{ij}^{el}$, $\dot{\varepsilon}_{ij}^{vs}$, $\dot{\varepsilon}_{ij}^{pl}$ are the elastic, viscous and plastic components, respectively, $\overset{\diamond}{\tau}_{ij} = \frac{\partial \tau_{ij}}{\partial t} + \tau_{ik}\omega_{kj} - \omega_{ik}\tau_{kj}$ is the Jaumann objective stress rate, $\omega_{ij} = \frac{1}{2}(\frac{\partial v_i}{\partial x_j} - \frac{\partial v_j}{\partial x_i})$ is the spin tensor, G is the elastic shear modulus, and the subscript $_{II}$ denotes the square root of the second invariant of a corresponding tensor. The viscous strain rate takes into account both diffusion ($\dot{\varepsilon}_l$) and dislocation ($\dot{\varepsilon}_n$) creep:

$$\dot{\varepsilon}_{II}^{vs} = \dot{\varepsilon}_l + \dot{\varepsilon}_n = A_{diff}\,\tau_{II} + A_{disl}\,(\tau_{II})^n, \tag{4.6}$$

where n is the stress exponent of the dislocation creep, and the pre-exponential factor (A) of each creep mechanism is defined by:

$$A_{diff} = B_{diff}\,\exp\left[-\frac{H_{diff}}{RT}\right], \tag{4.7}$$

$$A_{disl} = B_{disl}\,\exp\left[-\frac{H_{disl}}{RT}\right], \tag{4.8}$$

where B, $H = E + pV$, E, and V denote the creep constant, enthalpy, activation energy, and activation volume, respectively, of the corresponding creep mechanism, and R is the gas constant. The failure of rocks is modelled using a Drucker-Prager yield criterion, which limits the stresses after the relationship:

$$\tau_{II} \leq \tau_Y = \sin(\phi)\,p + \cos(\phi)\,c, \tag{4.9}$$

where ϕ is the friction angle, and c is the cohesion. Finally, the volumetric heat source includes shear heating, controlled by efficiency parameter $0 \leq \chi \leq 1$ (we keep $\chi = 1$ throughout our simulations), and the radiogenic heat (A):

$$H = \chi\,\tau_{ij}\left(\dot{\varepsilon}_{ij} - \dot{\varepsilon}_{ij}^{el}\right) + \rho A. \tag{4.10}$$

The discrete system of equations resulting from the discretization of conservation equations is solved using a Galerkin multigrid approach. The domain is a 3-D Cartesian box in which a Lagrangian marker-in-cell method [*Gerya*, 2010; *Gerya and Yuen*, 2003; *Harlow and Welch*, 1965] is used for accurately tracking distinct material domains as they undergo extensive deformation due to creeping flow. A sticky air layer [*Crameri et al.*, 2012] and an internal free surface with a free surface stabilization algorithm [*Kaus et al.*, 2010] are employed to allow for the development of topography. The code is written in C and uses the PETSc library [*Balay et al.*, 2014].

4.3.1 Model Setup

The 3-D model domain (Figure 4.1) extends 5100 km in x-direction and y-direction and 1000 km in the z-direction. The numerical domain has a resolution of 256 x 256 x 64 cells. It consists of an oceanic plate subducting beneath a continental upper plate. A large indentor is located in the middle of the oceanic plate, such that the model will transition from oceanic subduction to continental collision. In the continental domain, the initial material field incorporates a 40 km thick continental crust composed of 20 km upper crust and 20 km lower crust, resting on the 60 km continental lithospheric mantle. In the oceanic domain, the lithosphere has a thickness of 100 km with a 20 km thick crust. Subduction is already initiated along a $\sim$10 km thick weak zone dipping 45° in the lithospheric mantle and the downgoing plate extends to 250 km depth, such that the dynamics of the system is entirely driven by slab pull, commonly referred as "free subduction"

The plate structure is kept simple and includes two major components: crust (with subsequent lower and upper crust for continents) and upper mantle lithosphere, and they are referred as phases. All phases are shown and labeled in Figure 4.1 and in the figure caption. At 660 km depth, the transition to the lower mantle is marked by a viscosity jump of at least 50 and a density difference of 50 kg/m^3 [*Quinteros et al.*, 2010], which gives the best results of slab behaviour in numerical models compared to tomographic observations. All boundaries have free-slip boundary conditions. The top surface of the lithosphere is calculated dynamically as an essentially internal free surface by using a buffer layer of "sticky air" [*Crameri et al.*, 2012; *Gerya and Yuen*, 2003; *Schmeling et al.*, 2008]. For simplicity, surface erosion and sedimentation are neglected, which is a first order approximation acceptable at the considered time and spacial scales.

The initial thermal structure of the model is shown in Figure 4.1b. A half-space cooling model with a thermal age of 80 Ma is assigned for oceanic lithosphere, a constant temperature gradient of 13°C/km is given to the continental lithosphere, and a temperature adiabat is

assigned to the mantle and lower mantle. These temperature-variations with depth are laterally uniform. The surface and sticky-air are set to 0°C.

In order to study the effect of rheological approximations, the geometry, the phase density and thermal structure are kept the same throughout all simulations. Density is kept constant per phase to avoid buoyancy effects due to temperature advection and diffusion (see Parameters Table 4.1). Details on the rheology and approximations are explained next.

4.3.2 Rheological approximations

Figure 4.2 shows the 1-D strength profiles (deviatoric stress with depth) and effective viscosities for the rheological approximations used in this study for continental, oceanic lithosphere and mantle. The black line represents the non-linear visco-elasto-plastic strength profile (NVEP) used as reference model for the rheological approximations. We use laboratory derived flow laws, as follows: "diabase" dislocation creep for continental upper crust (*Carter and Tsenn* [1987], used in *Huismans et al.* [2001]), "granite" dislocation creep for continental lower crust (*Carter and Tsenn* [1987], used in *Huismans et al.* [2001]), "wet quartzite" dislocation creep for oceanic crust [*Ranalli*, 1995] and "dry olivine" dislocation and diffusion creep for mantle [*Hirth and Kohlstedt*, 2003] (Tables 4.1 and 4.2). The domain in which diffusion is dominant depends on temperature, such that at higher temperatures (i.e., lower asthenosphere) diffusion creep is the dominant deformation mechanism. The strength profile for continental lithosphere resembles a typical "Christmas tree" profile or a "jelly-sandwich" profile [*Burov and Watts*, 2006]. The strength profiles in Figure 4.2 are calculated for a background strain rate of 10^{-15} s^{-1}.

To construct the rheological approximations, the following steps were taken: 1) start from the 1-D non-linear visco-elasto-plastic strength profile (NVEP), 2) integrate the strength with depth for each unit and approximate with a constitutive equation of the form $\tau = 2\eta_{eff}\dot{\varepsilon}$ such that, 3) an effective viscosity is obtained for the respective layer (i.e., η_{eff}). Four different linear viscous approximations are then created: (i) LV01 - describing a depth averaged stress, (ii) LV02 - with 90% of the maximum stress in the layer, (iii) LV03 - with 50% of the maximum stress in the layer, and (iv) LV04 - with a sub-layered depth-averaged stress. The last approximation, LV04, takes into account a sub-division of each layer to resolve better the weakening with depth of the continental lower crust and the lower part of the mantle lithosphere. The parameter values for all approximations are found in Table 4.1 with complementary information in Table 4.2.

Table 4.3 summarises all the numerical tests performed with different rheological approximations. We have run models with the non-linear visco-elasto-plastic rheology (NVEP), all linear viscous approximations (LV01-LV04), in combination with plasticity (P) and elas-

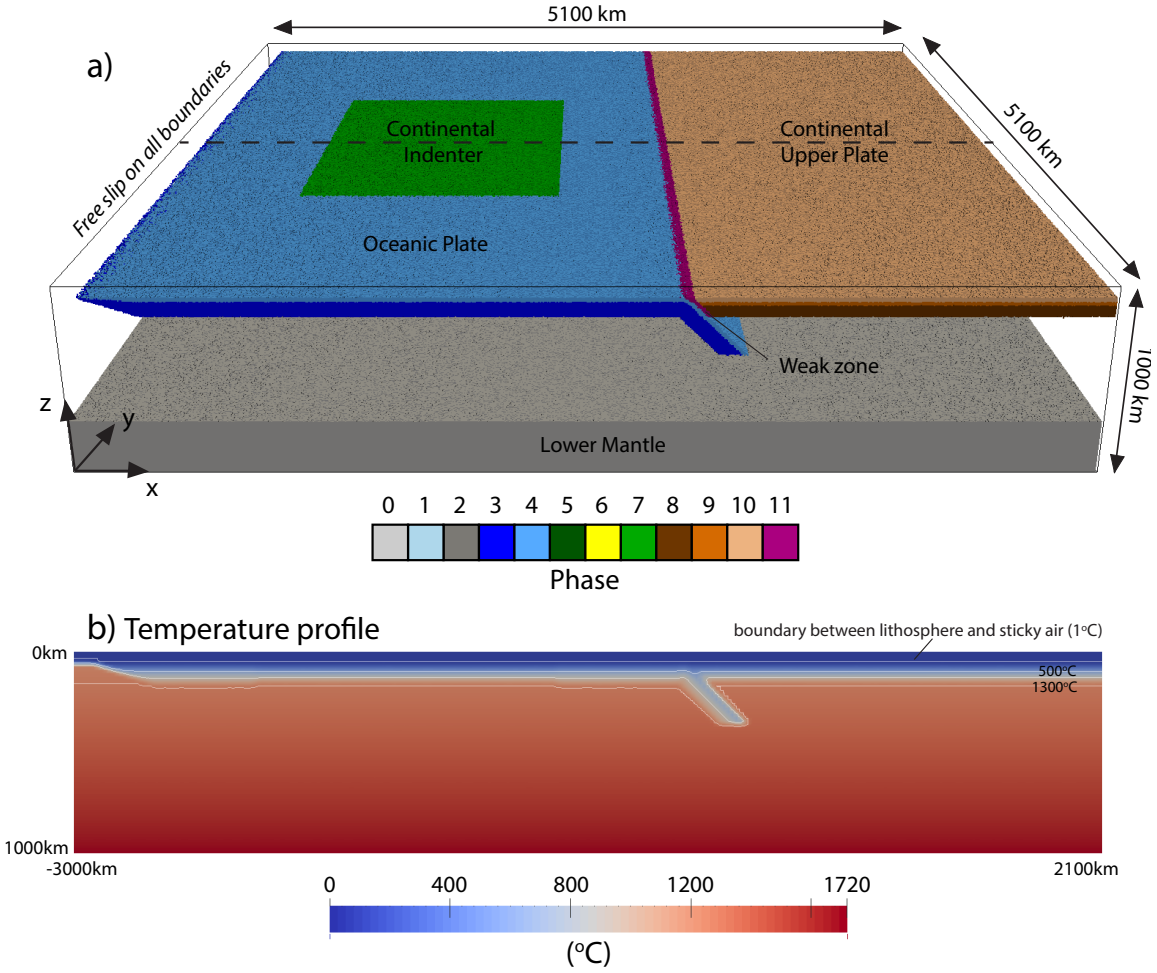

Fig. 4.1 Model Setup. a) 3-D perspective of model setup. The model consists of an oceanic plate subducting beneath a continental upper plate. A continental indentor is located in the middle of the subducting plate. The continental lithosphere is composed of upper and lower crust and an upper mantle lithosphere, while the components of oceanic lithosphere are crust and upper mantle lithosphere. Phases: 0-mantle asthenosphere, 1-sticky air, 2-lower mantle, 3-oceanic upper mantle, 4-oceanic crust, 5-continental upper mantle lithosphere (indentor), 6-lower crust (indentor), 7-upper crust (indentor), 8-continental upper mantle lithosphere (upper plate), 9-lower crust (upper plate), 10-upper crust (upper plate), 11-weak zone. Parameters values are listed in Table 4.1. b) Cross-section of temperature profile. The oceanic plate has a half space cooling model with a thermal age of 80 Ma, the continental lithosphere has a constant temperature gradient of 13°C/km and the mantle and lower mantle are assigned a mantle adiabat.

Fig. 4.2 Rheological approximations for continental and oceanic lithosphere and for the mantle. The non-linear strength profiles (NVEP) were calculated for a background strain rate of $\dot{\varepsilon}_{bg} = 10^{-15}$ s^{-1}. The strength profile for continental lithosphere resembles a typical "Christmas tree" profile [*Burov and Watts*, 2006]. The strength of the upper crust is limited by plasticity, where the yield stress is the lowest and equal to the cohesion. The left column shows the structure of the lithosphere and mantle, the middle column shows the deviatoric stress versus depth and on the right shows the variation of effective viscosity with depth. Temperature profile: 1) constant gradient of 13°C/km for continental lithosphere, 2) half-space cooling model with a thermal age of 80 Ma for oceanic lithosphere and 3) mantle adiabat for the asthenosphere and lower mantle. Linear approximations: LV01 - depth averaged stress, LV02 - 90% of the maximum stress in the layer, LV03 - 50% of the maximum stress in the layer and LV04 - sub-layered depth-averaged stress.

ticity (E), shear weakening (SW) and temperature diffusion (Tdiff). The last case, when temperature diffusion is lacking, the rheology is only dependent on temperature in a passive way, meaning that markers transport temperature information, but diffusion is not activated. Shear weakening is set only for continental crust, such that the friction angle of the material is lowered depending on the accumulated plastic strain. It is worth noting that elasticity might affect lithospheric flexure in collision zone, however the general dynamics of subduction/collision and underlying mantle flow remain well established by the visco-plastic rheology.

A second set of simulations "with weaker lithosphere" is also tested, in which the NVEP strength profile has an upper cut-off viscosity of $\eta_{max} = 10^{23}$ Pa.s, meaning that viscosity contrast between lithosphere and asthenosphere is $\Delta\eta \sim 10^3$, compared to original case, in which the $\Delta\eta > 10^4$. All simulations performed and the nomenclature are listed in Table 4.3.

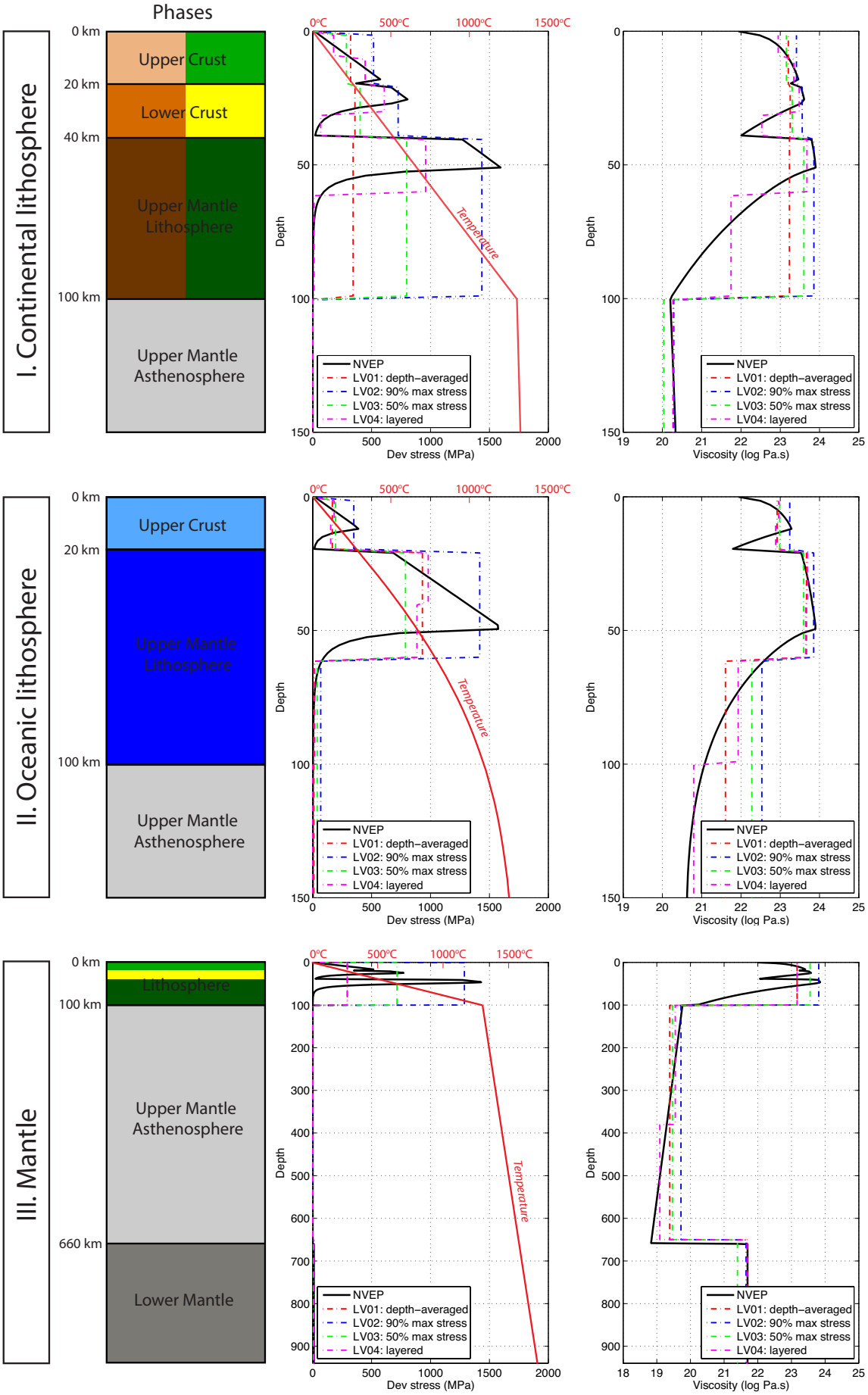
Phases
I. Continental lithosphere
0 km
20 km
40 km
100 km
Upper Crust
Lower Crust
Upper Mantle Lithosphere
Upper Mantle Asthenosphere
0°C
500°C
1000°C
1500°C
Depth
Temperature
NVEP
LV01: depth−averaged
LV02: 90% max stress
LV03: 50% max stress
LV04: layered
Dev stress (MPa)
Viscosity (log Pa.s)
II. Oceanic lithosphere
0 km
20 km
100 km
Upper Crust
Upper Mantle Lithosphere
Upper Mantle Asthenosphere
III. Mantle
0 km
100 km
660 km
Lithosphere
Upper Mantle Asthenosphere
Lower Mantle

4.4 Results

The following section shows results using the non-linear visco-elasto-plastic rheology (NVEP) and linear viscous approximations (LV01-LV04). We begin by describing the evolution of our reference model (simulation S104), with visco-elasto-plastic rheology, shear weakening and temperature-diffusion (NVEP+SW+Tdiff). Then, we focus on effects on slab dynamics, trench motion and topography for all simulations in a systematic way.

4.4.1 Results with temperature-dependent visco-elasto-plastic rheology

The evolution of the reference model (NVEP+SW+Tdiff) is shown in Figure 4.3 through material phase fields with crustal velocity vectors (left column), strain rate field of the lithosphere (middle column) and topography maps (right column) for different stages of subduction/collision. At the initial stages of our reference model, the relatively strong oceanic plate subducts along the prescribed weak zone. This short stage of oceanic subduction is dominated by low strain rates and uniform subduction (Figure 4.3a), which then transitions into continental collision. The influence of the colliding continent is rapidly felt by the system, which accommodates trench advance at the collision boundary and trench retreat during oceanic subduction at the sides of the continent. This combination leads to vigorous lateral extrusion of material in the upper plate, shown with high velocity vectors. The collision of the indentor with the upper plate also produces a narrow topographic front.

As continental collision evolves in time, more lateral extrusion is promoted at the sides. However, the resistance of the upper plate material to deformation, leads to plastic failure close to the subduction trench, leading to the opening of a back-arc basin (Figure 4.3b). Moreover, as a response to the different regimes between continental collision and oceanic subduction, higher strain rates are accumulated on the retreating slab. The effect of elasticity is seen in the high stresses (and thus strain rates) due to plate bending during subduction. The topography also reacts in an unusual way, such that the topographic front has increased in amplitude, at the same time as the opening of the back-arc basin, lowering the amplitudes in the upper plate. It is interesting to see that once the opening of the basin was initiated, the lateral extrusion of material decreases in vigour, while the upper plate maintains a relatively high amplitude, especially in front of the indentor.

Finally, the stresses accumulated at the confluence of the two different regimes - collision and subduction, are enough to break the slab (Figure 4.3c). The break-off initiates at the corners of the continent and is characterised by extremely high strain rates of more than 10^{-12} s^{-1}. The amplitude of the topographic front is further increasing by this point, suggesting that the non-linear rheology of the upper plate is strong enough to store relatively high amounts

of gravitational potential energy. At this stage, lateral extrusion of material is not efficient anymore because the system has found an efficient way to accommodate both trench advance and trench retreat by building a topographic front and opening a back-arc basin.

4.4.2 Effects on slab dynamics

Comparisson of the rest of the simulations reveal that the features of the reference model are restricted only to the simulations with non-linear visco-elasto-plastic rheology, with/without temperature-diffusion or shear weakening (NVEP). Shear weakening and temperature diffusion are processes that mainly affect the timing and duration of opening of back-arc basin or slab break-off and will be discussed later.

Figure 4.4 shows the most distinct behaviours of slab break-off across simulations. Firstly, all linear approximations (LV01-LV04) result in a continuous slab that buckles at the transition to the lower mantle, with no break off (Figure 4.4). The results are also dominated by low strain rates and slow trench retreat rates, with little lateral extrusion. This is consistent with the fact that linear viscous rheology diffuses stresses, such that stress accumulations do not occur. If the linear approximations are coupled with plasticity and elasticity (E+P), the slab becomes weaker due to plastic failure in the crust and breaks-off beneath the continent.

More experiments were run with thinner oceanic lithosphere (60 km, not shown here) and weaker lithosphere ($\Delta\eta \sim 10^3$) by setting an upper viscosity cutoff $\eta_{max} = 10^{23}$ Pa.s (Figure 4.4b,d). The effect of both these features is that the oceanic lithosphere loses strength, overall, it is weaker and slab break-off occurs much easier. Interestingly, in all these cases the nucleation is located beneath the continent and not at the corners as for NVEP (S104). This suggests that with a weaker lithosphere, the positive buoyancy of the indentor exerts enough force on the slab to break-it. Moreover, the Maxwell relaxation time, $\tau_M = \eta/G$, between a) S104 and b) S105, with $\tau_M^a > \tau_M^b$, also indicates that elasticity is less important when the lithosphere is weaker, and the deformation is dominated by viscous creep.

Figure 4.5 shows the variability in slab shapes and trench positions across all simulations, while Figure 4.6 shows the slab shapes in more detail for different rheological approximations. The snapshots are taken when all simulations reached the same stage of evolution, meaning that 80% of initial slab length was subducted on the oceanic side. Both figures show two cross-sections, one in the center of the domain, across continental collision and one on the side, across oceanic subduction. The red triangle marks the initial position of the trench, while circles marks the current trench positions. Figure 4.5 shows that the trench position varies approximately 250 km across simulations during continental collision and 1000 km during oceanic subduction. This suggests that oceanic subduction is affected much more by rheological approximations than continental collision. The slab shapes also vary much more

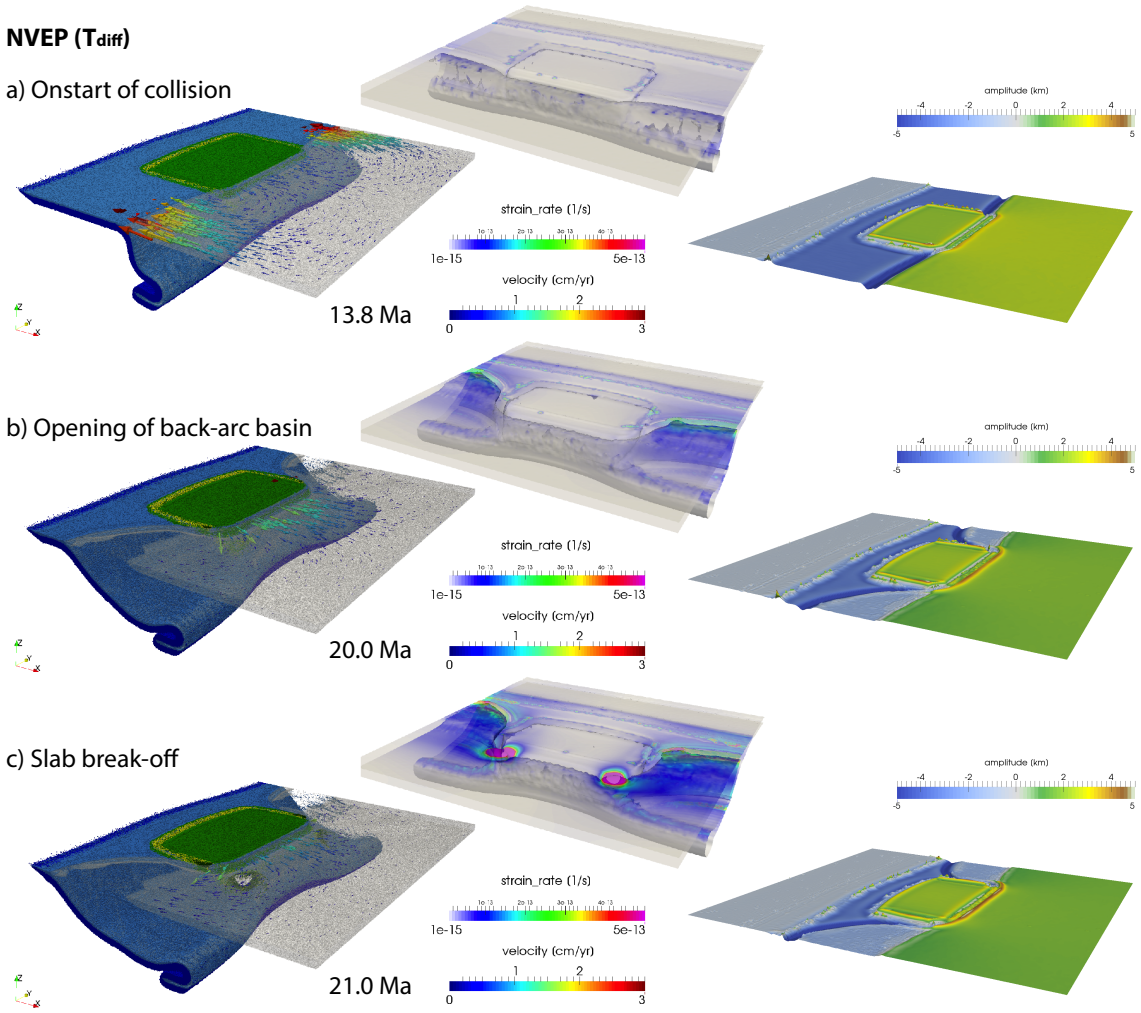

Fig. 4.3 Results of the reference model with non-linear visco-elasto-plastic rheology and temperature diffusion (S104, NVEP+SW+Tdiff). Three evolution stages are shown: a) onstart of collision that registers a change in the dynamics, b) rapid opening of a back-arc basin, and c) slab break-off. The evolution of these stages is controlled by the non-linear rheology, able to store large stress accumulations that lead to the failure of the upper plate: opening of a back-arc basin and slab break-off. The break-off is initiated at the corners of the continent. The topography shows a non-linear distribution of amplitudes, with a high topographic front at the collision boundary and a proximal back arc basin that widens in time.

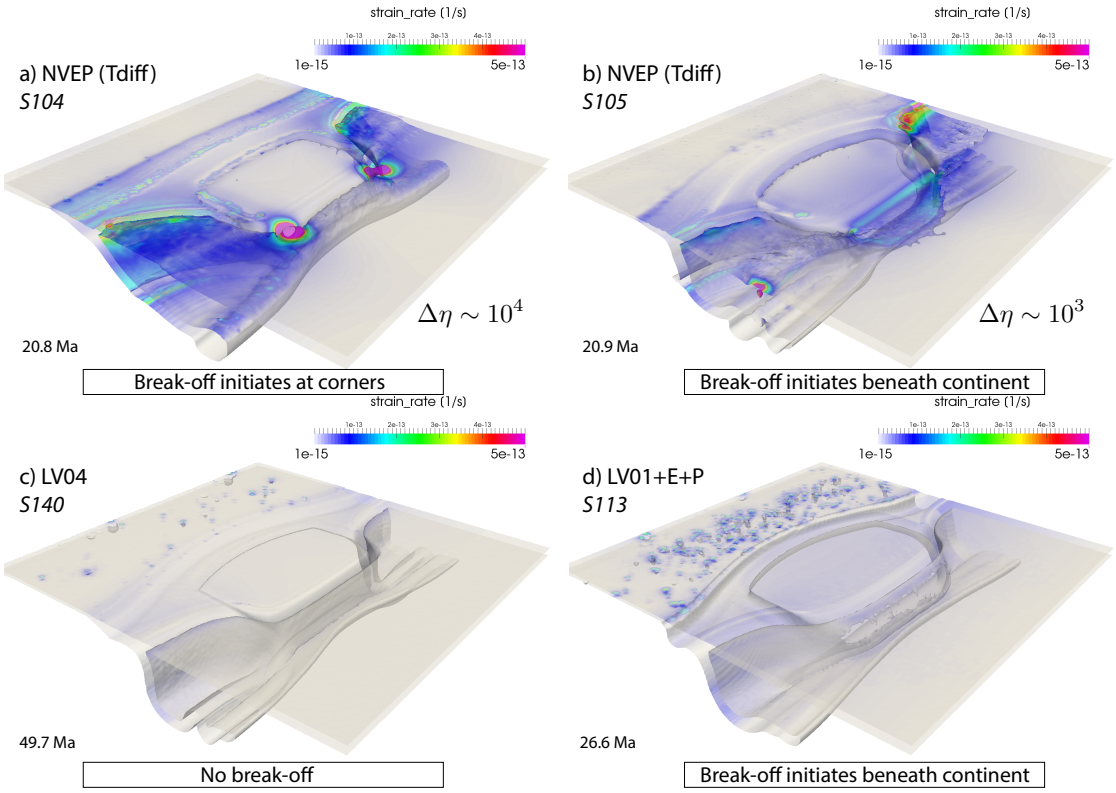

Fig. 4.4 Different slab break off dynamics. a) with NVEP rheology, slab break-off is initiated at the corners where the stress is concentrated. b) with a weaker NVEP rheology of the lithosphere, the break-off is initiated beneath the continent where the influence of the buoyancy of the indentor is the maximum, c) linear viscous approximations produce no slab-break off, with a continous slab that buckles at the transition to the lower mantle, and d) if linear viscous approximations are coupled with plasticity and elasticity (E+P), the slab becomes weaker and breaks beneath the continent. Comparison between b) and d) suggests that a break-off beneath the continent is more characteristic for cases where viscous deformation is dominant compared to where elasticity is important. Artefacts due to high viscosity contrast between mantle and free surface can be seen in d), though they do not affect the general pattern of results. These artefacts seem to occur mainly in simulations with linear viscous approximations.

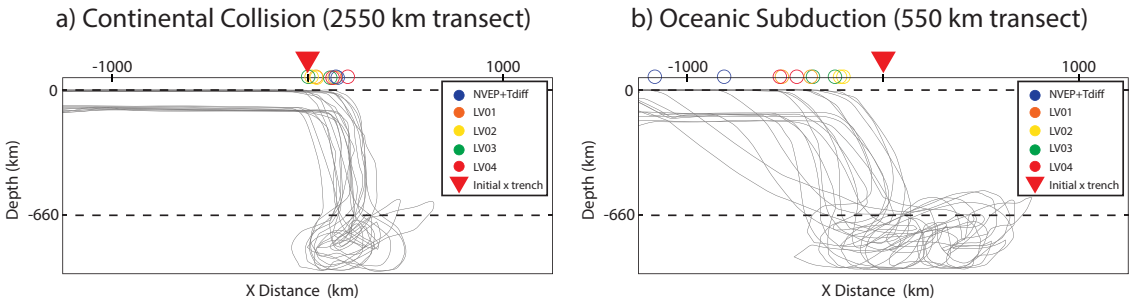

Fig. 4.5 Variability of slab shapes and trench positions after 80% of initial slab length was subducted. Cross-sections are taken for (a) continental collision, and (b) oceanic subduction. For continental collision, the slab shape and trench position are fairly consistent across simulations and approximations. However, during oceanic subduction, trench position can vary up to 1000 km and a larger variability is noticed for the slab shape.

during oceanic subduction compared to continental collision. Slab shapes for individual rheological approximations can be seen in Figure 4.6. During continental collision, all approximations give a similar folding (i.e., backwards) of the slab, except the linear viscous approximations combined with elasticity and plasticity (LV+E+P), that result in an opposite folding (i.e., forward). During oceanic subduction, the trench has retreated the most for NVEP simulations. The closest approximation to NVEP for trench motion seems to be the LV04 approximation, with a sub-layered structure.

4.4.3 Effects on trench motion

We introduced the concept of trench motion in the previous section and showed how the trench position varies across simulations for a similar stage of evolution. Figure 4.7 shows the evolution of the trench position (a-b) and the trench velocity (c-d) in time. The transect for continental collision registers a short episode of trench retreat for about 5-10 Ma, followed by trench advance for the rest of the simulation. This is reflected in the velocity plot (c) where the velocities are negative for trench retreat and positive for trench advance. It is clear that linear viscous approximations produce little trench motion and have small trench velocities. Simulations with elasticity and plasticity register faster trench motions. The LV04 case produces faster trench motions than the other linear viscous approximations, for both the continental and ocean side. They are comparable to the NVEP case, suggesting that resolving the weakening of the lower lithosphere is very important for the dynamics of the system. However, the evolution of the trench position and velocity for NVEP cases is dramatic. There is an initial stage, in which both the continental and oceanic trench velocities

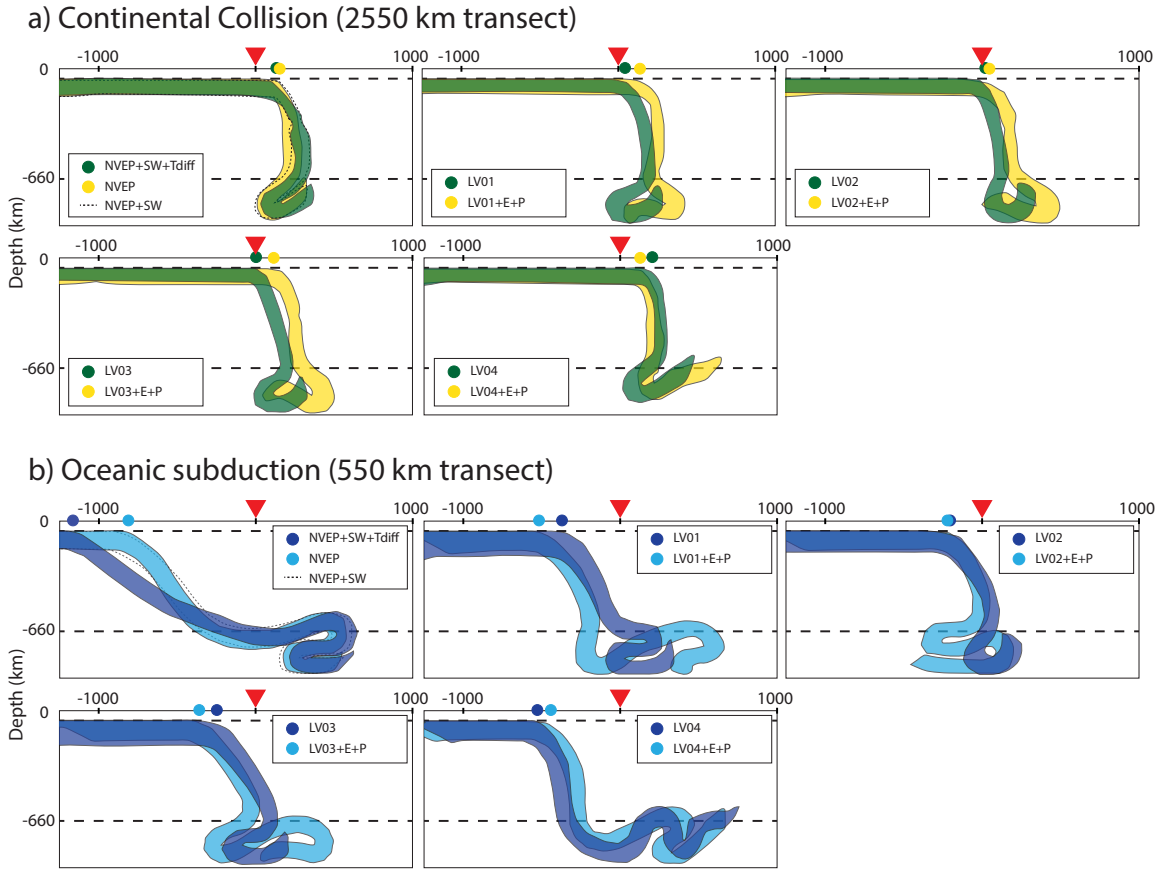

Fig. 4.6 Slab shapes and trench positions for different rheological approximations. a) Continental collision: all approximations result in the same vergence of the slab, except for the linear viscous approximations combined with elasticity and plasticity, which result in an opposite polarity of vergence. b) Oceanic subduction: large trench motions are registered for the NVEP cases, with the largest when temperature diffusion is activated. Linear viscous approximations (LV01-03) produce little trench motion, suggesting that subduction is not efficient in this case. The LV04 approximations produce intermediate trench motion and shapes to NVEP and the other linear viscous approximations.

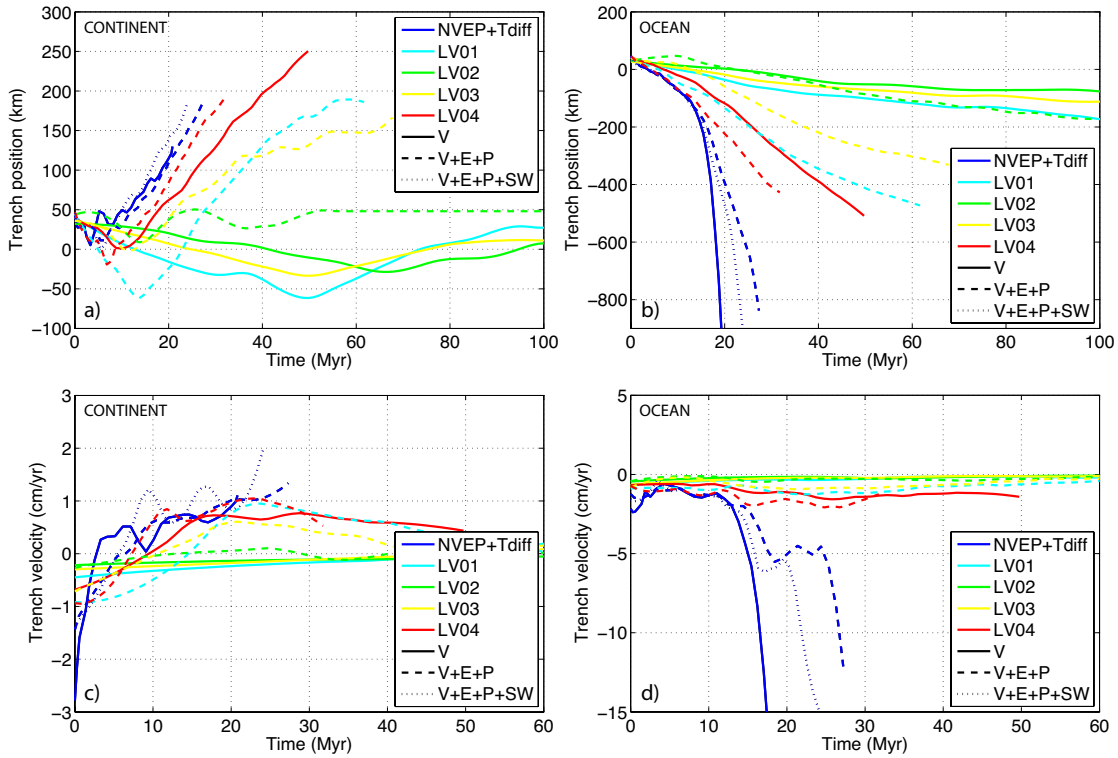

Fig. 4.7 Trench position and velocity over time for continental collision (a, c) and oceanic subduction (b, d). Simulations with linear viscous approximations have a sub-horizontal trend in both the position and the velocity evolution, suggesting little trench motion over time. The LV04 approximation registers faster trench retreat rates on the oceanic side, similar to NVEP case. However, the NVEP simulations show a non-linear evolution of the trench position, showing two trends: an initial stage with slower and linearly increasing trench positions, followed by a stage of rapid trench retreat, coincident with the opening of a back-arc basin. The effect is more pronounced if shear weakening and temperature diffusion are activated.

move constant in time (time interval 0-15 Ma), followed by a rapid increase in trench retreat velocity. During this last stage, the trench has retreated more than 600 km in less than 5 Ma during oceanic subduction, and coincides with the opening of the back-arc basin. This "runaway effect" is more pronounced for simulations with shear weakening and temperature diffusion, suggesting that once the upper plate is broken apart, the opening of the basin is facilitated by the weakening of material and the advection of heat from the mantle inside the basin, which weakens the material further.

Figures 4.5, 4.6, and 4.7 show that different approximations take different times to reach the same evolution stage. This suggests that the biggest impact of rheological approximations on the dynamics of the system is on the efficiency of subduction, by either facilitating subduction or resisting it.

4.4.4 Effects on topography

We next present the effect of rheology on topography. *Pusok and Kaus* [2015] have shown that different topographic modes can occur in linear viscous models, depending on the internal rheology, boundary conditions (pushing velocity, presence of heterogenous crustal blocks) or the evolution stage they are in. Figure 4.8 shows the topographic maps for the simulations shown in Figure 4.4 and the same evolution stage. It is clear that NVEP rheology produces a more heterogenous distribution of amplitudes, with a high topographic front and a back-arc basin at the sides. As explained before, that is because once the opening of the back-arc basin was initiated, the system has found an efficient way to accommodate both trench advance and trench retreat by promoting high amplitudes at the collision front and lowering them in the back-arc basin. Lateral extrusion of material then becomes less important. On the other hand, linear viscous approximations produce a more homogeneous distribution of mean amplitudes (Figure 4.8c), with strong lateral extrusion (viscous flow) of material that averages the amplitudes in the upper plate. When the lithosphere is weaker, the topography resembles more the linear viscous cases (i.e., Figure 4.8b).

The narrow topographic fronts such as the ones in Figure 4.8a,d are the only high topography expression in all simulations. None of the simulations produced a high topographic plateau similar to the Tibetan Plateau, and that is because the convergence of the indentor into the upper plate is not high enough. *Pusok and Kaus* [2015] have shown that high convergence velocities are important to build-up topography. However, the simulations here are "free subduction", meaning that the driving force is slab-pull, and mechanisms such as slab break-off or subduction locking due to stiffness of the plates reduce the work done to the system.

Figure 4.9 shows the evolution of maximum and mean topographic amplitudes in time. All simulations register a general decrease of mean amplitudes in time, due to trench retreat during oceanic subduction, which promotes lowering the topographic amplitudes. An interesting observation is that the linear viscous approximations produce relatively low variations between the maximum and mean topographic amplitudes, meaning that during the viscous flow of material the stresses diffuse. However, the NVEP rheology promotes both the highest maximum amplitudes and the lowest mean amplitudes, suggesting that it can sustain higher energies over time, but in the presence of weakening mechanisms (accumulated strain rate, weakening due to temperature diffusion and advection), the rheology will become very weak and promote low amplitudes (i.e., opening of back-arc basin).

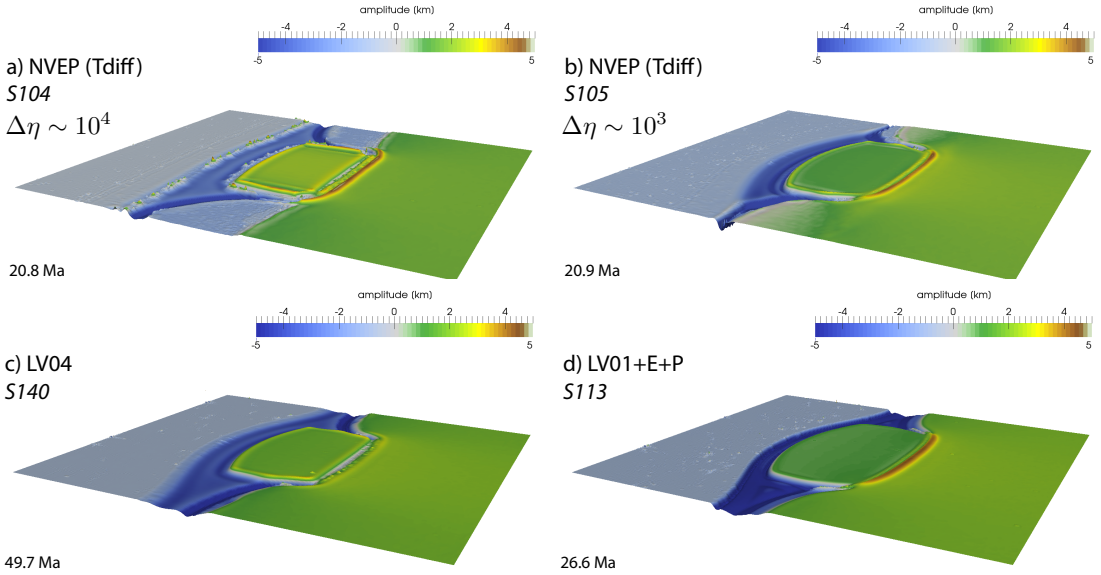

Fig. 4.8 Topography maps for simulations shown in Figure 4.4. NVEP rheology produces an uneven distribution of topographic amplitudes, with a high and narrow topographic front at the collision front and a low-amplitude back-arc basin at the sides.

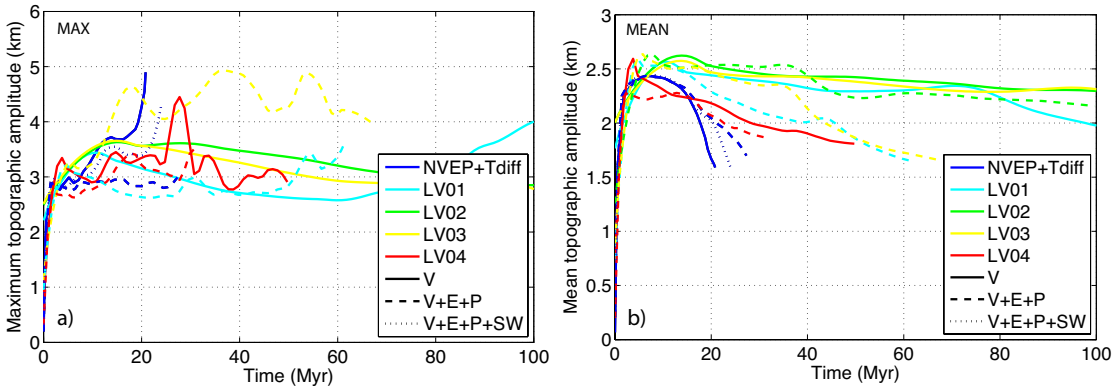

Fig. 4.9 Evolution of maximum and mean topographic amplitudes in time.

4.5 Discussion

The models shown here exhibit a wide range of behaviours depending on the rheological law employed: from linear viscous (LV01-LV04) to temperature-dependent visco-elasto-plastic rheology that takes into account both diffusion and dislocation creep (NVEP). Our results show that rheology exerts a strong effect on slab morphology, trench migration rates and topography in the upper plate.

One of the most important outcomes of this study is the style of break-off. Not only there are variations in break-off between different rheological approximations, but also between relative strengths within the same approximation (i.e., results of S104 and S105). In non-linear viscous models with strong lithosphere, slab break-off is initiated at the corners of the continent, while in linear viscous models no break-off is produced, unless they are coupled with plasticity and elasticity, in which break-off occurs beneath the continental indentor. Therefore, if the lithosphere is relatively strong and has a non-linear rheology able to accumulate stresses, points of maximum stress accumulation are the ones nucleating slab break-off, while if the lithosphere is weaker, the factor controlling break-off is the buoyancy of the indentor. Previous numerical models obtained slab break-off beneath the continental indentor (e.g., *Duretz et al.* [2011a]; *Li et al.* [2013]; *Pusok and Kaus* [2015]; *van Hunen and Allen* [2011]).

Trench migration was also used as a comparison proxy because it is the surface expression of subduction. As such, it is an integral part of the subduction process and arises naturally from the forces that govern subduction. Trench motion can be either retrograde (trench retreat) or prograde (trench advance) [*Elsasser*, 1971; *Funiciello et al.*, 2003; *Jacoby*, 1973; *Molnar and Atwater*, 1978; *Schellart*, 2008]. The factors controlling trench motion are not well understood, and include a combination of forces from the subducting plate and overriding plate [*Sharples et al.*, 2014]. In our simulations, non-linear rheology produces the fastest trench motion, while the linear viscous approximations produce the slowest trench motion. This suggests that rheology controls how efficient subduction is. Efficiency of subduction might be an ambiguous term to use because there are many terms controlling subduction dynamics, but we believe some effort should be put in finding more qualitative measures to assess this efficiency of subduction, which should improve our understanding.

In general, experiments with analogue and numerical models [*Bellahsen et al.*, 2005; *Di Giuseppe et al.*, 2008; *Li and Ribe*, 2012; *Stegman et al.*, 2010a] suggest that the trench retreating mode is favoured by relatively thin, narrow and dense plates, whereas the trench advancing mode occurs when the plate is thick, wide and less dense. All these previous studies have used either linear viscous models (i.e., simplified rheological approximations) or excluded the presence of an upper plate. In all our results, oceanic subduction is characterised

by trench retreat (the most trench retreat is observed with NVEP rheology) and continental collision is characterised by trench advance. Simulations with a thinner or weaker lithosphere (i.e., S105) also follow these observations, suggesting that the style of subduction depends on the interaction of the slab with the mantle, but also on the interaction of the slab with the upper plate.

Another important result in our models is the opening of back-arc basins, unique to simulations with non-linear viscous rheology. Stress accumulations prove again to be important in creating a basin-opening extensional regime. Linear viscous approximations fail to achieve this because stresses are diffuse and material is free to flow laterally to accommodate trench retreat. Topography is also strongly affected by rheology. NVEP provides a heterogeneous topographic distribution of amplitudes, with high topographic fronts during continental collision and back-arc basins in close proximity during oceanic subduction. This suggests that non-linear rheology is able to generate and sustain high amplitudes in time.

Our results show that rheological approximations can yield different results. This does not imply that rheological approximations are not useful to the scientific community. On the contrary, they allow for a good understanding of the system, since analytical solutions and scaling laws are easier to derive (e.g., *Li and Ribe* [2012]; *Stegman et al.* [2010a]). However, applying numerical models with various rheological approximations to tectonic specific regions (for example, the India-Asia collision zone) should be done with care. The slab structure beneath India-Asia collision is very complex with multiple phases of slab break-off [*Replumaz et al.*, 2004, 2010]. Reproducing such a complex structure with numerical models might be biased depending on the choice of rheology. A way forward would be to also derive scaling laws to understand better the dynamics of complex systems.

Like any numerical model, our model also has some limitations, the most important being the resolution. A low resolution averages out potential weakening of material with depth (i.e., lower crust, weak zone). On the other hand, plasticity combined with shear weakening and temperature diffusion can generate very high strain rates and velocities. Then, the time evolution in high resolution simulations is deteriorated (i.e., very small time steps) because time stepping is limited by maximum velocity and grid size (i.e., using a Courant-Levy criterion). Thus, care must be taken because the effect of plasticity depends on the resolution.

Finally, rheology of natural rocks is in general not well constrained. Our choice of non-linear rheology is random, with the aim to construct a common "Christmas tree" strength profile (Figure 4.2). It is expected that variations using different laboratory flow laws will occur in numerical models; variations that could help explain differences between natural subduction and collision systems. On the quality of our rheological approximations, the

sub-layered approximation (LV04) produced the closest results to simulations with non-linear rheology, suggesting that material weakening with depth is important. Moreover, different processes have not been accounted for, such as dependence of rheology on pressure, water content or grain size. Other processes such as phase transformations, water migration or multi-phase flow will most likely affect the dynamics, but that is outside the scope of this study.

4.6 Conclusion

The effect of rheological approximations on subduction and collision dynamics is tested in a geometrically simplified 3-D model setup of an integrated lithospheric and upper-mantle scale model of "free subduction". The results exhibit a wide range of behaviours depending on the rheological law employed: from linear viscous (LV01-LV04) to temperature-dependent visco-elasto-plastic rheology that takes into account both diffusion and dislocation creep (NVEP). Most importantly, rheology exerts a strong effect on slab morphology, trench migration rates and topography in the upper plate. In simulations with non-linear visco-elasto-plastic rheology, break-off is initiated at the corners in places with maximum accumulated stress, opening of a back-arc basin is fast and topography has a heterogenous distribution of amplitudes. On the other hand, in simulations with linear viscous approximations, slab does not break-off, instead it buckles at the transition zone, the dynamics is dominated by low strain rates and diffuse stresses, and topography is controlled by lateral extrusion of material which homogenizes amplitudes in the upper plate. When using a linear viscous approximation, a sub-layered rheological structure that mimics the effect of material weakening with depth produces closer results to non-linear viscous rheology.

#	Phase	ρ (kg/m^3)	C_p (J/kg/K)	k (W/m/K)	T profile	Viscous Flow Law (NVEP)	C (MPa)	ϕ	G (MPa)
0	mantle asthenosphere	3200	1200	2.5	adiabat 0.5°C/km	Dry olivine (disl+diff)	20×10^6	30°	15×10^{10}
1	sticky air	0	1200	2.5	0°C/km	1×10^{18} Pa.s	-	-	-
2	lower mantle	3250	1200	2.5	adiabat 0.5°C/km	5×10^{21} Pa.s	20×10^6	30°	20×10^{10}
3	ocean UM	3300	1200	2.5	half-space 80Ma	Dry olivine (disl+diff)	20×10^6	30°	7.4×10^{10}
4	oceanic crust	3200	1200	2.5	half-space 80Ma	Quartzite (disl)	1×10^6	1°	3.6×10^{10}
5,8	continental UM	3100	1200	2.5	cont. gradient 13°C/km	Dry olivine (disl+diff)	20×10^6	30°	7.4×10^{10}
6,9	continental LC	3100	1200	2.5	cont. gradient 13°C/km	Diabase (disl)	20×10^6	30°	4×10^{10}
7,10	continental UC	3100,3000	1200	2.5	cont. gradient 13°C/km	Granite (disl)	20×10^6	30°	3.6×10^{10}
11	weak zone	3000	1200	2.5	cont. gradient 13°C/km	1×10^{19} Pa.s	-	-	-

#	Phase	LV01 (Pa.s)		LV02 (Pa.s)		LV03 (Pa.s)		LV04 (Pa.s)	
0	mantle asthenosphere	2.41×10^{19}	2.41×10^{19}	5.24×10^{19}	5.24×10^{19}	2.91×10^{19}	2.91×10^{19}	*up* 3.55×10^{19} *dn* 1.22×10^{19}	3.55×10^{19} 1.22×10^{19}
1	sticky air	1×10^{18}	1×10^{18}	1×10^{18}	1×10^{18}	1×10^{18}	1×10^{18}	1×10^{18}	1×10^{18}
2	lower mantle	5×10^{21}	5×10^{21}	5×10^{21}	5×10^{21}	5×10^{21}	5×10^{21}	5×10^{21}	5×10^{21}
3	ocean UM	2.41×10^{23}	4.68×10^{22}	7.08×10^{23}	9×10^{22}	3.93×10^{23}	5×10^{22}	*up* 4.65×10^{23} *dn* 8.48×10^{21}	8.49×10^{22} 7.18×10^{21}
4	oceanic crust	8.32×10^{22}	5.5×10^{22}	1.74×10^{23}	8.94×10^{22}	9.69×10^{22}	4.96×10^{22}	*up* 9.11×10^{22} *dn* 7.64×10^{22}	7.61×10^{22} 3.69×10^{22}
5,8	continental UM	1.7×10^{23}	2.95×10^{22}	7.17×10^{23}	8.92×10^{22}	3.98×10^{23}	3.98×10^{23}	*up* 4.8×10^{23} *dn* 5.6×10^{21}	7.55×10^{22} 4.75×10^{21}
6,9	continental LC	1.8×10^{23}	5.44×10^{22}	3.62×10^{23}	8.78×10^{22}	2.01×10^{23}	4.88×10^{22}	*up* 3.04×10^{23} *dn* 3.4×10^{22}	8.11×10^{22} 2.32×10^{22}
7,10	continental UC	1.6×10^{23}	8.19×10^{22}	2.58×10^{23}	8.97×10^{22}	1.43×10^{23}	4.98×10^{22}	*up* 8.87×10^{22} *dn* 2.23×10^{23}	7.68×10^{22} 8.63×10^{22}
11	weak zone	1×10^{19}	1×10^{19}	1×10^{19}	1×10^{19}	1×10^{19}	1×10^{19}	1×10^{19}	1×10^{19}

Table 4.1 Parameters table for all rheological approximations. Density is kept constant for each phase throughout all simulations. Values in black are for $\eta_{max} = 10^{24}$Pa.s, while values in grey are for the case $\eta_{max} = 10^{23}$Pa.s. When shear weakening is activated, only the continental crust is affected, such that the friction angle of the material is linearly softened by 90% when the accumulated plastic strain (APS) is between 0.1 and 0.5. After APS = 0.5, there is a constant 90% softening of the friction angle.

Flow laws	B	E	V	n	Tensor correction	Reference
Dry olivine (diff)	1.5×10^{9}	375×10^{3}	5×10^{-6}*	1	*Simple shear*	*Hirth and Kohlstedt* [2003]
Dry olivine (disl)	1.1×10^{5}	530×10^{3}	15×10^{-6}*	3.5	*Simple shear*	*Hirth and Kohlstedt* [2003]
Wet quartzite (disl)	3.2×10^{-4}	154×10^{3}	0	2.3	*Uniaxial*	*Ranalli* [1995]
Diabase (disl)	3.2×10^{-20}	276×10^{3}	0	3.05	*Uniaxial*	*Carter and Tsenn* [1987]**
Granite (disl)	3.16×10^{-26}	186.5×10^{3}	0	3.3	*Uniaxial*	*Carter and Tsenn* [1987]**

Table 4.2 Viscous flow laws used in numerical experiments. Effective viscosity is calculated as in *Gerya* [2010], (Ch 6.2), based on the type of tensor correction needed. (*) Activation volumes for mantle asthenosphere are zero. (**) Values also used in *Huismans et al.* [2001].

No.	Description	Simulation name	
		$\eta_{max} = 10^{24}$ Pa.s	$\eta_{max} = 10^{23}$ Pa.s
1	NV+E+P	S100	S101
2	NV+E+P+SW	S102	S103
3	NV+E+P+SW+Tdiff	S104	S105
4	LV01	S110	S112
5	LV01+E+P	S111	S113
6	LV02	S120	S122
7	LV02+E+P	S121	S123
8	LV03	S130	S132
9	LV03+E+P	S131	S133
10	LV04	S140	S142
11	LV04+E+P	S141	S143

Table 4.3 Simulations performed and nomenclature.

Chapter 5

3-D Simulations of Greater India reconstructions and its convergence with Eurasia for the last 120 Ma

5.1 Summary

The geological evolution of the Himalayas and Tibetan Plateau is best viewed in a broader context of a dynamic system related to India's convergence northwards and subduction beneath Eurasia. Here, we present a new type of 3-D lithospheric and mantle-scale numerical models to investigate how the India-Eurasia convergence has been accommodated by subduction in the Neo-Tethys, and how the shape of Greater India affects collision dynamics. The model setup resembles a reconstruction from 120 Ma, and includes information on the convergence velocity based on previous published data and Greater India reconstructions. Our numerical models show the spontaneous formation and merging of a double subduction system, which resulted in a stable intra-oceanic subduction with a trench-trench-trench triple junction. The collision dynamics is controlled by the upper plate rheology and the size and shape of the Greater India extension, which controls the timing of collision and deformation pattern. Despite the fact that the Greater India extension has intermediate density between oceanic and continental crust and has the same thickness as the oceanic crust, it mostly acts as an indentor in simulations, instead of subducting, raising the question under which conditions continental material can subduct.

5.2 Introduction

One of the fundamental assumptions of plate tectonics theory is that most of the deformation occurs at plate boundaries. However, this is not the case for continental collision zones, where the crust of both converging plates is often shortened for many hundreds of kilometers, resulting in some of the world's largest mountain belts. The Himalayas and Tibetan Plateau represent the most remarkable mountain belt, formed as the result of collision of Indian and Eurasian plates. It is no surprise then, that this region has been extensively studied since early on to better understand both continental dynamics and global plate tectonics system.

As early as the 1920s, *Argand* [1924] postulated that the Tibetan plateau formed as the result of collision and post-collisional convergence of the Indian subcontinent with Eurasia, causing more than 2000 km of north-south crustal shortening and thickening of the crust to $\sim$80 km and producing the magnificent mountain ranges of the Himalaya, Karakorum, and Tien Shan. This perspective remains widely accepted and we know that the Indian sub-continent collided with Eurasia sometime in the last 50 million years (e.g., *Aitchison and Davis* [2004]; *Besse and Courtillot* [1988]; *Molnar and Stock* [2009]; *Patriat and Achache* [1984]). Some authors (e.g., *Yin and Harrison* [2000]) suggest that collision started possibly as early as $\sim$70 Ma, while others advocate for a late collision time, as little as $\sim$20 Ma (i.e., *van Hinsbergen et al.* [2012]).

But most of the controversy remains over basic aspects of Tibetan geology. For example, there is a lot of emphasis put into understanding the complex present-day structure of the Tibetan Plateau, including the degree of mechanical coupling between the crust and deeper lithosphere or the nature of large-scale deformation. Several models have been proposed for the mechanism responsible for the deformation and uplift of Tibetan Plateau: continuous deformation, multiple continental underthrusting, eastward propagating extrusion or mosaic tectonics (e.g., *Argand* [1924]; *Dewey and Burke* [1973]; *England and Houseman* [1986]; *England and McKenzie* [1982]; *Molnar* [1988]; *Molnar et al.* [1993]; *Owens and Zandt* [1997]; *Tapponnier et al.* [2001]).

It is clear that understanding the processes that have formed the plateau requires reconstruction of changing patterns of deformation and uplift across a wide range of temporal and spatial scales. Mostly, the geological evolution of the Tibetan plateau should be viewed in a broader context of a dynamic system related to subduction of oceanic lithosphere beneath eastern Eurasia and Indonesia.

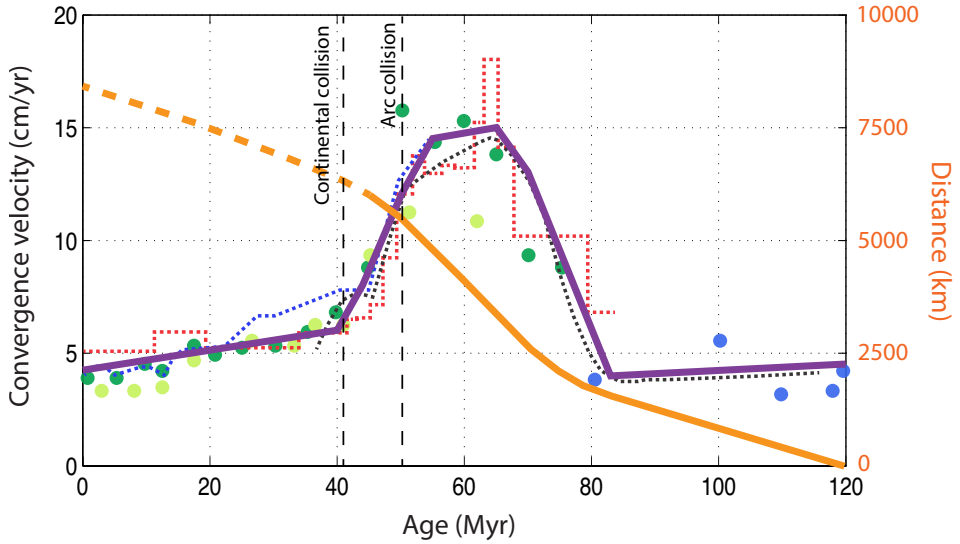

Fig. 5.1 India-Eurasia convergence rates (adapted from *Jagoutz et al.* [2015]). Dotted lines and circles show plate circuit [*Copley et al.*, 2010; *Molnar and Stock*, 2009], sea floor magnetic anomalies [*Cande et al.*, 2010; *Cande and Stegman*, 2011] and palaeolatitude data [*van Hinsbergen et al.*, 2012], constraining the convergence history of India and Eurasia. The data shows that India-Eurasia convergence rates began to increase rapidly by 80 Ma ago, reaching a peak around 60-65 Ma and slowing down after 50 Ma ago, presumably due to collision. The purple solid line represents the velocity function for influx boundary conditions in the numerical model created in this study. The orange line also displayed was calculated to get an estimate of the distance India travelled northward in the last 120 Ma. The model setup was built on the assumption that India was at least 7000 km away from Eurasia at around 120 Ma.

5.2.1 Convergence of India with Eurasia

Before its collision with Eurasia [*Besse and Courtillot*, 1988; *Cande et al.*, 2010; *Cande and Stegman*, 2011; *Copley et al.*, 2010; *Molnar and Stock*, 2009], India is most famous for the speed it attained during the Late Cretaceous-early Palaeogene when it was traveling at more than 16 cm/yr [*Besse and Courtillot*, 1988; *Klootwijk et al.*, 1992; *Lee and Lawver*, 1995; *Patriat and Achache*, 1984]. Figure 5.1 shows plate circuit, sea floor magnetic anomalies and palaeolatitude data constraining the convergence history of India and Eurasia [*Copley et al.*, 2010; *Molnar and Stock*, 2009; *van Hinsbergen et al.*, 2012]. *Acton* [1999] provides a detailed analysis of India's motion history, which is summarized below.

The break up of the super-continent Gondwana from the latest Paleozoic onwards (e.g., *Garzanti* [1993]; *Santosh et al.* [2009]) led to the formation of the Indian plate in Late Jurassic-Early Cretaceous (e.g., *Metcalfe* [1996]; *Müller et al.* [2000]; *Powell et al.* [1988]; *Seton et al.* [2012]; *Storey et al.* [1995]; *Torsvik et al.* [2000]). The northward motion of India from the Early Cretaceous period to the Early Cenozoic era is related to the subduction of oceanic lithosphere north of India, which consumed the Neo-Tethys Ocean [*Sengor and Natalin*, 1996], and to seafloor spreading south of India, which created the Indian Ocean [*McKenzie and Sclater*, 1971]. The rate of northward drift of India was approximately 6 - 7 cm/yr at its beginning, accelerated up to 15 - 25 cm/yr for a period of 20 Ma [*Besse and Courtillot*, 1988; *Cande and Stegman*, 2011; *Copley et al.*, 2010; *Molnar and Stock*, 2009; *Patriat and Achache*, 1984] until ca. 50 Ma ago when the motion of India experienced several changes in direction and the convergence rate decreased to 4 - 5 cm/yr, presumably due to continental collision (e.g., *Acton* [1999]; *Molnar and Tapponnier* [1975]; *Patriat and Achache* [1984]).

The cause of such anomalous high rates of convergence is unclear and in general is not reproduced by numerical models [*Capitanio et al.*, 2010; *van Hinsbergen et al.*, 2011]. The influence of the Reunion plume was initially proposed as an explanation [*Cande and Stegman*, 2011], but was later agreed that the influence of the plume is short-lived, limited to the short time interval around 66 Myr when spreading rates in the Indian Ocean reached 18 cm/yr. More recently, *Jagoutz et al.* [2015] proposed that the existence of two, almost parallel, northward dipping subduction zones between the Indian and Eurasian plates, could explain the high convergence during the Early Cretaceous period. Their proposal is consistent with the presence of two relict slabs below India [*Replumaz et al.*, 2004; *Van der Voo et al.*, 1999] and the geochemical signature of magmatism in Tibet [*Bouilhol et al.*, 2013].

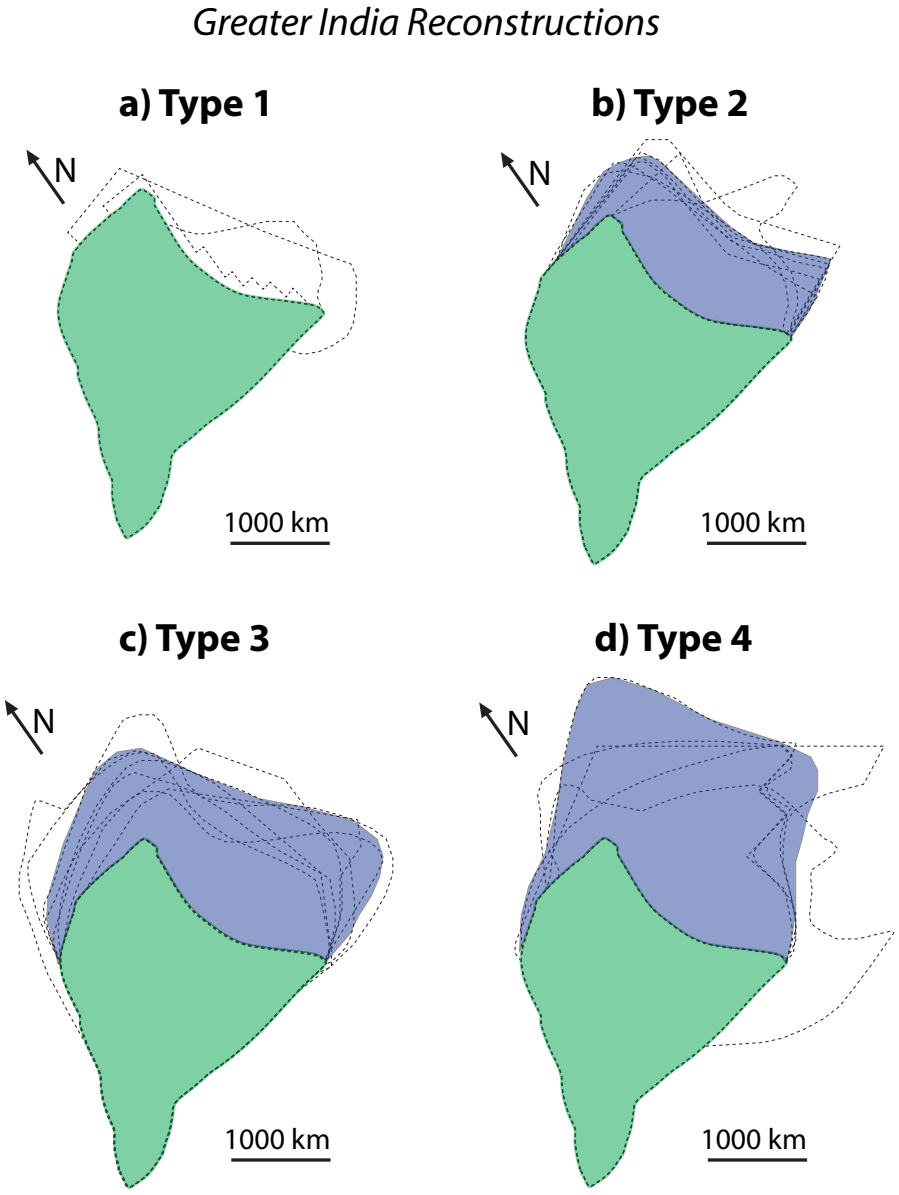

Fig. 5.2 Summary of Greater India reconstructions. The Greater India reconstructions are classified into 4 groups solely based on the size and shape of the extension: **Type 1** with little or no extension [*Dewey et al.*, 1989; *Gnos et al.*, 1997; *Molnar and Tapponnier*, 1975, 1977; *Reeves and de Wit*, 2000], **Type 2** with medium extension in the North and East [*Ali and Aitchison*, 2004, 2005; *Crawford*, 1974; *Kosarev*, 1999; *Powell and Conaghan*, 1973, 1975; *Treloar and Coward*, 1991; *Veevers et al.*, 1971, 1975; *Zhou and Murphy*, 2005], **Type 3** with a larger extension in the West, North and East [*Argand*, 1924; *Besse and Courtillot*, 1988; *Hall*, 2002; *Holmes*, 1965; *Klootwijk et al.*, 1992; *Le Pichon et al.*, 1992; *Patzelt et al.*, 1996; *Replumaz and Tapponnier*, 2003; *Stampfli and Borel*, 2002], and **Type 4** with a very large extension in all directions [*Barazangi and Ni*, 1982; *Gaina et al.*, 1998; *Lawver and Gahagan*, 2003; *Lee and Lawver*, 1995; *Matte et al.*, 1997; *Müller et al.*, 1997, 1993; *Rotstein et al.*, 2001]. The individual reconstructions are not labelled for simplicity, but they are indicated with dotted lines. The review work of *Ali and Aitchison* [2005] has been at the basis of these classifications. The shaded green region is the present-day shape of the sub-continental India and the blue is the proposed extension of Greater India.

5.2.2 Greater India

"Greater India" is an 80-yr-old concept proposed by geologists to describe the Indian sub-continent (present-day shape) plus a postulated northern extension. Over time, numerous authors working on the India-Asia collision have added various sized parts of continental lithosphere to the Indian sub-continent. Reviews of Greater India have been carried out by *Ali and Aitchison* [2005]; *DeCelles et al.* [2002]; *Harrison et al.* [1992]; *Le Pichon et al.* [1992]; *Matte et al.* [1997]; *Packham* [1996]; *Powell and Conaghan* [1975].

A key assumption in all models of the system is the idea that the pre-collision sub-continent was larger than the present-day craton, therefore the concept of "Greater India". The earliest Greater India models were based upon the idea that continental lithosphere ahead of the Indian craton had been thrust under Asia (e.g., *Argand* [1924]; *Holmes* [1965]; *Powell and Conaghan* [1973, 1975]; *Veevers et al.* [1975]). More recent Greater India proposals have been based mainly on four lines of logic.

One group of workers have based their Greater India models on reconstructions of eastern Gondwana back in the Mesozoic (e.g., *Lee and Lawver* [1995]; *Müller et al.* [2000]). A second form of reconstruction is based on estimates of crustal-shortening in the Himalayas, between the Indian craton and the Yarlung Tsangpo suture zone (e.g., *Treloar and Coward* [1991]). A third type of proposals was designed to close a large physical gap between the cratonic part of the sub-continent and the southern margin of Tibet to allow collision with Eurasia at a particular time and site (e.g., *Besse and Courtillot* [1988]; *Klootwijk et al.* [1992]; *Patzelt et al.* [1996]), in what is also called "fill-the-gap" solutions. Occasionally, Greater India extensions have been based on a combination of fill-the-gap and shortening estimate arguments. And finally, more recently, a fourth group has taken into account the pre break-up position and shape India in eastern Gondwana (prior to the Early Cretaceous) and the bathymetry of the Indian Ocean west of Australia, in particular the Wallaby-Zenith Plateau Ridge and the Wallaby-Zenith Fracture Zone (e.g., *Ali and Aitchison* [2005]; *Gibbons et al.* [2012]).

Here, we use a different approach to constrain previous Greater India estimates. First, we classify existing conceptual models into categories based on the shape and size of the proposed extensions, after which we describe the results of forward numerical simulations with each type of Greater India extension.

We identify 4 types of Greater India reconstructions: **Type 1** based on *Dewey et al.* [1989]; *Gnos et al.* [1997]; *Molnar and Tapponnier* [1975, 1977]; *Reeves and de Wit* [2000], **Type 2** based on *Ali and Aitchison* [2004, 2005]; *Crawford* [1974]; *Kosarev* [1999]; *Powell and Conaghan* [1973, 1975]; *Treloar and Coward* [1991]; *Veevers et al.* [1971, 1975]; *Zhou and Murphy* [2005], **Type 3** based on *Argand* [1924]; *Besse and Courtillot* [1988]; *Hall*

[2002]; *Holmes* [1965]; *Klootwijk et al.* [1992]; *Le Pichon et al.* [1992]; *Patzelt et al.* [1996]; *Replumaz and Tapponnier* [2003]; *Stampfli and Borel* [2002], and **Type 4** based on *Barazangi and Ni* [1982]; *Gaina et al.* [1998]; *Lawver and Gahagan* [2003]; *Lee and Lawver* [1995]; *Matte et al.* [1997]; *Müller et al.* [1997, 1993]; *Rotstein et al.* [2001]. Figure 5.2 shows each type of extension and the reconstructions they were based on, displayed as dotted contours.

5.2.3 Goals of this study

It is clear that two important aspects need to be considered in models reproducing the geological evolution of the India-Asia collision zone and the uplift of the Himalayas and Tibetan Plateau: the convergence profile of India northwards since the break-up from Gondwana (at least 120 Ma) and the shape of Greater India prior to collision in such way that fits reconstructions and deformation in present-day India-Asia collision. The first aspect is usually ignored in models due to the uncertainty in the nature of the convergence velocity. Previously, all analogue or 3-D numerical studies have modelled the most recent stage of evolution (approximately last 50-70 Ma of evolution) involving some oceanic subduction and full-head collision [*Bajolet et al.*, 2013; *Capitanio and Replumaz*, 2013; *Li et al.*, 2013; *Pusok and Kaus*, 2015; *Replumaz et al.*, 2014; *Sternai et al.*, 2016]. However, questions such as: (i) how is the convergence of India accommodated by subduction in the Neo-Tethys, or (ii) how has the southern margin of Eurasia evolved in time, require a longer time frame of modelling than previously considered.

The second aspect, the shape of Greater India, has also been ignored due to simplicity in models and usually a rectangular block is used (e.g., *Bajolet et al.* [2013]; *Pusok and Kaus* [2015]). This is because an irregular shape of the indentor is susceptible to deformation due to boundary conditions, especially when pushing boundary conditions are involved, like in most models ([*Duretz et al.*, 2014; *Li et al.*, 2013; *Pusok and Kaus*, 2015; *Sternai et al.*, 2016]). But using a more realistic shape is important for the study of deformation at the Eastern and Western syntaxes or the curvature of the Himalayas.

Here we employ the parallel 3-D code LaMEM [*Kaus et al.*, 2016] capable of simulating lithospheric deformation while simultaneously taking mantle flow and an internal free surface into account. We present a new type of 3-D lithospheric and mantle-scale numerical models, which accommodate a large time frame of the convergence of India-Eurasia and the irregular shape of Greater India. We configure a geodynamical model, which resembles a reconstruction from 120 Ma of the India-Asia collisional system, and we constrain the convergence velocity based on previous published data (Figure 5.1) and Greater India reconstructions (Figure 5.2). We aim to investigate how the India-Eurasia convergence has

been accommodated by subduction in the Neo-Tethys, and how the shape of Greater India affects collision dynamics.

After the description of our numerical model and model setup, we present a series of 3-D large scale long-term numerical simulations of the northward convergence of India in the last 100-120 Ma with different Greater India sizes. The results are then related to observations in India-Asia collision zone.

5.3 Method and Model Setup

In the following section we briefly describe the methodology and numerical setup used in this study. We present a new type of simulations with influx boundary conditions, in which we control the influx/outflux of material on one of the boundaries. This type of boundary conditions have been used before (i.e., *Duretz et al.* [2014]; *Li et al.* [2013]), but in general the influx velocity was kept constant and as mentioned above, the time frame of the simulations was relatively short. Here, our influx velocity will follow the function shown in Figure 5.1.

In order to model 3-D subduction and collision processes, we employ the 3-D finite difference staggered grid code LaMEM (Lithosphere and Mantle Evolution Model) [*Kaus et al.*, 2016] that solves a set of equations for conservation of mass, momentum and energy together with their constitutive relationships. While LaMEM handles temperature-dependent visco-elasto-plastic rheologies, here we test our new model with linear viscous approximations. In this case, the Stokes equations for conservation of mass and momentum, assuming incompressibility and neglecting thermal diffusion, are given by:

$$\frac{\partial \sigma_{ij}}{\partial x_j} = -\rho g_i, \tag{5.1}$$

$$\frac{\partial v_i}{\partial x_i} = 0. \tag{5.2}$$

where i, j represent spatial directions following the Einstein summation convention, $\sigma_{ij} = -P + \tau_{ij}$ is the total stress tensor with $P = -\sigma_{ij}/3$ being the pressure and τ_{ij} the deviatoric stress tensor, ρ the fluid density, g_i the gravitational acceleration, v_i the velocity and x_i is the spatial coordinate. The linear viscous constitutive relationship is given by $\tau_{ij} = 2\eta\dot{\varepsilon}_{ij}$, where η is the Newtonian viscosity, constant for each material phase, and $\dot{\varepsilon}_{ij}$ is the deviatoric strain rate tensor, defined as $\dot{\varepsilon}_{ij} = \frac{1}{2}\left(\frac{\partial v_i}{\partial x_j} + \frac{\partial v_j}{\partial x_i}\right)$.

The discrete system of equations resulting from the discretization of conservation equations is solved using a Galerkin multigrid approach. The domain is a 3-D Cartesian box in

which a Lagrangian marker-in-cell method is used for accurately tracking distinct material domains as they undergo extensive deformation due to creeping flow. A sticky air layer [*Crameri et al.*, 2012] and an internal free surface with a free surface stabilization algorithm [*Kaus et al.*, 2010] are employed to allow for the development of topography. The code is written in C and uses the PETSc library [*Balay et al.*, 2014].

The initial model setup (Figure 5.3) is based on plate reconstructions (e.g., *Seton et al.* [2012]; *Zahirovic et al.* [2012]) of the Late Jurassic or approximately 120 Ma ago (Figure 5.3a). By this time, India has completely separated from Gondwana and the Lhasa block was annexed to the Eurasian plate [*Van der Voo et al.*, 1999]. In this way, we can assume that after this age the Indian plate moved freely relative to Gondwana, and that no other major geological blocks were incorporated into the Eurasian plate until the India-Asia collision in the Cenozoic. Calculations based on convergence velocity suggest that India was at least 7000 km away from the Eurasian continental plate at 120 Ma (see Figure 5.1). Paleo-tectonic reconstructions and apparent polar wander studies provide information mainly about the latitudinal motion (i.e., N-S), while the longitudinal motion of India is not well constrained. For this reason, we simplify our model setup and align it with the North direction such that the Indian continent converges perpendicularly to the upper plate (Figure 5.3c).

The 3-D model domain (Figure 5.3c-d) extends 6400 km in x-direction, 6400 km in y-direction and 1000 km in the z-direction, and has a resolution of 256 x 256 x 128 cells. It consists of a continental upper plate with different geological blocks and a subducting oceanic plate. Both oceanic and continental lithospheres have a uniform thickness of 100 km. The continental crust has a thickness of 30 km, while the oceanic crust has a thickness of 20 km. The subduction is already initiated and the downgoing plate extends to 250 km depth.

The upper plate consists of different geological units (Figure 5.3c) motivated by the fact the Tibetan lithosphere is complex, composed of fragments of different ages, compositions, temperatures, and rheology (e.g., *Tapponnier et al.* [2001]). We impose lateral heterogeneities based on simplified geological reconstruction maps such as the one from *Royden et al.* [2008] (Figure 5.3b).

The plate structure is kept simple and includes two components: crust and upper mantle lithosphere, and they are referred as phases. All phases are shown and labeled in Figure 5.3c-d and in the figure caption. In terms of rheology, as described above in the constitutive equations, each phase is defined by two properties: viscosity and density (see Table 5.1 for parameter values). At 660 km depth, the transition to the lower mantle is marked by a viscosity jump of 50 and a density difference of 50 kg/m^3 [*Quinteros et al.*, 2010], which gives the best results of slab behaviour in numerical models compared to tomographic observations.

We use influx/outflux boundary conditions on the end of the oceanic plate, meaning that new lithosphere material is injected with an influx velocity, which is constrained to be equal to the convergence velocity in Figure 5.1. To preserve incompressibility, the inflow in the lithosphere (top part of domain) is balanced by outflow in asthenosphere (lower part of domain). All other boundaries have free-slip boundary conditions and sticky-air on top [*Schmeling et al.*, 2008]. As the model progresses in time, new oceanic material is injected into the model, such that after a certain time, the Indian continent will have moved into the model domain to collide with Eurasia. The influx material can be seen both in map view and in 3-D perspective.

Finally, we run two series of models in which we vary: (i) the shape of Greater India (Type 1-4), and (ii) the rheological parameters of the upper plate (Model 01 and Model 02). The differences between models Type 1-4 are shown in Figure 5.2, and differences between Model 01 and Model 02 types are listed in Table 5.1. Model 01 has on average five times higher viscosities for the crust in the upper plate and can be considered a model with a “stiff upper plate", while Model 02 has a “weak upper plate".

Phases	0	1	2	3	4	5	6	7	8	9
ρ (kg/m^3)	3200	0	3250	3300	3300	3200	3000	3050	3000	3050
M01 η (Pa.s)	1e20	1e18	5e21	1e23	1e20	1e22	5e22	5e22	5e22	5e22
M02 η (Pa.s)	1e20	1e18	5e21	1e23	1e20	1e22	1e22	1e22	1e22	1e22

Phases (cont.)	10	11	12	13	14	15	16	17	18
ρ (kg/m^3)	3000	3100	3050	3050	3200	3050	3070	3200	3100
M01 η (Pa.s)	5e22	5e22	5e22	5e22	5e23	5e22	5e21	1e23	1e23
M02 η (Pa.s)	1e22	1e22	1e22	1e22	5e23	1e22	1e21	1e23	1e23

Table 5.1 Summary of parameter values in this study. M01 and M02 stand for Model 01 and Model 02, respectively. The continental units in the upper plate have the same viscosity distribution within Model 01 and Model 02, with the exception of Tarim Basin (Phase 14) and South China Sea (Phase 16). However, they have different densities relative to each other.Moreover, Model 01 has on average five times higher viscosities for the crust in the upper plate compared to Model 02.

5.4 Results

In this section we present simulation results of India’s convergence with Eurasia, starting with a reconstruction of approximately 120 Ma ago. All simulations have two major stages of evolution: 1) oceanic subduction and 2) continental collision. The first stage, oceanic subduction, lasts about 60 Ma of evolution and is similar across simulations from one set of

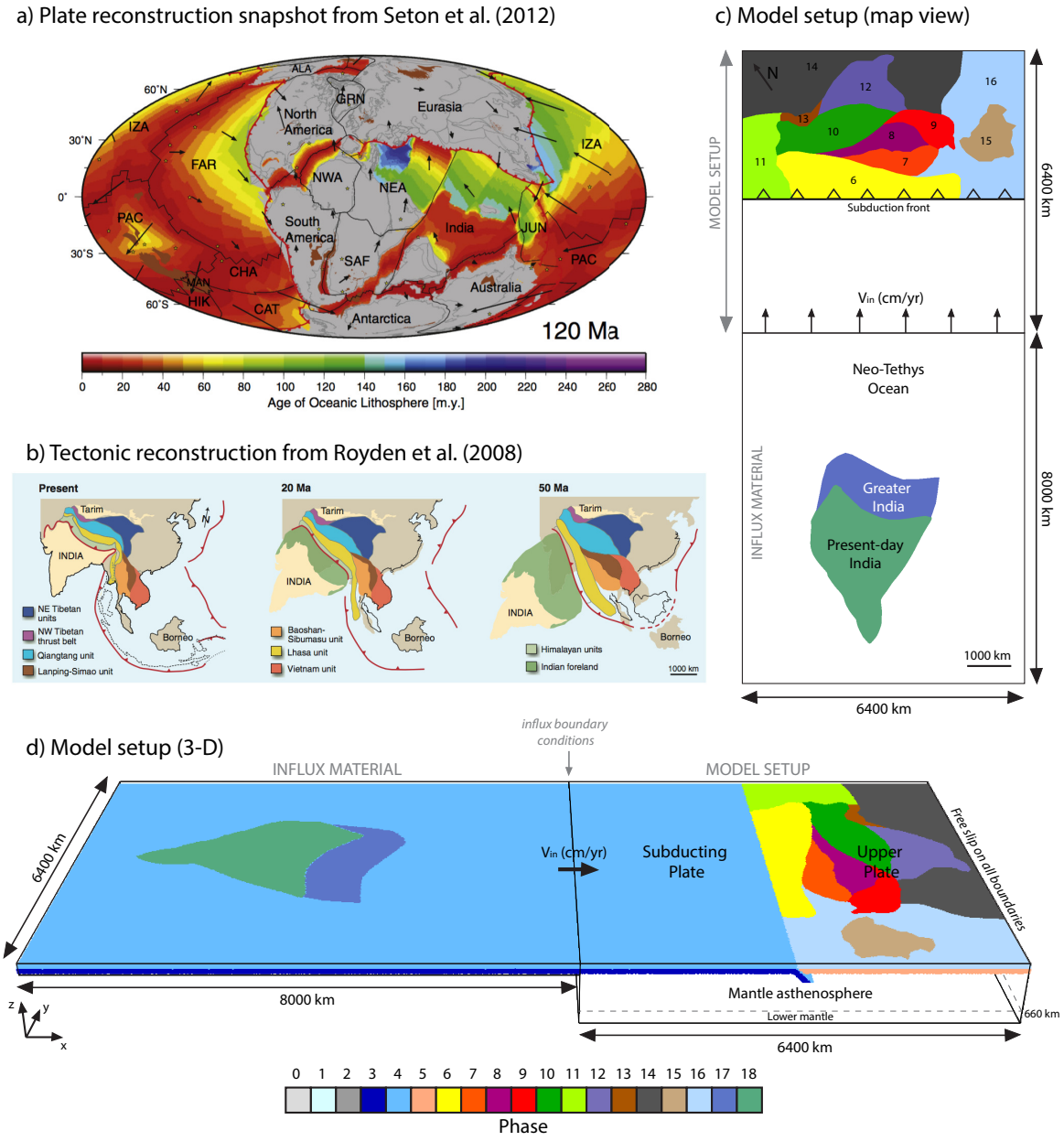

Fig. 5.3 Model setup. a-b) Plate reconstructions from *Seton et al.* [2012] and *Royden et al.* [2008] to highlight the tectonic context modelled in this study. c-d) Numerical model setup resembling a 120 Ma reconstruction. The 3-D model setup, which extends 6400 km in x-direction, 6400 km in y-direction, and 1000 km in z-direction, is shown in the lower-right part of d), and includes an oceanic subducting plate and a continental upper plate. The Eurasian upper plate is formed of multiple blocks, as shown in b), that are also present in our model setup. The influx material is also shown, and includes the extension of the oceanic plate with the Greater India continent located approximately 7000 km away from the upper plate (i.e., width of Neo-Tethys Ocean). The initial position of the Indian sub-continent is always the same. After every timestep, material is injected into the model domain (as shown in c-d) based on the velocity and size of timestep. Phases: 0-mantle asthenosphere, 1-sticky air, 2-lower mantle, 3-oceanic upper mantle lithosphere, 4-oceanic crust, 5-continental upper mantle lithosphere, 6-Lhasa unit, 7-Baoshan-Sibumasu unit, 8-Lanping-Simao unit, 9-Vietnam unit, 10-Qiantang block, 11-Western unit, 12-NE Tibet unit, 13-NW Tibet unit, 14-Tarim basin (also including basins to the East), 15-Borneo, 16-South China Sea, 17-Greater India (extension), 18-Indian sub-continent.

models (i.e., Model 01 and Model 02). On the other hand, evolution of continental collision is different due to the different shapes and sizes of Greater India (i.e., Types 1-4). Therefore, we first describe the general evolution of oceanic subduction for Model 01, and then describe features of continental collision for different types of the indenting continent. Later on, results of simulation series Model 02 are contrasted with results from Model 01, to investigate the role that the upper plate parameters have on the dynamics of the system.

In order to be consistent, we make two distinctions between the time scale shown in figures. If the time is displayed as “Age" it follows the same reasoning as in Figure 5.1 to represent time relative to present day. On the other hand, if time is represented as “Time", then it shows the numerical model evolution time (i.e., time evolved since start of numerical simulation). We will also refer to positions as “N, S, E, W" , for a better spatial orientation of our models, where N points the direction of initial subduction.

5.4.1 Model 01 - Formation of double subduction

Evolution of oceanic subduction. The evolution of Model 01 Type 1 is shown in Figure 5.4. On the left, we have a 3-D perspective of the phases from the subducting plate, and on the right a similar perspective from the upper plate. The trench is indicated with a continuous line with circles and the current influx velocity is shown with a red marker in the boxes in upper right corners.

As subduction progresses in time, we first notice that the lateral heterogeneities in the upper plate (i.e., different geological units) affect the subduction of the oceanic plate, resulting in different trench velocities and irregular subduction trench (25.9 Ma). By 45.8 Ma, the trench at the contact with the Lhasa unit (yellow) has retreated considerably, compared to the trench at the Western unit (light green). Surprisingly, this is created by different densities of the green and yellow units (100 kg/m^3 contrast) and not their viscosities (see Table 5.1). It suggests that the buoyancy of the upper plate acts as an important force on the subduction front that can either resist (higher density) or facilitate subduction (lower density).

Also by this point in time, the subduction convergence rates cannot keep up with the increasing influx velocities and the oceanic lithosphere starts buckling, producing a spontaneous subduction initiation (Figure 5.4 right column, 45.8 Ma). This incipient fold of the lithosphere has a higher amplitude in places where the trench retreat is slower (i.e., it is higher in front of the green unit compared to the amplitude in front of eastern units). The amplitude of the folding instability starts growing, and by 49.6 Ma there is an incipient subduction and the negative pull of the instability is already sustaining a newly-formed subduction. This is an important stage, because the new subduction system also reaches the site of the original subduction, which is still active. The way the two subductions merge suggests that

the merging depends mainly on the convergence velocities of the original subduction. That is for three reasons which can be seen at evolution stage 60.9 Ma: 1) The newly-formed subduction has a linear shape and is observed to migrate forward in time (between 45 - 50 Ma), meaning that the main driving force is the slab-pull of original subduction. 2) The new subduction is absorbed in the old subduction in places where trench retreat is faster (i.e., Lhasa, Eastern part), such that the trench takes the shape of the old subduction front. 3) In the Western part, where trench retreat is slow on the old subduction, the new subduction front minimizes energy of migration by avoiding tearing of the slab at depth, maintaining its original shape. Thus, a stable intra-oceanic subduction with a trench-trench-trench triple junction has now formed as the result of merging the two subductions. Subduction now resumes on all sites of the marked subduction trenches, with slower convergence rates on the branch of triple junction belonging to the original subduction system.

The evolution of the slab and topography throughout all these stages is very complex (Figure 5.5). On the eastern side of the domain, one slab dominates during the entire oceanic subduction evolution, while on the western side we observe the development of two slab systems. Beneath the triple junction, the slab branches are connected, though they evolve separately. The deformation in this place is viscous due to the constitutive equations solved, but with a complex rheology we can expect the slab to tear apart vertically. The merging of the two subductions also has a strong, but short-lived signature on the topography. A rapid high topographic growth can be noticed at 49.6 Ma, but disappears within 5 Ma, due to the amplified trench retreat that results from the subduction of accumulated slab material at depth. The subduction front becomes highly irregular at 60.9 Ma, just prior to continental collision. The Indian continent is already seen to approach the subduction from the South.

Continental collision. Figure 5.6 shows snapshots at 100 Ma after the start of the simulation for each type of the Greater India reconstructions. The first row of figures represents phases, the second row represents topography maps, and the bottom row shows the respective slab shapes. A comparison of the four types of reconstructions indicates that the major difference between them is the amount of lateral extrusion of material. The largest Greater India shapes (Type 3, 4) produce the most lateral extrusion of material by the time the simulations reach 100 Ma. Oceanic subduction continues at the side of continent collision even after the collision started. Continental collision, however, has a dramatic effect on the shape of the subduction/collision front. In front of the indenting continent, the trench has migrated forward (i.e., trench advance), while on the oceanic side, the trench has retreated considerably, almost enveloping the Indian sub-continent.

Despite the fact that the Greater India extension has intermediate density between oceanic and continental crust and has the same thickness as the oceanic crust, it mostly acts as an

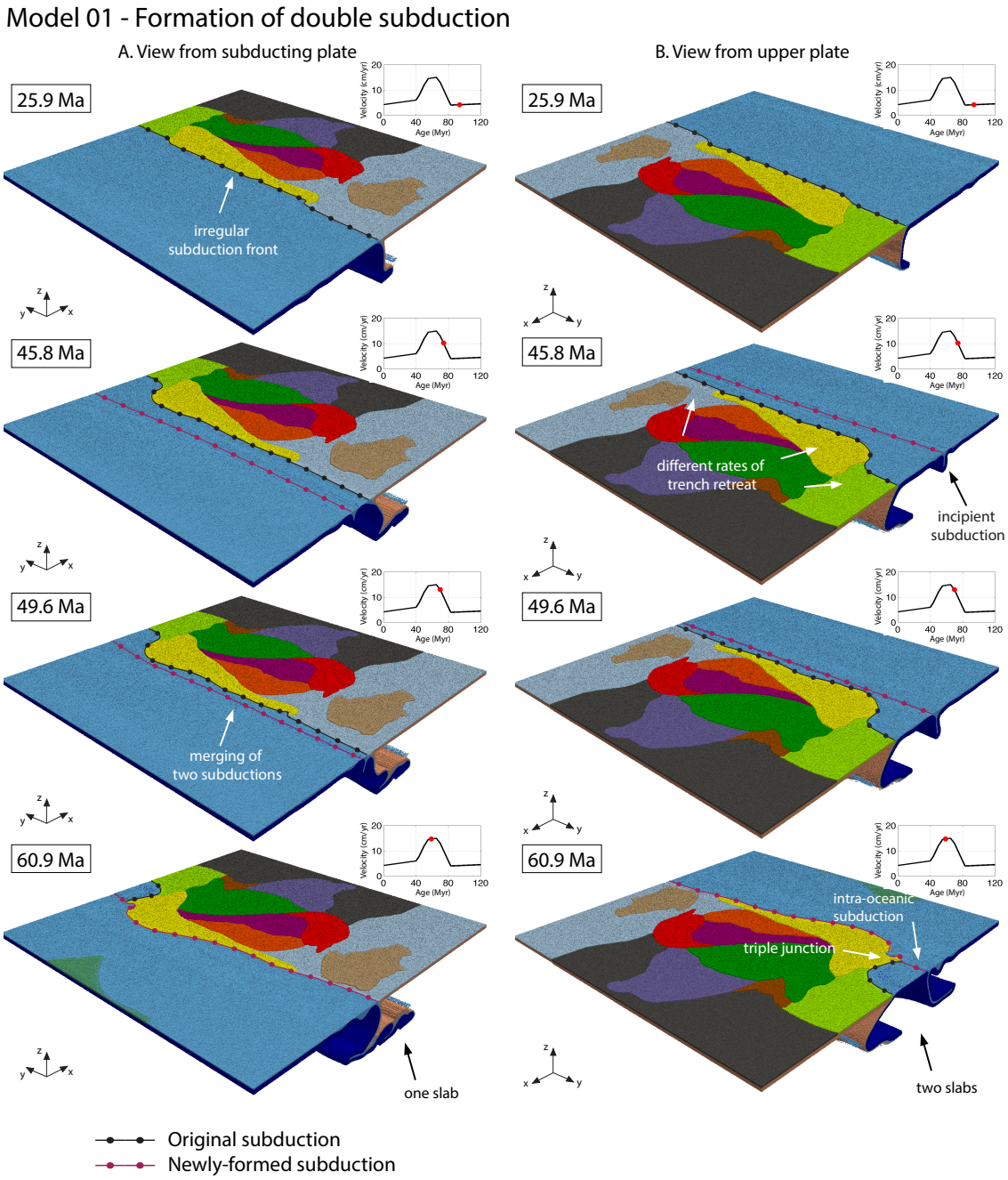

Fig. 5.4 Model 01 - Evolution of oceanic subduction (phases). The figure shows snapshots of different timesteps for simulation Model 01 Type 1. The left column shows a 3-D perspective from the subducting plate or the Eastern side of the domain, and the right column shows a perspective from the upper plate, or the Western side subduction. The fields represent the phases and same colorscale as in the model setup (Figure 5.3). The trenches are shown with continuous lines with circles. In upper corners, the influx velocity is plotted versus age (120 Ma minus evolution time), with corresponding value highlighted for the current timestep. The results show the development of a spontanous subduction initiation supported by the increasing influx velocities. The newly-formed subduction merges with the old subduction to form a highly irregular subduction front on the Eastern side, and an intraoceanic subduction with a stable trench triple junction configuration on the Western side.

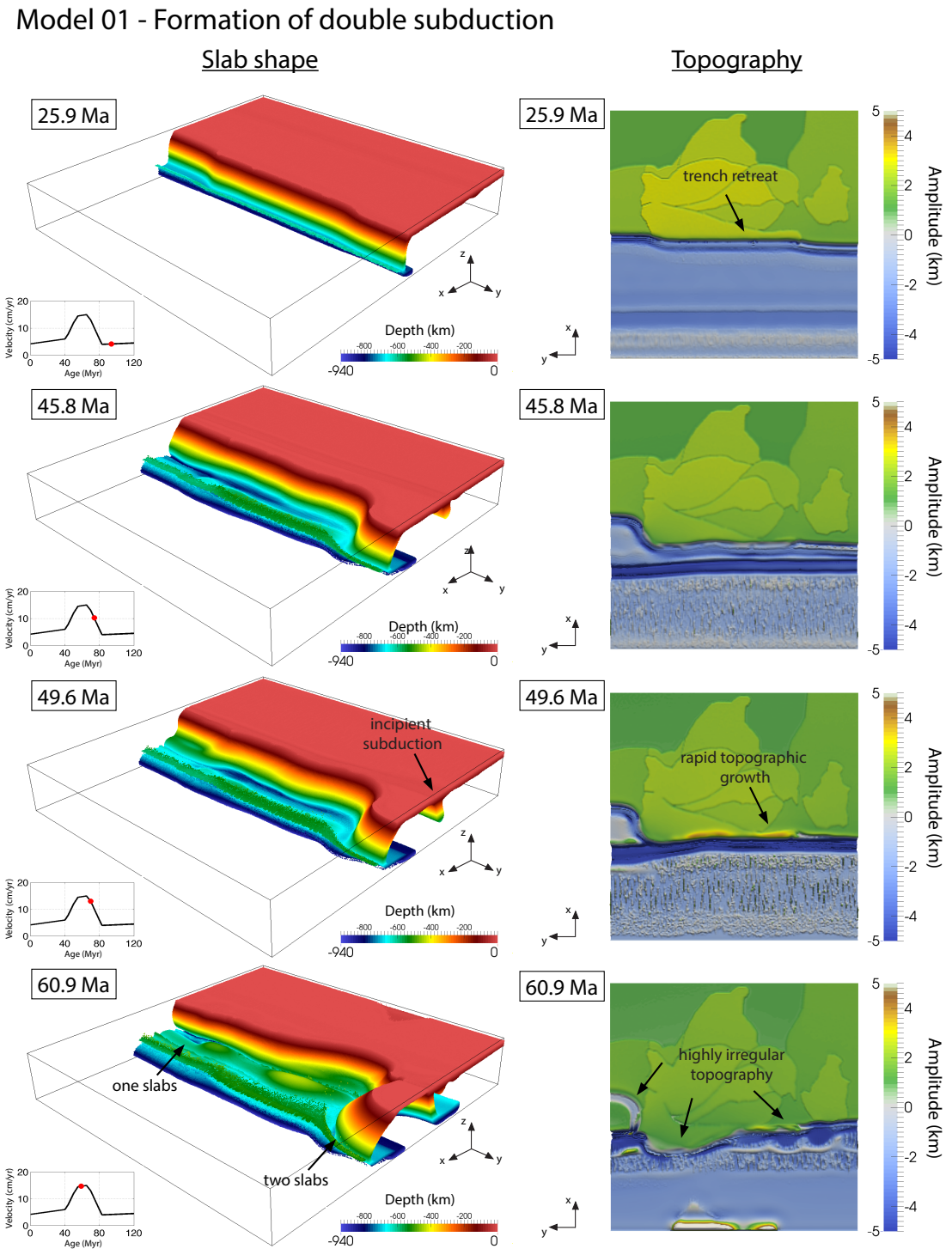

Fig. 5.5 Model 01 - Evolution of oceanic subduction (slab shape and topography). Similar to Figure 5.4, the figure shows snapshots of different timesteps for simulation Model 01 Type 1. The left column shows the slab shape, with colorscale representing the depth, and the right column shows the topography maps. The slab takes a very complex shape with the development of a new subduction system and the merging with the old one. The topographic amplitude generally decreases in time due to trench retreat. The rapid merging of subduction systems induces a short-lived high-amplitude topographic growth (at 49.6 Ma), lasting approximately 5 Ma.

indentor in simulations, instead of subducting, raising the question under which conditions continental material can subduct. Most probably, a non-linear rheology could provide a more efficient mechanism to weaken the subduction channel and facilitate subduction of continental material. As the result of this limitation, the shape of the collision front is rounded for all Types with an extension (2-4).

The double subduction in the western side of the domain is still active and stable with some migration of the triple junction in time. Comparing the eastern and western sides, it is clear that the double subduction system promotes more lateral extension of material in the upper plate than the single subduction system in the East.

The influence of continental collision on subduction dynamics can be best seen when looking at the slab shapes in Figure 5.6 (c,f,i,l). Simulations with no or little Greater India extension (Type 1, 2) show a much more complex structure of the slab, with multiple foldings of the slab in front of the continental indentor (red circular patterns). The comparison between the different types highlights how dramatic the continental collision through lateral extrusion affects trench retreat rates. The greater the extension, the earlier the continental collision occurs within the simulation. Thus, trench retreat is faster during continental collision due to the lateral extrusion of material away from the path of the continental indentor.

Figure 5.7 shows the evolution of the maximum topographic amplitude for all simulations of Model 01. Each coloured solid line shows the evolution for a different type of Greater India reconstruction. The grey dotted line at the bottom shows the influx convergence velocity. The coloured vertical dotted lines represent approximate times for onstart of continental collision and the colour is consistent with the simulation Type. The maximum amplitude highlights all the major stages of evolution and processes. The first 30-35 Ma show an almost identical evolution between simulations, which indicates a steady state oceanic subduction. Close to 40 Ma, however, influx velocities start increasing, and this is when the oceanic lithosphere starts buckling giving rise to a new subduction system. Then, around 50-55 Ma, the two subduction systems merge, with the newly-formed subduction being consumed into the old one. This is followed immediately by a rapid and considerable topographic jump. Finally, each simulation transitions to continental collision between 62-70 Ma. This coincides with the decrease in influx velocity, which was intended from the beginning to match the evolution of India. The topographic response to collision is immediate, with a high topographic front at the collision boundary. Further convergence of the indentor in the upper plate is followed by constant topographic build-up. These results are consistent with previous studies of evolution of topography in subduction/collision models (e.g., *François et al.* [2014]; *Magni et al.* [2014, 2012]; *Pusok and Kaus* [2015]). However, we do not obtain anomalously high topographic amplitudes similar to the Himalayas and Tibetan Plateau. This is due to the fact that the

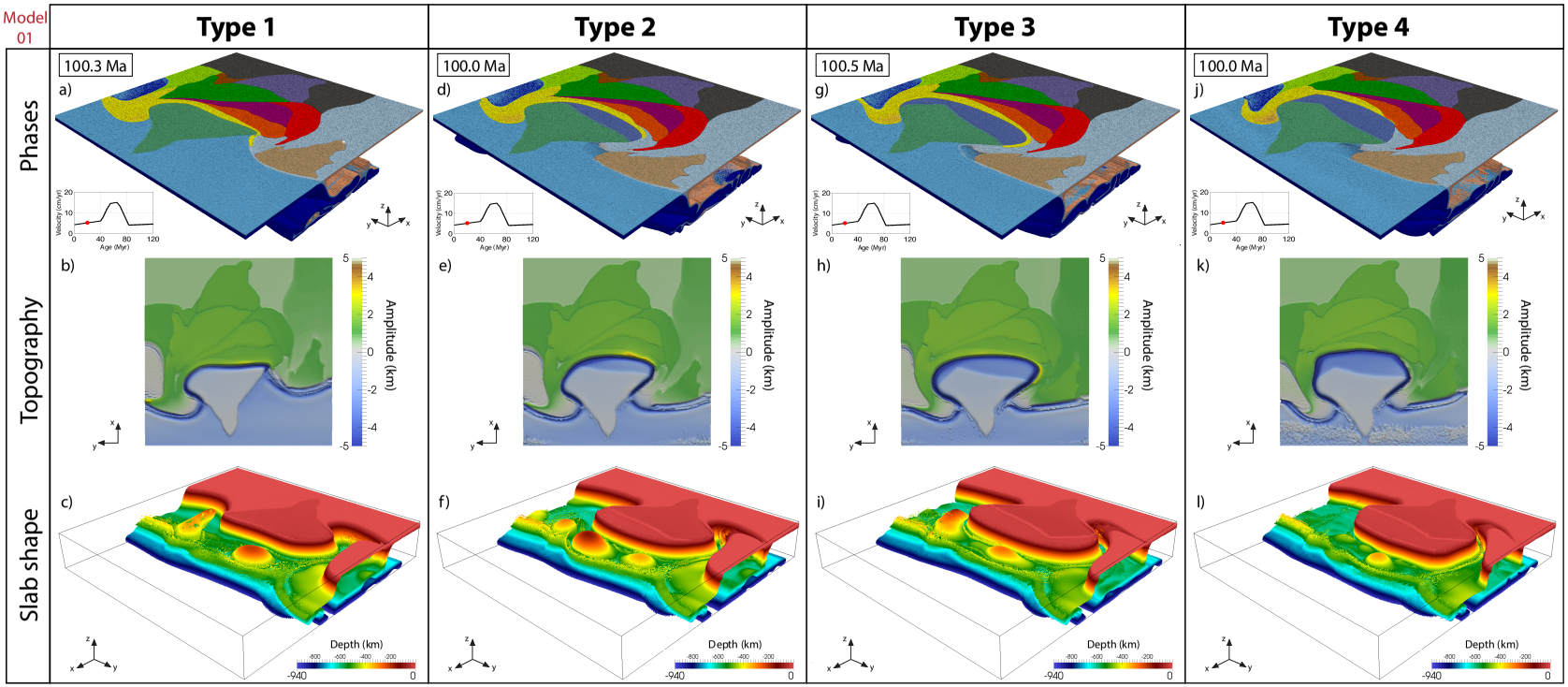

Fig. 5.6 Model 01 - Continental collision. Every column shows snapshots at 100 Ma after the start of simulation for each type of the Greater India reconstructions (as in Figure 5.2). The first row represents phases field, the second row represents topography maps, and the bottom row shows the respective slab shapes. The shape of Greater India influences the timing of continental collision and the relative importance of processes related to oceanic subduction (i.e., trench retreat) and continental collision (i.e., trench advance and lateral extrusion). Larger Greater India shapes (Types 3, 4) reach the subduction front at an earlier stage, thus indentation and continental subduction starts at a younger age, producing more lateral extrusion of material. On the other hand, smaller Greater India reconstructions (Type 1, 2) reached the subduction at a later stage. In this case, trench retreat was mainly dictated by the subduction of the oceanic lithosphere, and only later influenced by continental collision. The comparison between the different types highlights how dramatic the continental collision through lateral extrusion affects trench retreat rates. Trench lines have moved considerably more for Types 3 and 4 than for Types 1 and 2. Slab dynamics is also influenced by the size and shape of the indentor and the relative timing of continental collision.

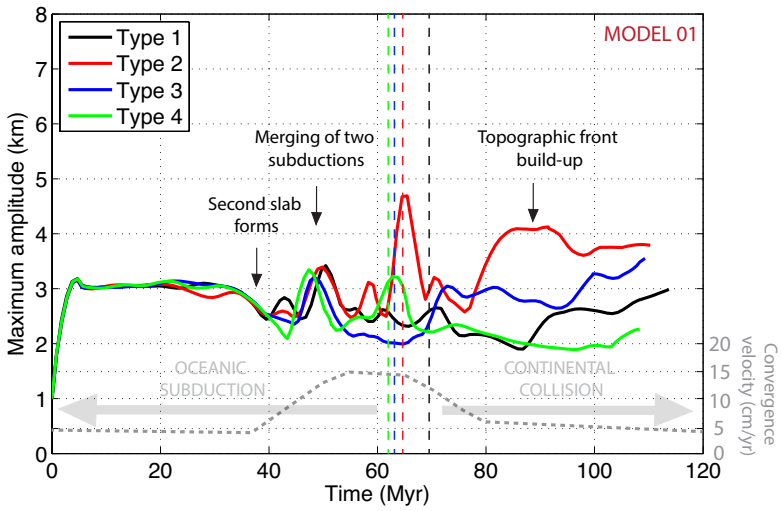

Fig. 5.7 Model 01 - Evolution of maximum topography in upper plate. Each coloured solid line shows the evolution for a different Type of Greater India reconstruction. The grey dotted line at the bottom shows the influx convergence velocities. The coloured vertical dotted lines represent approximate times for onstart of continental collision and colour is consistent with the simulation Type. The two major stages of evolution are clearly registered by the maximum topographic amplitude: oceanic subduction and continental collision. All simulations follow the same trajectory for oceanic subduction, but the shape of Greater India controls the timing and evolution of continental collision.

upper plate in the present study is weaker than the one in the simulations in *Pusok and Kaus* [2015], where amplitudes of more than 5 km high were obtained.

Moreover, there is no direct correlation between the topographic amplitude and the size of the Greater India extension. Type 1 and Type 4 (smallest and largest extension) produced lower topographic amplitudes than intermediate size extensions (Type 2 and 3). The fact that Type 2 produced the largest amplitudes suggests that the shape of the extension or the timing of collision might be more important than the extent of Greater India. Comparing the timing of collision of Type 2 and 3, which is very similar, indicates that the cause of higher amplitudes is the more convex or irregular shape of Type 2 compared to Type 3. Therefore, results show that the shape is more important than the size of the extension.

5.4.2 Model 02 - Failed double subduction

The second set of simulations highlights the importance of upper plate parameters and shows the feedback of the upper plate to the subduction system. Results of Model 01 indicate that differences in densities in the upper plate produces an irregular subduction front, which

controls further the evolution of the system. In this section, we test the effect of viscosity on the dynamics of subduction and collision. Model 02 set of simulations has on average five times lower viscosities in the upper plate crust (see Table 5.1). We display the results in the same consistent manner as for Model 01, shown before.

Evolution of oceanic subduction. Figure 5.8 shows the evolution of the oceanic subduction for Model 02 Type 2, though the evolution of this case is shared by all other simulations of Model02. The subduction front is much more uniform as compared to Model 01. This is because the upper plate is weaker and poses less resistance to subduction. Therefore, subduction is more efficient across its entire front, making the effect of density differences less important.

The increasing influx velocities also lead to the formation of a secondary slab (at 45.8 Ma), but the faster subduction rates on the original subduction front do not allow the incipient subduction to develop into a self-sustaining system. The new slab has a weak pull and as a result, will be absorbed in the old subduction system. By 60.4 Ma, the original subduction has consumed the incipient slab and has gained further momentum. The failed slab is seen as an irregularity within the original slab (Figure 5.8 at 60.4 Ma).

Figure 5.9 provides further insights, in which the slab shape and the topography maps are displayed. Deformation of the slab is much more uniform than for Model 01 in Figure 5.5 due to the fast subduction rates. The fast subduction rates are promoted by the weak resistance of the upper plate on subduction. When the incipient subduction approaches the trench at 50.3 Ma, short lived intra-oceanic subduction systems form locally where trench retreat rates are the lowest, but are soon absorbed in the original subduction system. Snapshots at 60.4 Ma shows that the increased slab-pull generated after the merging of two subduction systems induces very fast trench retreat rates.

Continental collision. The weaker influence of the upper plate in Model 02 is also observed for the continental collision stage (Figure 5.10). Compared to the results of Model 01, all simulations of Model 02 produce more lateral extrusion of upper plate material, thus lowering the average topographic amplitude in the upper plate. The absence of a double subduction means less extrusion of the Lhasa unit (yellow) on the Western side. Moreover, subduction of the Greater India extension is even more problematic for Model 02 as compared to Model 01 and acts more as an indentor. Slab deformation is also more similar across different Types than it was for the different cases in Model 01.

The impact on topography evolution can be seen in Figure 5.11. The oceanic subduction stage (0-40 Ma) is characterised by rapid trench rates and lowering of topographic amplitudes. From 40 Ma to 60 Ma, the increasing influx velocities also produce lithosphere buckling,

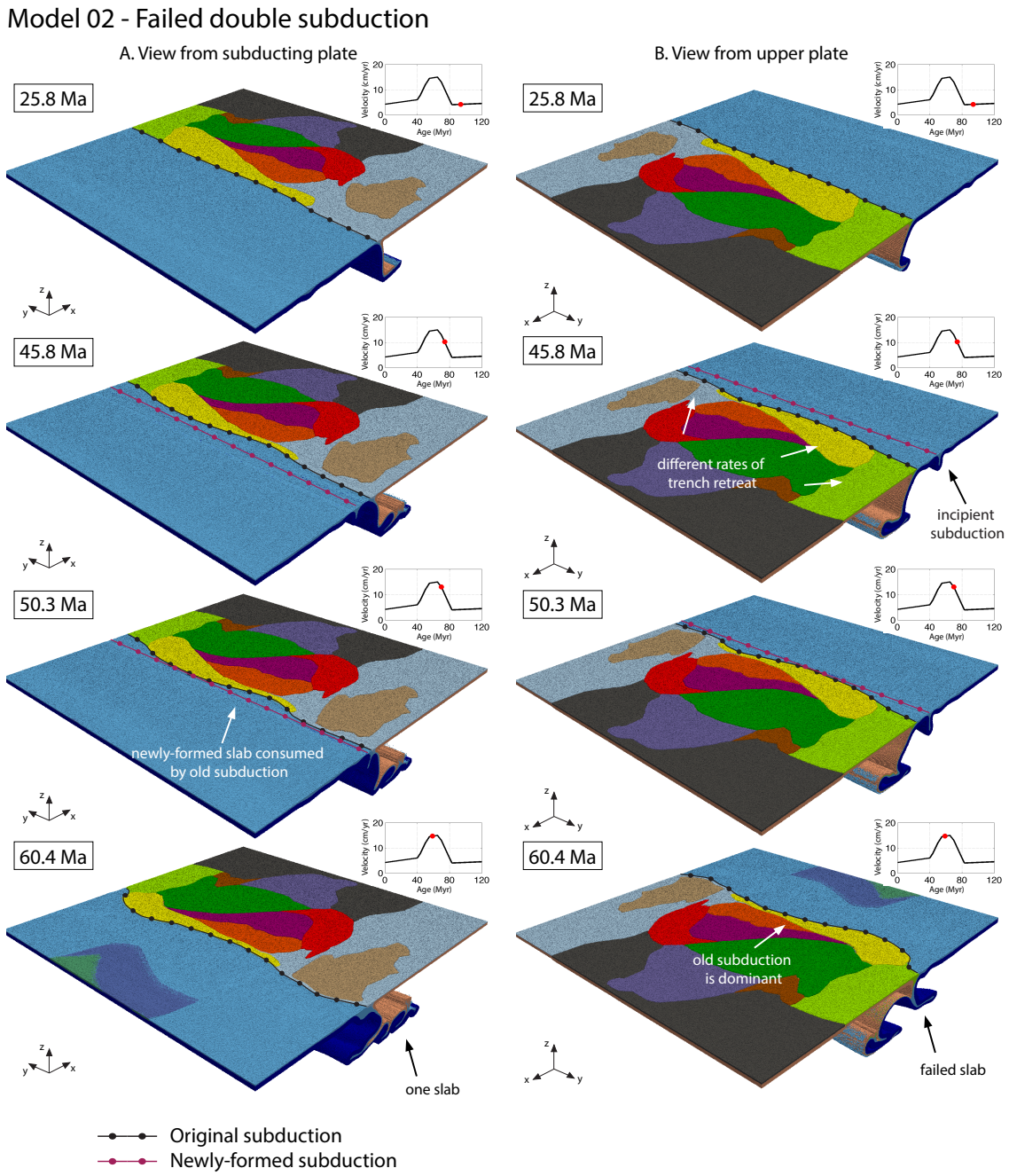

Fig. 5.8 Model 02 - Evolution of oceanic subduction (phases). Compared to Model 01, the upper plate's resistance to subduction is small. Therefore, faster trench retreat rates are possible across the entire subduction front. The result of this is a more uniform trench line. When a second subduction system forms, the original subduction is too vigorous and will absorb the new slab before it can be self-sustaining. For consistency, same viewing perspectives are displayed as in Figure 5.4. The figure shows snapshots of different timesteps for simulation Model 02 Type 2.

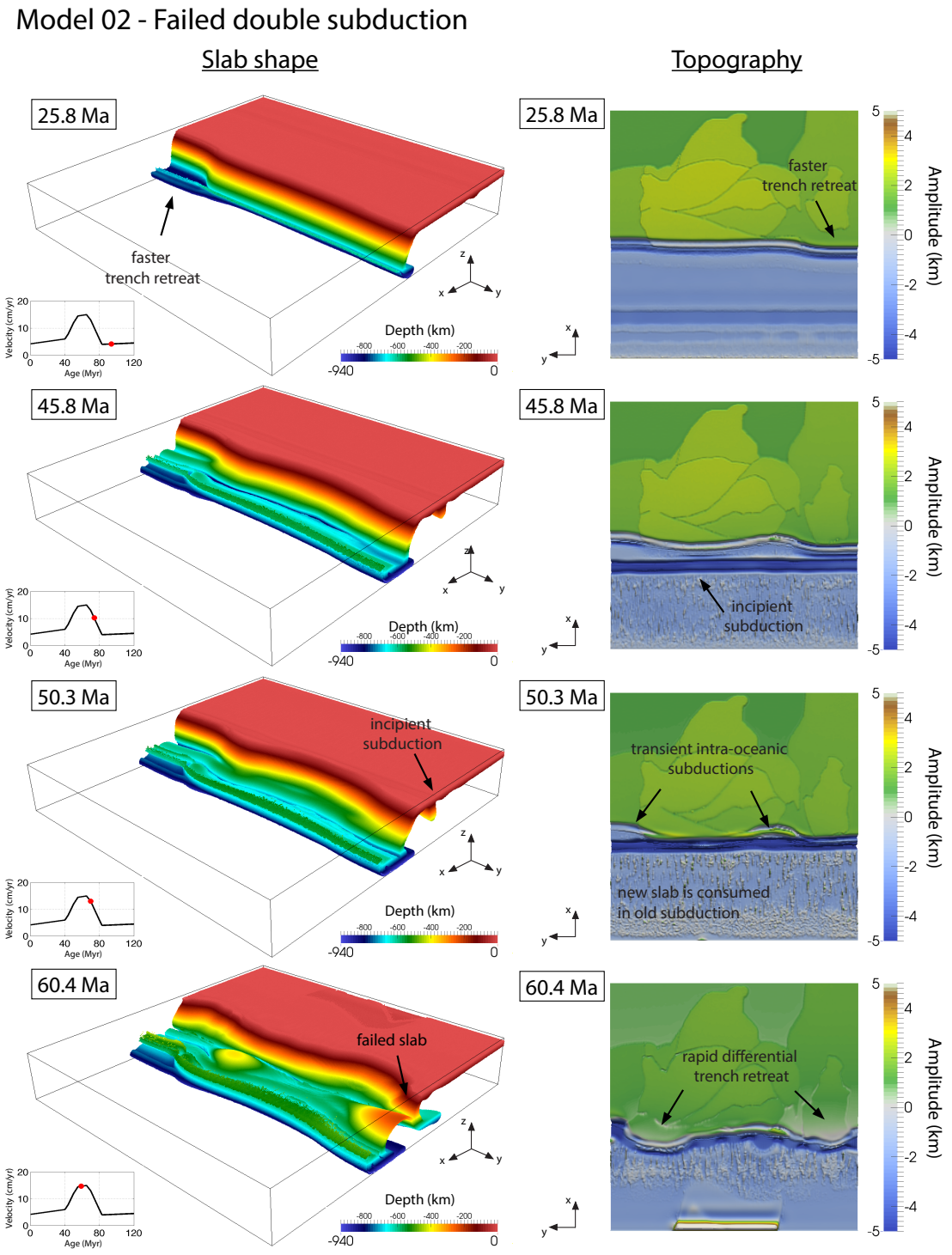

Fig. 5.9 Model 02 - Evolution of oceanic subduction (slab shape and topography). Same time evolution snapshots as Figure 5.8. The slab shape shows clearly how the newly-formed slab has not enough pull of its own and is absorbed in the old subduction. A transient intra-oceanic subduction systems form during the merging of two subductions. The consumed failed slab gives more negative pull to the original slab, producing faster trench retreat rates.

but they are not gaining momentum and are absorbed in the original subduction system. The topographic signature of these episodes is smaller compared to simulations Model 01.

However, the largest impact on topography is the easiness with which the upper plate deforms, which promotes the formation of a relatively high topographic front at the onstart of collision, reaching even 5 km high for Model 02 Type 2 (Figures 5.10 and 5.11). However, the low crustal viscosities cannot sustain the high amplitudes for too long, and lateral extrusion takes over, lowering the amplitudes after 85 Ma. The topographic fronts in Model 02 have a higher amplitude, but they are also short-lived compared to their analogous in Model 01.

5.5 Discussion

Previous geodynamical models of the convergence of India with Eurasia have covered less than 60 Ma of evolution [*Bajolet et al.*, 2013; *Capitanio and Replumaz*, 2013; *Li et al.*, 2013; *Pusok and Kaus*, 2015; *Replumaz et al.*, 2014; *Sternai et al.*, 2016]. We present here a new type of forward numerical simulations, in which we integrate plate convergence information for India-Eurasia for the last 120 Ma available from geophysical and geochemical studies (e.g., *Jagoutz et al.* [2015]). In general, plate velocities and motions are well constrained for a couple hundreds of million of years (e.g., GPlates-*Seton et al.* [2012]). We suggest that using this information in numerical models in order to test different evolution hypotheses for various tectonic regions could be a powerful new tool.

A major outcome of our numerical experiments is the spontaneous formation and evolution of a double subduction system. Studies of double subduction either introduce weak zones to initiate subduction [*Mishin et al.*, 2008] or both the subduction systems are already initiated [*Jagoutz et al.*, 2015]. Initiation of the second subduction system happens for two reasons in our models: (i) increasing influx velocity coupled with slow convergence rates at the original subduction site, and (ii) differential trench retreat rates in the upper plate which create an irregular subduction front. The timing of the development is also important, because a newly formed subduction needs to become mature, so that the new slab-pull can be strong enough to keep the system self-sustaining. This can be seen for the results in Model 01, but not for Model 02, where the incipient subduction and intra-oceanic subduction systems are only transient.

Jagoutz et al. [2015] proposed that rates of convergence across coupled double subduction systems are significantly faster than across single subduction systems because of slab pull by two slabs. This could explain the high convergence rate observed for the India-Eurasia convergence. In their model they propose a double subduction system running all the way across the Kshiroda Plate, which carries India northward, and is bounded by large transform

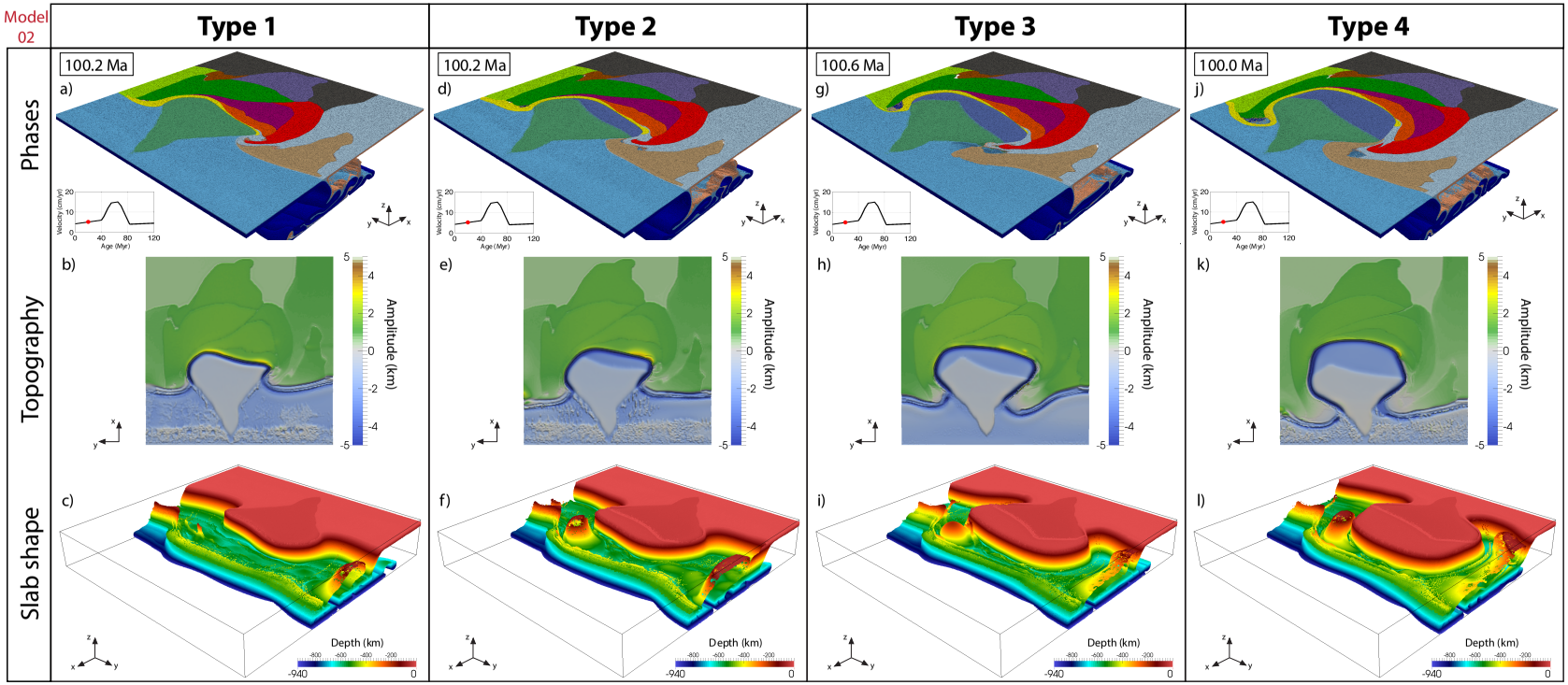

Fig. 5.10 Model 02 - Continental collision. Every column shows snapshots at 100 Ma after the start of simulation for each type of the Greater India reconstructions. The first row represents phases field, the second row represents topography maps, and the bottom row shows the respective slab shapes. Compared to results of Model 01, all simulations of Model 02 produce faster trench retreat rates both for the oceanic and continental subduction stages. Also the absence of a double subduction means less extrusion of the Lhasa block (yellow) on the Western side. Subduction of the Greater India extension is even harder for Model 02 as compared to Model 01 because the upper plate is weak and deforms easily. Slab shapes are also more similar across different Types than it was the case for Model 01.

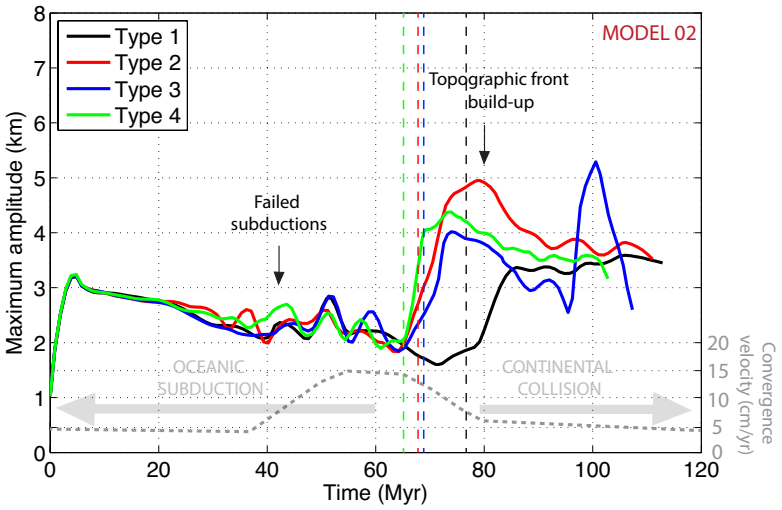

Fig. 5.11 Model 02 - Evolution of maximum topography in upper plate. Each coloured solid line shows the evolution for a different Type of Greater India reconstruction. The grey dotted line at the bottom shows the influx converge velocities and the coloured vertical dotted lines represent approximate times for onset of continental collision and colour is consistent with the simulation Type. The oceanic subduction stage (0-40 Ma) is characterized by rapid trench rates and lowering of topographic amplitudes. From 40 Ma to 60 Ma, the increasing influx velocities also produce lithosphere buckling, but they are not gaining momentum and are absorbed in the original subduction system. The topographic signature of these episodes is smaller compared to simulations Model 01. The greatest impact on topography is the onset of collision, which promotes the formation of a topographic front reaching even 5 km high for Model 02 Type 2. The initial jump in amplitudes immediately after the collision are on average 1 km higher than results for Model 01. However, the low crustal viscosities cannot sustain the high amplitudes for too long, and lateral extrusion takes over, lowering the amplitudes after 85 Ma.

faults. Their proposal is supported by increasing evidence of the presence of two relict slabs below India [*Replumaz et al.*, 2004; *Van der Voo et al.*, 1999]. This scenario is also consistent with our models because initially the incipient subduction forms across the entire domain, but then merges with the original subduction system to form a stable trench triple junction and a smaller intra-oceanic subduction system. However, a major assumption in our model is that the rapid increase in convergence velocity between 70-50 Ma ago is due to external factors (i.e., large scale mantle flow), while *Jagoutz et al.* [2015] explain the jump as the result of internal dynamics of double subduction. We agree that double subduction systems produce higher convergence velocities, but in *Jagoutz et al.* [2015] the presence of two subduction systems is an *a priori* assumption, while in our model the double subduction system is spontaneously generated.

In fact, the subduction initiation in our models is also an interesting outcome in itself. Subduction initiation has been a popular and challenging topic in the research community for the last few years, and different mechanisms (i.e., collapse at a passive margin or transform fault [*Gerya et al.*, 2008; *Stern*, 2004], driven by compression [*Hall et al.*, 2003; *Toth and Gurnis*, 1998], due to shear heating [*Thielmann and Kaus*, 2012] or plume induced initiation [*Gerya et al.*, 2015]) have been proposed. The initiation here might be considered crude (i.e., the oceanic plate buckles until it transforms into a subducting slab) in comparison with those studies, mainly because of the simple geometry and rheology of the oceanic plate. However, the idea that increasing plate velocities can initiate subduction is worth exploring in future models with more complex rheology. Moreover, we believe that heterogeneities in the lithosphere, such as mid-ocean ridges, age variations (and thus variations in strength), or transform faults, might facilitate subduction initiation.

It is estimated that at least 7000 km of subducted material in the Neo-Tethys now lies in the mantle beneath India-Asia and SE Asia. Tomographic studies show that indeed this is the case [*Replumaz et al.*, 2004; *Van der Voo et al.*, 1999], with large slab accumulations extending up to 1000 km deep. In our models, the slab sinks to the 660 km transition to the lower mantle and it starts piling up and sinking further until it reaches the lower boundary of the model (940 km). However, incorporating phase transformations in the numerical model could provide us with a better understanding of how such large slab accumulations interact with the mantle asthenosphere and lower mantle.

Another finding of the seismic tomography study of *Van der Voo et al.* [1999] was the presence of a high velocity anomaly (often called the IN anomaly) beneath the India-Tibet region, which was used to infer on the nature of the northern India. *Van der Voo et al.* [1999] and *Replumaz et al.* [2012, 2004] correlated this anomaly with subducted continental Indian lithosphere. They also suggested that the continent was sinking into the mantle almost

directly beneath the Yarlung Tsangpo suture zone in Tibet, where it had been dragged down with the oceanic lithosphere that was once attached to its northern passive margin prior to its consumption beneath Tibet. However, the interpretation of this anomaly is controversial, with the nature of the subducted lithosphere, whether oceanic or continental, being matter of debate. The other interpretation is that the IN anomaly corresponds to a slab of oceanic lithosphere (e.g., *Hafkenscheid et al.* [2006]; *Van der Voo et al.* [1999]; *van Hinsbergen et al.* [2012]; *Zahirovic et al.* [2012]), related to the subduction of the Spongtang oceanic back-arc basin, located between the Neo-Tethys and Eurasian continental margin [*Stampfli and Borel*, 2002].

The larger extensions of Greater India (Type 3-4) in our models subducted very little, definitely not until depths of 500-800 km as suggested by the IN anomaly, and acted more as indenters. This observation is not to discard one proposal or another, but to point out that subducting continental lithosphere to large depths is very difficult to reproduce in 3-D numerical models. Some authors proposed that if the crust is scrapped off the lithosphere and with continued convergence, the lithosphere can subduct deeper [*Capitanio et al.*, 2010]. This is a subject for further investigation as well. Understanding better under which circumstances continental lithosphere can be subducted can help constraining further the shape of Greater India. Type 2 of reconstructions is the preferred model within the community and it is also the one that produced higher amplitudes, suggesting that the shape or curvature of the extension is important. Maybe in future models of the India-Asia collision system this should be taken into account.

Although our models are complex enough to capture most of the first-order physical processes, they are still a simplification of reality. Probably the largest changes to the dynamics would be by using a more complex rheology in the model. This will be taken into account in future models since LaMEM is capable of solving for visco-elasto-plastic temperature-dependent rheology. These are preliminary models using the influx boundary conditions and shows that they are numerically stable for long time scales, even with sticky air approach, which usually introduces high viscosity contrasts that are not easy to solve numerically. Other aspects of our model to improve include the geometry and resolution. The model results have evolved until about 100 Ma, which means we have underestimated our initial configuration of India relative to Eurasia. Furthermore, the structure of the upper plate (based on 50 Ma reconstruction) might also be misleading, since we are trying to model forward in time a reconstruction from 120 Ma. The extent of geological units in the Eurasian plate might have looked completely different 120 Ma ago. The collision of Arabia with Eurasia in the West of the India-Asia collision zone should also be considered in models, as it is expected that it would limit lateral extrusion in that part.

5.6 Conclusion

In conclusion, two important aspects need to be considered in models reproducing the geological evolution of the India-Asia collision zone and the uplift of the Himalayas and Tibetan Plateau: the convergence profile of India northwards since the break-up from Gondwana (at least 120 Ma), and the shape of Greater India prior to collision in such way that fits reconstructions and deformation in present-day India-Asia collision. We are proposing here a new type of 3-D models that include this information. First, we classified existing Greater India proposals into categories based on the shape and size of the proposed extensions, and then we performed long term forward numerical simulations with each type of Greater India extension.

We distinguish between two stages of evolution in our models: oceanic subduction and continental collision. The first stage, oceanic subduction has revealed some interesting dynamics, resulting in the spontaneous formation and merging of a double subduction system. The way two subductions merged suggests that the merging depends mainly on the subduction velocities of the original subduction combined with the influx boundary condition velocities. Lateral heterogeneities in the upper plate (i.e., different geological units with different densities and viscosities) also affect subduction dynamics, by modifying trench velocities and producing irregular subduction trenches.

The second stage, continental collision, is mainly influenced by the size and shape of the Greater India extension. Larger sizes of Greater India (Types 3-4) collide with the upper plate at an earlier stage, such that the collision episode lasts longer. However, a longer collision stage also promotes more lateral extrusion of material, lowering the topographic amplitudes in the upper plate. Type 2 extension produced the largest maximum topographic amplitudes in the upper plate, suggesting that the shape is also crucial in focusing the deformation in the upper plate.

Even if crude at this stage, the evolution scenario presented here can be used to obtain a first-order reconstruction of the change in position and dynamics of the convergent India-Eurasia boundary. Finer resolution, a better understanding of time constants and deformation of Earth materials, and improvements in reconstructing surface deformation will be needed to constrain with greater accuracy both the onset of India's collision, the size of greater India, and possible irregularities in the subduction (i.e., break-off) of continental lithospheric mantle.

Chapter 6

Conclusions and perspectives

6.1 Thesis summary

In this thesis, numerical models were used to investigate: (i) how subduction and collision affect mountain-building processes and how large topographic plateaus can form in an integrated lithospheric and upper-mantle scale model, (ii) appropriate numerical and theoretical techniques for studying lithospheric deformation at convergent margins, and (iii) how the shape and convergence of Greater India affected the subsequent tectonic evolution of central and SE Asia. The main findings of previous research chapters are briefly summarized below.

- Chapter 2 evaluates the quality of velocity interpolation schemes for marker-in-cell method and 2-D and 3-D staggered grids. The results show that the choice of interpolation scheme can reduce numerical artefacts due to marker advection such as dispersion or clustering of markers. An empirical adaptation of the linear direct interpolation and the correction method, provided that the choice of interpolation method from the staggered points to grid nodes is appropriate (i.e., using a *minmod* limiter), give the best results. This study represents an important step forward in improving the numerical techniques used in geodynamics since the marker-in-cell technique is widely popular.

- Chapter 3 shows that anomalously high topography develops only under certain circumstances in models with linear viscous rheology. These circumstances can be predicted using the Argand number and an initial buoyancy ratio. The results also show that building topography is an interplay between providing the energy to the system and the ability of that system to store it over longer periods of time. Thus, the shape and elevation of mountain ranges can vary depending on the boundary conditions (i.e., external pushing and the presence of heterogenous crustal blocks) or internal factors (i.e., rheology of upper plate), but also on the evolution stage they are in.

- Chapter 4 goes a step further into our understanding of subduction/collision models, by investigating the effect of rheological approximations on the dynamics and topography. The results in this chapter show that a non-linear temperature dependent visco-elasto-plastic rheology produces considerable differences in dynamics compared to results employing various linear viscous approximations. For example, different styles of break-off, opening/no opening of back-arc basins or heterogenous/homogenous topographic distributions are obtained. Further effort will be needed to attain a quantitative analysis on the extent of these rheological approximations.

- Chapter 5 proposes a new type of models that takes into account the convergence profile of India northwards since the break-up from Gondwana (at least 120 Ma), and the shape of Greater India prior to collision in such way that fits reconstructions and deformation in present-day India-Asia collision. The results have revealed some interesting dynamics, with the spontaneous formation and merging of a double subduction system. The merging of the two subduction systems depends on the magnitude of the original subduction velocity relative to the influx velocity imposed by the boundary conditions. The evolution scenario presented here can be used to obtain a first-order reconstruction of the change in position and dynamics of the convergent India-Eurasia boundary.

6.2 Lessons and future challenges

Much work is needed before all questions raised in Chapter 1, Introduction, can be addressed and interpreted. The chapters of this thesis describe my research on subduction/collision dynamics, with a special focus on the India-Asia collision zone, that will be useful in reaching that long-term goal. With that in mind, the results in this thesis provide some important lessons and insights.

- Dynamic models (i.e., "free subduction" with no kinematic boundary conditions) are useful for studying generic processes such as understanding general subduction and collision dynamics (i.e., style of subduction, recipe to create high mountain belts, effect of rheology, etc.). However, these models will not be able to model the uplift of Himalaya-Tibet successfully because the effectiveness of slab-pull driving convergence is likely to be diminished by episodes of slab break-off. Results in Chapters 3 and 4 perfectly illustrate this for different geometries and rheologies.

- Tectonic specific models should then consider a full account of the forces and boundary conditions active in the respective tectonic setting. That is because the theory of plate

tectonics describes a complex system of interlinked plates that are also part of the thermal cycle, and at any point in time, the plates influence each other. For example, Chapter 3 demonstrates that high convergence rates and the presence of crustal blocks (such as the Tarim Basin in the north of the Tibetan Plateau) are needed to obtain topographic amplitudes comparable to the ones observed in the India-Asia collision. Furthermore, Chapter 5 suggests that taking into account the convergence history of India could provide us with new insights into the evolution of the collision zone.

Both types of models, generic and tectonic specific models, are important for our understanding of how the planet works. For example, to construct better models of India-Asia collision zone requires reconstruction of changing patterns of deformation and uplift across a wide range of temporal and spatial scales. In particular, we need to understand the factors sustaining the convergence of India over time, how rheology affects subduction and collision, and then take into account the present-day geology and geological history of both Indian and Eurasian plates. Most likely, exciting new results will be obtained.

- The effect of rheology on the dynamics of tectonic systems remains one of the most challenging topics in earth sciences. An integrated effort of modelling, field work and laboratory experiments to understand the effect of rheology will be needed for both generic and tectonic specific studies. Although recent geological and geophysical studies had improved our data resolution, lack of complete data sets and observed complexity still prevents us from discriminating among the different models for the uplift of the Tibetan Plateau.

- In terms of modelling, future 3-D models of lithosphere deformation need to include: fast calculations of time-dependent governing and constitutive equations, of accurate compositional fields, high resolution capabilities, fast and stable non-linear solvers, water and melt migration, stable plastic behaviour, etc. Such a model will be a significant challenge to construct as well as to interpret. Thus, a clear understanding of complex models with non-linear physics will also require techniques of analysis able to handle such non-linearities.

  Before it is even feasible, many smaller research problems must be solved to develop and understand the petrological, geodynamical and computational infrastructure required. In this respect, I believe the use of 2-D and 3-D models should be complementary for developing a solid theoretical understanding of various processes (i.e., multi-phase physics) and good numerical practices. Developments reported in this thesis are a step in the construction of such models.

References

Acton, G. D. (1999). Apparent Polar Wander of India since the Cretaceous with implications for regional tectonics and True Polar Wander. *Memoir Geological Society of India*, (44):129–175.

Agrusta, R., van Hunen, J., and Goes, S. (2014). The effect of metastable pyroxene on the slab dynamics. *Geophys. Res. Lett.*, 41(24):8800–8808.

Aitchison, J. C. and Davis, A. M. (2004). Evidence for the multiphase nature of the India-Asia collision from the Yarlung Tsangpo suture zone, Tibet. *Geological Society, London, Special Publications*, 226(1):217–233.

Ali, J. R. and Aitchison, J. C. (2004). Problem of positioning Paleogene Eurasia: A review. Efforts to resolve the issue. Implications for the India-Asia collision. In *Continent-Ocean Interactions Within East Asian Marginal Seas*, pages 23–35. American Geophysical Union, Washington, D. C.

Ali, J. R. and Aitchison, J. C. (2005). Greater India. *Earth Science Reviews*, 72(3-4):169–188.

Allegre, C. J., Courtillot, V., Tapponnier, P., Hirn, A., Mattauer, M., Coulon, C., Jaeger, J. J., Achache, J., Scharer, U., Marcoux, J., Burg, J. P., Girardeau, J., Armijo, R., Gariepy, C., Gopel, C., Tindong, L., Xuchang, X., Chenfa, C., Guangqin, L., Baoyu, L., Teng, J., Naiwen, W., Guoming, C., Tonglin, H., Xibin, W., Wanming, D., Huaibin, S., Yougong, C., Ji, Z., Hongrong, Q., Peisheng, B., Songchan, W., Bixiang, W., Yaoxiu, Z., and Xu, R. (1984). Structure and Evolution of the Himalaya-Tibet Orogenic Belt. *Nature*, 307:17–22.

Amante, C. and Eakins, B. W. (2009). ETOPO1 1 Arc-Minute Global Relief Model: Procedures, Data Sources and Analysis. Technical Report NESDIS NGDC-24, National Geophysical Data Center, NOAA.

Argand, E. (1924). La tectonique de l'Asie. *Proc. 13th Int. Geol. Cong.*, 7:171–372.

Bajolet, F., Replumaz, A., and Lainé, R. (2013). Orocline and syntaxes formation during subduction and collision. *Tectonics*, 32(1-2):1529–1546.

Balay, S., Abhyankar, S., Adams, M. F., Brown, J., Brune, P., Buschelman, K., Eijkhout, V., Gropp, W. D., Kaushik, D., Knepley, M., Curfman McInnes, L., Rupp, K., Smith, B. F., and Zhang, H. (2014). PETSc Users Manual. Technical Report ANL-95/11-Revision 3.5, Argonne National Laboratory.

Bao, X., Eaton, D. W., and Guest, B. (2015). Plateau uplift in western Canada caused by lithospheric delamination along a craton edge. *Nature Geoscience*, 7:830–833.

Barazangi, M. and Ni, J. (1982). Velocities and propagation characteristics of Pn and Sn beneath the Himalayan arc and Tibetan plateau: Possible evidence for underthrusting of Indian continental lithosphere beneath Tibet. *Geology*, 10(4):179.

Barnes, J. B. and Ehlers, T. A. (2009). End member models for Andean Plateau uplift. *Earth Science Reviews*, 97:105–132.

Beaumont, C., Jamieson, R. A., Nguyen, M. H., and Lee, B. (2001). Himalayan Tectonics Explained by Extrusion of a Low-Viscosity Crustal Channel Coupled to Focused Surface Denudation. *Nature*, 414:738–742.

Beaumont, C., Jamieson, R. A., Nguyen, M. H., and Medvedev, S. (2004). Crustal channel flows: 1. Numerical models with applications to the tectonics of the Himalayan-Tibetan orogen. *Journal of Geophysical Research*, 109(B6):1–29.

Becker, T. W. and Faccenna, C. (2011). Mantle conveyor beneath the Tethyan collisional belt. *Earth and Planetary Science Letters*, 310(3-4):453–461.

Becker, T. W., O'Connell, R. J., and Faccenna, C. (1999). The development of slabs in the upper mantle- Insights from numerical and laboratory experiments. *Journal of Geophysical Research*, 104:15207–15226.

Bellahsen, N., Faccenna, C., and Funiciello, F. (2005). Dynamics of subduction and plate motion in laboratory experiments: Insights into the "plate tectonics" behavior of the Earth. *Journal of Geophysical Research: Solid Earth*, 110(B1).

Besse, J. and Courtillot, V. (1988). Paleogeographic maps of the continents bordering the Indian Ocean since the Early Jurassic. *Journal of Geophysical Research*, 93(B10):1791–1808.

Bilham, R., Larson, K. M., Freymueller, J. T., and Idylhim, P. (1997). GPS measurements of present-day convergence across the Nepal Himalaya. *Nature*, 386:61–64.

Bouilhol, P., Jagoutz, O., Hanchar, J. M., and Dudas, F. O. (2013). Dating the India-Eurasia Collision Through Arc Magmatic Records. *Earth and Planetary Science Letters*, 366(C):163–175.

Buck, W. R. and Sokoutis, D. (1994). Analogue model of gravitational collapse and surface extension during continental convergence. *Nature*, 369(6483):737–740.

Burg, J. P. and Chen, G. M. (1984). Tectonics and Structural Zonation of Southern Tibet, China. *Nature*, 311:219–223.

Burg, J. P., Davy, P., and Martinod, J. (1994). Shortening of Analogue Models of the Continental Lithosphere: New Hypothesis for the Formation of the Tibetan Plateau. *Tectonics*, 13:475–483.

Burov, E. B. and Watts, A. B. (2006). The long-term strength of continental lithosphere: "jelly sandwich" or "crème brûlée"? *GSA Today*, 16(1):4.

Cande, S. C., Patriat, P., and Dyment, J. (2010). Motion between the Indian, Antarctic and African plates in the early Cenozoic. *Geophysical Journal International*, 183(1):127–149.

Cande, S. C. and Stegman, D. R. (2011). Indian and African plate motions driven by the push force of the Reunion plume head. *Nature*, 475(7354):47–52.

Capitanio, F. A., Faccenna, C., Zlotnik, S., and Stegman, D. R. (2011). Subduction dynamics and the origin of Andean orogeny and the Bolivian orocline. *Nature*, 480(7375):83–86.

Capitanio, F. A. and Morra, G. (2012). The bending mechanics in a dynamic subduction system: Constraints from numerical modelling and global compilation analysis. *Tectonophysics*, 522-523:224–234.

Capitanio, F. A., Morra, G., and Goes, S. (2009). Dynamics of plate bending at the trench and slab-plate coupling. *Geochemistry, Geophysics, Geosystems*, 10(4).

Capitanio, F. A., Morra, G., Goes, S., Weinberg, R. F., and Moresi, L. (2010). India–Asia convergence driven by the subduction of the Greater Indian continent. *Nature Geoscience*, 3(2):136–139.

Capitanio, F. A. and Replumaz, A. (2013). Subduction and slab breakoff controls on Asian Indentation tectonics and Himalayan Western Syntaxis formation. *Geochemistry, Geophysics, Geosystems*, 14:3515–3531.

Carter, N. L. and Tsenn, M. C. (1987). Flow Properties Of Continental Lithosphere. *Tectonophysics*, 136:27–63.

Chemenda, A. I., Burg, J.-P., and Mattauer, M. (2000). Evolutionary model of the Himalaya-Tibet system: geopoem based on new modelling, geological and geophysical data. *Earth and Planetary Science Letters*, 174:397–409.

Clark, M. K., Bush, J. W. M., and Royden, L. H. (2005). Dynamic topography produced by lower crustal flow against rheological strength heterogeneities bordering the Tibetan Plateau. *Geophysical Journal International*, 162(2):575–590.

Clark, M. K. and Royden, L. H. (2000). Topographic ooze: Building the eastern margin of Tibet by lower crustal flow. *Geology*, 28(8):703–706.

Conrad, C. P. and Hager, B. H. (1999). Effects of plate bending and fault strength at subduction zones on plate dynamics. *Journal of Geophysical Research: Solid Earth*, 104(B8):17551–17571.

Conrad, C. P. and Lithgow-Bertelloni, C. (2004). The temporal evolution of plate driving forces: Importance of "slab suction" versus "slab pull" during the Cenozoic. *Journal of Geophysical Research*, 109(B10407).

Cook, K. L. and Royden, L. H. (2008). The role of crustal strength variations in shaping orogenic plateaus, with application to Tibet. *Journal of Geophysical Research*, 113(B8):B08407.

Copley, A., Avouac, J.-P., and Royer, J.-Y. (2010). India-Asia collision and the Cenozoic slowdown of the Indian plate: Implications for the forces driving plate motions. *Journal of Geophysical Research*, 115(B3):B03410.

Copley, A. and McKenzie, D. (2007). Models of crustal flow in the India-Asia collision zone. *Geophysical Journal International*, 169(2):683–698.

Crameri, F. and Kaus, B. J. P. (2010). Parameters that control lithospheric-scale thermal localization on terrestrial planets. *Geophysical Research Letters*, 37:1–6.

Crameri, F., Schmeling, H., Golabek, G., Duretz, T., Orendt, R., Buiter, S., May, D., Kaus, B., Gerya, T., and Tackley, P. (2012). A comparison of numerical surface topography calculations in geodynamic modelling: an evaluation of the 'sticky air' method. *Geophys. J. Int.*, 189(1):38–54.

Crawford, A. R. (1974). A Greater Gondwanaland. *Science*, 184(4142):1179–1181.

DeCelles, P. G., Robinson, D. M., and Zandt, G. (2002). Implications of shortening in the Himalayan fold-thrust belt for uplift of the Tibetan Plateau. *Tectonics*, 21(6):12–1–12–25.

Dewey, J. F. and Bird, J. M. (1970). Mountain belts and the new global tectonics. *Journal of Geophysical Research*, 75(14):2625–2647.

Dewey, J. F. and Burke, K. (1973). Tibetan, Variscan, and Precambrian Basement Reactivation: Products of Continental Collision. *The Journal of Geology*, 81(6):683–692.

Dewey, J. F., Cande, S., and Pitman, W. C. (1989). Tectonic evolution of the India/Eurasia collision zone. *Eclogae Geologicae Helvetiae*, 82(3):717–734.

Di Giuseppe, E., van Hunen, J., Funiciello, F., Faccenna, C., and Giardini, D. (2008). Slab stiffness control of trench motion: Insights from numerical models. *Geochemistry, Geophysics, Geosystems*, 9(2).

Ding, L., Kapp, P., and Wan, X. (2005). Paleocene–Eocene record of ophiolite obduction and initial India-Asia collision, south central Tibet. *Tectonics*, 24(TC3001).

Ding, L., Xu, Q., Yue, Y., Wang, H., Cai, F., and Li, S. (2014). The Andean-type Gangdese Mountains: Paleoelevation record from the Paleocene–Eocene Linzhou Basin. *Earth and Planetary Science Letters*, 392:250–264.

Duretz, T., Gerya, T. V., and May, D. A. (2011a). Numerical modelling of spontaneous slab breakoff and subsequent topographic response. *Tectonophysics*, 502:244–256.

Duretz, T., Gerya, T. V., and Spakman, W. (2014). Slab detachment in laterally varying subduction zones: 3-D numerical modeling. *Geophysical Research Letters*, 41.

Duretz, T., May, D., Gerya, T., and Tackley, P. (2011b). Discretization errors and free surface stabilization in the finite difference and marker-in-cell method for applied geodynamics: A numerical study. *Geochem., Geophys., Geosyst.*, 12(7):1–26.

Ellouz-Zimmermann, N., Lallemant, S. J., Castilla, R., Mouchot, N., Leturmy, P., Battani, A., Buret, C., Cherel, L., Desaubliaux, G., Deville, E., Ferrand, J., Lügcke, A., Mahieux, G., Mascle, G., Mühr, P., Pierson-Wickmann, A. C., Robion, P., Schmitz, J., Danish, M., Hasany, S., Shahzad, A., and Tabreez, A. (2007). Offshore Frontal Part of the Makran Accretionary Prism: The Chamak Survey (Pakistan). In *Thrust belts and foreland basins*, pages 351–366. Springer Berlin Heidelberg, Berlin, Heidelberg.

Elsasser, W. M. (1971). Sea-floor spreading as thermal convection. *Journal of Geophysical Research: Solid Earth*, 76(5):1101–1112.

England, P. and Houseman, G. A. (1985). Role of Lithospheric Stregth Heterogeneities in the Tectonics of Tibet and Neighbouring Regions. *Nature*, 315:297–301.

England, P. and Houseman, G. A. (1986). Finite Strain Calculations of Continental Deformation 2. Comparison with the India-Asia Collision Zone. *Journal of Geophysical Research*, 91(B3):3664–3676.

England, P. and Houseman, G. A. (1989). Extension During Continental Convergence, with Application to the Tibetan Plateau. *Journal of Geophysical Research*, 94(B12):17561–17579.

England, P. and McKenzie, D. (1982). A Thin Viscous Sheet Model for Continental Deformation. *Geophys. J. R. astr. Soc.*, 70:295–321.

England, P. C., Houseman, G. A., Osmaston, M. F., and Ghosh, S. (1988). The Mechanics of the Tibetan Plateau [and Discussion]. *Philosophical Transactions of the Royal Society A: Mathematical, Physical and Engineering Sciences*, 326(1589):301–320.

Enns, A., Becker, T. W., and Schmeling, H. (2005). The dynamics of subduction and trench migration for viscosity stratification. *Geophysical Journal International*, 160(2):761–775.

Faccenna, C., Becker, T. W., Conrad, C. P., and Husson, L. (2013). Mountain building and mantle dynamics. *Tectonics*, 32(1):80–93.

Faccenna, C., Heuret, A., Funiciello, F., Lallemand, S., and Becker, T. W. (2007). Predicting trench and plate motion from the dynamics of a strong slab. *Earth and Planetary Science Letters*, 257(1-2):29–36.

Fernandez, N. and Kaus, B. J. P. (2014). Fold interaction and wavelength selection in 3D models of multilayer detachment folding. *Tectonophysics*, 632:199–217.

Fielding, E. J. (1996). Tibet Uplift and Erosion. *Tectonophysics*, 260:55–84.

Fornberg, B. (1995). *A practical guide to pseudospectral methods*. Cambridge Monographs on Applied and Computational Mathematics. Cambridge University Press.

Forsyth, D. and Uyeda, S. (1975). On the Relative Importance of the Driving Forces of Plate Motion. *Geophysical Journal International*, 43(1):163–200.

François, T., Burov, E., and Agard, P. (2014). Buildup of a dynamically supported orogenic plateau: Numerical modeling of the Zagros/Central Iran case study. *Geochemistry, Geophysics, Geosystems*, 15:2632–2654.

Funiciello, F., Faccenna, C., Heuret, A., Lallemand, S., Di Giuseppe, E., and Becker, T. W. (2008). Trench migration, net rotation and slab–mantle coupling. *Earth and Planetary Science Letters*, 271(1-4):233–240.

Funiciello, F., Moroni, M., Piromallo, C., Faccenna, C., Cenedese, A., and Bui, H. A. (2006). Mapping mantle flow during retreating subduction: Laboratory models analyzed by feature tracking. *Journal of Geophysical Research: Solid Earth*, 111(B3).

Funiciello, F., Morra, G., Regenauer-Lieb, K., and Giardini, D. (2003). Dynamics of retreating slabs: 1. Insights from two-dimensional numerical experiments. *Journal of Geophysical Research: Solid Earth*, 108(B4).

Gaina, C., Müller, D. R., Royer, J.-Y., Stock, J., Hardebeck, J., and Symonds, P. (1998). The tectonic history of the Tasman Sea: A puzzle with 13 pieces. *Journal of Geophysical Research: Solid Earth*, 103(B6):12413–12433.

Gan, W., Zhang, P., Shen, Z.-K., Niu, Z., Wang, M., Wan, Y., Zhou, D., and Cheng, J. (2007). Present-day crustal motion within the Tibetan Plateau inferred from GPS measurements. *Journal of Geophysical Research*, 112(B8):B08416.

Garzanti, E. (1993). Himalayan ironstones, “superplumes," and the breakup of Gondwana. *Geology*, 21(2):105.

Garzione, C. N., Quade, J., DeCelles, P. G., and English, N. B. (2000). Predicting paleoelevation of Tibet and the Himalaya from δ18O vs. altitude gradients in meteoric water across the Nepal Himalaya. *Earth and Planetary Science Letters*, 183(1-2):215–229.

Gerya, T. (2010). *Introduction to Numerical Geodynamic Modelling*. Cambridge University Press.

Gerya, T., Stern, R., Baes, M., Sobolev, S., and Whattam, S. (2015). Plume-induced subduction initiation: dynamics and significance for modern and early Earth.

Gerya, T. and Yuen, D. (2003). Characteristics-based marker-in-cell method with conservative finite-differences schemes for modeling geological flows with strongly variable transport properties. *Phys. Earth Planet. Inter.*, 140:293–318.

Gerya, T. V., Connolly, J. A. D., and Yuen, D. A. (2008). Why is terrestrial subduction one-sided? *Geology*, 36(1):43.

Ghosh, A., Holt, W. E., Flesch, L. M., and Haines, A. J. (2006). Gravitational potential energy of the Tibetan Plateau and the forces driving the Indian plate. *Geology*, 34(5):321–324.

Gibbons, A. D., Barckhausen, U., van den Bogaard, P., Hoernle, K., Werner, R., Whittaker, J., and Müller, R. D. (2012). Constraining the Jurassic extent of Greater India: Tectonic evolution of the West Australian margin . *Geochemistry, Geophysics, Geosystems*, 13.

Gnos, E., Immenhauser, A., and Peters, T. J. (1997). Late Cretaceous/early Tertiary convergence between the Indian and Arabian plates recorded in ophiolites and related sediments. *Tectonophysics*, 271(1–2):1–19.

Hafkenscheid, E., Wortel, M. J. R., and Spakman, W. (2006). Subduction history of the Tethyan region derived from seismic tomography and tectonic reconstructions. *Journal of Geophysical Research*, 111(B8):B08401.

Hall, C. E., Gurnis, M., Sdrolias, M., and Lavier, L. L. (2003). Catastrophic initiation of subduction following forced convergence across fracture zones. *Earth Planet. Sci. Lett.*, 212:15–30.

Hall, R. (2002). Cenozoic geological and plate tectonic evolution of SE Asia and the SW Pacific: computer-based reconstructions, model and animations. *Cenozoic geological and plate tectonic evolution of SE Asia and the SW Pacific: Computer-based reconstructions, model and animations*, 20(4):353–431.

Harlow, F. and Welch, J. (1965). Numerical Calculation of Time-Dependent Viscous Incompressible Flow of Fluid with Free Surface. *The Physics of Fluids*, 8(2):2182–2189.

Harrison, T. M., Copeland, P., Kidd, W. S. F., and Yin, A. (1992). Raising Tibet. *Science*, 255(5052):1663–1670.

Hatzfeld, D. and Molnar, P. (2010). Comparisons of the Kinematics and Deep Structures of the Zagros and Himalaya and of the Iranian and Tibetan Plateaus and Geodynamic Implications . *Reviews of Geophysics*, 48.

Hirth, G. and Kohlstedt, D. (2003). Rheology of the upper mantle and the mantle wedge: A view from the experimentalists. volume 138, pages 83–105. American Geophysical Union, Washington, D. C.

Hoke, G. D., Liu-Zeng, J., Hren, M. T., Wissink, G. K., and Garzione, C. N. (2014). Stable isotopes reveal high southeast Tibetan Plateau margin since the Paleogene. *Earth and Planetary Science Letters*, 394:270–278.

Holmes, A. (1965). *Principles of Physical Geology*. The Ronald Press Company, New York, second edition edition.

Houseman, G. A. and England, P. (1986). Finite Strain Calculations of Continental Deformation 1. Method and General Results for Convergent Zones. *Journal of Geophysical Research*, 91(B3):3651–3663.

Houseman, G. A., McKenzie, D. P., and Molnar, P. (1981). Convective instability of a thickened boundary layer and its relevance for the thermal evolution of continental convergent belts. *Journal of Geophysical Research*, 86(B7):6115–6132.

Huismans, R. S., Podladchikov, Y. Y., and Cloetingh, S. (2001). Transition from passive to active rifting: Relative importance of asthenospheric doming and passive extension of the lithosphere. *Journal of Geophysical Research: Solid Earth*, 106(B6):11271–11291.

Jackson, J. (2002). Strength of the Continental Lithosphere: Time to Abandon the Jelly Sandwich? *GSA Today*, pages 4–9.

Jacoby, W. R. (1973). Model Experiment of Plate Movements. *Nature Physical Science*, 242(122):130–134.

Jacoby, W. R. (1976). Paraffin model experiment of plate tectonics. *Tectonophysics*, 35(1-3):103–113.

Jagoutz, O., Royden, L., Holt, A. F., and Becker, T. W. (2015). Anomalously fast convergence of India and Eurasia caused by double subduction. *Nature Geoscience*, 8(6):475–478.

Jenny, P., Pope, S., Muradoglu, M., and Caughey, D. (2001). A Hybrid Algorithm for the Joint PDF Equation of Turbulent Reactive Flows. *J. Comp. Phys.*, 166:218–252.

Jiang, M., Zhou, S., Sandvol, E., Chen, X., Liang, X., Chen, Y. J., and Fan, W. (2011). 3-D lithospheric structure beneath southern Tibet from Rayleigh-wave tomography with a 2-D seismic array. *Geophysical Journal International*, 185(2):593–608.

Kameyama, M., Yuen, D. A., and Karato, S. I. (1999). Thermal-mechanical effects of low-temperature plasticity (the Peierls mechanism) on the deformation of a viscoelastic shear zone. *Earth and Planetary Science Letters*.

Kaus, B., Mühlhaus, H., and May, D. (2010). A Stabilization Algorithm for Geodynamic Numerical Simulations with a Free Surface. *Phys. Earth Planet. Inter.*, 181:12–20.

Kaus, B., Popov, A., Baumann, T., Pusok, A., Bauville, A., Fernandez, N., and Collignon, M. (2016). Forward and inverse modeling of lithospheric deformation on geological timescales. *NIC Symposium 2016 - Proceedings*, 48:1–8.

Kaus, B. J. P. (2010). Factors that control the angle of shear bands in geodynamic numerical models of brittle deformation. *Tectonophysics*, 484(1-4):36–47.

Kincaid, C. and Olson, P. (1987). An experimental study of subduction and slab migration. *Journal of Geophysical Research: Solid Earth*, 92(B13):13832–13840.

Klemperer, S. L. (2006). Crustal Flow in Tibet: Geophysical Evidence for the Physical State of Tibetan Lithosphere, and Inferred Patterns of Active Flow. *Geological Society, London, Special Publications*, 268:39–70.

Klootwijk, C. T., Gee, J. S., Peirce, J. W., Smith, G. M., and McFadden, P. L. (1992). An early India-Asia contact: Paleomagnetic constraints from Ninetyeast Ridge, ODP Leg 121. *Geology*, 20(5):395.

Kosarev, G. (1999). Seismic Evidence for a Detached Indian Lithospheric Mantle Beneath Tibet. *Science*, 283(5406):1306–1309.

Kukowski, N., Schillhorn, T., Huhn, K., von Rad, U., Husen, S., and Flueh, E. R. (2001). Morphotectonics and mechanics of the central Makran accretionary wedge off Pakistan. *Marine Geology*, 173:1–19.

Lamb, S. and Hoke, L. (2007). Origin of the high plateau in the central Andes, Bolivia, South America. *Tectonics*, 16(4):623–649.

Lawver, L. A. and Gahagan, L. M. (2003). Evolution of Cenozoic seaways in the circum-Antarctic region. *Palaeogeography, Palaeoclimatology, Palaeoecology*, 198(1–2):11–37.

Le Pichon, X., Fournier, M., and Jolivet, L. (1992). Kinematics, topography, shortening, and extrusion in the India-Eurasia collision. *Tectonics*, 11(6):1085–1098.

Le Pourhiet, L., Gurnis, M., and Saleeby, J. (2006). Mantle instability beneath the Sierra Nevada Mountains in California and Death Valley extension. *Earth and Planetary Science Letters*, 251(1-2):104–119.

Lechmann, S. M., May, D. A., Kaus, B. J. P., and Schmalholz, S. M. (2011). Comparing thin-sheet models with 3-D multilayer models for continental collision. *Geophysical Journal International*, 187(1):10–33.

Lee, T.-Y. and Lawver, L. A. (1995). Cenozoic plate reconstruction of Southeast Asia. *Tectonophysics*, 251(1-4):85–138.

Li, C., van der Hilst, R. D., Meltzer, A. S., and Engdahl, E. R. (2008). Subduction of the Indian lithosphere beneath the Tibetan Plateau and Burma. *Earth and Planetary Science Letters*, 274(1-2):157–168.

Li, Z.-H. and Ribe, N. M. (2012). Dynamics of free subduction from 3-D boundary element modeling. *Journal of Geophysical Research*, 117(B6):B06408.

Li, Z.-H., Xu, Z., Gerya, T., and Burg, J.-P. (2013). Collision of continental corner from 3-D numerical modeling. *Earth and Planetary Science Letters*, 380(C):98–111.

Liang, S., Gan, W., Shen, C., Xiao, G., Liu, J., Chen, W., Ding, X., and Zhou, D. (2013). Three-dimensional velocity field of present-day crustal motion of the Tibetan Plateau derived from GPS measurements. *Journal of Geophysical Research: Solid Earth*, 118:1–11.

Lippert, P. C., van Hinsbergen, D., and Dupont-Nivet, G. (2014). Early Cretaceous to present latitude of the central proto-Tibetan Plateau: A paleomagnetic synthesis with implications for Cenozoic tectonics, paleogeography, and climate of Asia. *GSA Special Papers*, 507.

Liu-Zeng, J., Tapponnier, P., Gaudemer, Y., and Ding, L. (2008). Quantifying landscape differences across the Tibetan plateau: Implications for topographic relief evolution. *Journal of Geophysical Research*, 113(F4):F04018.

Maggi, A., Jackson, J. A., Priestley, K., and Baker, C. (2000). A re-assessment of focal depth distributions in southern Iran, the Tien Shan and northern India: do earthquakes really occur in the continental mantle? *Geophysical Journal International*, 143(3):629–661.

Magni, V., Faccenna, C., van Hunen, J., and Funiciello, F. (2014). How collision triggers backarc extension: Insight into Mediterranean style of extension from 3-D numerical models. *Geology*, 42(6):511–514.

Magni, V., van Hunen, J., Funiciello, F., and Faccenna, C. (2012). Numerical models of slab migration in continental collision zones. *Solid Earth*, 3(2):293–306.

Manea, V. and Gurnis, M. (2007). Subduction zone evolution and low viscosity wedges and channels. *Earth and Planetary Science Letters*, 264(1-2):22–45.

Manea, V. C., Perez-Gussinye, M., and Manea, M. (2011). Chilean flat slab subduction controlled by overriding plate thickness and trench rollback. *Geology*, 40(1):35–38.

Matte, P., Mattauer, M., Olivet, J. M., and Griot, D. A. (1997). Continental subductions beneath Tibet and the Himalayan orogeny: a review. *Terra Nova*, 9(5-6):264–270.

McKenzie, D. and Sclater, J. G. (1971). The Evolution of the Indian Ocean since the Late Cretaceous. *Geophysical Journal International*, 24(5):437–528.

McNamara, A. and Zhong, S. (2004). The influence of thermochemical convection on the fixity of mantle plumes. *Earth Planet. Sci. Lett.*, 222(2):485–500.

McQuarrie, N. and Chase, C. G. (2000). Raising the Colorado Plateau. *Geology*, 28(1):91–94.

Medvedev, S. (2002). Mechanics of viscous wedges: Modeling by analytical and numerical approaches. *Journal of Geophysical Research*, 107(B6).

Medvedev, S. and Podladchikov, Y. Y. (1999a). New extended thin-sheet approximation for geodynamic applications - I. Model formulation. *Geophysical Journal International*, 136:567–585.

Medvedev, S. E. and Podladchikov, Y. Y. (1999b). New extended thin-sheet approximation for geodynamic applications II. Two-dimensional examples. *Geophysical Journal International*, 136:586–608.

Metcalfe, I. (1996). Gondwanaland dispersion, Asian accretion and evolution of eastern Tethys. *Australian Journal of Earth Sciences*, 43(6):605–623.

Meyer, D. and Jenny, P. (2004). Conservative Velocity Interpolation for PDF Methods. *Proc. Appl. Math. Mech.*, 4:466–467.

Mishin, Y. (2011). *Adaptive multiresolution methods for problems of computational geodynamics*, volume Ph.D. DISS. NO. 20167. ETH, Zurich.

Mishin, Y. A., Gerya, T. V., Burg, J.-P., and Connolly, J. A. D. (2008). Dynamics of double subduction: Numerical modeling. *Physics of the Earth and Planetary Interiors*, 171(1-4):280–295.

Molnar, P. (1988). A Review of Geophysical Constraints on the Deep Structure of the Tibetan Plateau, the Himalaya and the Karakoram, and their Tectonic Implications. *Philosophical Transactions of the Royal Society A: Mathematical, Physical and Engineering Sciences*, 326(1589):33–88.

Molnar, P. and Atwater, T. (1978). Interarc spreading and Cordilleran tectonics as alternates related to the age of subducted oceanic lithosphere. *Earth and Planetary Science Letters*, 41(3):330–340.

Molnar, P., England, P., and Martinod, J. (1993). Mantle Dynamics, Uplift of the Tibetan Plateau, and the Indian Monsoon. *Reviews of Geophysics*, 31:357–396.

Molnar, P. and Lyon-Caen, H. (1988). Some Simple Physical Aspects of the Support, Structure, and Evolution of Mountain Belts. *Geological Society of America Special Paper*, 218:179–207.

Molnar, P. and Stock, J. M. (2009). Slowing of India's convergence with Eurasia since 20 Ma and its implications for Tibetan mantle dynamics. *Tectonics*, 28(3):1–11.

Molnar, P. and Tapponnier, P. (1975). Cenozoic Tectonics of Asia: Effects of a Continental Collision. *Science*, 189:419–426.

Molnar, P. and Tapponnier, P. (1977). The collision between India and Eurasia. *Scientific American*, 236:30–41.

Molnar, P. and Tapponnier, P. (1981). A Possible Dependence of Tectonic Strength on the Age of the Crust in Asia. *Earth and Planetary Science Letters*, 52:107–114.

Moresi, L. (2015). Computational Plate Tectonics and the Geological Record in the Continents. *SIAM News*, 48:1–6.

Moresi, L., Betts, P. G., Miller, M. S., and Cayley, R. A. (2014). Dynamics of continental accretion. *Nature*, 508:245–248.

Moresi, L., Dufour, F., and Mühlhaus, H. (2003). A Lagrangian integration point finite element method for large deformation modeling of viscoelastic geomaterials. *J. Comput. Phys.*, 184(2):476–497.

Moresi, L., Zhong, S., and Gurnis, M. (1996). The accuracy of finite element solutions of Stokes's flow with strongly varying viscosity. *Phys. Earth Planet. Inter.*, 97(1-4):83–94.

Morra, G., Chatelain, P., Tackley, P., and Koumoutsakos, P. (2009). Earth curvature effects on subduction morphology: Modeling subduction in a spherical setting. *Acta Geotechnica*, 4(2):95–105.

Morra, G., Regenauer-Lieb, K., and Giardini, D. (2006). Curvature of oceanic arcs. *Geology*, 34(10):877.

Müller, R. D., Gaina, C., and Clark, S. (2000). Seafloor spreading around Australia. In *Billion-year earth history of Australia and neighbours in Gondwanaland*. University of Sydney, Sydney, Australia.

Müller, R. D., Roest, W. R., Royer, J.-Y., Gahagan, L. M., and Sclater, J. G. (1997). Digital isochrons of the world's ocean floor. *Journal of Geophysical Research: Solid Earth*, 102(B2):3211–3214.

Müller, R. D., Royer, J.-Y., and Lawver, L. A. (1993). Revised plate motions relative to the hotspots from combined Atlantic and Indian Ocean hotspot tracks. *Geology*, 21(3):275.

Nabelek, J., Hetenyi, G., Vergne, J., Sapkota, S., Kafle, B., Jiang, M., Su, H., Chen, J., Huang, B. S., and Team, t. H. C. (2009). Underplating in the Himalaya-Tibet Collision Zone Revealed by the Hi-CLIMB Experiment. *Science*, 325(5946):1371–1374.

Neil, E. A. and Houseman, G. A. (1997). Geodynamics of the Tarim basin and the Tian Shan in central Asia. *Tectonics*, 16(4):571–584.

Owens, T. J. and Zandt, G. (1997). Implications of crustal property variations for models of Tibetan plateau evolution. *Nature*, 387:1–7.

Packham, G. (1996). Cenozoic SE Asia: reconstructing its aggregation and reorganization. *Geological Society, London, Special Publications*, 106(1):123–152.

Patriat, P. and Achache, J. (1984). India-Eurasia collision chronology has implications for crustal shortening and driving mechanism of plates. *Nature*, 311:615–621.

Patzelt, A., Li, H., Wang, J., and Appel, E. (1996). Palaeomagnetism of Cretaceous to Tertiary sediments from southern Tibet: evidence for the extent of the northern margin of India prior to the collision with Eurasia. *Tectonophysics*, 259(4):259–284.

Popov, A. A. and Sobolev, S. V. (2008). SLIM3D: A tool for three-dimensional thermomechanical modeling of lithospheric deformation with elasto-visco-plastic rheology. *Physics of the Earth and Planetary Interiors*, 171(1-4):55–75.

Powell, C. M. and Conaghan, P. J. (1973). Plate tectonics and the Himalayas. *Earth and Planetary Science Letters*, 20(1):1–12.

Powell, C. M. and Conaghan, P. J. (1975). Tectonic models of the Tibetan plateau. *Geology*, 3(12):727.

Powell, C. M., Roots, S. R., and Veevers, J. J. (1988). Pre-breakup continental extension in East Gondwanaland and the early opening of the eastern Indian Ocean. *Tectonophysics*, 155(1-4):261–283.

Pusok, A. E. and Kaus, B. J. P. (2015). Development of topography in 3-D continental-collision models. *Geochemistry, Geophysics, Geosystems*, 16(5):1378–1400.

Quinteros, J., Sobolev, S. V., and Popov, A. A. (2010). Viscosity in transition zone and lower mantle: Implications for slab penetration. *Geophysical Research Letters*, 37(L09307):1–5.

Ranalli, G. (1995). *Rheology of the Earth*. Chapman & Hall, London., 2nd edition.

Reeves, C. and de Wit, M. (2000). Making ends meet in Gondwana: retracing the transforms of the Indian Ocean and reconnecting continental shear zones. *Terra Nova*, 12(6):272–280.

Replumaz, A., Capitanio, F. A., Guillot, S., Negredo, A. M., and Villaseñor, A. (2014). The coupling of Indian subduction and Asian continental tectonics. *Gondwana Research*, 26:608–626.

Replumaz, A., Guillot, S., Villaseñor, A., and Negredo, A. M. (2012). Amount of Asian lithospheric mantle subducted during the India/Asia collision . *Gondwana Research*, pages 1–10.

Replumaz, A., Kárason, H., van der Hilst, R. D., Besse, J., and Tapponnier, P. (2004). 4-D evolution of SE Asia's mantle from geological reconstructions and seismic tomography. *Earth and Planetary Science Letters*, 221(1-4):103–115.

Replumaz, A., Negredo, A. M., Guillot, S., and Villaseñor, A. (2010). Multiple episodes of continental subduction during India/Asia convergence: Insight from seismic tomography and tectonic reconstruction. *Tectonophysics*, 483(1-2):125–134.

Replumaz, A. and Tapponnier, P. (2003). Reconstruction of the deformed collision zone Between India and Asia by backward motion of lithospheric blocks. *Journal of Geophysical Research*, 108(B6):2285.

Ribe, N. M. (2010). Bending mechanics and mode selection in free subduction: a thin-sheet analysis. *Geophysical Journal International*, 180(2):559–576.

Ribe, N. M., Stutzmann, E., Ren, Y., and van der Hilst, R. (2007). Buckling instabilities of subducted lithosphere beneath the transition zone. *Earth and Planetary Science Letters*, 254(1-2):173–179.

Richter, F. M. (1973). Dynamical models for sea floor spreading. *Reviews of Geophysics*, 11(2):223–287.

Rotstein, Y., Munschy, M., and Bernard, A. (2001). The Kerguelen Province revisited: Additional constraints on the early development of the Southeast Indian Ocean. *Marine Geophysical Researches*, 22(2):81–100.

Rowley, D. B. (2007). Stable Isotope-Based Paleoaltimetry: Theory and Validation. *Reviews in Mineralogy and Geochemistry*, 66(1):23–52.

Royden, L. H. (1993). The tectonic expression slab pull at continental convergent boundaries. *Tectonics*, 12(2):303–325.

Royden, L. H. (1996). Coupling and Decoupling of Crust and Mantle in Convergent Orogens: Implications for Strain Partitioning in the Crust. *Journal of Geophysical Research*, 101(B8):17679–17705.

Royden, L. H., Burchfiel, B. C., King, R., Wang, E., Chen, Z., Shen, F., and Liu, Y. (1997). Surface Deformation and Lower Crustal Flow in Eastern Tibet. *Science*, 276(5313):788–790.

Royden, L. H., Burchfiel, B. C., and van der Hilst, R. D. (2008). The Geological Evolution of the Tibetan Plateau. *Science*, 321(5892):1054–1058.

Santosh, M., Maruyama, S., and Yamamoto, S. (2009). Gondwana Research. *Gondwana Research*, 15(3-4):324–341.

Schellart, W. P. (2004). Kinematics of subduction and subduction-induced flow in the upper mantle. *Journal of Geophysical Research: Solid Earth*, 109(B7).

Schellart, W. P. (2008). Kinematics and flow patterns in deep mantle and upper mantle subduction models: Influence of the mantle depth and slab to mantle viscosity ratio. *Geochemistry, Geophysics, Geosystems*, 9(3).

Schellart, W. P. (2010). Evolution of Subduction Zone Curvature and its Dependence on the Trench Velocity and the Slab to Upper Mantle Viscosity Ratio. *Journal of Geophysical Research: Solid Earth*, 115(B11).

Schellart, W. P., Freeman, J., Stegman, D. R., Moresi, L., and May, D. (2007). Evolution and diversity of subduction zones controlled by slab width. *Nature*, 446(7133):308–311.

Schmalholz, S. M., Medvedev, S., Lechmann, S. M., and Podladchikov, Y. (2014). Relationship between tectonic overpressure, deviatoric stress, driving force, isostasy and gravitational potential energy. *Geophysical Journal International*, 197(2):680–696.

Schmeling, H., Babeyko, A. Y., Enns, A., Faccenna, C., Funiciello, F., Gerya, T., Golabek, G. J., Grigull, S., Kaus, B. J. P., Morra, G., Schmalholz, S. M., and van Hunen, J. (2008). A benchmark comparison of spontaneous subduction models - Towards a free surface. *Physics of the Earth and Planetary Interiors*, 171(1-4):198–223.

Schmid, S. M., F genschuh, B., Kissling, E., and Schuster, R. (2004). Tectonic map and overall architecture of the Alpine orogen. *Eclogae Geologicae Helvetiae*, 97(1):93–117.

Schulte-Pelkum, V., Monsalve, G., Sheehan, A., Pandey, M. R., Sapkota, S., Bilham, R., and Wu, F. (2005). Imaging the Indian subcontinent beneath the Himalaya. *Nature*, 435(7046):1222–1225.

Searle, M. P. (2007). Diagnostic features and processes in the construction and evolution of Oman-, Zagros-, Himalayan-, Karakoram-, and Tibetan-type orogenic belts. *Geological Society of America Memoirs*.

Sengor, A. M. C. and Natalin, B. A. (1996). Paleotectonics of Asia: fragments of a synthesis. *The Tectonic Evolution of Asia*, pages 486–641.

Seton, M., Müller, R. D., Zahirovic, S., Gaina, C., Torsvik, T., Shephard, G., Talsma, A., Gurnis, M., Turner, M., Maus, S., and Chandler, M. (2012). Global continental and ocean basin reconstructions since 200 Ma. *Earth Science Reviews*, 113(3-4):212–270.

Sharples, W., Jamadec, M. A., Moresi, L. N., and Capitanio, F. A. (2014). Overriding plate controls on subduction evolution. *Journal of Geophysical Research*, 119:1–21.

Stampfli, G. M. and Borel, G. D. (2002). A plate tectonic model for the Paleozoic and Mesozoic constrained by dynamic plate boundaries and restored synthetic oceanic isochrons. *Earth and Planetary Science Letters*, 196(1–2):17–33.

Stegman, D. R., Farrington, R., Capitanio, F. A., and Schellart, W. P. (2010a). A regime diagram for subduction styles from 3-D numerical models of free subduction . *Tectonophysics*, 483(1-2):29–45.

Stegman, D. R., Freeman, J., Schellart, W. P., Moresi, L., and May, D. (2006). Influence of trench width on subduction hinge retreat rates in 3-D models of slab rollback. *Geochemistry, Geophysics, Geosystems*, 7(3):Q03012.

Stegman, D. R., Schellart, W. P., and Freeman, J. (2010b). Competing influences of plate width and far-field boundary conditions on trench migration and morphology of subducted slabs in the upper mantle . *Tectonophysics*, 483(1-2):46–57.

Steinberger, B. (2000). Plumes in a convecting mantle: Models and observations for individual hotspots. *Journal of Geophysical Research*, 105:11127–11152.

Stern, R. J. (2004). Subduction initiation: spontaneous and induced. *Earth and Planetary Science Letters*, 226(3–4):275–292.

Sternai, P., Avouac, J.-P., Jolivet, L., Faccenna, C., Gerya, T., Becker, T. W., and Menant, A. (2016). On the influence of the asthenospheric flow on the tectonics and topography at a collision-subduction transition zones: Comparison with the eastern Tibetan margin. *Journal of Geodynamics*.

Sternai, P., Jolivet, L., Menant, A., and Gerya, T. (2014). Driving the upper plate surface deformation by slab rollback and mantle flow. *Earth and Planetary Science Letters*, 405:110–118.

Storey, M., Mahoney, J. J., Saunders, A. D., Duncan, R. A., Kelley, S. P., and Coffin, M. F. (1995). Timing of Hot Spot–Related Volcanism and the Breakup of Madagascar and India. *Science*, 267(5199):852–855.

Tackley, P. and King, S. (2003). Testing the tracer ratio method for modeling active compositional fields in mantle convection simulations. *Geochem., Geophys., Geosyst.*, 4(4):1–15.

Tapponnier, P. and Molnar, P. (1976). Slip-Line Field Theory and Large-Scale Continental Tectonics. *Nature*, 264:319–324.

Tapponnier, P., Peltzer, G., and Armijo, R. (1986). On the mechanics of the collision between India and Asia. *Geological Society, London, Special Publications*, 19(1):113–157.

Tapponnier, P., Zhiqin, X., Roger, F., Meyer, B., Arnaud, N., Wittlinger, G., and Jingsui, Y. (2001). Oblique Stepwise Rise and Growth of the Tibet Plateau. *Science*, 294(5547):1671–1677.

Thielmann, M. and Kaus, B. J. P. (2012). Earth and Planetary Science Letters. *Earth and Planetary Science Letters*, 359-360(C):1–13.

Thielmann, M., May, D., and Kaus, B. (2014). Discretization errors in the hybrid finite element particle-in-cell method. *Pure Appl. Geophys.*, 171(9):2165–2184.

Tilmann, F., Ni, J., and INDEPTH, III, S. T. (2003). Seismic imaging of the Downwelling Indian Lithosphere beneath Central Tibet. *Science*, 300(5624):1434–1436.

Torsvik, T. H., Steinberger, B., Gurnis, M., and Gaina, C. (2010). Earth and Planetary Science Letters. *Earth and Planetary Science Letters*, 291(1-4):106–112.

Torsvik, T. H., Tucker, R. D., Ashwal, L. D., Carter, L. M., Jamtveit, B., Vidyadharan, K. T., and Venkataramana, P. (2000). Late Cretaceous India-Madagascar fit and timing of break-up related magmatism. *Terra Nova*, 12(5):220–224.

Toth, J. and Gurnis, M. (1998). Dynamics of subduction initiation at preexisting fault zones. *Journal of Geophysical Research*, 103(B8):18053–18067.

Treloar, P. J. and Coward, M. P. (1991). Indian Plate motion and shape: constraints on the geometry of the Himalayan orogen. *Tectonophysics*, 191(3-4):189–198.

Turcotte, D. L. and Schubert, G. (2002). *Geodynamics*. Cambridge University Press, 2nd edition.

Van der Voo, R., Spakman, W., and Bijwaard, H. (1999). Tethyan Subducted Slabs Under India. *Earth and Planetary Science Letters*, 171:7–20.

van Hinsbergen, D., Steinberger, B., Doubrovine, P., and Gassmölle, R. (2011). Acceleration and deceleration of India-Asia convergence since the Cretaceous: Roles of mantle plumes and continental collision . *J. Geophys. Res: Solid Earth*, 116(B06101).

van Hinsbergen, D. J. J., Lippert, P. C., Dupont-Nivet, G., McQuarrie, N., Doubrovine, P. V., Spakman, W., and Torsvik, T. H. (2012). Greater India Basin hypothesis and a two-stage Cenozoic collision between India and Asia. *PNAS*, 109(20):7659–7664.

van Hunen, J. and Allen, M. B. (2011). Continental collision and slab break-off: A comparison of 3-D numerical models with observations. *Earth and Planetary Science Letters*, 302(1-2):27–37.

van Keken, P., King, S., Schmeling, H., Christensen, U., Neumeister, D., and Doin, M. (1997). A comparison of methods for the modeling of thermochemical convection. *J. Geophys. Res.*, 102(B10):22477–22495.

Veevers, J. J., Jones, J. G., and Talent, J. A. (1971). Indo-Australian Stratigraphy and the Configuration and Dispersal of Gondwanaland. *Nature*, 229(5284):383–388.

Veevers, J. J., Powell, C. M., and Johnson, B. D. (1975). Greater India's place in Gondwanaland and in Asia. *Earth and Planetary Science Letters*, 27(3):383–387.

Velić, M., May, D., and Moresi, L. (2008). A Fast Robust Algorithm for Computing Discrete Voronoi Diagrams. *J. Math. Model. Algor.*, 8(3):343–355.

Vermeer, P. A. and de Borst, R. (1984). Non-Associated Plasticity for Soils, Concrete and Rock. *Heron*, 29:1–64.

Vilotte, J. P., Daignieres, M., Madariaga, R., and Zienkiewicz, O. C. (1984). The role of a heterogeneous inclusion during continental collision. *Physics of the Earth and Planetary Interiors*, 36:236–259.

Vilotte, J. P., Madariaga, R., Daignieres, M., and Zienkiewicz, O. C. (1986). Numerical Study of Continental Collision: Influence of Buoyancy Forces and an Initial Stiff Inclusion. *Geophys. J. R. astr. Soc.*, 84:279–310.

Wang, C., Zhao, X., Liu, Z., Lippert, P. C., Graham, S. A., Coe, R. S., Yi, H., Zhu, L., Liu, S., and Li, Y. (2008). Constraints on the Early Uplift History of the Tibetan Plateau. *PNAS*, 105:4987–4992.

Wang, H., Agrusta, R., and van Hunen, J. (2015). Advantages of a conservative velocity interpolation (CVI) scheme for particle-in-cell methods with application in geodynamic modelling. *Geochem., Geophys., Geosyst.*, 16.

Wang, Y., Mooney, W. D., Yuan, X., and Okaya, N. (2013). Tectonophysics. *Tectonophysics*, 584(C):191–208.

Wei, S., Chen, Y. J., Sandvol, E., Zhou, S., Yue, H., Jin, G., Hearn, T. M., Jiang, M., Wang, H., Fan, W., Liu, Z., Ge, Z., Wang, Y., Feng, Y., and Ni, J. (2010). Regional earthquakes

in northern Tibetan Plateau: Implications for lithospheric strength in Tibet. *Geophysical Research Letters*, 37(19).

Weijermars, R. and Schmeling, H. (1986). Scaling of newtonian and non newtonian fluid dynamics without inertia for quantative modelling of rock flow due to gravity (including the concept of rheological similarity). *Phys. Earth Planet. Inter.*, 43:938–954.

Woidt, W. (1978). Finite-element calculations applied to salt dome analysis. *Tectonophys.*, 50:369–386.

Yang, Y. and Liu, M. (2009). Crustal thickening and lateral extrusion during the Indo-Asian collision: A 3D viscous flow model. *Tectonophysics*, 465(1-4):128–135.

Yang, Y. and Liu, M. (2013). The Indo-Asian continental collision: A 3-D viscous model. *Tectonophysics*, 606:198–211.

Yin, A. and Harrison, T. (2000). Geologic Evolution of the Himalayan-Tibetan Orogen. *Annual Review of Earth and Planetary Sciences*, 28(1):211–280.

Zahirovic, S., Müller, R. D., Seton, M., Flament, N., Gurnis, M., and Whittaker, J. (2012). Insights on the kinematics of the India-Eurasia collision from global geodynamic models. *Geochemistry, Geophysics, Geosystems*, 13(4).

Zeitler, P. K., Meltzer, A. S., Koons, P. O., Craw, D., Hallet, B., Chamberlain, C. P., Kidd, W. S. F., Park, S. K., Seeber, L., Bishop, M., and Shroder, J. (2001). Erosion, Himalayan Geodynamics, and the Geomorphology of Metamorphism. *GSA Today*, pages 1–6.

Zhong, S. (1996). Analytic solutions for Stokes' flow with lateral variations in viscosity. *Geophys. J. Int.*, 124:18–28.

Zhou, H.-w. and Murphy, M. A. (2005). Tomographic evidence for wholesale underthrusting of India beneath the entire Tibetan plateau. *Journal of Asian Earth Sciences*, 25(3):445–457.

Appendix A

A.1 Integration Equations

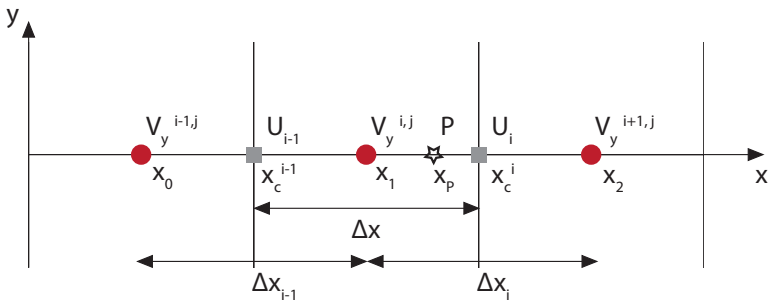

Fig. A.1 Interpolation sketch for staggered grid and V_y velocity component.

The general interpolation schemes used in Chapter 2 are explained in more details below for one velocity component in 1-D. In Figure A.1, three staggered grid points, $V_y^{i-1,j}, V_y^{i,j}, V_y^{i+1,j}$, are located at (x_0, x_1, x_2) points. $(U_{i-1}(x_c^{i-1}), U_i(x_c^i))$ are grid nodes and $P(x_p)$ is a marker point. Whether it is direct interpolation, from staggered points to markers directly, or correction interpolation, that requires interpolation from staggered points to grid nodes, the velocity in the nodes, U_i, is calculated in the following way:

a) Linear interpolation

$$U_i = (1 - x_c^i)(V_y^{i,j} + V_y^{i+1,j}), \tag{A.1}$$

where x_c^i is the local coordinate of the node U_i. The same principle is applied to the other nodes and velocity components. The 3-D tri-linear interpolation scheme is represented by Eq. 2.5 in the main text.

b) Linear interpolation combined with a *minmod* limiter

$$U_i = V_y^{i,j} - \frac{\Delta x}{2} minmod\left(\frac{V_y^{i+1,j} - V_y^{i,j}}{\Delta x_i}, \frac{V_y^{i,j} - V_y^{i-1,j}}{\Delta x_{i-1}}\right), \tag{A.2}$$

$$U_{i-1} = V_y^{i,j} + \frac{\Delta x}{2} minmod\left(\frac{V_y^{i+1,j} - V_y^{i,j}}{\Delta x_i}, \frac{V_y^{i,j} - V_y^{i-1,j}}{\Delta x_{i-1}}\right), \tag{A.3}$$

where the *minmod* slope limiter is defined as:

$$minmod(A,B) = \begin{cases} A, & \text{if } A \cdot B > 0 \text{ and } |A| \leq |B| \\ B, & \text{if } A \cdot B > 0 \text{ and } |A| > |B| \\ 0, & \text{if } A \cdot B \leq 0 \end{cases} \tag{A.4}$$

c) Quadratic interpolation - calculates one quadratic curve, passing through all three staggered velocity points. As such, the velocity at the node or any point is calculated as:

$$U_i = ax^2 + bx + c, \tag{A.5}$$

where $x = x_c^i$ and the coefficients a, b, c are given by:

$$a = \frac{V_y^{i-1,j}}{(x_0 - x_1)(x_0 - x_2)} + \frac{V_y^{i,j}}{(x_1 - x_0)(x_1 - x_2)} + \frac{V_y^{i+1,j}}{(x_2 - x_0)(x_2 - x_1)} \tag{A.6}$$

$$b = \frac{V_y^{i-1,j} - V_y^{i,j}}{x_0 - x_1} - a(x_0 + x_1) \tag{A.7}$$

$$c = V_y^{i-1,j} - ax_0^2 - bx_0. \tag{A.8}$$

d) Spline quadratic interpolation - calculates two quadratic curves, one between $V_y^{i-1,j}$ and $V_y^{i,j}$ and another between $V_y^{i,j}$ and $V_y^{i+1,j}$, and the derivative is continuous at $V_y^{i,j}$. As such, the velocity at the node is calculated as:

$$U_{i-1} = a_1 x^2 + b_1 x + c_1, \text{with } x = x_c^{i-1} \tag{A.9}$$

$$U_i = a_2 x^2 + b_2 x + c_2, \text{with } x = x_c^{i} \tag{A.10}$$

and where the coefficients $a_1, b_1, c_1, a_2, b_2, c_2$ are given by:

$$a_1 = 0 \tag{A.11}$$

$$b_1 = \frac{V_y^{i,j} - V_y^{i-1,j}}{x_1 - x_0} \tag{A.12}$$

$$c_1 = V_y^{i-1,j} - b_1 x_0 \tag{A.13}$$

$$a_2 = \left(\frac{V_y^{i,j} - V_y^{i+1,j}}{x_1 - x_2} - b_1 \right) \frac{1}{x_2 - x_1} \tag{A.14}$$

$$b_2 = b_1 - 2a_2 x_1 \tag{A.15}$$

$$c_2 = V_y^{i,j} - b_2 x_1 - a_2 x_1^2 \tag{A.16}$$

A.2 Extended results

In this section we present the full results for the experiments performed in the Section 2.4. Figure A.2 shows results for the SolCx benchmark for different resolutions, initial marker distribution and viscosity contrasts. Figure A.2a-b show that marker artifacts occur for all interpolation schemes, with the exception of **LinP** and **CorrMinmod**, and are independent of initial marker distribution and resolution. Further tests (Figure A.2c) suggest that artifacts become visible and problematic for $\Delta\eta > 10^3$. Figure A.3 shows results for all the interpolation methods for the Rayleigh-Taylor instability test.

A.3 Efficient marker control routine for marker-in-cell method

While an effective marker-in-cell (MIC) method should have an even distribution of markers, in fact the method requires only non-empty cells. Clustering of markers then becomes mainly a problem of increasing computational memory required by the simulation. LaMEM is more sensitive to the non-uniform distribution of markers because interpolation of material properties from markers to the grid is performed in four control volumes (centre cells, and three edge cells related to each velocity component). This implies that, if there are empty

SolCx benchmark

a) Resolution (same initial marker distribution)

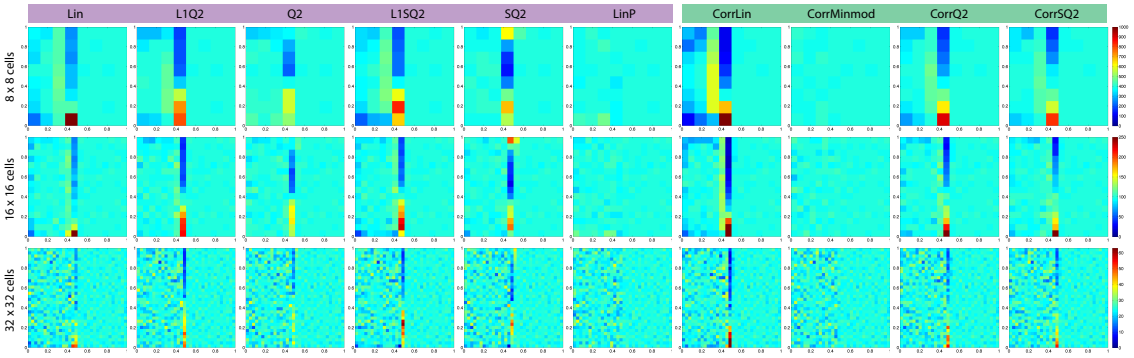

b) Higher initial marker distribution (resolution 32 x 32 cells)

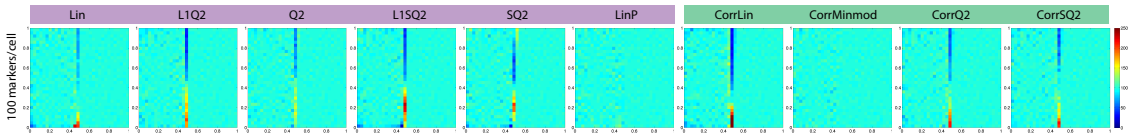

b) Viscosity contrast

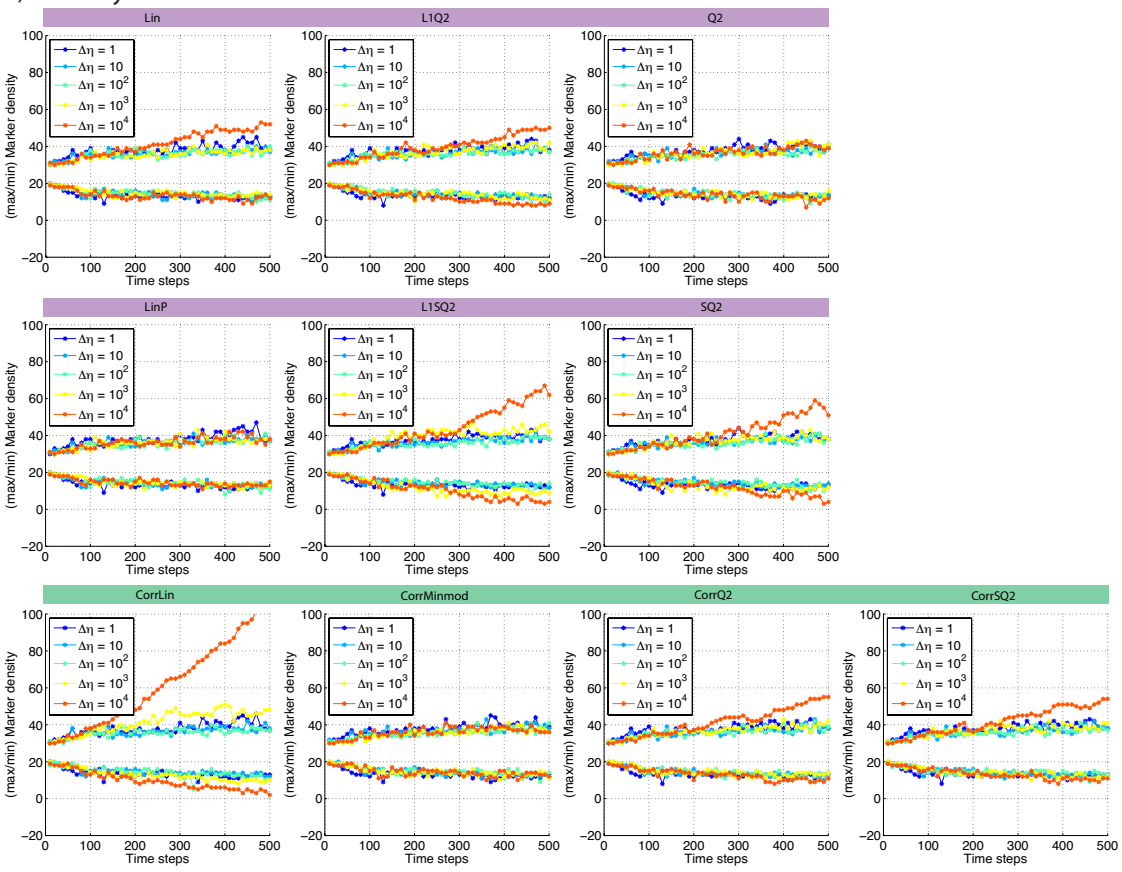

Fig. A.2 Extended results for the SolCx benchmark.

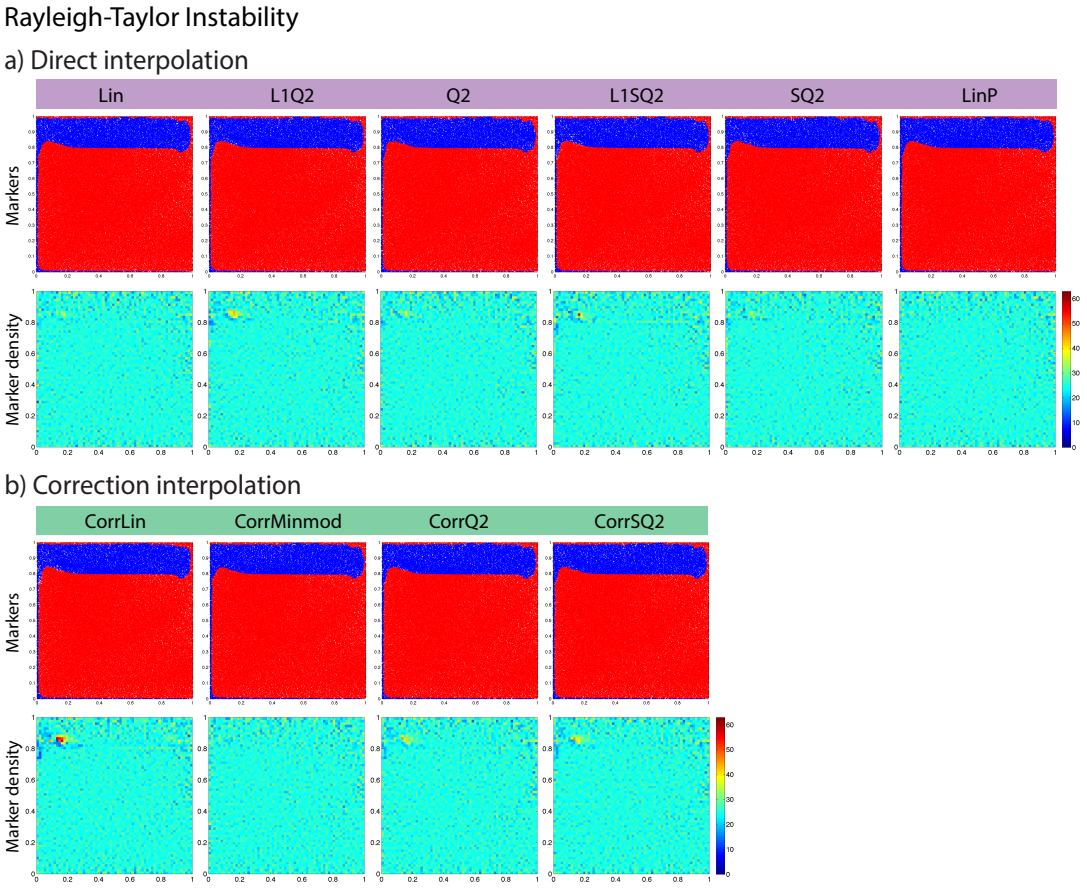

Fig. A.3 Extended results for the Rayleigh-Taylor instability test.

edge volumes regardless that all centre volumes have non-zero marker density, the simulation will stop.

Chapter 2 shows that the choice of velocity interpolation (i.e. **CorrMinmod**, **LinP**) reduces considerably the occurrence of empty cells, but might not eliminate the problem completely. Increasing the resolution and/or marker densities potentially solves this. However, the MIC is a computationally expensive method, especially in 3-D, such that limiting the number of markers is preferable. As such, controlling the marker distribution (i.e. inject/delete) can be useful in cases when it happens. We propose that a marker control routine based on an approximate Voronoi diagram algorithm [*Velić et al.*, 2008], combined with a conservative velocity interpolation and a 4th order Runge-Kutta advection scheme can provide a powerful advection tool in geodynamic models.

In the following part, we describe here two methods of performing marker control:

1. **Distance based method.** This algorithm, popular among geodynamicists, generates a random marker within an empty control volume, by calculating the closest marker (parent) to that point. The new marker then inherits the material properties of the parent marker. The advantage of this routine is that it is easy to implement and the choice of control volume is flexible (i.e. either an entire cell volume or a subgrid of the cell). However, this algorithm does not have a control on the upper limit of marker number (i.e. markers are only injected, but not deleted) and this can increase the memory considerably.

2. **Using an approximate Voronoi diagram algorithm (AVD).** The AVD algorithm [*Velić et al.*, 2008] allows to calculate Voronoi ownership domains for every marker in the control volume and insert markers where there is more empty space or delete markers from large accumulations. The algorithm is executed every time the marker population in the control volume is outside the minimum and maximum number of markers per cell allowed (i.e. N_{min} and N_{max}), which are user defined. The challenge of this algorithm is that its accuracy depends on AVD resolution, such that setting up good numerical parameters requires some practice.

   Previous authors used a centroid based method to calculate the position of new markers [*Mishin*, 2011]. This means that the new particle is added to the centroid of corresponding Voronoi cell. The centroid coordinate vector $x_{centroid}$ is computed as in *Mishin* [2011]:

$$x_{centroid} = \frac{\sum_{i=1}^{n_{cl}} x_{cl}^{i}}{n_{cl}}, \tag{A.17}$$

where x_{cl}^{i} and n_{cl} are the coordinate vectors and the total number of the lattice cells constituting the Voronoi cell. We noticed that with this formulation combined with low resolution of the Voronoi diagram, the location of the centroid often coincides with the location of the parent particle (i.e. for a square Voronoi cell). For this reason, we propose to use a half centroid method to distribute markers more evenly and relax the Voronoi resolution parameters. The method is as follows:

(a) Calculate the maximum elongation axis of the Voronoi cell: $h = max(x_{axis}, y_{axis})$,

(b) Split the Voronoi cell in two along the maximum elongation axis and check the location of the parent marker, such that one sub-cell contains the marker and another one is "empty",

(c) Calculate the centroid of the "empty" sub-cell.

To show the advantages of one method over another, they have both been implemented in a 2-D Matlab code (the same as the one used in Chapter 2 and written by the author), and the 3-D code LaMEM [*Kaus et al.*, 2016]. Here, we show some tests in Matlab and some performance results in LaMEM. For LaMEM we run the AVD algorithm in all 4 control volumes (centre cells, and three cells related to each velocity component). A single-cell based implementation would require only one AVD cycle (i.e. for the centre cells.)

Figure A.4 shows the behaviour of the AVD algorithm with different values of N_{min} and N_{max} and the difference between centroid-formulations and half-centroid formulations. The half-centroid method (injected markers are plotted as stars) behaves significantly better than the centroid method (injected markers plotted as empty circles), in which the new marker coordinate is closer to the parent marker (filled circles).

Figure A.5 shows how a combined AVD algorithm works for all control volumes (i.e. centre cell, V_x and V_y).

Figure A.6 shows an example of full AVD algorithm and that with multiple control volumes, the parameters N_{min} and N_{max} can be relaxed considerably. The results show that an efficient marker control routine is obtained by performing an AVD cycle for every control volume with a half-centroid method for calculating the position of new markers.

Figure A.7 shows the performance of the distance-based method and the AVD method for LaMEM for the subduction setup with sticky air (same as in Chapter 2, Results section). We test these 2 methods in LaMEM, and for different interpolation and advection methods. The first method involves doing an AVD check for centre cells and then a corner check (old method), while the second method involves doing AVD checks for all control volumes (new method).

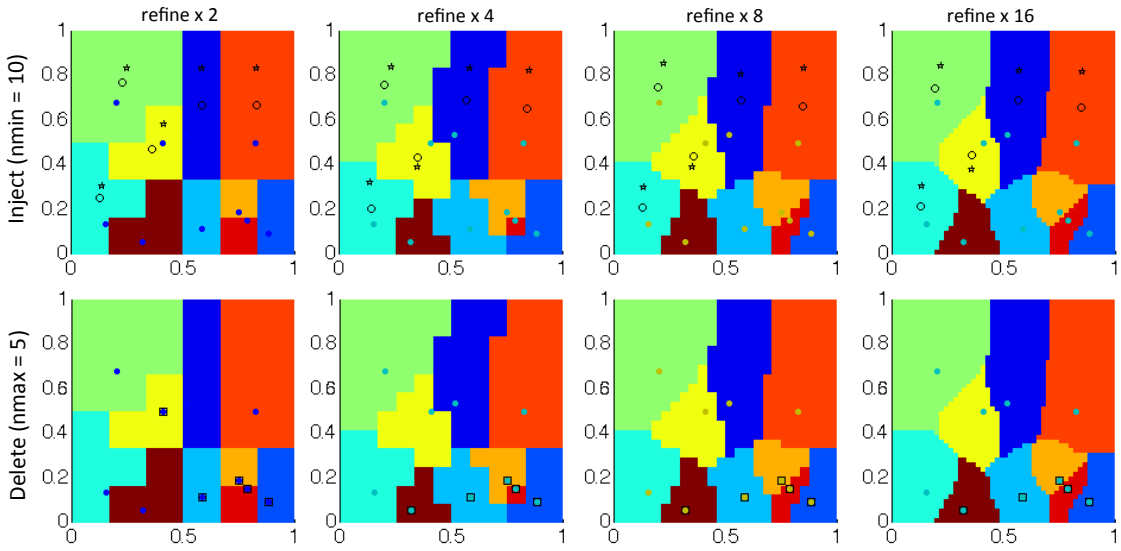

Fig. A.4 Example of AVD algorithm in one control volume. a) A case when $N_{min} = 10$, and the algorithm injects markers. The empty circles are the new markers calculated using the centroid method, while stars are new markers based on half-centroid method. b) A case when $N_{max} = 5$, and the algorithm deletes markers. The markers to be deleted are indicated with squares.

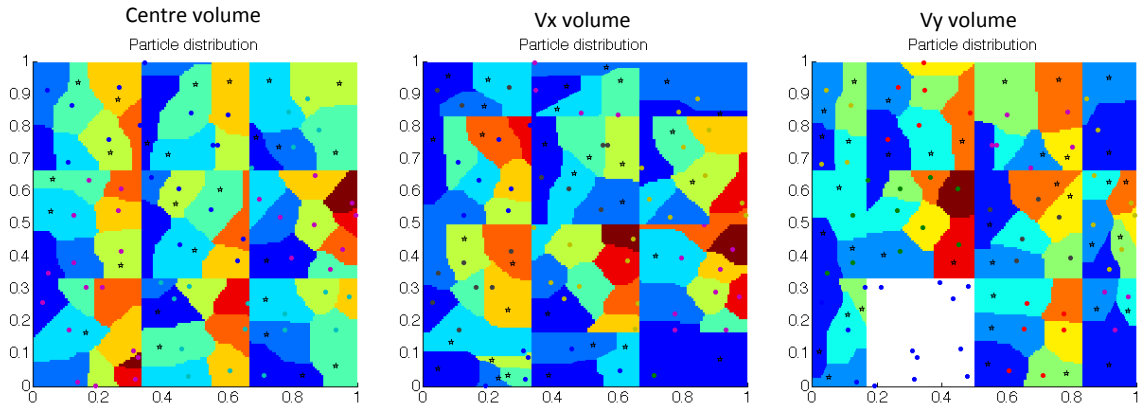

Fig. A.5 Example of AVD algorithm for every control volume.

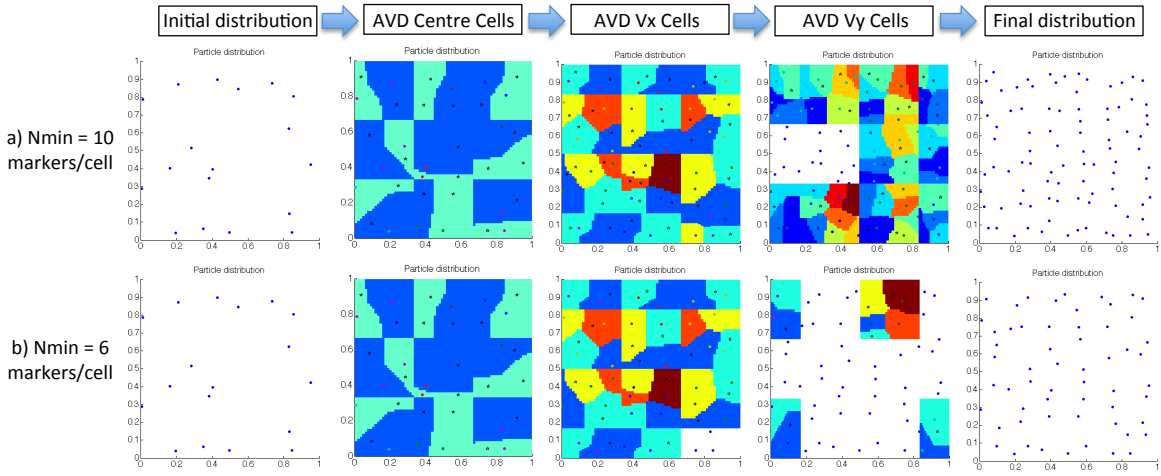

Fig. A.6 Example of an entire AVD cycle.

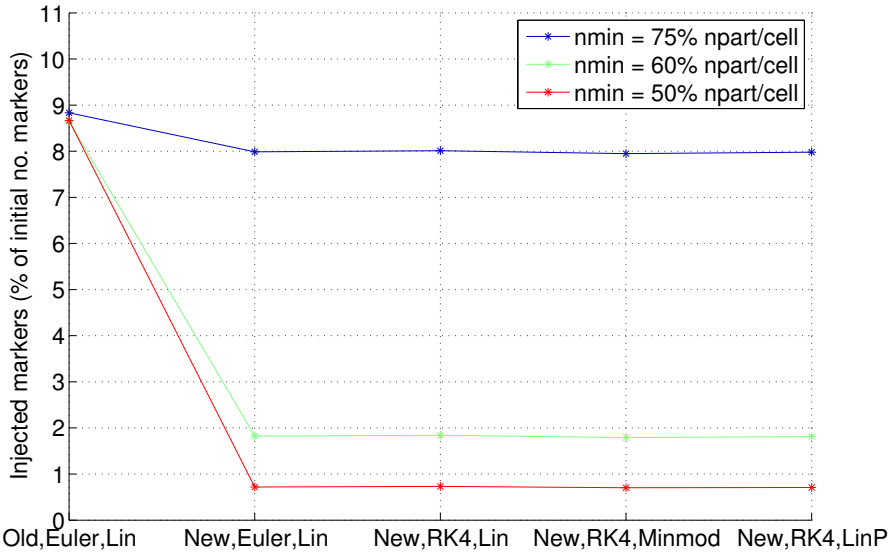

Fig. A.7 Performance of the marker control routines for a subduction setup with sticky air.

Appendix B

B.1 Scaling analysis

B.1.1 Mountain building processes

To form mountain ranges, horizontal forces must be applied to lithospheric plates, to drive them together and to cause crustal shortening and thickening. Isostatic compensation of the thickened crust then buoys up the mountain range to form high topographic amplitudes relative to the lowlands. When crustal shortening occurs, the forces driving the material together do work against resistive stresses, mainly against gravity. Thus the formation of both mountains and crustal roots is associated with an increase in gravitational potential energy, and part of the work done by forces that drive the plates together creates that potential energy.

Gravitational potential energy

The potential energy is defined as the line integral of a force causing displacement integrated along the component of displacement:

$$\int \overrightarrow{F} \cdot \overrightarrow{ds}. \tag{B.1}$$

We consider the potential energy stored in a column of material of unit cross-sectional area, which is the potential energy per unit surface of the earth (Fig. B.1a) [*England and McKenzie*, 1982; *Molnar and Lyon-Caen*, 1988; *Schmalholz et al.*, 2014; *Turcotte and Schubert*, 2002]. The vertical force per unit area is the product of gravity, density, and thickness of the overlying layer (ρgh). Work is done against such a force in the vertical direction. The potential energy per unit area of a column of material above a given depth can be calculated as the integral of the lithostatic pressure from the Earth's surface to that depth.

If the compensation depth is taken at a certain depth in the mantle ($z = H_0 + \Delta H + h_m$), the lithostatic pressure in the lowlands, $P_L(z)$, is given by:

$$P_L(z) = \rho_c g H_0 + \rho_m g(\Delta H + h_m) \tag{B.2}$$

where ρ_c and ρ_m are the densities of the crust and mantle, assumed constant here, and H_0 is the crustal thickness. In a mountainous region or a plateau with an elevation of h and a crustal root extending to a depth ΔH beneath the normal crustal thickness H_0, the lithostatic pressure, $P_M(z)$ can written as:

$$P_M(z) = \rho_c g(h + H_0 + \Delta H) + \rho_m g h_m \tag{B.3}$$

with $-h \leq 0 \leq H_0 + \Delta H + h_m$. Isostatic compensation requires that the lithostatic pressure at depth $z = H_0 + \Delta H$ is constant, and $P_L = P_M$, therefore, $\Delta\rho\Delta H = \rho_c H$, where $\Delta\rho = \rho_m - \rho_c$.

The difference in potential energy per unit area beneath the mountains and lowlands is:

$$\begin{aligned} \Delta GPE &= \int_{-h}^{H_0+\Delta H+h_m} [P_M(z) - P_L(z)]dz \\ &= \rho_c g h(\frac{h}{2} + H_0 + \Delta H + h_m) \\ &\quad -\Delta\rho g \Delta H(\frac{\Delta H}{2} + h_m) \end{aligned} \tag{B.4}$$

Considering the depth of compensation at the bottom of the crustal root ($z = H_0 + \Delta H$), the change in potential energy between mountains and lowlands becomes:

$$\begin{aligned} \Delta GPE &= \rho_c g h(\frac{h}{2} + H_0 + \Delta H) - \Delta\rho g \frac{\Delta H^2}{2} \\ &= \rho_c g h(\frac{h}{2} + H_0 + \frac{\Delta H}{2}). \end{aligned} \tag{B.5}$$

Change in GPE per unit length

Molnar and Lyon-Caen [1988] explored further the considerations for gravitational potential energy in the formation of mountain ranges. They showed that when the forces driving the plates together can no longer supply the energy needed to elevate a high range or a plateau higher, the mountain range is likely to grow laterally in width instead of increasing in height. This can be shown with a simple mathematical argument.

As shown previously, the potential energy created in a crustal layer displaced horizontally by an amount d, such that a mountain range of width w and height h forms (Eq. B.6), is

given by:

$$\Delta GPE(w,h,d) = \rho_c g w h(\frac{h}{2} + H_0 + \frac{\Delta H}{2}). \tag{B.6}$$

If there is a further displacement d, such that the total displacement is $2d$, *Molnar and Lyon-Caen* [1988] note that there are 2 possibilities for deformation: one in which the elevation could increase to $2h$ and the thickness of root would increase to $2\Delta H$, or another when the width increases to $2w$. In the first case, the potential energy per unit length is:

$$\Delta GPE(w,2h,2d) = 2\rho_c g w h(h + H_0 + \Delta H). \tag{B.7}$$

And in the second, is:

$$\Delta GPE(2w,h,2d) = 2\rho_c g w h(\frac{h}{2} + H_0 + \frac{\Delta H}{2}). \tag{B.8}$$

The difference in potential energy per unit length of a range created by doubling its width from that created by doubling its height is:

$$\begin{aligned} \delta GPE &= \Delta GPE(w,2h,2d) - \Delta GPE(2w,h,2d) \\ &= \rho_c g w h(h + \Delta H) \\ &= \frac{\rho_c \rho_m}{\Delta\rho} g w h^2. \end{aligned} \tag{B.9}$$

Equation (B.10) shows that due the square dependence on h, more work must be done to increase the range in height than laterally.

A similar reasoning can be done to illustrate that shortening a half-width area $w/2$ to elevate it to a height h, requires half the energy required to elevate an area of width w. This suggests that extra energy is available to elevate the mountain range of width $w/2$ by at least 50% more ($> 1.5h$).

$$\Delta GPE(w/2,1.5h) = \frac{3}{4}\rho_c g w h(\frac{3h}{4} + H_0 + \frac{3\Delta H}{4}). \tag{B.10}$$

Then the difference in potential energy per unit length is:

$$\begin{aligned} \delta GPE &= \Delta GPE(w,h) - \Delta GPE(w/2,1.5h) \\ &= \rho_c g w h(\frac{7H_0}{16} - \frac{h}{16} - \frac{\Delta H}{16}) \\ &= \rho_c g w h(\frac{7H_0}{16} - \frac{h}{16}(1 + \frac{\rho_c}{\Delta\rho})) > \frac{h}{4} > 0 \end{aligned} \tag{B.11}$$

The inequality in (B.12) is true for natural parameters, for example, if one assumes that $H_0 > 2h$ and that $(1+\frac{\rho_c}{\Delta\rho}) < 10$, which are reasonable assumptions for crustal geometries and materials. We explore the importance of this inequality, due to its connection to shortening a homogeneous layer versus shortening a heterogeneous layer (i.e. with strong crustal blocks). In the presence of heterogenous crustal blocks, less material is available for deformation (i.e. shorter width), the energy has a finite space for propagation, and we can expect further uplift, compared to a homogenous layer case. This will be seen later in simulation results with or without the presence of strong blocks.

Resisting stresses

Viscous forces also resist the deformation driven by the compressional forces. In a viscous medium, these stresses can be approximated as:

$$\sigma = 2\eta\dot{\varepsilon} \sim 2\eta\frac{u_0}{L} \tag{B.12}$$

where L is a characteristic length, $\dot{\varepsilon_0} = \frac{u_0}{L}$ is the characteristic strain rate of the system, η_0 is the viscosity of the crustal material and u_0 is the horizontal convergence velocity.

Maximum height

As seen before, it is more favourable to propagate higher amplitudes laterally than vertically. Therefore, for a given driving force, the mountain range will not necessarily reach a higher elevation. Instead, the mountain range should reach a limiting elevation and crustal thickness before the energy starts spreading laterally, regardless of how strong the materials constituting them. The maximum elevation of a mountain range for a certain applied force, is found from:

$$\rho_c g h(\frac{h}{2} + H_0 + \frac{\rho_c h}{2\Delta\rho}) = 2\eta\frac{u_0}{L}d \tag{B.13}$$

$$\frac{1}{2}\rho_c g h^2(1+\frac{\rho_c}{\Delta\rho}) + \rho_c g H_0 h - 2\eta\frac{u_0}{L}d = 0 \tag{B.14}$$

The last equation is a quadratic equation in h of the form $ah^2+bh+c=0$, where the maximum elevation can be calculated as:

$$h_{max} = \frac{b}{2a} = \frac{\Delta\rho}{\rho_m}H_0 \tag{B.15}$$

B.1.2 Argand number

Based on the above considerations, *England and McKenzie* [1982] defined the Argand number, which is the ratio between an estimate of the excess pressure arising from a crustal thickness contrast of order L and the stress required to deform the medium at a strain rate characteristic of the system:

$$Ar = \frac{P(L)}{\tau(\dot{\varepsilon}_0)} \tag{B.16}$$

where $P(L)$ is the excess pressure in the system and $\tau(\dot{\varepsilon}_0)$ is the viscous resistive stresses at the characteristic strain rate.

The Argand number predicts that at high values, the excess pressure will dominate and the material will flow due to pressure gradients, while for a low Argand number, the viscous stresses are high and can sustain higher pressures and higher elevations. As such, the Argand number can be interpreted as a measure of the competition between two processes: relaxation in the vertical plane due to buoyancy forces which tends to produce a plane strain situation, and a horizontal flow controlled by the geometry and the boundary conditions in the horizontal plane.

However, different formulations of the Argand number can be found in the published literature, depending on the complexity assumed in models and the definition of the characteristic length scale, L: original formulation for power-law rheology [*England and McKenzie*, 1982], plastic rheology [*Vilotte et al.*, 1986], temperature formulation [*England and Houseman*, 1989], or more recently, a buoyancy formulation [*Bajolet et al.*, 2013]. The Argand number was also applied to other phenomena such as salt tectonics [*Fernandez and Kaus*, 2014]. Moreover, some authors have used a variation of the Argand number, called the Ramberg number, *Rm* [*Medvedev*, 2002; *Weijermars and Schmeling*, 1986].

The Argand number was calculated here using different choices of the characteristic length scale, L, as defined in the literature: the initial thickness of the lithosphere $L = H_0$, the indenting distance $L = W_0 - W_f$, and the width of the continental indentor $L = W_0$ [*Vilotte et al.*, 1986]. Despite the different choices, all formulations show the same trend. Moreover, we note that formulations that contain only initial values [*England and McKenzie*, 1982] have a greater advantage over those that need information about the final stages of evolution (i.e. *Bajolet et al.* [2013]). This suggests that initial conditions prior to collision already allows prediction of the outcome of the simulation. Therefore, we keep with the original formulation from *England and McKenzie* [1982], where the Argand number for a viscous material is given by:

$$Ar = \frac{\rho_c g H_0 (1 - \frac{\rho_c}{\rho_m})}{\eta (u_0 / H_0)} \tag{B.17}$$

where $\dot{\varepsilon}_0 = u_0/H_0$ is the characteristic strain rate, η is the effective viscosity, ρ_c and ρ_m are the densities of the crust and mantle, u_0 characteristic velocity (convergence velocity), H_0 thickness of lithosphere, and g is the gravitational acceleration.

Gravitational flow

When the forces driving convergence and sustaining mountain growth are removed or diminished (as a result of slab break-off), the system will try to minimize the excess of potential energy. In this case, the material will flow laterally by gravitational flow, and we show that the topographic amplitude decreases exponentially with time. Let us consider an elevated area of radius r as in Fig. B.1b, surrounded by lowlands, with a difference in height of h. The compensation depth is taken at $z = H_0$. The upward and downward force acting on the flanks of the mountains are:

$$\begin{aligned} F_{up} &= p_M A = \rho_c g (H_0 + h) \pi r^2 \\ F_{down} &= p_L A = \rho_c g H_0 \pi r^2 \end{aligned} \tag{B.18}$$

Therefore, the net buoyancy force is:

$$F_{buoy} = F_{up} - F_{down} = \rho_c g h \pi r^2. \tag{B.19}$$

The viscous resistance acts to hamper the fast lateral collapse of the flanks. The viscous resistance in a cylinder can be approximated as:

$$\begin{aligned} F_{res} &= \tau \times 2\pi r H_0 \\ &= 2\eta \dot{\varepsilon} \times 2\pi r H_0 \\ &\sim 4\pi H_0 \eta u_o \end{aligned} \tag{B.20}$$

From the force balance, $F_{buoy} = F_{res}$, we have:

$$\frac{u_0}{h} = \frac{\rho g r^2}{4\eta H_0}. \tag{B.21}$$

The time dependence of h can be determined from the continuity equation [*England and McKenzie*, 1982]:

$$\frac{\partial u}{\partial t} = -\nabla \cdot (hu) \tag{B.22}$$

Combining the last two equations, it follows that:

$$\frac{u_0}{h} = \frac{\rho g r^2}{4\eta H_0} = -\frac{1}{h}\frac{\partial h}{\partial t} \tag{B.23}$$

Integrating, we obtain an exponential decay of h with time t:

$$h = h_0 \mathrm{e}^{-\frac{\rho_c g r^2 t}{4\eta H_0}} \tag{B.24}$$

where h_0 is the maximum amplitude before gravitational flow. Equation B.24 can be rewritten as:

$$h = h_0 \mathrm{e}^{-\frac{t}{t_r}} \tag{B.25}$$

where t_r, the characteristic time for exponential relaxation of the flanks, is given by:

$$t_r = \frac{4\eta H_0}{\rho_c g r^2} \tag{B.26}$$

B.2 Initial buoyancy ratio

Fig. B.2 shows the evolution of topographic amplitude during homogenous shortening for different densities of the crust. The evolution of topographic amplitude is given by [*Turcotte and Schubert*, 2002]:

$$\begin{aligned} h &= H_0(1-\frac{\rho_c}{\rho_m})(\beta-1) \\ \beta &= \frac{W_0}{W} \end{aligned} \tag{B.27}$$

where β is the compression factor and is the ratio between the initial width and the current width, H_0 is the initial thickness, ρ_c is the density of the crust, and ρ_m is the density of the mantle. Fig. B.2 shows that with increasing compression (or with time if compressional forces are kept constant), the topographic amplitude of a lighter crust increases faster than for a denser crust. This phenomenon is also observed in our numerical results, that simulations with a lighter crust that are subjected to compression, will develop higher topographic amplitudes on average compared to simulations with a less dense crust.

B.3 Numerical simulations

Parameters for the simulations displayed in figures are given in Table B.1.

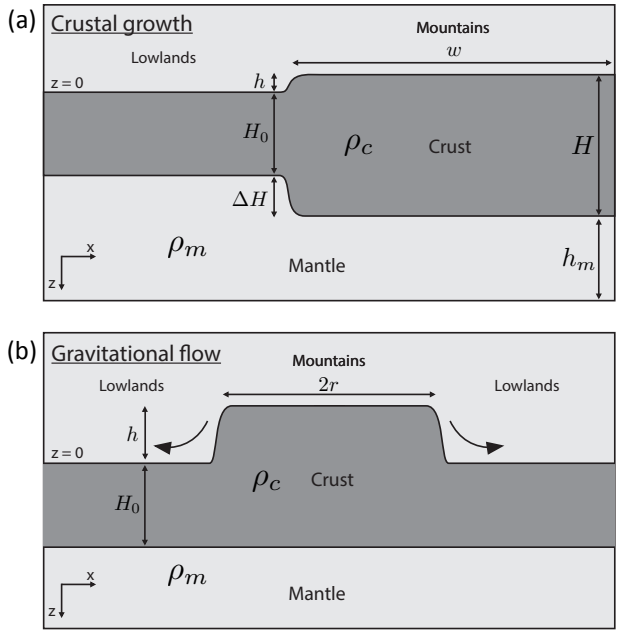

Fig. B.1 a) Sketch of building gravitational potential energy in mountain building. b) Sketch of forces during gravitational flow.

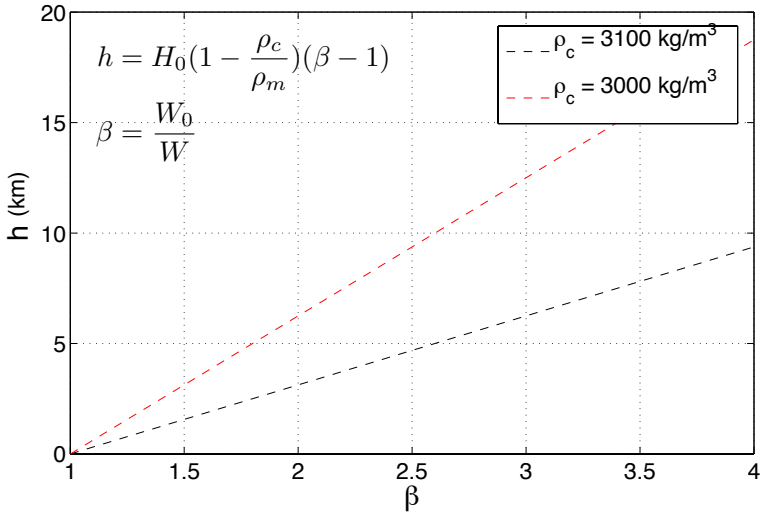

Fig. B.2 Topographic amplitude growth during homogenous shortening. h represents topography amplitude in km, and β represents the compression factor and is the ratio between the initial width and the current width. Calculations are done for two crustal densities to show that for a lighter crust, topographic amplitude increases faster during shortening compared for the case with a denser crust.

Parameter values displayed in the figures													
Simulation	ρ_{OUM}	η_{OUM}	ρ_{OC}	η_{OC}	ρ_{IUM}	η_{IUM}	ρ_{IC}	η_{IC}	ρ_{AUM}	η_{AUM}	ρ_{AC}	η_{AC}	Forcing
B00	3300	1e23	3200	1e20	3100	1e23	3100	5e20	3000	1e22	3000	1e22	FS
C00 (ref)	3300	1e23	3200	1e20	3100	1e23	3100	5e20	3000	1e21	3000	1e22	FS
SBB00	3300	1e23	3200	1e20	3100	1e23	3100	5e20	3000	1e22	3000	1e22	SB
P5B00	3300	1e23	3200	1e20	3100	1e23	3100	5e20	3000	1e22	3000	1e22	EF
SBP5B00	3300	1e23	3200	1e20	3100	1e23	3100	5e20	3000	1e22	3000	1e22	EF+SB
SBP5UPA01	3300	1e23	3100	1e20	3100	1e23	3100	5e20	3000	1e21	3000	1e21	EF+SB
SBP5UPA08	3300	1e23	3100	1e20	3100	1e23	3100	5e20	3100	1e21	3100	1e21	EF+SB
SBP5UPA29	3300	1e23	3100	1e20	3100	1e23	3100	5e20	3000	1e23	3000	1e23	EF+SB
SBP5UPA36	3300	1e23	3100	1e20	3100	1e23	3100	5e20	3100	1e23	3100	1e23	EF+SB

Table B.1 Parameters table for the simulations displayed in figures. Each phase has 2 properties: density (ρ) and viscosity (η). Values are in [ρ] = kg/m^3 and [η] = Pa.s. Phases: OUM - Oceanic Upper Mantle Lithosphere, OC - Oceanic Crust, IUM - Indentor Upper Mantle Lithosphere, IC - Indentor Crust, AUM - Asian Upper Mantle Lithosphere, AC - Asian Crust. In addition, the properties of the asthenospheric mantle ($\rho_m = 3200$ kg/m^3, $\eta_m =$ 1e20 Pa.s), the air ($\rho_{air} = 0$ kg/m^3, $\eta_{air} =$ 1e18 Pa.s) and lower mantle ($\rho_{LM} = 3250$ kg/m^3, $\eta_{LM} =$ 1e21 Pa.s) are the same for all simulations. Symbols in the right column mean: FS - free subduction, SB - with strong blocks ($\rho_{SB} = 3100$ kg/m^3, $\eta_{SB} =$ 5e23 Pa.s) and EF - external forcing with V_{push} = 5 cm/yr. Due to the small number of models displayed in this paper, the nomenclature of all models is as follows: 1) a set of simulations with FS are labeled A, B, C and represent simulations where slab and continental indentor parameters were tested, 2) another set of simulations with FS are labeled UPA, UPB, UPC in which upper plate parameters were tested, and 3) simulations with EF just have an additional prefix SB for strong blocks and/or P5 for pushing with V_{push} = 5 cm/yr.

Curriculum Vitae